A thesis entitled

Studies on the Fabrication of GaAs Nanoparticles and Nanostructures by Ultrafast Laser Ablation: Applications in SERS and Photonics

Submitted to

University of Hyderabad

Towards partial fulfillment for the degree of

Doctor of Philosophy

in

Physics

by

Akkanaboina Mangababu

(17PHPH19)

Under the supervision of

Prof. S V S Nageswara Rao

School of Physics, University of Hyderabad
Hyderabad 500046, Telangana, India

June 2023

Declaration

I, **Akkanaboina Mangababu**, hereby declare that the work reported in this thesis entitled **"Studies on the Fabrication of GaAs Nanoparticles and Nanostructures by Ultrafast Laser Ablation: Applications in SERS and Photonics"** is original and has been carried out by me under the supervision of **Prof. S V S Nageswara Rao**, Professor in School of Physics, University of Hyderabad, Hyderabad, Telangana, India. As per the Ph.D. ordinances of the University, the thesis plagiarism is within the permissible limits. I further declare that this work has not been submitted previously in part or in full to this or any other university or institution for the award of any degree or diploma. I hereby agree that my thesis can be deposited in Shodhganga/INFLIBNET.

A report on plagiarism statistics from the University Librarian is enclosed.

Mangababu 22/06/2023

(Akkanaboina Mangababu)

Reg. No: 17PHPH19

Certificate

This is to certify that the thesis entitled "**Studies on the Fabrication of GaAs Nanoparticles and Nanostructures by Ultrafast Laser Ablation: Applications in SERS and Photonics**" submitted by **Mr. AKKANABOINA MANGABABU** bearing Reg. No. 17PHPH19 in fulfilment of the requirements for the award of Doctor of Philosophy in Physics is a bonafide work carried out by him under my supervision and guidance.

As per the Ph.D. ordinances of the University, the thesis plagiarism is within the permissible limits and it has not been submitted previously in part or in full to this or any other university or institution for the award of any degree or diploma.

Further, the student has the following publications before the submission of the thesis for adjudication.

[1] **Mangababu Akkanaboina**, Dipanjan Banerjee, Kanaka Ravi Kumar, R Sai Prasad Goud, Venugopal Rao Soma, SVS Nageswara Rao, **Surfaces and Interfaces 36, 102563 (2023).** https://doi.org/10.1016/j.surfin.2022.102563. [**Chapter-5]**

[2] **A Mangababu**, R Sai Prasad Goud, Chandu Byram, Jagannath Rathod, Dipanjan Banerjee, Venugopal Rao Soma, SVS Nageswara Rao, **Applied Surface Science 589, 152802 (2022)**. https://doi.org/10.1016/j.apsusc.2022.152802. [**Chapter-4]**

[3] **A Mangababu**, Dipanjan Banerjee, Kanaka Ravi Kumar, R. Sai Prasad Goud, Venugopal Rao Soma, and S. V. S. Nageswara Rao, **Journal of Laser Applications 34, 032014 (2022)**. https://doi.org/10.2351/7.0000750. **[Chapter-4]**

[4] **A Mangababu**, Ch. Sianglam, B. Chandu, DK Avasthi, S. Venugopal Rao, M. Motapothula, and S. V. S. Nageswara Rao, **Journal of Electronic Materials volume 50, 1742–1751 (2021)**. https://doi.org/10.1007/s11664-020-08610-zÓ2021. **[Chapter-3]**

(P.T.O).

[5] **Mangababu**, G. Sarang Dev, B. Chandu, M.S.S. Bharati, P. Debashish, S. Venugopal Rao, and S.V.S. Nageswara Rao, **Materials Today: Proceedings (2020).** https://doi.org/10.1016/j.matpr.2020.05.727. **[Chapter-3]**

[6] **Mangababu**, G. Sarang Dev, B. Chandu, M.S.S. Bharati, S. Venugopal Rao, and S.V.S. Nageswara Rao, **Nano-structures & Nano-Objects 23, 100509 (2020).** https://doi.org/10.1016/j.nanoso.2020.100509. **[Chapter-3]**

Further, the student has passed the following courses towards the fulfilment of course-work required for Ph.D.

S. No.	Course Code	Name	Credits	Pass/Fail
1	PY801	Research methodology	4	Pass
2	PY802	Advanced Quantum Mechanics	4	Pass
3	PY803	Advanced Experimental Techniques	4	Pass
4	PY804	Advanced Condensed Matter Physics	4	Pass

S. V. S. Nageswara Rao

Prof. S V S Nageswara Rao

Thesis Supervisor, 22/06/2023.

School Of Physics,

University of Hyderabad.

Prof. S.V.S. NAGESWARA RAO
School of Physics
University of Hyderabad
Hyderabad-500 046, INDIA.

22/6/2023

Dean

School Of Physics,

University of Hyderabad.

DEAN
School of Physics
University of Hyderabad
HYDERABAD - 500 046

Place: Hyderabad

Date: 22/06/2023.

This Thesis is Dedicated

To

All My Family Members

&

My Guru (Sri Patri Chalapathi Garu)

Acknowledgements

First, I would like to convey sincere gratitude to my supervisor, **Prof. S V S Nageswara Rao**, for his remarkable guidance, motivation, and uncompromising support throughout the thesis work. I consider myself fortunate to have had the opportunity to pursue my research carrier with him. I have thoroughly enjoyed working with him over the last six years, and his expert guidance and patience are highly regarded.

I sincerely express my gratitude to **Prof. Soma Venugopal Rao,** for his exceptional support in providing access to his lab and ultrafast laser systems. I would like to acknowledge his suggestions, motivation, and constant support throughout the thesis work. I sincerely thank my doctoral committee members **Prof. M Ghanashyam Krishna**, **Dr Ashok Vudayagiri, and Prof. B V R Tata** for their valuable suggestions during the doctoral committee meetings. I would like to thank **Prof. A P Pathak** for his suggestions and motivation throughout the Ph.D. I thank Prof. D K Avasthi of UPES, Dr. Sai Santosh Kumar of IIT Hyderabad, and Dr. M. Mallikarjuna Rao of SRM University for their intellectual support. I would like to thank the **Council of Scientific and Industrial Research (CSIR)**, **India** for providing the financial support (CSIR-JRF and SRF) throughout my PhD.

I would like to thank the present Dean (**Prof. K C James Raju**), and former deans of School of Physics (SoP), University of Hyderabad, for the academic support. I also thank Dr. Venkataiah Gorige, Dr. N Sri Ramgopal, and all other teaching and non-teaching staff of SoP. I specially thank Prof. Ashok Chatterjee for the exceptional and motivational teaching during my Ph.D. course work. I would like to thank my seniors Dr. V S Vendamani, Dr. N. Manikantababu, Dr. M Dhanunjaya, Dr. N Arun, Dr. K Vinod Kumar, for several productive discussions, and support during the experimental work. I would like to acknowledge the support from Dr. Chandu Byrum and Dr. M S S Bharathi in carrying laser ablation experiments. I would also like to thank my colleagues, collaborators Mr. Dipanjan Banerjee, Mr. Kanaka Ravi Kumar, Mr. R. Sai Prasad, Mr. Jagannadh Rathod, Ms. Reshma for their continuous collaborative research work carried. I also thank Mr. Sarang Dev, Mr. Ch. Sianglam, Mr. Debashish Patra, and Mr. Abhishek for their help in the experiments.

I would like to thank all the instrument operators who helped me during the measurements, special thanks to Mr. Santosh, Mr. Naresh, Mr. Durga Prasad, Ms. Jyothi Yarram, Mr. Udaya Bhanu, and Mr. Dhamodaran.

I thank Advanced Centre for Research in High Energy Materials (ACRHEM), Centre for Nanotechnology (CFN), School of Chemistry, University Grants Commission-Networking

Resource Centre (UGC-NRC) at School of Physics for providing access to sophisticated instrumental facilities. I specially thank the CFN staff, Mr. Prasanth, Mr. Rajeev, Ms. Sravani, Ms. Saloni, Mrs. Grace Leena, and Mr. Srikanth.

I would like to acknowledge the SPACES Degree College management, teaching and non-teaching staff for the help, motivation, and suggestions received during my under graduation. I specially thank Chalapathi sir, Santosh sir, Veerraju sir, Subbarao sir, Eswara Rao sir, and Gangadhar sir.

I would like to thank Kumar master (T Vivekananda Kumar Garu), Manga Teacher, and Venkata Ramana sir for their caring in my school education.

I thank Institute of Eminence (IOE-UOH), UGC-DAE-CSR, DST PURSE, DRDO, and IUAC New Delhi for various funding supports during my Ph.D.

I would like to thank all my friends from University of Hyderabad Mr. Akshay Chatla, Mr. Vishnu Easam, Mr. B. Venkatesulu Reddy, Mr. Shivaram Vintha, Mr. Dhanunjaya, Mr. Naresh Shyaga, Dr. Pundareekam, Mr. Ravinder Tirupati, Dr. Avishek Das, Mrs. Praneetha, Mr. Rahul, Mr. Vikram, Mr. Pawan Kumar Varma, Mr. Jeevan, Mr. Linga Murthy, Mr. Nagaraju, Mr. Sajin, Mr. Saisav, Ms. Devika, Mr. Dinesh Kumar, Mr. Venkatesh Pusa, Mr. Vivek, and Mr. Krishna. I also would like to thank all my best friends during my academic life Mr. Devudu Kuramdasu, Mr. Appala Swami Naidu, Mr. Govindu Kallepalli, Mr. Vamsi Katta, Mr. Anand Kurakula, Mr. Venky (darling), Mr. Santhosh, Mr. Durga karri, Mr. Harish Aadhi, Mr. Srinu, Mrs. Sithara, Mrs. Devi, Mrs. Jyothi.

Most importantly I am highly grateful to my loving family for their love and wishes. I am indebted to my mother (Smt. Nookalamma Garu), mavayya & attayya (M. Apparao Garu, Jaggamma Garu), annayya & vodina (A. Venkata Ramana Garu, Venkata Lakshmi Garu), and bava & akka (M. Anand Rao Garu, Lakshmi Garu) for their unconditional love, endless support, and encouragement in achieving my ambitions. I also thank Srinu mavayya, Sattibabu mavayya, Ramana akka, satyaveni akka, Dongababu annayya, Mani vodina for their well wishes.

I would like to thank my better half Mrs. Hemalakshmi for her continuous support, understanding, and for caring about my health.

List of Abbreviations

Abbreviation	Description
cm	Centimetre
CW	Continuous Wave
DW	Distilled Water
EF	Enhancement Factor
EM	Electromagnetic
FESEM	Field Emission Electron Microscopy
Fs/fs	Femtosecond
GaAs	Gallium Arsenide
HAZ	Heat Affected Zone
HSFL	High Spatial Frequency LIPSS
LAL	Laser Ablation in Liquids
LASER	Light Amplification by Stimulated Emission of Radiation
LIPSS	Laser Induced Periodic Surface Structures
LSFL	Low Spatial Frequency LIPSS
LSPR	Localized Surface Plasmon Resonance
MB	Methylene Blue ($C_{16}H_{18}ClN_3S$)
MG	Malachite Green ($C_{23}H_{25}N_2$)
mm	Millimeter
nm	Nanometre
NMs	Nanomaterials
NPs	Nanoparticles
Ns/ns	Nanosecond
NSs	Nanostructures

PLAA	Pulsed Laser Ablation in Air
PLAL	Pulsed Laser Ablation in Liquids
Ps/ps	Picosecond
PVA	Polyvinyl Alcohol $(C_2H_4O)_x$
RDX	1, 3, 5-Trinitroperhydro-1, 3, 5-triazine ($C_3H_6N_6O_6$)
RSD	Relative Standard Deviation
SAED	Selected Area Electron Diffraction
SEM	Scanning Electron Microscopy
SERS	Surface Enhanced Raman Spectroscopy
Si	Silicon
TEM	Transmission Electron Microscopy
THz	Terahertz
XRD	X-ray Diffraction

Table of Contents

Part: B

Abstract

This thesis presents a detailed study of the ultrafast laser ablation of Gallium Arsenide in liquids and air under different conditions. The subsequent formation of nanostructures and nanoparticles of GaAs and associated compounds have been examined in detail. Exotic high temperature/high-pressure stable phases like hexagonal GaAs and other compounds like As_2O_3, and Ga_2O_3 have been produced when GaAs target was ablated at higher fluence. In contrast, room temperature stable cubic GaAs nanoparticles were produced when ablated at lower fluences. So this study devises a method to selectively produce either the high-temperature or high-pressure stable particles or pure cubic-GaAs particles depending on the requirement. The formation of exotic phases is possible because of the intrinsic nature of the laser ablation that involves rapid heating and quenching.

Further, the GaAs nanoparticles and quasiperiodic surface structures have been produced simultaneously and analyzed in detail. The GaAs NPs have shown nonlinear optical behavior (two-photon absorption), which may be helpful in optical filters, wavelength doublers, quantum LEDs etc. The surface structures have been employed for different applications, particularly surface-enhanced Raman spectroscopy (SERS), wettability, and antireflective applications. These GaAs NSs acted as excellent hybrid SERS substrates for detecting trace levels of explosives, pesticides, and other dye molecules. Further, the formation of subwavelength and deep-subwavelength structures on the surface of GaAs have been thoroughly examined by analyzing each track drawn at different laser fluences. The structures formed as a function of radial distance from the center in each track and the mechanisms responsible for forming different structures have been discussed. The deep-subwavelength (below 70 nm) DNA-like structures have also been observed towards the end of the track where fluence is low. This is further confirmed by ablating GaAs at lower fluence. These detailed studies have been presented in various chapters of this thesis.

Finally, this study provides deep insights into the understanding of laser-induced patterns on GaAs substrates, and the formation of nanoparticles of GaAs and other exotic phases as a function of fluence in different media and a critical dose for producing pure GaAs is discussed. So, this study provides valuable information for understanding the basic phenomena of laser ablation in GaAs and its applications in various fields.

Chapter 1

Introduction and Motivation

This chapter presents a detailed introduction to the importance of nano-dimensional materials and their applications in diverse fields. It explains the synthesis methods for making nanomaterials and its associated devices. This also includes our motivation towards choosing "GaAs" as investigating material for its exotic physical and chemical properties. In addition, its significance/importance in scientific and industrial applications is elaborated in detail. In this connection, the electronic and optoelectronic applications of bulk as well as nano-dimensional GaAs are presented. The synthesis methods used in this study, Pulsed Laser Ablation in Liquids (PLAL) and Pulsed Laser Ablation in Air (PLAA) for creating GaAs NPs and NSs, respectively, are explained in detail with the schematic representations. A brief literature survey, definition of the thesis problem and the outline of the thesis are also presented in this chapter.

1.1 Introduction to nanomaterials and their advantages

Scientific communities all over the world are working to create energy-efficient, fast, and affordable gadgets to meet the needs of a rapidly growing population. Nanomaterials and nano-devices are the best choices to fulfil the purpose[1,2]. Researchers have developed numerous techniques for synthesis, processing and examination of these nano-devices and the materials used to make them. When the physical size of a material reduces to nano dimensions, it shows a different behavior than when it is in bulk form. A familiar example is gold, which is yellow in its bulk form and turns pink when converted to nanoparticles[3]. Similarly, Cu nanoparticles with lower size (high surface-to-volume ratio) have higher catalytic activity in CO_2 reduction reactions[4]. Not only color/reactivity, one can tweak all the physical, mechanical, chemical, and electrical properties by tuning the material's dimensions[5]. The reasons for such tunability are associated with (a) the quantum confinement effects, (b) the dominance of electromagnetic forces over gravitational forces, (c) surface-to-volume ratio, and (d) material shape. Suppose, spherical NPs, NWs, NRs, dendrites etc., of the same material (Au, Ag, or GaAs) have different absorptions, emissions, and electrical properties.

Hence, a handful of elements (periodic table) with possible shapes and sizes provides a lot of scope for obtaining unique structural materials with novel properties for enhanced device performance. It motivates researchers and industrialists to study and develop specific nanomaterials for technological improvements. In this thesis, GaAs is chosen as the material of study due to its increased importance in various fields, as discussed below.

1.2 Introduction to GaAs, GaAs nanoparticles, and GaAs nanostructures

In recent decades, nano-dimensional materials, nano-devices, and their technology have been mounting rapidly. One of the intriguing materials for such device applications is GaAs[6–8]. It is a promising and proven semiconductor for optoelectronic device applications. Owing to its high electron mobility, it is a preferred substrate material in the field of high-speed and high-frequency electronic applications[9]. At ambient temperatures and pressures, GaAs typically exists in the cubic zinc blende phase; however, at high pressures, hexagonal and orthorhombic phases can be formed. Its characteristics are well known when GaAs is in bulk and thin-film forms. Recently, GaAs-based three-dimensional nanomaterials (NPs and NSs) have been widely researched for their potential to create numerous functional devices. Some of the current research interests for the GaAs NPs include quantum LEDs, solar cells, nonlinear optical (NLO) studies etc. For example, as reported by Ashalley et al.[10], Ga and Au

nanoparticles capped GaAs/AlGaAs quantum wall structures have shown superior light emission properties as quantum LEDs.

On the other hand, GaAs surface structures have a wide range of uses in optoelectronics, solar cells, antireflective technology, terahertz antennas, SERS, and other areas[11–14]. Ionin et al.[11], have produced GaAs periodic surface structures by laser ablation and have showed its antireflective and grating applications. Similarly, Trukhin et al.[15] reported TeraHertz emission from GaAs Nanowires, which is several orders of magnitude greater than that of the bulk epitaxial GaAs surface. Fengyuan et al.[6] also reported the applicability of these GaAs NWs decorated with Au NPs as photodetectors. Various other studies concentrate on the fabrication of GaAs Nanomaterials with different feature sizes and shapes for realizing/improving the above-mentioned applications. Hence, there is a significant need for the development of reliable and efficient synthesis techniques as well as to understand various properties of these GaAs nano-entities (NPs and NSs). The important techniques used to fabricate various nanomaterials are mentioned in the next section.

1.3 Fabrication methods for nanomaterials (NPs and NSs)

The rapid growth in the field of nanomaterials has led to numerous fabrication methods. A few important techniques are mechanical/ball milling[16], chemical etching[17], chemical/electrochemical precipitation[18], plasma etching[19], lithography-based techniques[20], sol-gel method[21], hydrothermal, microwave hydrothermal, sputtering[22,23], thermal evaporation[5], e-beam evaporation[24], chemical vapor deposition[25], atomic layer deposition[26], molecular beam epitaxy (MBE)[27], pulsed laser ablation[28–30] etc. Some post-synthesis processing techniques like thermal annealing, laser annealing[31] and ion irradiation techniques[32] have also been employed to realize nanoparticles of various materials.

All these techniques can be divided into two categories (1) top-down process, and (2) bottom-up process. In the top-down process, bulk material will be broken/reduced into small size particles in single/multiple steps. The bottom-up process is exactly opposite to the former process; in this method, atoms or molecules will be added together to form nano-size particles/structures. The schematic representation of these two processes with examples is presented in Fig. 1.0. In this study, laser ablation, a top-down process, is used as a synthesis method for fabricating GaAs NPs and NSs. The details of the method and its advantages over other available methods is mentioned below.

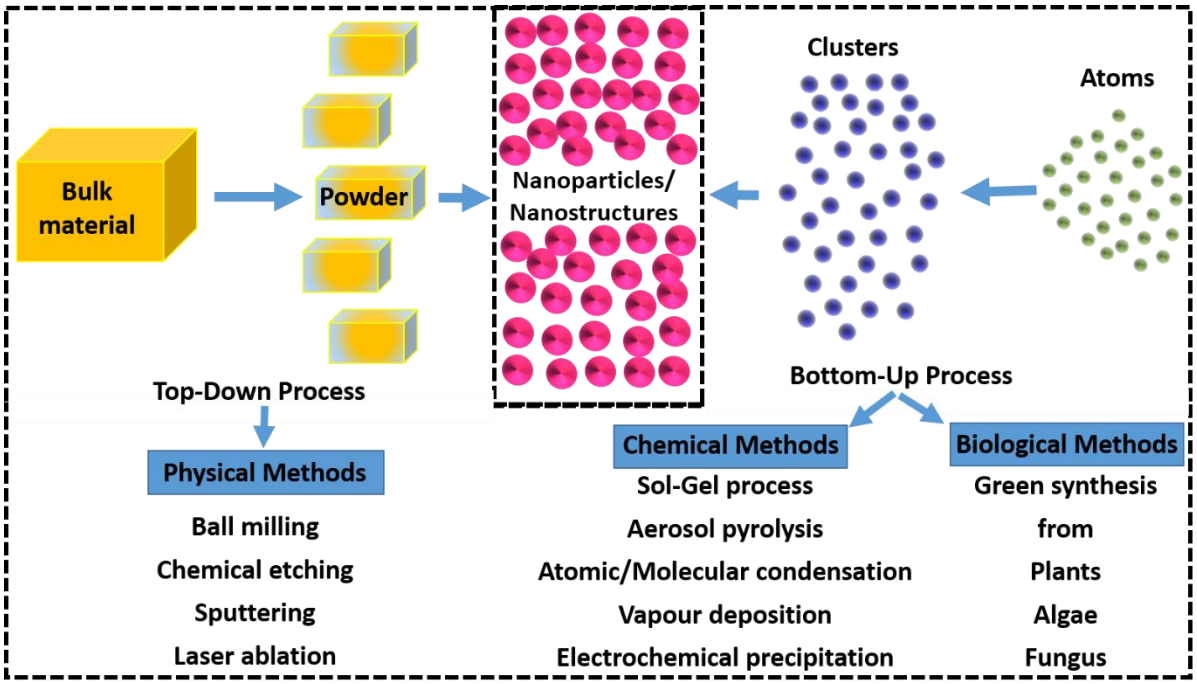

Fig. 1.0 Schematic representation with examples of top-down and bottom-up processes for NPs generation.

1.4 Introduction to Pulsed Laser Ablation in Liquids (PLAL)

In PLAL, a bulk substrate will be irradiated with an ultrafast pulsed laser to obtain NPs and NSs. This PLAL is a simple and quick approach for the fabrication of NPs in the colloidal solution. Compared to the other available methods (mentioned in the earlier section 1.3), this PLAL technique has greater advantages such as, (1) quick and easy, (2) less or no chemical reactions involved, (3) NPs and NSs can be created in a single experiment, and (4) due to the presence of surrounding liquid media, formation of unstable/exotic phases is possible at room temperatures due the rapid quenching at liquid-solid interface. Above all, with the recent advances in this process, it can be scaled up for synthesizing NPs and NSs up to industrial needs.

In this process, as shown in the schematic Fig. 1.1, high-energy laser pulses will hit the substrate material, the target absorbs the laser energy, causing the material to vaporize rapidly leading to the formation of plasma plume. It further leads to the formation of a shock wave, cavitation bubble, and then nucleation /growth of nanoparticles that are released into the liquid once the cavitation bubble explodes. This whole process completes in the order of 10^{-4} to 10^{-3} s, a new cavitation bubble forms again and the process repeats. The presence of this surrounding liquid medium provides the advantage of confining the plasma near the target. The density, pressure, and temperature inside this cavitation bubble is completely different from

that of the remaining liquid medium. These conditions inside the cavitation bubble control/effects the size, shape, and composition of NPs; hence, the surrounding liquid medium has greater significance in the ablation process. It is also well known that the ablated NPs' properties depend upon the pulsed laser's parameters. In this thesis, ultrafast lasers with 50 fs and 30 ps pulse durations are used. The role of pulse duration and advantages of the ultrafast laser ablation process are mentioned below.

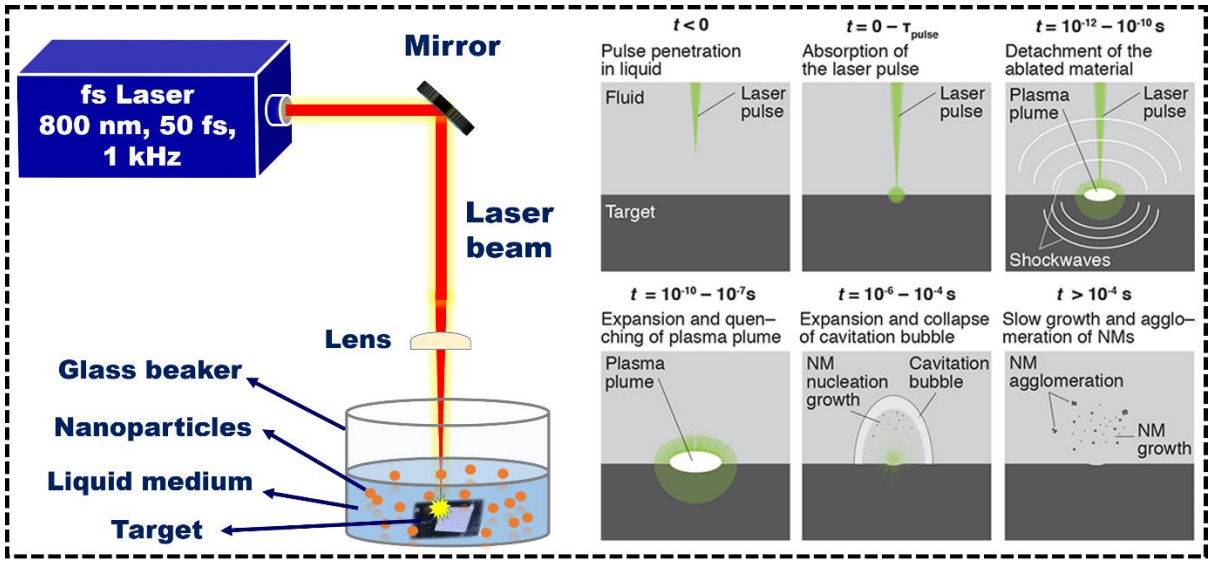

Fig. 1.1 Schematic representation of pulsed laser ablation in liquids (PLAL) technique (Part of this figure is adapted from ref.[33]).

1.5 Significance of Ultrafast Lasers

Ultrafast laser is indeed a type of laser that produces extremely short light pulses, usually in the range of 10^{-12} seconds (picoseconds) to 10^{-15} seconds (femtoseconds). Compared to the continuous wave (CW) and long pulse (typically nanosecond) lasers, ultrafast lasers have several advantages. The CW laser ablation is predominantly controlled by thermal processes (material is removed by melting), which creates a large heat-affected zone (HAZ). In the case of nanosecond lasers, incedent photons interact with both electrons and phonons of the target. The photon-electron interaction then causes a rapid rise in electron temperature, resulting in vaporization of the target. Hence, nanosecond lasers have a smaller HAZ than CW lasers. As ultrafast lasers produce extremely short pulses, the photon energy is mainly transferred to the free electrons. The timescales required for the transfer of energy from electrons to the lattice is higher than the laser pulse duration; hence lattice of the ablating material does not get heated. A narrow layer near the surface of the target (few microns/within penetration depth of the light) gets high pressures and temperatures, leading the material to evaporate quickly. This leads to the plasma formation and material removal. As a result, in the ultrafast ablation process, the

heated volume is controlled by the photon absorption depth, with thermal diffusion depth having a less significant impact. Thus, in femtosecond and picosecond ablations, HAZs are not seen.

Coming to the LAL using ultrafast lasers, as the target is being ablated in the presence of liquid medium, it creates a plasma and a shock wave generation, which will lead to the formation of cavitation bubble. Inside this cavitation bubble, the coalescence of the evaporated material takes place, leads to the formation of nanoparticles. This bubble plays a crucial role in determining the size, shape, and composition of the NPs formed after the ablation process. Initially, the cavitation bubble expands, shrinks, and collapses. Once the bubble is collapsed, the NPs formed inside this cavitation bubble release into the surrounding liquid media, and any possible reactions with the liquid may occur. It is observed that the pulse duration (CW, long, short, ultrashort) significantly affects the collpse and regrowth times of the caviation bubble, there by affecting the properties of the nanoparticles formed inside the bubble. Even though LAL is well studied in the last few decades, the ultrafast processes at the liquid-solid interface are not well known. Hence, there is a need to explore the effects of this pulse duration on the GaAs NPs formed.

Moreover, ultrafast lasers offer the following advantages, (1) laser energy is confined to a very narrow region, damage to adjacent material is minimized, (2) they produce relatively minimal heat, thermal damage towards the material being treated is minimized, (3) variety of materials can be treated, including metals, alloys, semiconductors, plastics, polymers, and biological products, (4) ability to cut, drill, ablate, and mark, (5) Its high peak power can cause nonlinear effects in the materials, such as harmonic generation/multiphoton absorption, and (6) ultrafast lasers can treat material significantly quicker than traditional lasers, lowering processing time and boosting throughput. Overall, the characteristics listed above make ultrafast lasers a powerful tool in various applications ranging from scientific research to industrial material processing.

1.6 Introduction to Pulsed Laser Ablation in Air (PLAA)

In PLAA the laser ablation of target is carried out in air medium. In general, this technique is widely used for the surface structuring of materials. In terms of ablation set up, the only difference between PLAL and PLAA is that the presence of surrounding media, in the first case surrounding medium is a liquid, whereas in the later case it is ambient air. As a result of the change in the surrounding media, many ultrafast processes will differ from each other. In the PLAA also the laser energy is primarily absorbed by the target material, leading to the

evaporation/ablation of the material into the air. Confinement of plasma and the formation of cavation bubble are not applicable in this case. Within the ablated tracks/spots various surface structures will be formed depending on the laser parameters used and the nature of the material. The most commonly formed structures in PLAA are the Laser-Induced Periodic Surface Structures (LIPPS), also called ripples. Depending upon the periodicity ($\wedge$), these LIPSS are categorized into two kinds, (a) Low-Frequency LIPSS ($\lambda<\wedge<\lambda/2$), also called LSFL structures and (b) High-Frequency LIPSS ($\wedge<\lambda/2$), also called as HSFL structures. Here, λ is the wavelength of the laser used for the creation of LIPSS. Another way of categorizing these LIPSS is (a) Near Subwavelength LIPSS ($0.4<\wedge/\lambda<1$), and (b) Deep Subwavelength LIPSS ($\wedge/\lambda<0.4$). There are numerous models/theories that exist to explain the formation of these structures; a few important models are mentioned in the next section.

1.7 LIPSS formation mechanisms

Based on the rigorous literature survey, all the LIPSS formation mechanisms/models mainly fall under two categories (a) Material Reorganization Models and (b) Electromagnetic Models. Although the study of LIPSS is very well established (first experimental observation was in the year 1965)[34], the underlying formation mechanisms are still debatable.

In most of the EM models (SEW, SPPs, Drude, Sipe etc. see ref [34] for detailed information), it is well accepted that a few initial incident pulses create roughness on the surface, the further coming pulses/beam excites surface plasmon polaritons (SPPs), these SPPs interact with the incoming light's EM filed and modulates the energy dissipation to form a grating like/interference structures. On the other hand, the mater reorganization models predict that the intense light absorbed on the surface of the material creates instability/disturbance/defects. In some cases, it is stated as molten/soft material, and this material flows/moves spatially and resolidifies as ridges and grooves. However, these matter reorganization theories can not explain the orientation of LIPSS with reference to the laser polarization direction, whereas EM models could do that. Recently, combining these two theories at different spatail and temporal regions of ablation process, a few simulations have been performed to match the experimental observations closely. A detailed literature survey of the laser ablation of GaAs for the synthesis of NPs, and quasi-periodic/periodic surface structures was presented in the next section 1.8.

1.8 Literature survey

Overall literature pertaining to laser ablation processes, fabrication and applications of various nanoparticles and nano structures is covered in the previous sections. This section focuses on the literature that is specific to the laser ablation of GaAs.

1.8 (a) GaAs NPs by Laser Ablation

Pulsed Laser ablation has recently been employed for the creation of GaAs NPs/films (in the decade 2000-2010). Initial ablation experiments were conducted in vacuum/various gas environments, and this process is also called as pulsed laser deposition (PLD)[35]. The number of laser pulses and the pressure/nature of the surrounding gas significantly affect the composition and size of the NPs/NSs created. Perriere et al.[36] described the preliminary results of synthesizing GaAs NPs by nanosecond laser in a vacuum chamber operated at an optimized N_2 gas pressure. Schamp et al.[12] fabricated ice-cream-cone-like structures of Ga/GaAs and Ga/GaSb by dual-wavelength PLD technique at high vacuum (10^{-6} Torr). Further, utilizing 500 ps laser pulses, Trelenberg et al.[37] created GaAs nanocrystals. They found an excess amorphous Ga or As material along with the cubic zinc blende GaAs NPs. They also studied the morphology of the underneath surface structures. There are fewer studies involving PLD as a tool for creating GaAs NPs. Later, the experiments were tuned/developed to ablate GaAs directly in the liquid medium. The advantages of ablating in the presence of solvents are the ease of collecting NPs into the colloidal solutions, it also confines the ablated plasma near the liquid-solid interface, it offers fast cooling of the plasma, and it can also lead to the formation of non-equilibrium phases/chemical compounds. More importantly, it does not need high vacuum chambers. It just needs a Borosil glass beaker filled with the required liquid, and a laser will be focused on it. The effect of liquid media on the physical properties of ablated GaAs NPs was discussed by Ganeev et al.[38,39], who reported two-photon absorption properties of GaAs NPs. Lalayan et el.[40] fabricated GaAs and CdS quantum dots with a picosecond laser and studied their luminescence properties, predicting them to be used in biomedical imaging. De Bonis et al. investigated the impact of pulse duration on the stoichiometry of GaAs NPs[41,42]. The ns laser ablation produces Ga-rich spherical NPs, while the fs laser ablation generated stoichiometric GaAs NPs. According to Salminen et al.[43], liquid media can affect the stability of formed GaAs NPs. While NPs in DW formed clusters and quickly settles at the bottom, GaAs NPs generated in ethanol and water plus ammonium sulphide solutions have longer lives. Surface passivation by sulfer or oxygen is attributed as the reason for long stability of these

GaAs colloidal NPs. A few other studies by Sharifi et al.[44] and Abderrafi et al.[45] have also investigated the basic properties of GaAs NPs created by LAL. However, to the best of our knowledge there is not much discussion of the formation of amorphous material surrounding the NPs in the GaAs ablation. Also, the exotic phases or other compounds comprised during GaAs ablation and their formation mechanism are unclear. Hence, the current thesis has conducted a detailed study to contribute to this area.

1.8 (b) GaAs NSs by Laser Ablation

Even though our primary objective is to study GaAs NPs by PLAL, we also found interest in understanding the surface structures of GaAs created during the ablation process. Hence, a detailed literature survey was conducted and presented in this section. Initially, GaAs ablation studies were conducted in vacuum chambers, as reported by Borowiec et al.[46], pit-like features were found on the surface of GaAs upon interaction with a single shot laser pulse; the width and depth of the trenches increased with energy. Later, the development of efficient ultrafast lasers led to the structuring of GaAs in ambient air. The formation of LIPSS on the surface of GaAs has recently begun. Ionin et al.[11,47–50] and Margiolakis et al.[51] investigated the ultrafast dynamics when fs laser interacted with GaAs. Excitation of surface plasmon polaritons (SPPs) was shown to be the primary mechanism responsible for forming LIPSS in GaAs. Michael et al.[52] suggested that the origin of HSFL structures was associated with the defect diffusion-induced bifurcation of the LSFL structures. Alex et al.[53] found from their comprehensive investigations that possible causes of the development of the LIPSS are surface defect creation and atomic constituent desorption. However, the formation mechanism of LIPSS on GaAs is still debatable. Especially for the deep subwavelength LIPSS, the mechanisms are still unclear; hence, further detailed analysis may be required. Thus to contribute to this unexplored area, the formation of GaAs LIPSS and its dependency on the laser beam fluence is investigated in this thesis. The SPP/SIPE-Drude model best suits for the GaAs LIPSS obtained in this thesis. Further, as stated in the earlier section 1.5 (a), the role of liquid medium in the formation of GaAs NPs and GaAs NSs/LIPSS has been studied.

Aside from the fundamental mechanics of creation, GaAs LIPSS are being investigated for their potential applications in nanoscale devices, terahertz antennas, solar energy harvesting, antireflection surfaces and so on[13,54]. These periodic nanostructures can also be utilized in various sensors[55]. Recently, plasmonic NPs decorated semiconducting periodic NSs were employed as SERS platforms for sensing trace hazardous chemicals, particularly biomolecules[56–58]. There is a high demand for tracing poisonous and explosive compounds in

small concentrations as a result of rising civilian/industrial explosions and terrorist strikes. In this context, hybrid SERS substrates (Au/Ag coated semiconductors) are being investigated for their ability to detect diverse trace elements[59,60]. Further, these hybrid SERS substrates have high potential in the detection of trace bio-molecules because they generate less heat compared to the metallic substrates during the SERS measurements. Hence, plasmonic NPs coated GaAs LIPSS could be a good choice in this field. The following factors (a) ease of preparation, (b) flexibility in achieving diverse LIPSS, and (c) the possibility of large-scale production with a simple experimental setup, makes the Au/GaAs LIPSS as efficient/good candidates among hybrid SERS substrates. Hence, in this thesis, gold coated GaAs LIPSS will be studied for its SERS response and other possible applications.

1.9 Definition of thesis problem

After a thorough understanding of the current literature, the present thesis is designed to address the following gaps/problems.

1. Synthesis and characterization of GaAs NPs: Analysis of different novel structural phases and other exotic compounds. Simultaneous fabrication of multifunctional GaAs NPs and NSs by ps pulsed laser ablation in liquids.
2. To elucidate the physical mechanisms governing the formation of GaAs NPs and NSs during laser ablation in liquid media. Further, it is proposed to explore and implement applications of these ablation products (i.e., of GaAs NPs and NSs).
3. Fabrication and study of GaAs NSs in Air and DW in detail with demonstration of their possible applications.
4. Understanding the role of laser fluence on the quality of GaAs surface structures.
5. The main objective of the study is to elucidate the underlying mechanisms that are governing the ultra-fast laser ablation of semiconductors in general and GaAs in particular. Further, this study helps in optimizing the process to fabricate particles and structures in required size, shape, composition and phase in a reproducible manner for various practical applications.

1.10 Outline of the Thesis

This thesis presents the synthesis of GaAs nanoparticles and nanostructures under different ablation conditions and their possible/feasible applications.

This thesis is organized into the following chapters

Chapter 1. Introduction and Motivation

This chapter briefly explains the role of nanomaterials and their fabrication processes for developing nanoscale devices. It primarily focuses on synthesizing novel structured nanomaterials (NPs and NSs) to realize their unique/novel aspects, which can boost the technology. The material of choice, i.e., GaAs, is well introduced along with the needs and objectives for studying GaAs NPs and NSs. The advantage of choosing an ultrafast laser ablation technique for synthesizing NPs and NSs is also discussed in detail. Brief insights about the ultrafast LAL mechanisms and surface structure formation models are presented with supporting literature. A literature review and a definition of the thesis problem are also provided.

Chapter 2. Experimental Details

This chapter presents all the information about the experimental setu-ups and the specifications of the instruments utilized during the current investigation. Mainly, ablation experiments using picosecond and femtosecond lasers are discussed. All the laser parameters are briefly mentioned. This chapter also includes a detailed description of the thin film deposition techniques (thermal evaporation) used in this thesis work. It also explains different characterization techniques, such as microscopy, spectroscopy, and diffraction.

Chapter 3. Structural Investigations of Ultrafast Laser Ablated HfO_2 & GaAs Nanoparticles[61–63]

This chapter presents experimental results on the fabrication of HfO_2 and GaAs NPs under various experimental conditions. It contains two parts, part-A describes the femtosecond laser ablated HfO_2 NPs, and part-B describes the formation of GaAs NPs using both femtosecond and picosecond lasers. At last, this chapter concludes the formation mechanisms of the NPs (especially GaAs NPs) with experimental evidence and a few literature analyses.

Part-A: Initially, the ablation was performed on HfO_2 target to optimize the femtosecond LAL setup and to continue our group's earlier study. Here, HfO_2 NPs are created using Ti:Sapphire laser with pulse duration ~50 fs, wavelength ~800 nm, a repetition rate of ~1 kHz, and energy ~750 µJ. This work studies the effect of the initial grain size of the HfO_2 target on the final ablated products. After the ablation, the smaller initial grain size led to the smaller spherical NPs. More interestingly, nano-fibre-like structures connecting the spherical NPs are noticed irrespective of the initial target conditions and laser parameters. Further, the coexistence/appearance of the high-temperature HfO_2 phase is observed.

Part-B: Using the femtosecond LAL process, GaAs NPs are created at different laser energies and liquids. With the increase in the laser energy, it is observed that there is an increase in the particle size and ablation yield. It is also realized that the fs LAL process has led to the formation of a stable room temperature phase of GaAs (i.e., cubic zinc blende). However, some background mesh-like material is noticed along with the spherical GaAs NPs. Later, to see the pulse duration effects, a picosecond laser is utilized for NPs generation. Picosecond pulses with 15 mJ laser energy have formed more background material, exotic phases (like As_2O_3, Ga_2O_3, GaAsO), and spherical GaAs NPs. The colloidal solutions are thoroughly analyzed to understand various other phases/compounds formed along with the ablated GaAs NPs.

Chapter 4. Multi-functional GaAs Nanoparticles and Nanostructures Fabricated using Picosecond Laser Ablation[64,65]

This chapter briefs the production of GaAs NPs and NSs using the picosecond laser ablation process and explores the possible applications of the ablated products. It is divided into two parts, part-A discusses the simultaneous synthesis of GaAs NPs and NSs, and part-B presents the influence of various ablation parameters on the quality of quasi-periodic GaAs NSs.

Part-A: This study presents the simultaneous fabrication of both NPs and NSs of GaAs using a picosecond LAL process. Furthermore, the NLO characteristics of NPs are investigated using the femtosecond MHz Z-scan approach. Anti-Reflective, hydrophilic, and SERS applications for NSs have been investigated in detail.

Part-B: This study presents the role of various experimental conditions in producing GaAs periodic surface structures. It also gives a comparative study of GaAs NSs created in Air and DW media. All these surface structures are coated with a thin layer of gold to record their SERS response. These plasmonic Au-coated GaAs surface structures (hybrid SERS substrates) have shown excellent SERS response with lower relative standard deviations and higher signal reproducibility.

Chapter 5. Effects of Laser Fluence on the Formation of GaAs Periodic Surface Structures by Femtosecond Laser Ablation in Air and Distilled Water[66]

This chapter presents the effects of laser fluence on the quality of GaAs surface structures. This chapter is divided into two parts, part-A presents the results of the study conducted in air medium, while part-B describes the results obtained in DW medium.

Part-A: As shown in the earlier chapter, we are fascinated to fabricate the best quality periodic surface structures on GaAs (popularly termed as LIPSS) due to their high potential in multifunctional applications. Hence, a detailed study using femtosecond laser pulses to

fabricate GaAs LIPSS at different laser energies was conducted and presented in part_A of this chapter. Single-line laser scans are drawn in ambient air varying input laser energy from 5 µJ to 100 µJ. The effects of laser energy on the periodicity and oxidation of the LIPSS are studied. The impact of laser beam profile on the quality of LIPSS at different radial positions of the beam spot is presented with experimental evidence.

Part-B: This study shows that when GaAs is ablated with femtosecond pulses in distilled water, it is possible for several ablation mechanisms to operate at various radial locations along the ablated track. Fascinating characteristics, including micron-sized cones, nano-pores, and deep sub-wavelength nano-DNA-like structures (average size of 60–70 nm), were seen from the center to the extremities of the ablated track. The necessity of models, including changes in the dynamics of the melt flow and surrounding medium, is discussed. To our knowledge, this is the first report of sub-70 nm surface nanostructures on GaAs. Also, after being coated with gold, these GaAs surface structures acted as outstanding hybrid SERS platforms.

Chapter 6. Conclusions and Future scope

This chapter enumerates the findings based on the overall outcomes obtained from the current research and suggests potential future directions.

It summarizes the effects of different liquid media on the ablated HfO_2 and GaAs NPs. The exotic/novel phases formed after the ablation process were discussed with possible mechanisms. Further, various surface structures of GaAs and their formation mechanisms were summarized.

The future scope (or directions) of this thesis can be summarized as follows. Fabrication of pure GaAs NPs with smaller size (without any background materials) will be an interesting study for finding applications in NLO, photonics, and Quantum LEDs. The GaAs's periodic surface structures at sub-wavelengths (620 nm) and deep sub-wavelengths (<100 nm) created in this work may enable subsequent research into the material's potential uses in nanodevices and nanotechnology.

1.11 Conclusion

Overall, this chapter provides a detailed introduction of nanomaterials, their importance, and the fabrication techniques used. A deep literature survey about the laser-based synthesis of GaAs NPs and NSs was presented. At the end of the chapter, the definition of the thesis problem and the thesis outline were also presented for a quick overview.

References

(1) Huang, X.; Xing, G.; Li, Y.; Nannen, E. Nanomaterials for Energy-Efficient Applications. *J. Nanomater.* **2015**, *2015*, 1–2. https://doi.org/10.1155/2015/524095.

(2) Triana, M. A.; Hsiang, E.-L.; Zhang, C.; Dong, Y.; Wu, S.-T. Luminescent Nanomaterials for Energy-Efficient Display and Healthcare. *ACS Energy Lett.* **2022**, *7* (3), 1001–1020. https://doi.org/10.1021/acsenergylett.1c02745.

(3) Njoki, P. N.; Lim, I.-I. S.; Mott, D.; Park, H.-Y.; Khan, B.; Mishra, S.; Sujakumar, R.; Luo, J.; Zhong, C.-J. Size Correlation of Optical and Spectroscopic Properties for Gold Nanoparticles. *J. Phys. Chem. C* **2007**, *111* (40), 14664–14669. https://doi.org/10.1021/jp074902z.

(4) Reske, R.; Mistry, H.; Behafarid, F.; Roldan Cuenya, B.; Strasser, P. Particle Size Effects in the Catalytic Electroreduction of CO 2 on Cu Nanoparticles. *J. Am. Chem. Soc.* **2014**, *136* (19), 6978–6986. https://doi.org/10.1021/ja500328k.

(5) Prusty, S.; Siva, V.; Shukla, N.; Satpati, B.; Senapati, K.; Sahoo, P. K. Unusual Ferromagnetic Behaviour of Embedded Non-Functionalized Au Nanoparticles in Bi/Au Bilayer Films. *RSC Adv.* **2016**, *6* (108), 106584–106590. https://doi.org/10.1039/C6RA23047D.

(6) Lin, F.; Cui, J.; Zhang, Z.; Wei, Z.; Hou, X.; Meng, B.; Liu, Y.; Tang, J.; Li, K.; Liao, L.; Hao, Q. GaAs Nanowire Photodetectors Based on Au Nanoparticles Modification. *Materials (Basel).* **2023**, *16* (4), 1735. https://doi.org/10.3390/ma16041735.

(7) Tapar, J.; Kishen, S.; Prashant, K.; Nayak, K.; Emani, N. K. Enhancement of the Optical Gain in GaAs Nanocylinders for Nanophotonic Applications. *J. Appl. Phys.* **2020**, *127* (15), 153102. https://doi.org/10.1063/1.5132613.

(8) Zhang, Z. Y.; Oehler, A. E. H.; Resan, B.; Kurmulis, S.; Zhou, K. J.; Wang, Q.; Mangold, M.; Süedmeyer, T.; Keller, U.; Weingarten, K. J.; Hogg, R. A. 1.55 Mm InAs/GaAs Quantum Dots and High Repetition Rate Quantum Dot SESAM Mode-Locked Laser. *Sci. Rep.* **2012**, *2* (1), 477. https://doi.org/10.1038/srep00477.

(9) Li, S. S. High-Speed III–V Semiconductor Devices. In *Semiconductor Physical Electronics*; Springer US: Boston, MA, 1993; pp 455–502. https://doi.org/10.1007/978-1-4613-0489-0_15.

(10) Ashalley, E.; Gryczynski, K.; Wang, Z.; Salamo, G.; Neogi, A. Plasmonically-Powered Hot Carrier Induced Modulation of Light Emission in a Two-Dimensional GaAs Semiconductor Quantum Well. *Nanoscale* **2019**, *11* (9), 3827–3836. https://doi.org/10.1039/C8NR07489E.

(11) Ionin, A. A.; Klimachev, Y. M.; Kozlov, A. Y.; Kudryashov, S. I.; Ligachev, A. E.; Makarov, S. V.; Seleznev, L. V.; Sinitsyn, D. V.; Rudenko, A. A.; Khmelnitsky, R. A. Direct Femtosecond Laser Fabrication of Antireflective Layer on GaAs Surface. *Appl. Phys. B* **2013**, *111* (3), 419–423. https://doi.org/10.1007/s00340-013-5350-4.

(12) Schamp, C. T.; Jesser, W. A.; Shivaram, B. S. Growth of GaAs "Nano Ice Cream Cones" by Dual Wavelength Pulsed Laser Ablation. *Appl. Surf. Sci.* **2007**, *253* (15), 6326–6329.

https://doi.org/10.1016/j.apsusc.2007.01.104.

(13) Hong, L.; Rusli; Yu, H.; Wang, X.; Wang, H.; Zheng, H. Surface Nanostructure Optimization for GaAs Solar Cell Application. *Jpn. J. Appl. Phys.* **2012**, *51* (10 PART 2), 13–16. https://doi.org/10.1143/JJAP.51.10ND13.

(14) Zhang, W.; Shi, Z.; Chen, C.; Yang, X.; Yang, L.; Zeng, Z.; Zhang, B.; Liu, Q. Super-Resolution GaAs Nano-Structures Fabricated by Laser Direct Writing. *Mater. Sci. Semicond. Process.* **2018**, *84* (March), 119–123. https://doi.org/10.1016/j.mssp.2018.05.016.

(15) Trukhin, V. N.; Buyskikh, A. S.; Kaliteevskaya, N. A.; Bourauleuv, A. D.; Samoilov, L. L.; Samsonenko, Y. B.; Cirlin, G. E.; Kaliteevski, M. A.; Gallant, A. J. Terahertz Generation by GaAs Nanowires. *Appl. Phys. Lett.* **2013**, *103* (7), 072108. https://doi.org/10.1063/1.4818719.

(16) Yashina, N. Y.; Al-Alwani, A. J. K.; Tsvetkova, O. Y.; Kolesnikova, A. S.; Glukhovskoy, E. G.; Sevostyanov, V. P. Properties of Semiconductor GaAs Nanoparticles, Synthesized by Combination of Mechanical Milling Methods and Chemical Etching. *J. Phys. Conf. Ser.* **2018**, *1124* (2), 022020. https://doi.org/10.1088/1742-6596/1124/2/022020.

(17) Hung, Y.-J.; Lee, S.-L.; Wu, K.-C.; Tai, Y.; Pan, Y.-T. Antireflective Silicon Surface with Vertical-Aligned Silicon Nanowires Realized by Simple Wet Chemical Etching Processes. *Opt. Express* **2011**, *19* (17), 15792. https://doi.org/10.1364/OE.19.015792.

(18) Yew, Y. T.; Ambrosi, A.; Pumera, M. Nitroaromatic Explosives Detection Using Electrochemically Exfoliated Graphene. *Sci. Rep.* **2016**, *6* (August), 1–11. https://doi.org/10.1038/srep33276.

(19) Silvestre, C. M.; Nguyen, V.; Jansen, H.; Hansen, O. Deep Reactive Ion Etching of 'Grass-Free' Widely-Spaced Periodic 2D Arrays, Using Sacrificial Structures. *Microelectron. Eng.* **2020**, *223* (January), 111228. https://doi.org/10.1016/j.mee.2020.111228.

(20) Li, R. R.; Dapkus, P. D.; Thompson, M. E.; Jeong, W. G.; Harrison, C.; Chaikin, P. M.; Register, R. A.; Adamson, D. H. Dense Arrays of Ordered GaAs Nanostructures by Selective Area Growth on Substrates Patterned by Block Copolymer Lithography. *Appl. Phys. Lett.* **2000**, *76* (13), 1689–1691. https://doi.org/10.1063/1.126137.

(21) Samuel, A. B.; Neethish, M. M.; Ravi Kanth Kumar, V. V.; Nalam, S. A.; Sree Harsha, S.; Prem Kiran, P. Supercontinuum Generation in Antimony Zinc Borate Glasses—A Material Perspective. *J. Appl. Phys.* **2023**, *133* (9), 093104. https://doi.org/10.1063/5.0134548.

(22) Saikiran, V.; Srinivasa Rao, N.; Devaraju, G.; Chang, G. S.; Pathak, A. P. Ion Beam Irradiation Effects on Ge Nanocrystals Synthesized by Using RF Sputtering Followed by RTA. *Nucl. Instruments Methods Phys. Res. Sect. B Beam Interact. with Mater. Atoms* **2013**, *315* (November), 161–164. https://doi.org/10.1016/j.nimb.2013.04.008.

(23) Nandhagopal, P.; Pal, A. K.; Bharathi Mohan, D. Fabrication of Silver and Silver-Copper Bimetal Thin Films Using Co-Sputtering for SERS Applications. *Opt. Mater. (Amst).* **2019**, *97* (August),

109381. https://doi.org/10.1016/j.optmat.2019.109381.

(24) Al-Kuhaili, M. F.; Durrani, S. M. A.; Khawaja, E. E. Characterization of Hafnium Oxide Thin Films Prepared by Electron Beam Evaporation. *J. Phys. D. Appl. Phys.* **2004**, *37* (8), 1254–1261. https://doi.org/10.1088/0022-3727/37/8/015.

(25) Portail, M.; Frayssinet, E.; Michon, A.; Rennesson, S.; Semond, F.; Courville, A.; Zielinski, M.; Comyn, R.; Nguyen, L.; Cordier, Y.; Vennéguès, P. CVD Elaboration of 3C-SiC on AlN/Si Heterostructures: Structural Trends and Evolution during Growth. *Crystals* **2022**, *12* (11), 1605. https://doi.org/10.3390/cryst12111605.

(26) Na, S.-Y.; Yoon, S.-M. Impacts of HfO 2 /ZnO Stack-Structured Charge-Trap Layers Controlled by Atomic Layer Deposition on Nonvolatile Memory Characteristics of In-Ga-Zn-O Channel Charge-Trap Memory Thin-Film Transistors. *IEEE J. Electron Devices Soc.* **2019**, *7* (February), 453–461. https://doi.org/10.1109/JEDS.2019.2908255.

(27) Alaskar, Y.; Arafin, S.; Wickramaratne, D.; Zurbuchen, M. A.; He, L.; McKay, J.; Lin, Q.; Goorsky, M. S.; Lake, R. K.; Wang, K. L. Towards van Der Waals Epitaxial Growth of GaAs on Si Using a Graphene Buffer Layer. *Adv. Funct. Mater.* **2014**, *24* (42), 6629–6638. https://doi.org/10.1002/adfm.201400960.

(28) Rawat, R.; Tiwari, A.; Arun, N.; Rao, S. V. S. N.; Pathak, A. P.; Rao, S. V.; Tripathi, A. Synthesis of CuO Hollow Nanoparticles Using Laser Ablation: Effect of Fluence and Solvents. *Appl. Phys. A* **2020**, *126* (3), 226. https://doi.org/10.1007/s00339-020-3403-1.

(29) Miotello, A.; Bonelli, M.; Marchi, G. De; Mattei, G.; Mazzoldi, P.; Sada, C.; Gonella, F. Formation of Silver Nanoclusters by Excimer–Laser Interaction in Silver-Exchanged Soda-Lime Glass. *Appl. Phys. Lett.* **2001**, *79* (15), 2456–2458. https://doi.org/10.1063/1.1406984.

(30) Hari, P.; Adair, J.; Tolk, N.; Sanghera, J.; Aggarwal, I. Infrared Laser Ablation of Glassy As2Se3. *J. Non. Cryst. Solids* **2006**, *352* (23–25), 2430–2433. https://doi.org/10.1016/j.jnoncrysol.2006.03.044.

(31) Zhou, Q.; Ong, E. B. L.; Lim, S. L.; Vajandar, S.; Osipowicz, T.; Gong, X.; Tok, E. S.; Yeo, Y.-C. Single Crystalline Germanium-Lead Formed by Laser-Induced Epitaxy. *ECS J. Solid State Sci. Technol.* **2016**, *5* (6), P353–P360. https://doi.org/10.1149/2.0331606jss.

(32) Kumar, A.; Singh, F.; Koinkar, P. M.; Avasthi, D. K.; Pivin, J. C.; More, M. A. Effect of Intense Laser and Energetic Ion Irradiation on Raman Modes of Multiwalled Carbon Nanotubes. *Thin Solid Films* **2009**, *517* (15), 4322–4324. https://doi.org/10.1016/j.tsf.2008.12.016.

(33) Stauss, S.; Urabe, K.; Muneoka, H.; Terashima, K. Pulsed Laser Ablation in High-Pressure Gases, Pressurized Liquids and Supercritical Fluids: Generation, Fundamental Characteristics and Applications. In *Applications of Laser Ablation - Thin Film Deposition, Nanomaterial Synthesis and Surface Modification*; InTech, 2016; Vol. 25, pp 275–281. https://doi.org/10.5772/65455.

(34) Bonse, J.; Gräf, S. Maxwell Meets Marangoni—A Review of Theories on Laser-Induced Periodic

Surface Structures. *Laser Photon. Rev.* **2020**, *14* (10), 2000215. https://doi.org/10.1002/lpor.202000215.

(35) Dinh, L. N.; Hayes, S.; Saw, C. K.; McLean, W.; Balooch, M.; Reimer, J. A. GaAs Nanostructures and Films Deposited by a Cu-Vapor Laser. *Appl. Phys. Lett.* **1999**, *75* (15), 2208–2210. https://doi.org/10.1063/1.124966.

(36) Perrière, J.; Millon, E.; Chamarro, M.; Morcrette, M.; Andreazza, C. Formation of GaAs Nanocrystals by Laser Ablation. *Appl. Phys. Lett.* **2001**, *78* (19), 2949–2951. https://doi.org/10.1063/1.1370992.

(37) Trelenberg, T. W.; Dinh, L. N.; Saw, C. K.; Stuart, B. C.; Balooch, M. Femtosecond Pulsed Laser Ablation of GaAs. *Appl. Surf. Sci.* **2004**, *221* (1–4), 364–369. https://doi.org/10.1016/S0169-4332(03)00937-1.

(38) Ganeev, R. A.; Baba, M.; Ryasnyansky, A. I.; Suzuki, M.; Kuroda, H. Laser Ablation of GaAs in Liquids: Structural, Optical, and Nonlinear Optical Characteristics of Colloidal Solutions. *Appl. Phys. B* **2005**, *80* (4–5), 595–601. https://doi.org/10.1007/s00340-004-1734-9.

(39) Ganeev, R. A.; Ryasnyanskii, A. I.; Kuroda, H. Laser Ablation of Gallium Arsenide in Different Solutions. *Opt. Spectrosc.* **2005**, *99* (6), 1006–1011. https://doi.org/10.1134/1.2149427.

(40) Lalayan, A. A. Formation of Colloidal GaAs and CdS Quantum Dots by Laser Ablation in Liquid Media. *Appl. Surf. Sci.* **2005**, *248* (1–4), 209–212. https://doi.org/10.1016/j.apsusc.2005.03.004.

(41) De Bonis, A.; Galasso, A.; Santagata, A.; Teghil, R. Laser Ablation of GaAs in Liquid: The Role of Laser Pulse Duration. *J. Phys. D. Appl. Phys.* **2016**, *49* (3), 035301. https://doi.org/10.1088/0022-3727/49/3/035301.

(42) De Bonis, A.; Santagata, A.; Galasso, A.; Teghil, R. Ultra-Short Pulsed Laser Deposition of Gallium Arsenide: A Comprehensive Study. *Appl. Phys. A* **2014**, *117* (1), 275–280. https://doi.org/10.1007/s00339-014-8543-8.

(43) Salminen, T.; Dahl, J.; Tuominen, M.; Laukkanen, P.; Arola, E.; Niemi, T. Single-Step Fabrication of Luminescent GaAs Nanocrystals by Pulsed Laser Ablation in Liquids. *Opt. Mater. Express* **2012**, *2* (6), 799. https://doi.org/10.1364/OME.2.000799.

(44) Sharifi, T.; Dorranian, D.; Torkamany, M. J. Optimisation of GaAs Nanocrystals Synthesis by Laser Ablation in Water. *J. Exp. Nanosci.* **2013**, *8* (6), 808–817. https://doi.org/10.1080/17458080.2011.608729.

(45) Abderrafi, K.; Jiménez, E.; Ben, T.; Molina, S. I.; Ibáñez, R.; Chirvony, V.; Martínez-Pastor, J. P. Production of Nanometer-Size GaAs Nanocristals by Nanosecond Laser Ablation in Liquid. *J. Nanosci. Nanotechnol.* **2012**, *12* (8), 6774–6778. https://doi.org/10.1166/jnn.2012.4548.

(46) Borowiec, A.; MacKenzie, M.; Weatherly, G. C.; Haugen, H. K. Femtosecond Laser Pulse Ablation of GaAs and InP: Studies Utilizing Scanning and Transmission Electron Microscopy. *Appl. Phys. A* **2003**, *77* (3–4), 411–417. https://doi.org/10.1007/s00339-002-1949-8.

(47) Ionin, A. A.; Kudryashov, S. I.; Seleznev, L. V.; Sinitsyn, D. V. Dynamics of the Spallative Ablation of a GaAs Surface Irradiated by Femtosecond Laser Pulses. *JETP Lett.* **2012**, *94* (10), 753–758. https://doi.org/10.1134/S002136401122005X.

(48) Apostolova, T.; Ionin, A. A.; Kudryashov, S. I.; Seleznev, L. V.; Sinitsyn, D. V. Self-Limited Ionization of GaAs at High Femtosecond Laser Intensities. In *AIP Conference Proceedings*; 2012; Vol. 1464, pp 146–157. https://doi.org/10.1063/1.4739869.

(49) Apostolova, T.; Ionin, A.; Kudryashov, S.; Seleznev, L.; Sinitsyn, D. <title>Carrier Dynamics-Induced Transient Photoexcitation and Energy Deposition in Femtosecond-Laser Irradiated GaAs</Title>. *XVIII Int. Symp. Gas Flow, Chem. Lasers, High-Power Lasers* **2010**, *7751*, 77511J-77511J – 6. https://doi.org/10.1117/12.880977.

(50) Ionin, A. A.; Kudryashov, S. I.; Makarov, S. V. Femtosecond Laser-Induced Periodical Nanomodification of Surface Composition. *Semiconductors* **2019**, *53* (16), 2094–2099. https://doi.org/10.1134/S106378261912011X.

(51) Margiolakis, A.; Tsibidis, G. D.; Dani, K. M.; Tsironis, G. P. Ultrafast Dynamics and Subwavelength Periodic Structure Formation Following Irradiation of GaAs with Femtosecond Laser Pulses. *Phys. Rev. B* **2018**, *98* (22), 224103. https://doi.org/10.1103/PhysRevB.98.224103.

(52) Abere, M. J.; Torralva, B.; Yalisove, S. M. Periodic Surface Structure Bifurcation Induced by Ultrafast Laser Generated Point Defect Diffusion in GaAs. *Appl. Phys. Lett.* **2016**, *108* (15), 153110. https://doi.org/10.1063/1.4946861.

(53) Sarracino, A.; Ansari, A. R.; Torralva, B.; Yalisove, S. Sub-100 Nm High Spatial Frequency Periodic Structures Driven by Femtosecond Laser Induced Desorption in GaAs. *Appl. Phys. Lett.* **2021**, *118* (24), 242106. https://doi.org/10.1063/5.0053037.

(54) Zhao, Z.; Song, Z.; Bai, F.; Shi, W.; Zhao, Q. Z. Terahertz Refractive Anisotropy on Femtosecond Laser Pulse Ablated Semi-Insulating Gallium Arsenide Surface. *Appl. Phys. A Mater. Sci. Process.* **2017**, *123* (4), 1–6. https://doi.org/10.1007/s00339-017-0852-2.

(55) Dostovalov, A.; Bronnikov, K.; Korolkov, V.; Babin, S.; Mitsai, E.; Mironenko, A.; Tutov, M.; Zhang, D.; Sugioka, K.; Maksimovic, J.; Katkus, T.; Juodkazis, S.; Zhizhchenko, A.; Kuchmizhak, A. Hierarchical Anti-Reflective Laser-Induced Periodic Surface Structures (LIPSSs) on Amorphous Si Films for Sensing Applications. *Nanoscale* **2020**, *12* (25), 13431–13441. https://doi.org/10.1039/d0nr02182b.

(56) Hamad, S.; Bharati Moram, S. S.; Yendeti, B.; Podagatlapalli, G. K.; Nageswara Rao, S. V. S.; Pathak, A. P.; Mohiddon, M. A.; Soma, V. R. Femtosecond Laser-Induced, Nanoparticle-Embedded Periodic Surface Structures on Crystalline Silicon for Reproducible and Multi-Utility SERS Platforms. *ACS Omega* **2018**, *3* (12), 18420–18432. https://doi.org/10.1021/acsomega.8b02629.

(57) Moram, S. S. B.; Shaik, A. K.; Byram, C.; Hamad, S.; Soma, V. R. Instantaneous Trace Detection

of Nitro-Explosives and Mixtures with Nanotextured Silicon Decorated with Ag–Au Alloy Nanoparticles Using the SERS Technique. *Anal. Chim. Acta* **2020**, *1101* (xxxx), 157–168. https://doi.org/10.1016/j.aca.2019.12.026.

(58) Kumar, K. R.; Banerjee, D.; Mangababu, A.; Prasad Goud, R. S.; Pathak, A. P.; Soma, V. R.; Nageswara Rao, S. V. S. Resistivity Dependence on Nanostructure Formation in Picosecond Ablation of Silicon and SERS-Based Sensing Applications. *J. Phys. D. Appl. Phys.* **2022**, *55* (40), 405103. https://doi.org/10.1088/1361-6463/ac818b.

(59) Podagatlapalli, G. K.; Hamad, S.; Rao, S. V. Trace-Level Detection of Secondary Explosives Using Hybrid Silver–Gold Nanoparticles and Nanostructures Achieved with Femtosecond Laser Ablation. *J. Phys. Chem. C* **2015**, *119* (29), 16972–16983. https://doi.org/10.1021/acs.jpcc.5b03958.

(60) Bharati, M. S. S.; Soma, V. R. Flexible Sers Substrates for Hazardous Materials Detection: Recent Advances. *Opto-Electronic Adv.* **2021**, *4* (11), 1–26. https://doi.org/10.29026/oea.2021.210048.

(61) Mangababu, A.; Sianglam, C.; Chandu, B.; Avasthi, D. K.; Rao, S. V.; Motapothula, M.; Rao, S. V. S. N. Effects of Initial Grain Size and Laser Parameters on HfO2 Nanoparticles Prepared Using Femtosecond Laser Ablation in Liquids. *J. Electron. Mater.* **2021**, *50* (4), 1742–1751. https://doi.org/10.1007/s11664-020-08610-z.

(62) Mangababu, A.; Sarang Dev, G.; Chandu, B.; Bharati, M. S. S.; Debashish, P.; Venugopal Rao, S.; Nageswara Rao, S. V. S. Fabrication and Characterization of GaAs Nanoparticles Achieved Using Femtosecond Laser Ablation. *Mater. Today Proc.* **2020**, *33* (5), 2385–2389. https://doi.org/10.1016/j.matpr.2020.05.727.

(63) Mangababu, A.; Sarang Dev, G.; Chandu, B.; Bharati, M. S. S.; Venugopal Rao, S.; Nageswara Rao, S. V. S. Structural Investigations of Picosecond Laser Ablated GaAs Nanoparticles in Different Liquids. *Nano-Structures & Nano-Objects* **2020**, *23*, 100509. https://doi.org/10.1016/j.nanoso.2020.100509.

(64) Mangababu, A.; Sai Prasad Goud, R.; Byram, C.; Rathod, J.; Banerjee, D.; Rao Soma, V.; Nageswara Rao, S. V. S. Multi-Functional Gallium Arsenide Nanoparticles and Nanostructures Fabricated Using Picosecond Laser Ablation. *Appl. Surf. Sci.* **2022**, *589* (January), 152802. https://doi.org/10.1016/j.apsusc.2022.152802.

(65) Mangababu, A.; Banerjee, D.; Ravi Kumar, K.; Sai Prasad Goud, R.; Rao Soma, V.; Nageswara Rao, S. V. S. Comparative Study of GaAs Nanostructures Synthesized in Air and Distilled Water by Picosecond Pulsed Laser Ablation and Application in Hazardous Molecules Detection. *Journal of Laser Applications*. 2022, p 032014. https://doi.org/10.2351/7.0000750.

(66) Akkanaboina, M.; Banerjee, D.; Kumar, K. R.; Goud, R. S. P.; Soma, V. R.; Rao, S. V. S. N. Gold Nanoparticles Coated LIPSS on GaAs for Trace Detection of RDX and Tetryl. *Surfaces and Interfaces* **2023**, *36*, 102563. https://doi.org/10.1016/j.surfin.2022.102563.

Chapter 2

Experimental Details

This chapter provides a detailed description of all of the experimental techniques used in this thesis for both the synthesis and characterization of nanomaterials. In this study, we used femtosecond and picosecond pulsed lasers for the synthesis of nanoparticles (NPs) and nanostructures (NSs). For morphology and compositional analysis, these NPs and NSs were subjected to various characterization techniques such as Transmission Electron Microscopy (TEM), Field Emission Scanning Electron Microscopy (FESEM), Optical Microscopy, Raman spectroscopy, and X-Ray Diffraction (XRD). The linear and nonlinear optical properties were also determined using UV-Vis-NIR spectroscopy, Photoluminescence (PL) spectroscopy, and Z-Scan techniques. All these techniques are explained in detail in this chapter.

2.1.0 Synthesis methods used in this work

As described in the previous chapter, in order to understand the formation and properties of GaAs NPs as well as NSs and its associated compounds, pulsed laser ablation (PLAL) was performed in air and different liquids. In this thesis, two different lasers with pulse durations of ~50 femtosecond (Ti: Sapphire) and ~30 picosecond (Nd:YAG) were used. More details about these lasers and specifications are given in the next sections 2.1.1 and 2.1.2.

2.1.1 Femtosecond Pulsed Laser Ablation in Liquids (fs PLAL)

In this study, we initially started optimizing the formation GaAs NPs and NSs using femtosecond laser[1,2]. The setup is as shown in the schematic Fig. 2.1. The laser beam produced by the Ti:Sapphire laser was directed onto the sample in the vertical geometry (top to down) using mirrors M_1-M_4. Using a half wave plate and Brewster polarizer combination placed externally in the laser beam path, energy of the beam was tuned in the range of 10-750 µJ. A focusing lens of focal length ~100 mm is used to focus the beam onto the sample. Sample was fixed at the bottom of a Borosil beaker, filled with 5 ml liquid, and placed on Newport; ESP 300 motion controller. This motion controller can precisely move the sample in micron size steps in both X and Y directions. The samples were raster scanned using this ESP controller programmed with LabVIEW for uniform exposure to the laser beam. Scan speeds/spacing etc. are mentioned in the respective chapters. Important specifications of the laser are given below.

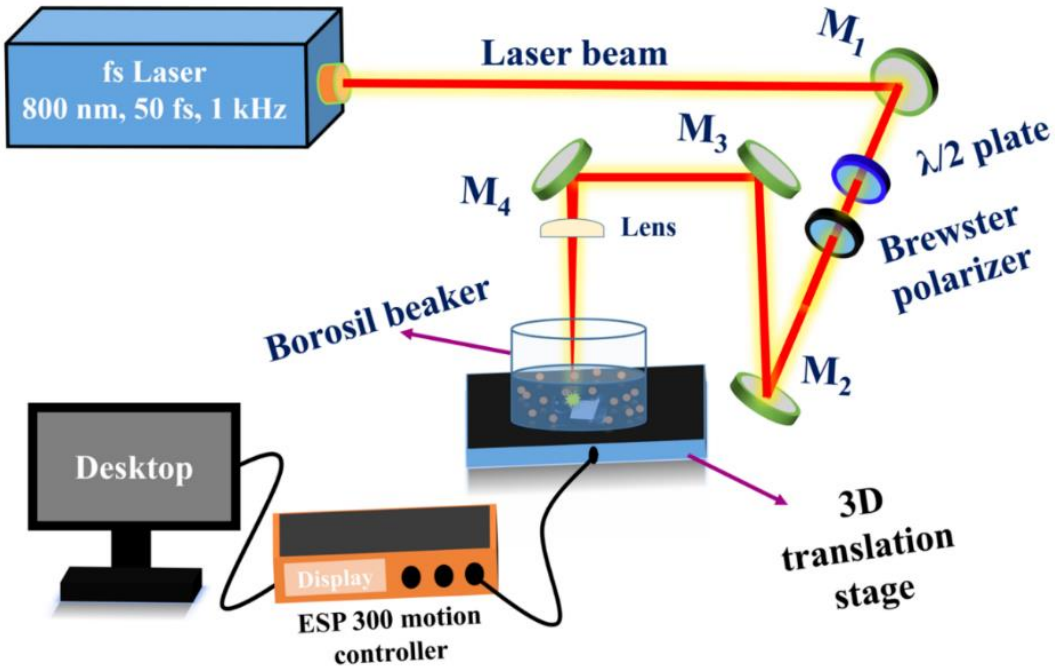

Fig. 2.1 Schematic representation of femtosecond laser ablation set-up used in this thesis [2].

Laser specifications

Make & Model	: M/s Coherent, LIBRA[3]
Lasing medium	: Ti:Sapphire crystal
Wavelength (λ)	: 800 nm
Pulse duration	: 50 fs
Repetition rate	: 1 kHz
Energy range	: 5-2000 µJ (varied by external optics)

2.1.2 Picosecond Pulsed Laser Ablation in Liquids (ps PLAL)

Further, experiments were also conducted using a picosecond laser to see the effect of laser pulse durations on the morphology of the resulting GaAs NPs and NSs[4–6]. The schematic of the setup was shown in Fig. 2.2. Ablation procedure conducted in this case is also similar to the procedure mentioned in the above section (2.1.1). Important specifications of the laser are given below.

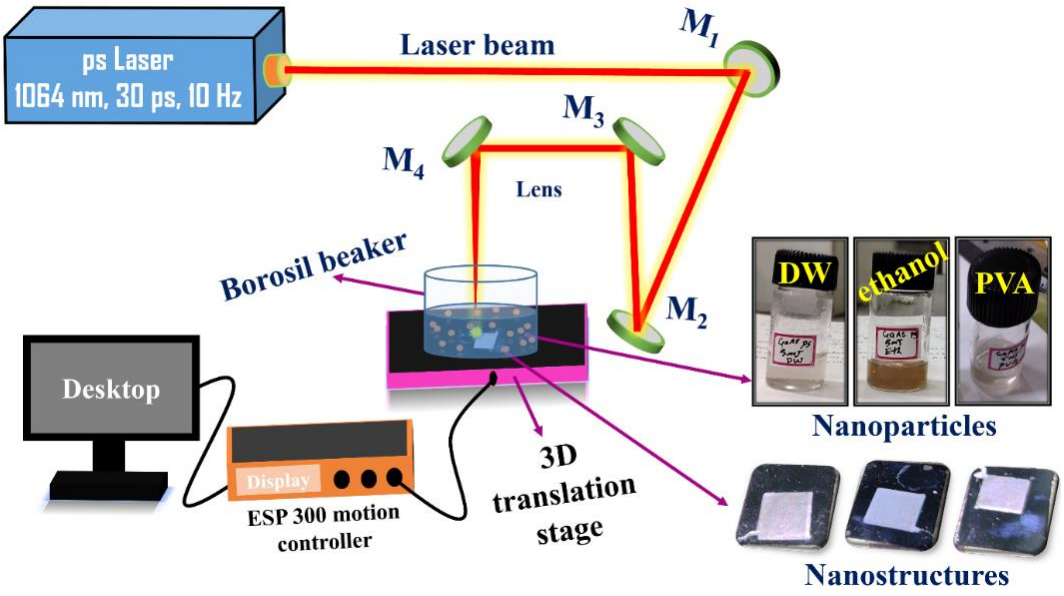

Fig. 2.2 Schematic representation of picosecond laser ablation set up used in this thesis.

Laser specifications

Make and Model	: EKSPLA, PL 2251[7]
Lasing medium	: Nd: YAG or Nd: $Y_3Al_5O_{12}$
Wavelength (λ)	: 532 and 1064 nm,
Pulse duration	: 30 ps,
Repetition rate	: 10 Hz
Energy range	: 1 - 15 mJ.

2.1.3 Pulsed laser ablation in air (PLAA)

For the study of surface structures on GaAs under different conditions, ablation/structuring was performed in air medium. The experimental setup of PLAA performed with fs laser (presented in chapter 5) and ps laser (presented in chapter 4) were similar to Fig. 2.1 and 2.2., respectively. However, in this PLAA, the sample was not placed inside the Borosil beaker, it was directly stuck on a metal plate which was placed on the ESP 300 motion controller as depicted in the Fig. 2.3.

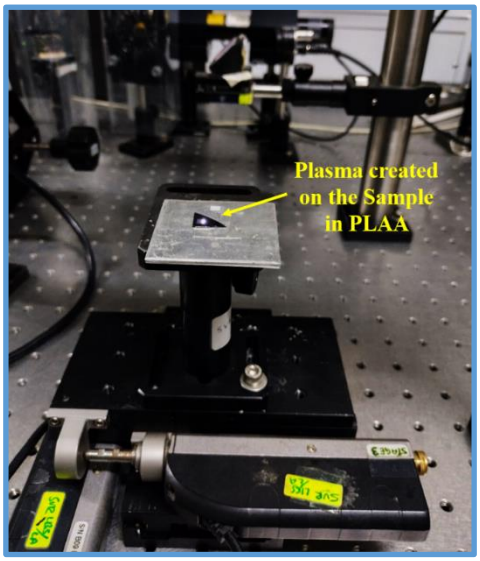

Fig. 2.3 Image of the plasma created on the surface of GaAs in the PLAA process. The image was captured with a mobile phone's camera.

2.2.0 Characterization techniques used in this thesis

For understanding the basic morphology, composition, and optical properties of the GaAs NPs and NSs, various well-established characterization techniques such as microscopy (Optical, TEM, FESEM, and EDAX), spectroscopy (UV-Vis-NIR, Photoluminescence, and Raman), and XRD were used. About each of these instruments and their specifications were mentioned below.

2.2.1 Optical microscope

After the formation of NSs on the ablated substrates/bulk materials, optical microscope is used to check if prominent lines/structures are formed. In this work, OLYMPUS, DP73 was used for obtaining optical images (shown in Fig. 2.4). The resolution of the optical microscope is around 200-300 nm. When the size of the NPs or NSs is below the resolution limit of this optical microscope, high resolution electron microscopes can be utilized for obtaining the morphology. Basically, optical microscopes work in combination of a few lenses and a visible light source, and an illumination detector. The light source will be shined on to the sample and scattered light will be captured through the objectives and eyepieces. These optical microscopes can offer magnifications in the range of 5X to 100X, whereas further magnifications are difficult.

As we know optical microscopes will have a diffraction limit when the particle/nano-entities size reaches to a certain lower value, this diffraction limit in general termed as Abbe diffraction limit (given below 2.1, adopted from ref [8]).

$$d = \frac{\lambda}{2nSin(\theta)} \quad \text{..... (2.1)}$$

Where, d is the length or size of the object, λ is wavelength of the light used, and n is the index of refraction of the medium in which imaging is performed, and θ is the half angle subtended by objective.

Suppose we use a light with wavelength of 600 nm, for imaging a sample, the particles below the size of 300 nm cannot be seen clearly. To further enhance the resolution of the microscopes, the accelerated particles such as electrons are used in the later stages. As per the De Broglie theory, the wavelength of the fast moving particles can be tuned by the following formula 2.2 (adopted from ref [9,10]).

$$\lambda = \frac{h}{\sqrt{2meE}} \quad \text{..... (2.2)}$$

Fig. 2.4 Image of an Optical microscope.

Where, 'λ' is the wavelength of the particle, 'h' is Planks constant, 'm' is mass of the particle, 'e' is charge of the particle and 'E' is Kinetic energy of the particle. This formula is applicable in non-relativistic limit. For accelerated electrons in the energy range of 20-200 KeV, the wavelength order is around 3-8 pm. Such a lower wavelengths can resolve the smaller features by overcoming the diffraction limits and can improve the magnifications up to 100-500 KX. These electron microscopies are of two kinds (1) Scanning Electron Microscopy, (2) Transmission Electron Microscopy.

2.2.2 Field Emission Scanning Electron Microscopy (FESEM)

FESEM works with electron beam instead of light and provides morphological information at higher magnifications ranging 10X-500KX. As shown in the schematic Fig. 2.5 (a) an accelerated and collimated electron beam extracted from a field emission gun will hit the target specimen/sample and generates secondary electrons. A detector in backscattering geometry

analyses the intensity profiles of these secondary electrons, which gives rise the morphology of the sample. Backscattered electrons and augur electrons can also be processed to image as well as to estimate the stoichiometry of the sample's surface. In this thesis, Carl Zeiss Smart SEM, Model: ULTRA 55 is used throughout the work[11], which is as shown in Fig. 2.5 (b).

2.2.2 (a) Energy Dispersive X-Ray Analysis (EDAX)

While examining materials using FESEM, there is a facility to reveal the composition of the material at a particular spot (or) very small area on the sample using the EDAX technique which employed in the FESEM instrument. Probing electron beam can ionize inner shells (like K, L etc.) of the target atoms. The filling of these vacancies in inner shells from outer shells will lead to the emission of characteristic X-rays (like K_α, K_β, L_α, L_β, etc.). Elemental analysis can be performed by using energy dispersive techniques as the energies of these X-rays are different for different elements (These are like a finger prints of atoms). This technique is thoroughly used in this thesis to determine the spatial composition profiles of various elements in samples.

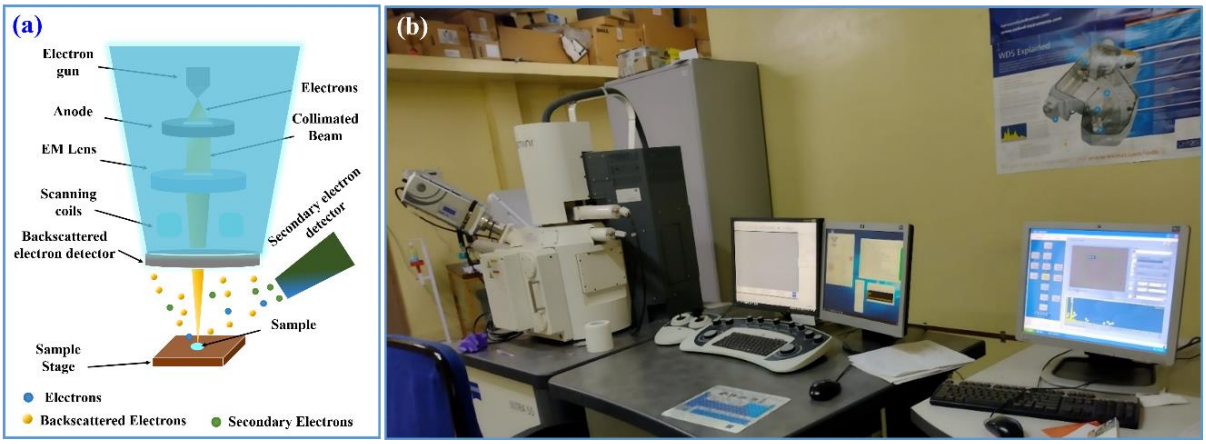

Fig. 2.5 (a) Schematic representation of FESEM and (b) image of the Zeiss smart SEM ULTRA 55 equipped with EDAX [11].

2.2.3 Transmission Electron Microscopy (TEM)

TEM is an advanced electron microscopy technique used for imaging the nano-scale entities which otherwise cannot be seen through regular optical or low-resolution microscopes. In this technique, highly accelerated, collimated electron beam passes through the thin sample which is placed on a specially designed TEM grids, reaches the detector at the other end of the sample carrying information of the sample to be imaged, as shown in the schematic Fig. 2.6 (a). In this thesis, we have utilized TEM EM FEI Tecnai G2 S Twin [shown in Fig. 2.6 (b)], 200 kV and JEM 2100 (HR) for imaging GaAs NPs. The power supply used is of 200 kV for the

acceleration of e-beam which in turn reduces its wavelength much lower to the order of angstroms, thereby facilitating the capture of features of the order of less than 1 nm.

2.2.3 (a) Selected Area Electron Diffraction (SAED)

SAED is an excellent tool for the detection of crystallographic orientations and inter-planar spacing (d-spacing) within the selected region with high special resolution. This selected area diffraction is an essential measurement for analyzing the nano-dimensional materials such as NPs and NWs. The SAED attached to the above-mentioned TEM facility has been utilized in the current thesis for determining the nature of the formed GaAs NPs.

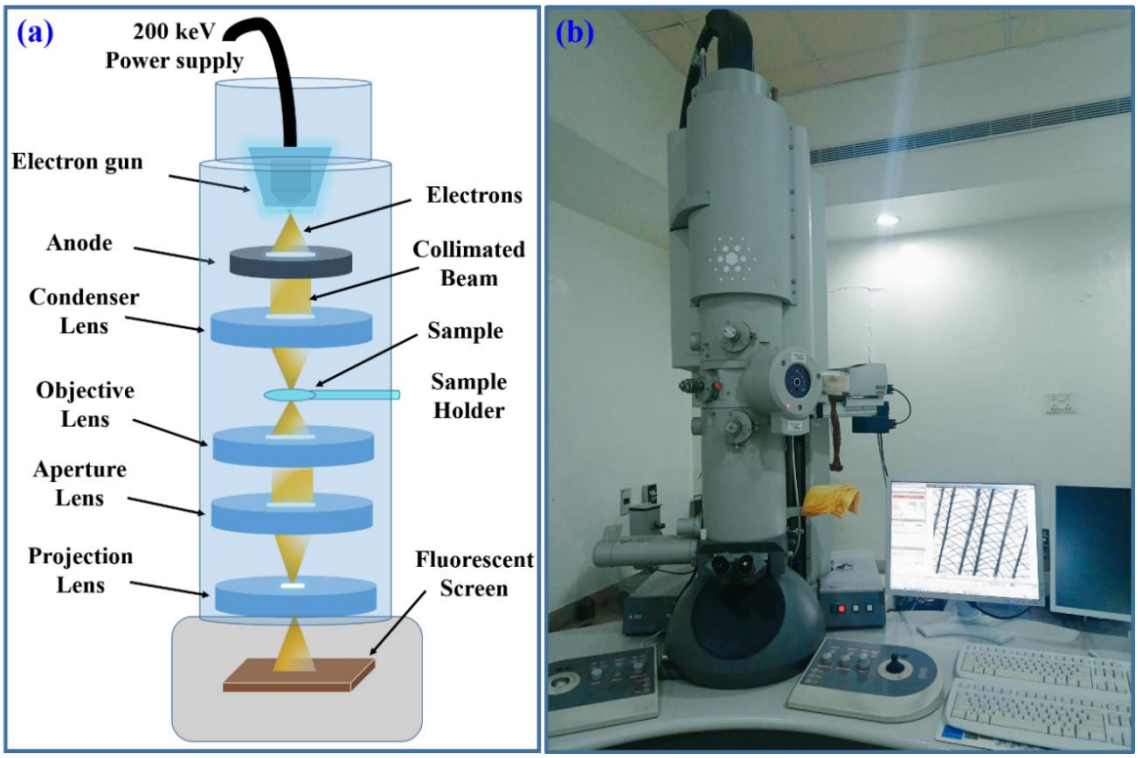

Fig. 2.6 Schematic representation and real image of TEM.

2.2.4 X-Ray Diffraction (XRD)

XRD is a tool used for obtaining the crystallographic orientations and lattice parameters of a material[12,13]. Here, in this thesis, XRD is utilized for obtaining the crystallographic information of the produced GaAs NPs. The image of the Glancing incident XRD (GIXRD) facility available in the School of Physics is shown in the Fig. 2.7.

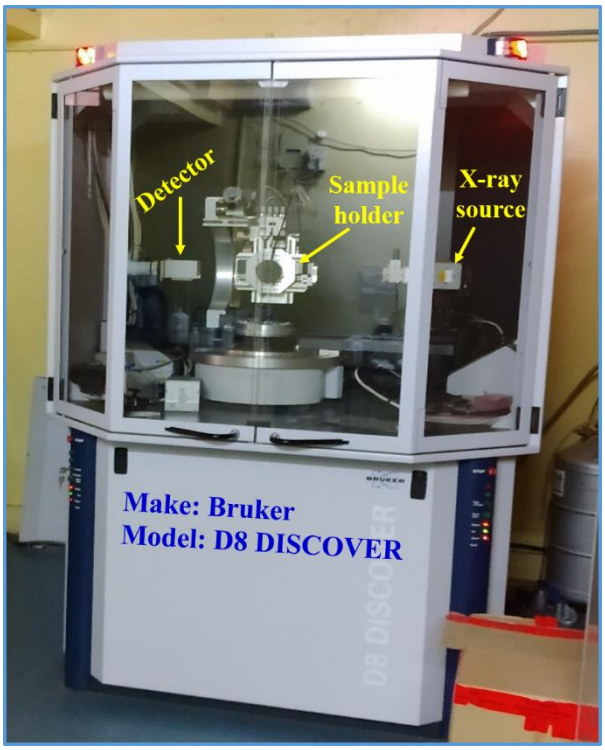

Fig 2.7 Image of Bruker: D8 DISCOVER XRD machine used in this thesis.

Specifications

Make	: BRUKER
Model	: D8 DISCOVER
Source	: Cu k alpha
2 theta range	: 0^0-170^0
Modes	: XRD and XRF modes available
Resolution	: 0.01 (angle in degrees)

2.2.5 Raman spectroscopy

Raman spectra measurements performed in this thesis are carried out using Horiba LabRAM HR Evolution, 532 nm. The image of the instrument is as shown in Fig. 2.8.

Specifications

Laser source	: 532 nm
Objective lens used	: 100X, spot size: 0.72 µm
Detector	: CCD detector
Spectral range	: 50 cm^{-1} to 4000 cm^{-1}
Accumulation	: 5
Acquisition time	: 10 sec

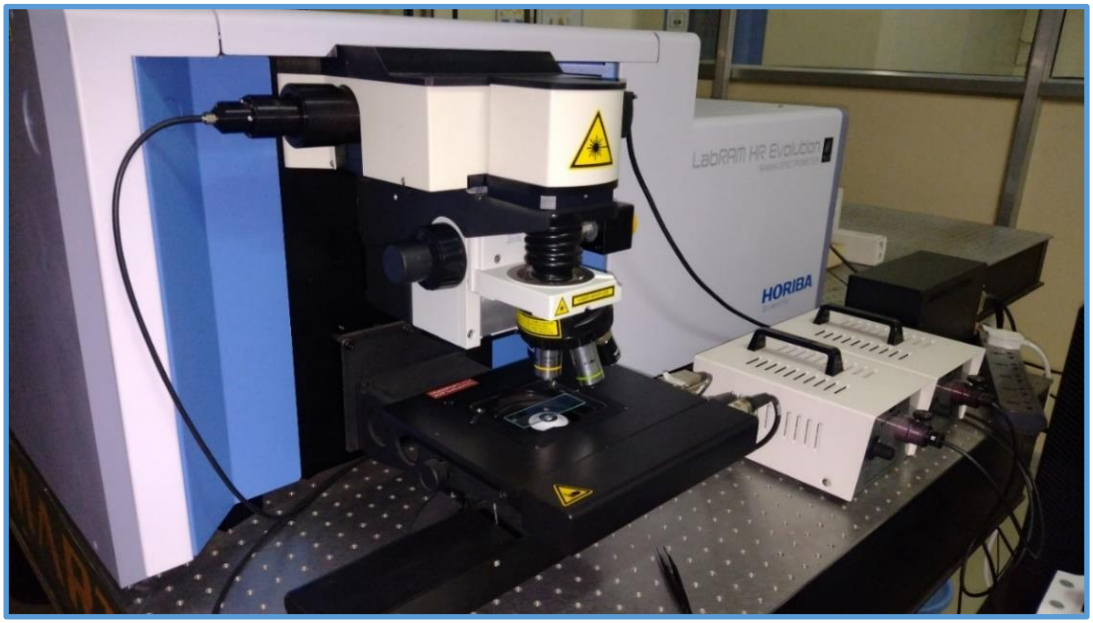

Fig. 2.8 Image of the Raman facility (Horiba LabRAM, HR Evolution) used in this thesis.

2.2.6 Photoluminescence spectroscopy

Photoluminescence measurements for the GaAs NPs colloidal solutions are performed using two instruments in different parts of this thesis. (1) Horiba Fluorolog spectrometer, excitation wavelength of ~355 nm (data shown in chapter 3). (2) Horiba LabRAM, HR Evolution shown in Fig. 2.8, operated in PL mode at an excitation wavelength of ~325 nm with a lens 40X, and spot size ~1 µm.

2.2.7 UV- Vis-NIR spectroscopy (NPs' absorption and NSs' antireflection)

Fig. 2.9 Image of the UV-Vis-NIR spectrometer (Agilent, Carry 5000 UMA).

The absorption spectra of GaAs NPs and antireflection properties of GaAs NSs were measured using Agilent technologies UV-Visible-NIR (Carry 5000 UMA) spectrometer. The UMA setup attached to the instrument provides flexibility of acquiring reflection data at different incident angles on the sample. Image of the instrument is shown in the Fig. 2.9.

2.3Application of GaAs NPs (Femtosecond NLO studies)

The produced GaAs NPs in the colloidal solution form were tested for their non-linear behavior. The NLO measurements were performed using the fs Z-scan approach reported in Ref [14]. A femtosecond oscillator (Coherent CHAMELEON, US) with ~80 MHz repetition rate and ~150 fs pulse duration was employed for this purpose. Data was collected at three distinct wavelengths: 800 nm, 850 nm, and 900 nm. The resulting NLO data are fitted using the conventional two-photon absorption model. The schematic setup was shown in the Fig. 2.10. The open aperture mode data [Fig. 2.10 (a)] was used to compute nonlinear absorption and the closed aperture mode data [Fig.2.10 (b)] was used to compute nonlinear refractive index of the GaAs NPs colloidal solutions. All the important observations are mentioned in the chapter 4.

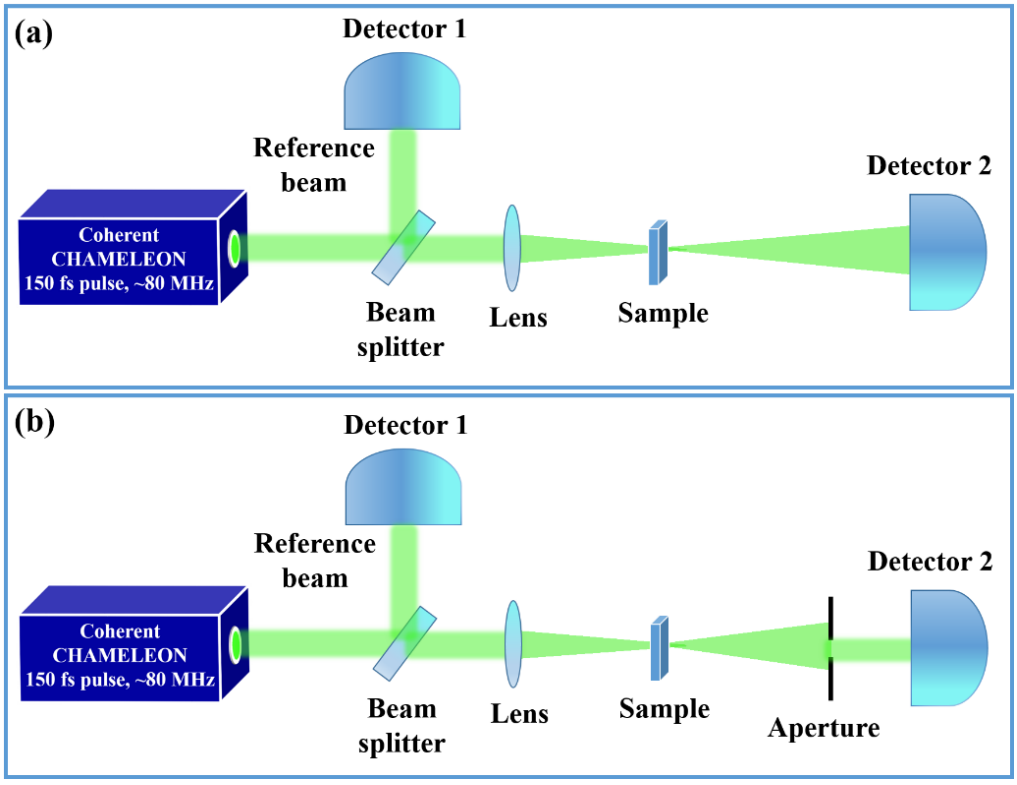

Fig. 2.10 Schematic representation of Z-scan technique used in this study, (a) open aperture mode, and (b) closed aperture mode.

2.4 Applications of GaAs surface structures (GaAs NSs)

Quasi-periodic and periodic surface structures of GaAs were tested for their antireflective and wettability properties. Further, upon on coating these GaAs NSs with Au NPs they were utilized as hybrid Surface Enhanced Raman Scattering (SERS) platforms. The following sections 2.4.1 and 2.4.2 describes all the specifications of instruments used for this purpose. Antireflection studies were conducted using Carry 5000 UMA set-up, these details were already mentioned in the section 2.2.7.

2.4.1 Wettability properties of GaAs NSs

Wettability properties of GaAs NSs fabricated were studied using Apex contact angle meter (ADCAM-02). It consists a visible light source, a sample holder, micro-syringe, and a CCD camera. A liquid drop (DW at a flow rate of 1 µL/s) will be released on to the GaAs NSs placed on sample holder. The images of the bubble will be collected with the CCD camera and will be analyzed for measuring contact angles. The contact angle measurements performed on three different GaAs NSs were presented in the chapter 4.

2.4.2 Surface Enhanced Raman Scattering (SERS)

Even though, a wide range of analytical methods are being employed for identifying hazardous molecules, Raman spectroscopy and its derived techniques remain promising[15]. Raman spectroscopy gives fingerprints of molecules and it is capable of real-time sensing. However, Raman is a relatively weak process with incredibly small scattering cross-sections, making molecular trace identification extremely challenging. An alternative method, SERS, has been developed for this purpose[16].

In SERS, a specially designed substrate is used to enhance the intensity of Raman signal. In general, the plasmonic NPs/NSs (Au, Ag, & Cu) are used as SERS substrates[17]. When an analyte molecule adsorbed near the plasmonic NPs/NSs, its Raman intensity gets enhanced due to the localized surface plasmon resonance (LSPR)[18]. Positive and negative charges in a plasmonic NP transit in opposite directions when it gets illuminated by an external electromagnetic (EM) field, creating an electric dipole. The nucleus' intrinsic field brings the electrons back into equilibrium, creating charged oscillations. When this oscillating frequency is in resonance with the applied field, these oscillations can be defined as localized surface plasmon resonance (LSPR)[19]. When compared to the equilibrium condition, the light scattering at this LSPR is at its highest level. As a result, the Raman scattering will increase, resulting in an increased Raman signal. This process of Raman signal enhancement in which LSPR is

involved is termed as EM enhancement. Apart from this there is another mechanism responsible for the enhancement of Raman signal in non-plasmonic materials such as graphene and other nanostructured semiconductors[20]. In this process, the charge/electron transfer between the analyte molecule and the SERS substrate contributes the increase in the Raman scattering. This process is called as chemical enhancement[19].

Now days, a variety of SERS substrates are being developed every day to obtain the advantage of both EM and chemical enhancements to achieve better signal enhancement and reliability. Hybrid SERS substrates are one among them[21], in which plasmonic films/NPs will be coated on a non-plasmonic structured semiconductor/dielectric. The size, shape, density of coated NPs and the morphology of the underneath structure will have significant role in the SERS. Hence, in this thesis, GaAs NSs with different surface morphologies are achieved by laser ablation and these are coated with Au films and annealed. These annealed Au/GaAs NSs are utilized as hybrid-SERS based sensors for detecting different analytes such as (expand) MG, MB, Thiram, RDX, and Tetryl. The enhancement factors are calculated using equation 2.3, given below [adopted from references[22,23]].

$$EF = \frac{I_{SERS}}{I_{Raman}} \times \frac{C_{Raman}}{C_{SERS}} \qquad \text{.....} \qquad \textbf{(2.3)}$$

2.4.2 (a) Au deposition by thermal evaporation technique

Fig. 2.11 Image of the thermal evaporation chamber and its controller used for Au deposition.

In order to make the GaAs NSs as active hybrid SERS substrates, gold coating has been performed. A thin layer of ~25 nm gold was deposited in a thermal evaporation chamber operating at a vacuum pressure of 5×10^{-6} mbar before deposition and 2×10^{-5} mbar during

deposition. The image of thermal evaporation chamber is shown in Fig. 2.11 (This is an assembled system with the help of HHV, India).

2.4.2 (b) Thermal Annealing

After coating a thin layer of gold on the GaAs NSs, thermal annealing has been carried out to uniformly decorate the ridges of GaAs with Au NPs. Initially, a gold film of thickness 25 nm was annealed at different temperatures ranging from 200-800 °C, an optimized temperature of 400 °C was chosen for further studies. Image of the furnace used in this thesis is depicted in Fig. 2.12.

Fig. 2.12 Thermal annealing chamber (ANTS, Copper Electric 1200 Degree C Horizontal tube furnace).

2.4.2 (c) SERS measurements by portable Raman instrument

A portable Raman spectrometer with 785 nm laser source is used for detecting the SERS signals of different analytes. This has very easy and quick measurement process. The image is as shown in Fig. 2.13. All the SERS data depicted in this thesis was ploted using orgin software and baseline corrected for clear presentation.

Specifications of the instrument

Wavelength of the laser	: 785 nm
Spot size	: ~100 µm
Acquisition	: 10 s
Accumulation	: 5

Fig. 2.13 Portable Raman instrument (i-Raman plus, B&W Tek) used for recording SERS data.

2.5 Summary

In this chapter, major synthesis and characterization techniques are mentioned in detail with their corresponding real images and specifications. For each technique, a short note on the background details and working principles are also described. Other specific details of the experiments are mentioned in the respective chapters.

References

(1) Mangababu, A.; Sarang Dev, G.; Chandu, B.; Bharati, M. S. S.; Debashish, P.; Venugopal Rao, S.; Nageswara Rao, S. V. S. Fabrication and Characterization of GaAs Nanoparticles Achieved Using Femtosecond Laser Ablation. *Mater. Today Proc.* **2020**, *33* (5), 2385–2389. https://doi.org/10.1016/j.matpr.2020.05.727.

(2) Akkanaboina, M.; Banerjee, D.; Kumar, K. R.; Goud, R. S. P.; Soma, V. R.; Rao, S. V. S. N. Gold Nanoparticles Coated LIPSS on GaAs for Trace Detection of RDX and Tetryl. *Surfaces and Interfaces* **2023**, *36*, 102563. https://doi.org/10.1016/j.surfin.2022.102563.

(3) Coherent Operator's Manual. Libra Ultrafast Ampflifier Laser System. *St. Cl.* **2013**, 95054.

(4) Mangababu, A.; Sarang Dev, G.; Chandu, B.; Bharati, M. S. S.; Venugopal Rao, S.; Nageswara Rao, S. V. S. Structural Investigations of Picosecond Laser Ablated GaAs Nanoparticles in Different Liquids. *Nano-Structures & Nano-Objects* **2020**, *23*, 100509. https://doi.org/10.1016/j.nanoso.2020.100509.

(5) Mangababu, A.; Banerjee, D.; Ravi Kumar, K.; Sai Prasad Goud, R.; Rao Soma, V.; Nageswara Rao, S. V. S. Comparative Study of GaAs Nanostructures Synthesized in Air and Distilled Water by Picosecond Pulsed Laser Ablation and Application in Hazardous Molecules Detection. *Journal of Laser Applications*. 2022, p 032014. https://doi.org/10.2351/7.0000750.

(6) Mangababu, A.; Sai Prasad Goud, R.; Byram, C.; Rathod, J.; Banerjee, D.; Rao Soma, V.; Nageswara Rao, S. V. S. Multi-Functional Gallium Arsenide Nanoparticles and Nanostructures Fabricated Using Picosecond Laser Ablation. *Appl. Surf. Sci.* **2022**, *589* (January), 152802. https://doi.org/10.1016/j.apsusc.2022.152802.

(7) EKSPLA Picosecond Laser Manual -PL2251; Lithuania. **2000**, P 17-19.

(8) Rahman, A. Nano-and Micro-Features on Semiconductor Chips Measured Via Terahertz Reconstructive Imaging Route. *Nov. Res. Sci.* **2019**, *1* (4). https://doi.org/10.31031/NRS.2019.01.000519.

(9) Kepner, G. R. Relating the DeBroglie and Compton Wavelengths to the Velocity of Light? *Appl. Phys. Res.* **2018**, *10* (4), 102. https://doi.org/10.5539/apr.v10n4p102.

(10) Lima, N. W.; Nascimento, M. M.; Cavalcanti, C.; Ostermann, F. Louis de Broglie's Wave-Particle Duality: From Textbooks' Blackboxes to a Chain of Reference Presentation. *Rev. Bras. Ensino Fis.* **2020**, *42*. https://doi.org/10.1590/1806-9126-RBEF-2019-0134.

(11) Smartsem, V. Operating Software for Scanning Electron Microscopes Software Manual. **2012**, 1–535.

(12) B.D.Cullity; UoNotreDame. *Elements of Diffraction*; 1994.

(13) Woolley, J. C. Introduction to Solid State Physics. *J. Mech. Phys. Solids* **1957**, *6* (1), 83. https://doi.org/10.1016/0022-5096(57)90051-0.

(14) Sheik-Bahae, M.; Said, A. A.; Wei, T. H.; Hagan, D. J.; Van Stryland, E. W. Sensitive

Measurement of Optical Nonlinearities Using a Single Beam. *IEEE J. Quantum Electron.* **1990**, *26* (4), 760–769. https://doi.org/10.1109/3.53394.

(15) Yadav, S.; Senapati, S.; Desai, D.; Gahlaut, S.; Kulkarni, S.; Singh, J. P. Portable and Sensitive Ag Nanorods Based SERS Platform for Rapid HIV-1 Detection and Tropism Determination. *Colloids Surfaces B Biointerfaces* **2021**, *198* (September 2020), 111477. https://doi.org/10.1016/j.colsurfb.2020.111477.

(16) Bharati, M. S. S.; Byram, C.; Soma, V. R. Femtosecond Laser Fabricated Ag@Au and Cu@Au Alloy Nanoparticles for Surface Enhanced Raman Spectroscopy Based Trace Explosives Detection. *Front. Phys.* **2018**, *6* (March), 1–13. https://doi.org/10.3389/fphy.2018.00028.

(17) Haidar, I.; Day, A.; Martino, U.; Chevillot-Biraud, A.; Félidj, N.; Boubekeur-Lecaque, L. Bottom-up Assembly of Au@Ag Plasmonic Nanocrystals: Issues to Be Addressed to Achieve a Good SERS Substrate. *Appl. Mater. Today* **2019**, *15*, 462–471. https://doi.org/10.1016/j.apmt.2019.02.015.

(18) Lin, Y.; Zhang, Y.-J.; Yang, W.-M.; Dong, J.-C.; Fan, F.-R.; Zhao, Y.; Zhang, H.; Bodappa, N.; Tian, X.-D.; Yang, Z.-L.; Stucky, G. D.; Tian, Z.-Q.; Li, J.-F. Size and Dimension Dependent Surface-Enhanced Raman Scattering Properties of Well-Defined Ag Nanocubes. *Appl. Mater. Today* **2019**, *14*, 224–232. https://doi.org/10.1016/j.apmt.2018.12.012.

(19) Pilot, R.; Signorini, R.; Durante, C.; Orian, L.; Bhamidipati, M.; Fabris, L. A Review on Surface-Enhanced Raman Scattering. Biosensors (Basel). **2019,** 9, 57. https://doi.org/10.3390/bios9020057.

(20) Tegegne, W. A.; Su, W.-N.; Tsai, M.-C.; Beyene, A. B.; Hwang, B.-J. Ag Nanocubes Decorated 1T-MoS2 Nanosheets SERS Substrate for Reliable and Ultrasensitive Detection of Pesticides. *Appl. Mater. Today* **2020**, *21*, 100871. https://doi.org/10.1016/j.apmt.2020.100871.

(21) Moram, S. S. B.; Shaik, A. K.; Byram, C.; Hamad, S.; Soma, V. R. Instantaneous Trace Detection of Nitro-Explosives and Mixtures with Nanotextured Silicon Decorated with Ag–Au Alloy Nanoparticles Using the SERS Technique. *Anal. Chim. Acta* **2020**, *1101* (xxxx), 157–168. https://doi.org/10.1016/j.aca.2019.12.026.

(22) Moram, S. S. B.; Byram, C.; Soma, V. R. Gold-Nanoparticle- and Nanostar-Loaded Paper-Based SERS Substrates for Sensing Nanogram-Level Picric Acid with a Portable Raman Spectrometer. *Bull. Mater. Sci.* **2020**, *43* (1), 53. https://doi.org/10.1007/s12034-019-2017-8.

(23) Byram, C.; Soma, V. R. 2,4-Dinitrotoluene Detected Using Portable Raman Spectrometer and Femtosecond Laser Fabricated Au–Ag Nanoparticles and Nanostructures. *Nano-Structures and Nano-Objects* **2017**, *12*, 121–129. https://doi.org/10.1016/j.nanoso.2017.09.019.

Chapter 3

Structural Investigations of Ultrafast Laser Ablated HfO_2 & GaAs Nanoparticles

The experimental results of the fabrication of HfO_2 and GaAs Nanoparticles is presented as two parts in this chapter. Part-A describes the effects of initial target properties, liquid medium, and laser parameters on the produced HfO_2 NPs after the ablation. In the part-B of this chapter, structural and optical properties of resulting GaAs NPs and associated compounds have been examined in detail. Effects of laser energy, liquid medium, and pulse durations on the formation of GaAs NPs and its exotic phases are presented.

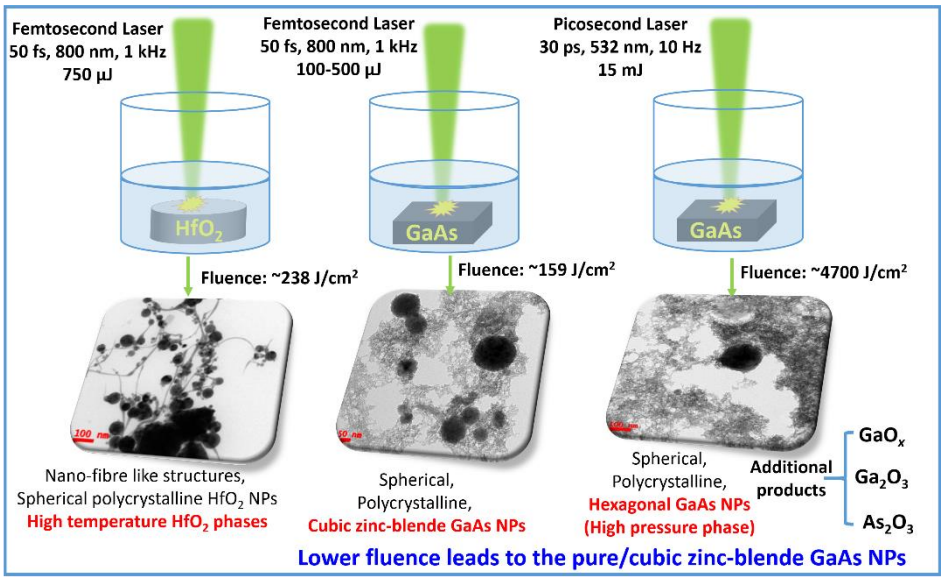

Graphical abstract

Publications from this chapter

1. A. Mangababu, Ch. Sianglam, B. Chandu, DK Avasthi, S. Venugopal Rao, M. Motapothula, and S. V. S. Nageswara Rao. Effects of Initial Grain Size and Laser Parameters on HfO_2 Nanoparticles Prepared Using Femtosecond Laser Ablation in Liquids. **Journal of Electronic Materials 50** (2021) 1742–1751. https://doi.org/10.1007/s11664-020-08610-zÓ2021.
2. A. Mangababu, G. Sarang Dev, B. Chandu, M.S.S. Bharati, S. Venugopal Rao, and S.V.S. Nageswara Rao. Structural Investigations of Picosecond Laser Ablated GaAs Nanoparticles in Different Liquids. **Nanostructures & Nano-Objects 23** (2020) 100509. https://doi.org/10.1016/j.nanoso.2020.100509.
3. A. Mangababu, G. Sarang Dev, B. Chandu, M.S.S. Bharati, P. Debashish, S. Venugopal Rao, and S.V.S. Nageswara Rao. Fabrication and Characterization of GaAs Nanoparticles Achieved using Femtosecond Laser Ablation. **Materials Today: Proceedings** (2020). https://doi.org/10.1016/j.matpr.2020.05.727.

Chapter 3 (Part-A)

Impacts of Initial Grain Size and Laser Parameters on HfO_2 Nanoparticles produced by ULAL.

By employing femtosecond (fs) laser ablation in liquids, an interesting nano-fiber structures interconnected to spherical NPs of HfO_2 have been fabricated. The purpose of this study is to determine the effects of initial grain size on the structural and optical properties of laser ablated products (i.e., NPs). The grain size may influence the laser-matter interaction thereby changing the plasma's overall density and composition. Hence, in this study, HfO_2 pellets with two distinct initial grain sizes were achieved by ball-milling process and were ablated using fs laser pulses in DW and ethanol. The NPs were discovered to be polycrystalline, while the fiber-like structures were discovered to be amorphous. In addition, the formation of high-temperature and high-pressure phases of HfO_x NPs (tetragonal /cubic HfO_x) were observed along with the formation of ambient monoclinic HfO_2. The combination of ball milling and femtosecond laser ablation appears to be the most effective technique for synthesizing smaller NPs of exotic non-equilibrium phases.

3.1.0 Introduction to HfO_2

HfO_2 is a large-bandgap (~5.7 eV) dielectric material with potential uses in high-speed and high-temperature electronics due to its high melting point (2800 °C) and high dielectric constant (~25)[1,2]. It exists in a variety of crystallographic phases, including monoclinic [room temperature (RT)-1700 °C], tetragonal (1700-2600 °C), and cubic (more than 2600 °C)[3]. These various crystallographic phases led to dielectric constants which vary from 25 to 75. The symmetric phase of HfO_2 (c- HfO_2) has the greatest dielectric value of approximately 75. It is also both thermally and chemically stable. HfO_2 has previously been implemented into IC technology as gate dielectric due to its outstanding features[4,5]. As SiO_2 technology approaches its scaling limit, scientists are looking for new high-dielectric-constant materials to address the problem[6]. HfO_2 is a popular material in metal-oxide semiconductor (MOS) capacitors, MOSFETs, transistors, and resistive random-access memory (RRAM) devices[7–9]. It is also employed in solar cell absorber coatings, energy-efficient windows, and capacitive field-effect pH-based sensors[10–12]. High-dielectric-constant materials are preferred for some of these applications, therefore within HfO_2, the high-temperature phase that has a high dielectric value

is being synthesized in various methods by diverse research groups[13,14]. It is worth noting here that stabilization of these high-temperature phases is extremely difficult unless fast quenching is conducted. One of the most difficulties is to synthesize and stabilize such high-temperature compounds at room temperature[15]. Doping zirconium into HfO_2[16], ion implantation/irradiation[17], and laser ablation in liquids (LAL) have all been utilized for this purpose[2,13,18,19]. LAL appears to be a natural choice among these because local heating and quick quenching are important aspects of the process. NPs of metal oxides, particularly HfO_2, ZrO_2, TiO_2, and ZnO, have found a wide range of uses in electronics and optoelectronics, including gas sensors, detectors, LEDs, and solar cells[20–27]. Zhang et al. [28] created HfO_2/ZnO core-shell nanowires that showed a considerable improvement in luminescence characteristics. Furthermore, HfO_2 NPs have potential for interesting medical applications such as radiotherapy, bioimplants, and biosensors[29–31]. It is critical to highlight that HfO_2 is a biocompatible substance. Jayaraman et al.[32] investigated the toxicity of various sized HfO_2 NPs in interactions with 3T3 fibroblast cell lines and discovered negligible toxicity even at higher NP concentrations. Because it has a high Z (atomic number), it absorbs radiation more efficiently than the surrounding biological medium during radiation therapy[30,32,33]. As a result, it was proposed to inject colloidal HfO_2 NPs near the target tumors prior to radiation therapy. Because these particles absorb radiation more effectively and generate heat in the surrounding medium, the dose need can be lowered. Hf-rich high-temperature phases of HfO_x, in particular, have applications as cladding materials in nuclear reactors and in other harsh environments[34]. As a result, understanding the fundamental physical, mechanical, and optical properties of HfO_2 NPs is critical for advanced electronic applications and thus forms the subject matter of this section.

3.1.1 Experimental details

In the current study, sintered HfO_2 pellets with varying initial grain sizes were manufactured with HfO_2 powder of 99.99% purity purchased commercially from M/S Quest Technology(s), Singapore. The average grain size of the pristine powder (as purchased) was estimated to be 34.9 nm. To further minimize the grain size, a ball-milling process was performed for ~24 hours. Then, these two sets of powders (pure and ball-milled) were pressed into pellets of 8 mm diameter and 6 mm thickness using a hydraulic press (at a pressure of 2.5 MPa), followed by sintering at 800 °C for 4 hours. Then, these pellets were ablated using Ti:sapphire laser (wavelength: 800 nm, repetition rate: 1 kHz, pulse duration: 50 fs, and input energy: 750 μJ)

in DW, and ethanol. In our previous investigation, the highest energy used was 500 µJ[35]. At 400 µJ, high-temperature and high-pressure phases were noticeable. As a result, a higher energy of 750 µJ was chosen in order to test the consistency of previous research and to further investigate the formation of new phases. In addition, we planned to examine the impact of initial particle size and liquid medium on the formation of nanostructures. During the ablation, these pellets were set in a liquid-filled glass beaker and on a motorized stage that can move in two horizontal directions orthogonal to the laser beam. The liquid in the container was maintained at a height of 5 mm. The scan speed of the stage was optimized to 0.1 mm/s for homogenous ablation over a 3×3 mm^2 area. For readers' convenience, the sample names and the corresponding ablation process, remarks are mentioned in table 3.1.

Table 3.1 Sample names and their descriptions

S. No.	**Sample Name**	**Pre-process before ablation**	**Ablating medium**	**Remarks**
1	Pristine powder	-	-	Not ablated (As purchased)
2	NPs_Pristine powder_DW	Pelletized	DW	NPs obtained by ablating pellet made of pristine powder
3	Ball-milled powder	Ball milled for 24 h and pelletized	-	Not ablated
4	NPs_Ball-milled powder_DW	Ball milled and pelletized	DW	NPs obtained by ablating pellet made of ball-milled powder
5	NPs_Ball-milled powder_Eth	Ball milled and pelletized	Ethanol	NPs obtained by ablating pellet made of ball-milled powder

3.1.2 Results and discussion

Understanding the structure as well as morphology of HfO_2 NPs is the primary focus of this research. As a result, we altered the grain size in HfO_2 pellets prior to ablation and the carbon content of the liquid during ablation. Morphological and structural characterizations were conducted on as-received (pristine) powder, ball-milled HfO_2 powder, and ball-milled powder-based pellets. Figure 3.1 XRD patterns confirm the existence of a monoclinic phase in all of these samples. The broadening of XRD peaks of the ball-milled powder [Fig. 3.1 (b)] and sintered pellets made from the ball-milled powder [Fig. 3.1 (c)] indicates a decrease in grain size relative to the pristine powder [Fig. 3.1 (a)]. Scherrer's equation from Ref[36] is utilized to estimate the grain sizes of the HfO_2 pellets. The average grain size of ball-milled powder is estimated to be around 10.2 nm, which is smaller than the average grain size of the pure powder

(34.9 nm). These two distinct materials were pelletized, sintered, and ablated in two distinct liquid environments, DW and ethanol, respectively.

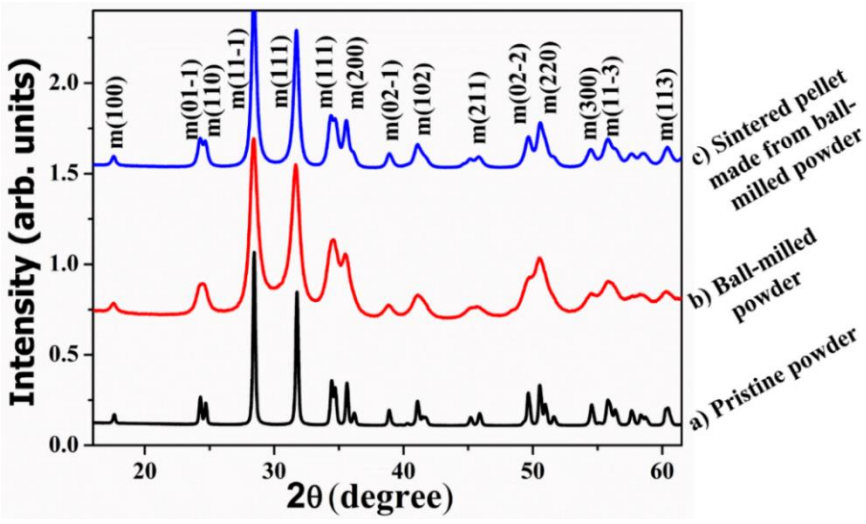

Fig. 3.1 XRD patterns of (a) pristine powder, (b) ball-milled powder, and (c) sintered pellets made from ball-milled powder.

The TEM analysis of the pristine powder and ablated NPs is depicted in Fig. 3.2, where (a-c) represent the TEM image, selected area electron diffraction (SAED) pattern, and particle size distribution, respectively of pristine powder. It has non-spherical particles with an estimated size of 105 nm and the crystal planes depicted in SAED i.e., (1 1 1), (1 1 -2), (2 2 0), and (3 0 -2) belong to the monoclinic phase of HfO_2 (ICDD: 00-034- 0104, ICDD: 98-002-7313). Upon laser ablation the formation of nanofiber-like structures that connect the spherical NPs is noticed (see the TEM images in Fig. 3.2, rows 2-4). These NPs are polycrystalline with crystalline planes (11-1), (111), (12–2), and (212) when ablated in DW; (1 1 1), (2 2 -1), and (2 1 -3) when ball milled and ablated in DW; (2 0 0), (2 2 -1) and (0 2 3) when ball milled and ablated in ethanol. The particle sizes determined to be 37 nm, 24 nm, and 27 nm for NPs ablated from pellets made of pristine powder in DW, Ball-milled powder in DW, and Ball- milled powder in Eth, respectively.

Figure 3.3 depicts the HRTEM analysis (using a software "Gatan Digital Micrograph"). Row 1, columns (a-c) show HRTEM, IFFT, and d-spacing profiles of HfO_2 pristine powder, from which a d-spacing of ~0.26 nm corresponds to (0 0 2) planes of m-HfO_2 is noticed. In a similar fashion, rows 2, 3, and 4 display HRTEM, IFFT, and d-spacing profiles for NPs obtained by ablating pellets made of pristine powder in DW, ball-milled powder in DW, and ball-milled powder in ethanol, respectively. For NPs derived from pristine powder pellets in DW, a d-spacing of ~0.28 nm is observed, which corresponds to (1 1 1) planes of m-HfO_2. Similarly, NPs from pellets made of ball-milled powder in DW have a d-spacing of ~0.37 nm, which

corresponds to (0 1 -1) planes of m-HfO_2, whereas NPs from pellets made of ball-milled powder in ethanol have a diameter of ~0.28 nm, which corresponds to (111) planes of m-HfO_2.

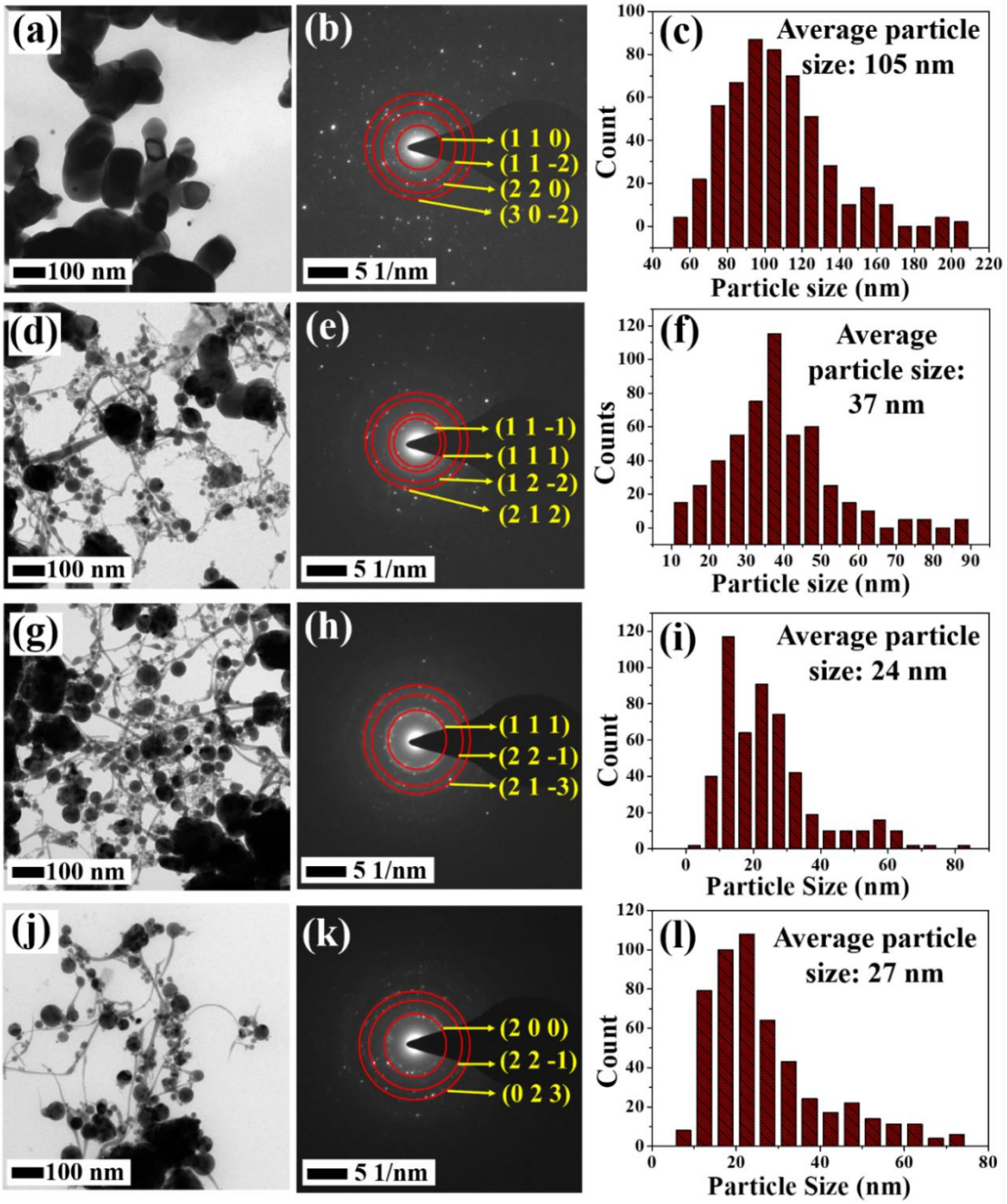

Fig. 3.2 TEM image, particle size distributions, and SAED patterns, respectively of (a-c) pristine powder, (d-f) NPs in DW obtained by ablating pellets made of pristine powder, (g-i) NPs in DW obtained by ablating pellets made of ball-milled powder, and (j-l) NPs in ethanol obtained by ablating pellets made of ball-milled powder.

Importantly, nanofiber-like structures were formed in all ablated NPs, regardless of the initial conditions of the target material. Hence, it is attributed to the inherent properties of HfO_2 (i.e., thermal or electrical conductivity). The crystallinity of these nano-fibers was investigated by conducting SAED on the fiber regions, the resulting pattern is depicted in Fig. 3.4. Although

the diffused rings suggest an amorphous nature, a faint polycrystalline phase can be observed in this pattern. At the laser fluence (750 µJ) utilized in this investigation, these fibers appeared to be transitioning from amorphous to polycrystalline phase. Importantly, these nano-fiber-like structures are not observed in the pristine powder depicted in Fig. 3.2, row 1. Formation of these nano-chains/nano-ribbons in the LAL process has also been reported in the literature, where ablation mechanisms, material properties, liquid media, target re-irradiation, etc. are hypothesized to be the causes[37–39]. Consequently, it is evident that these nanofiber-like structures were formed as a result of the ablation process, primarily due to the contrast in thermal and electrical conductivity between the solvent and the material.

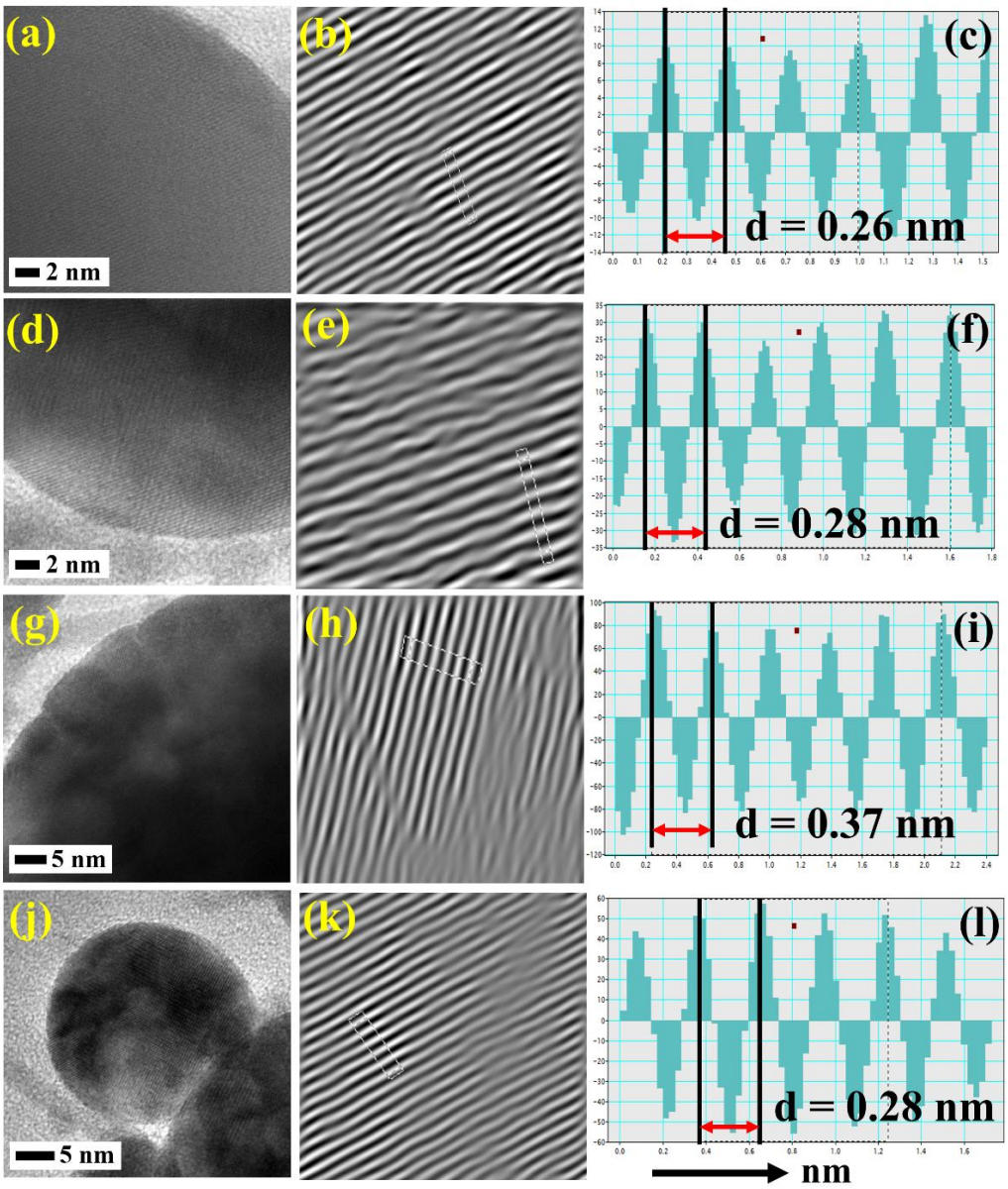

Fig. 3.3 HRTEM, inverse FFT image, and d-spacing profile of (a-c) pristine powder, (d-f) NPs in DW obtained from pellets made of pristine powder, (g-i) NPs in DW obtained from pellets made of ball-milled powder, and (j-l) NPs in ethanol obtained from pellets made of ball-milled powder.

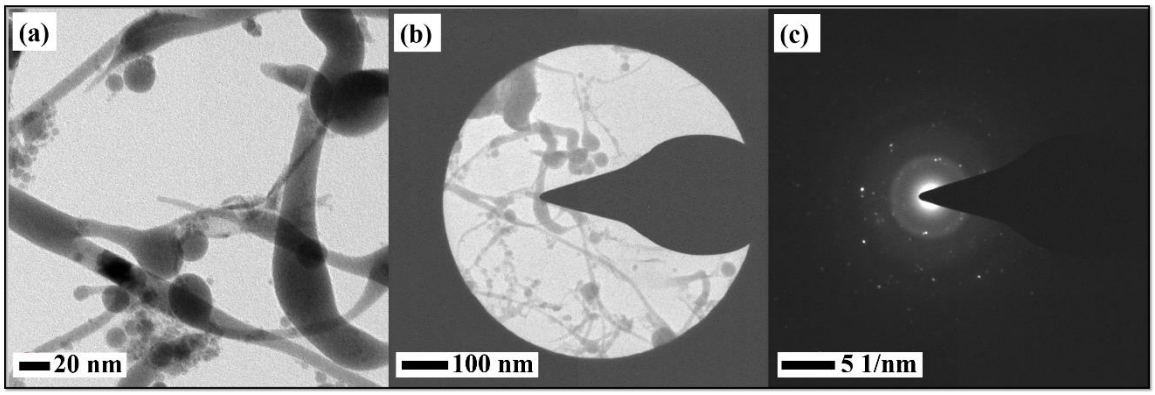

Fig. 3.4 Nano-fiber structures obtained in DW from pellets made of ball-milled powder: (a) TEM image, (b) nano-fiber location at which SAED is performed, and (c) SAED pattern of the nano-fiber.

Figure 3.5 (a-d) depicts the XRD patterns of pristine powder, NPs in DW ablated from pellets of pristine powder, NPs in DW produced from pellets of ball-milled powder, and NPs in ethanol obtained from pellets of ball-milled powder, respectively. The XRD peaks obtained at 2θ (degree) values of 17.6 (1 0 0), 24.2 (0 1 -1), 24.8 (1 1 0), 28.4 (1 1 -1), 31.8 (1 1 1), 34.5 (0 2 0), 35.6 (2 0 0), 38.9 (0 2 -1), 41.2 (1 0 2), 45.9 (2 1 1), 49.6 (0 2 -2), 50.5 (2 2 0), 54.6 (3 0 0), 55.9 (1 1 -3), and 61.8 (1 1 3) all belong to the monoclinic HfO_2. The extra two peaks at 30.5 and 33.3 represented as ''c/t'' in Fig. 3.5, are attributed to the tetragonal or cubic phase of HfO_x[2,40]. It is not possible to specify exactly the phase as the d-spacing of tetragonal and cubic phases of HfO_2 are close to each other. In XRD patterns of NPs ablated from pellets made of ball-milled powder (i.e., Fig. 3.5 (c, d)), two peaks have merged into one and appear as a broad peak. This is a result of the tension induced by ball milling followed by laser ablation. Nevertheless, it is evident that the high-temperature and high-pressure phases have formed along with the m-HfO_2 phase.

Table 3.2 displays calculated grain sizes from the XRD analysis, confirming that the pristine powder had an average grain size of ~34±9 nm. The ball-milled powder had an average grain size of ~10±2 nm, NPs made from pristine powder pellets in DW had an average grain size of ~42±5 nm, and NPs made of ball-milled pellets had sizes of ~16±3 nm and ~15±3 nm, respectively, for ablation in DW and ethanol liquids. These standard errors were computed using a formula for root mean square error for all peaks in the XRD patterns for each sample separately. The difference between XRD-calculated grain sizes and TEM-calculated particle

sizes (shown in Table 3.2) confirms the polycrystalline character of the NPs obtained. A few grains together form a particle.

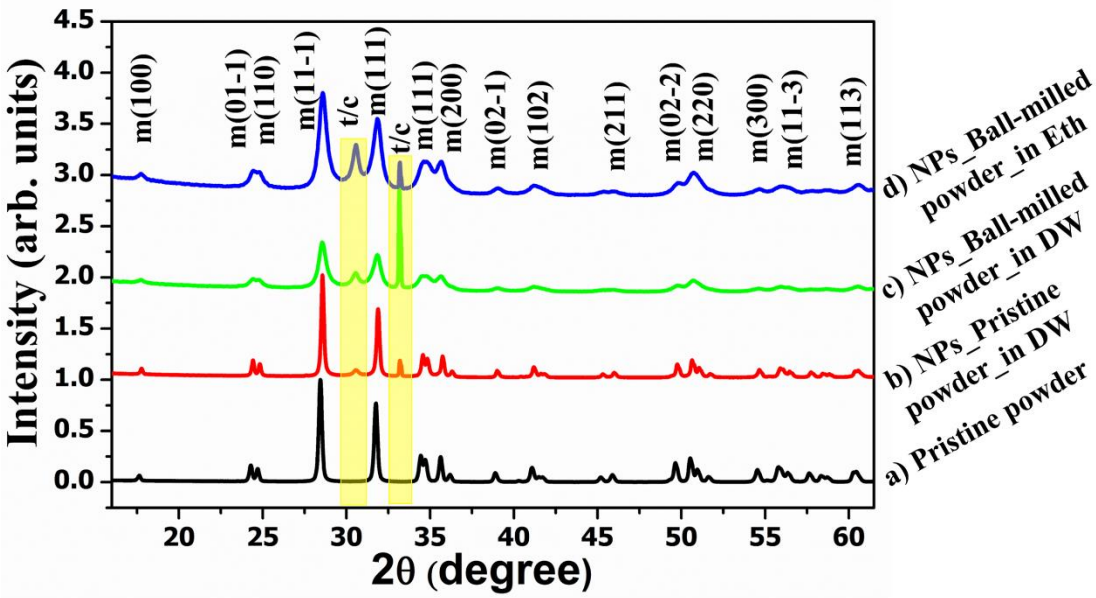

Fig. 3.5 XRD patterns of (a) pristine powder, (b) NPs in DW obtained from pellets made of pristine powder, (c) NPs in DW obtained from pellets made of ball-milled powder, and (d) NPs in ethanol obtained from pellets made of ball-milled powder.

Table 3.2 Grain size and particle size obtained from XRD and TEM analysis, respectively.

S. No.	Sample Name	Grain size from XRD (nm)	Particle size from TEM (nm)
1	Pristine powder	34 ± 9	105
2	NPs_Pristine powder_DW	42 ± 5	37
3	Ball-milled powder	10 ± 2	NA
4	NPs_Ball-milled powder_DW	16 ± 3	24
5	NPs_Ball-milled powder_Eth	15 ± 3	27

Fig. 3.6 (a-d) depicts the Raman spectra of pristine powder, NPs in DW produced from pellets made of pristine powder, NPs in DW produced from pellets made of ball-milled powder, and NPs in ethanol produced from pellets made of ball-milled powder, respectively. These spectra display Raman-active modes with wavenumbers of 111 cm^{-1}, 133 cm^{-1}, 149 cm^{-1}, 164 cm^{-1}, 240 cm^{-1}, 256 cm^{-1}, 331 cm^{-1}, 383 cm^{-1}, 397 cm^{-1}, 476 cm^{-1}, 498 cm^{-1}, 520 cm^{-1}, 551 cm^{-1}, 579 cm^{-1}, 641 cm^{-1}, and 672 cm^{-1} within the range of 100-700 cm^{-1}. Among them, the modes at 111 cm^{-1}, 133 cm^{-1}, 149 cm^{-1}, 164 cm^{-1}, 240 cm^{-1}, 256 cm^{-1}, 331 cm^{-1}, 383 cm^{-1}, 397 cm^{-1}, 498 cm^{-1}, 551 cm^{-1}, 579 cm^{-1}, 641 cm^{-1}, and 672 cm^{-1} correspond to the m-HfO_2 [41–43], whereas the peak at 520 cm^{-1} belonged to Si substrate. The extra peak identified at 476 cm^{-1} (highlighted in Fig.

3.6) is from the tetragonal phase of HfO_2[41]. According to the first-principles computations of Zhao et al.[43], there are a total of 18 ($9A_g$ +$9B_g$) Raman-active modes, 15 ($8A_u$ +$7B_u$) IR-active modes, and 3 ($2B_u$ +$1A_u$) acoustic modes for m-HfO_2, which precisely matches our results, in which we have observed 14 modes between 100-700 cm^{-1} (see Fig. 3.6). The extra peak observed at 476 cm^{-1} (represented as the high-temperature mode in Fig. 3.6 and Table 3.3) does not belong to the m-HfO_2. This peak corresponds to the high-temperature phase of HfO_2 (i.e., t-HfO_2), as reported by Zhou et al.,[41] who simulated the spectra of various HfO_2 polymorphs. In addition, XRD results (Fig. 3.5) and Raman studies (Fig. 3.6) corroborate the co-existence of m-HfO_2 and high-temperature tetragonal/cubic HfO_2 in ablated NPs.

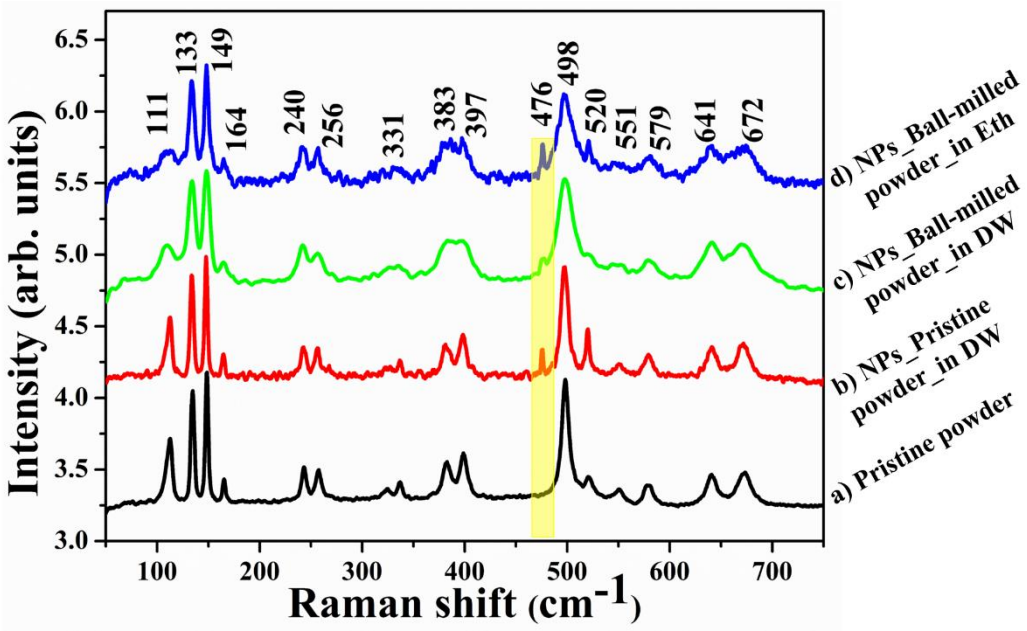

Fig. 3.6 Raman spectra of (a) pristine powder, (b) NPs in DW obtained from pellets made of pristine powder, (c) NPs in DW obtained from pellets made of ball-milled powder, and (d) NPs in ethanol obtained from pellets made of ball-milled powder.

The findings were consistent with the predictions made in the earlier study[35], in which HfO_2 NPs were created by laser ablation under nearly identical conditions, with the pellets sintered at 500 °C. The observed increase in particle size from 13.5 nm to 18.8 nm with an increase in pulse energy from 200 µJ to 500 µJ is attributed to probable inter-diffusion and NP agglomeration at higher energy. In the present investigation, NPs produced at further higher energy (750 µJ) have a larger particle size (~37 nm) than those produced at a lower energy (500 µJ). Higher energy is required to produce nonequilibrium (high-temperature/high-pressure) phases, but the particle size increases at such high energies not only because of the change in phase but also because of the inter-diffusion and agglomeration of NPs. Therefore, an effort has been made to begin with the finer particles produced by other methods such as

ball milling. The ball-milled NPs (~10 nm in grain size) were subjected to high-energy laser ablation to create smaller particles with nonequilibrium phases (~16 nm in DW and ~15 nm in ethanol). Due to laser ablation, the actual grain size of the ball-milled particles increased from 10 nm to 16 nm, which is consistent with the predicted agglomeration of NPs at higher energies. In this investigation, agglomeration is not unique to water, but is also observed in ethanol. Ball milling alone may generate smaller particles, yet nonequilibrium phases cannot be produced with this technique. High-energy ablation using lasers can produce nonequilibrium phases, but the process is limited by agglomeration. This study therefore proposes that a combination of ball milling and laser ablation can be used to produce smaller NPs in nonequilibrium phases. The formation of nanofibers extending from spherical NPs or interconnecting adjacent NPs is another significant finding. The increase in nanofiber density with increasing pulse energy is also supported by this study. Earlier, potential mechanisms for the construction of these nanofibers were discussed[37,38], but the actual mechanisms are still up for debate. These fibers appeared to be in the process of transforming from an amorphous to crystalline state. Electronic devices may get benefits from the formation of heterostructures with "amorphous HfO_x fiber/m-HfO_2" and "amorphous HfO_x fiber/nonequilibrium HfO_x" interfaces. In the future, these structures will be isolated and exotic phases will be stabilized.

Table 3.3 Raman modes of HfO_2 NPs obtained in the current work and in the literature.

Raman modes of monoclinic HfO_2 (Units: cm^{-1})				
S. No.	**Current work**	**From Ref.** [41,42]	**From Ref.** [43]	**Modes**
1	111	111	114	A_g
2	133	133	135	A_g
3	149	149	149	A_g
4	164	164	165	B_g
5	240	240	243	B_g
6	256	256	258	A_g
7	331	330	326	B_g
8	383	383	383	A_g
9	397	396	399	B_g
10	476	----	-----	High temperature (t-HfO_2)
11	498	499	498	A_g
12	520	----	---	Si substrate
13	551	547	553	B_g
14	579	580	579	A_g
15	641	642	641	B_g
16	672	671	672	A_g

3.1.3 Summary of HfO_2 laser ablation

In this investigation, fs laser pulses were used to ablate HfO_2 pellets with varying grain sizes produced by ball milling. The created NPs had a spherical shape connected to nanofiber-like structures. These nanofiber-like structures were observed in all samples, regardless of the initial conditions of the HfO_2 target material as well as liquid medium used. Further, the spherical particles have polycrystalline nature and the fiber-like structures are amorphous (poor crystallinity) in nature. The initial grain size of the target material influenced the grain size of the NPs formed after ablation, smaller the initial size the smaller are the NPs post ablation. XRD and Raman measurements revealed that the tetragonal/cubic HfO_2 phase coexists with the m-HfO_2 phase at ambient temperature. This study demonstrates conclusively that a combination of ball milling and laser ablation techniques can be used to produce smaller NPs in non-equilibrium phases. Sensing and photo detection applications are possible for the nanofiber network-like structures.

Chapter 3 (Part-B)

Structural investigations of laser ablated GaAs colloidal nanoparticles

In-depth research on the ultrafast laser ablation of gallium arsenide in various liquids, and at various laser parameters is presented in this section. Owing to the inherent characteristics of laser ablation, which involve fast heating and quenching, exotic phases of GaAs were developed. A detailed study was conducted to understand the creation of GaAs NPs and associated compounds. A mesh like background material formed along with spherical GaAs NPs was clearly analyzed and presented in this work. When the GaAs target was ablated at higher fluence, exotic high temperature/high pressure stable phases like hexagonal GaAs and other compounds like As_2O_3 and Ga_2O_3 were created. In contrast, when GaAs was ablated at lower fluences, stable cubic (zinc blende) GaAs NPs were created. Accordingly, this study develops a method for selectively producing pure cubic-GaAs particles or high-temperature / high-pressure hexagonal particles, depending on the need.

3.2.0 Introduction

Gallium arsenide is a compound semiconductor with wide and direct bandgap of ~1.42 eV at 300 K[44]. It has a cubic zinc blende crystal structure at ambient conditions, and at high pressures/temperatures it exists in hexagonal structure[45]. Because of its high electron mobility, GaAs is employed for high frequency and high temperature applications in the defense and aerospace industries to manufacture sensors, radars, and secure communications[46–48]. It has applications in the domains of infrared light emitting diodes, laser diodes, integrated circuits, and solar cells, etc.[49–51]. The bulk substrates and thin films of GaAs were well explored in the past few decades[52]. However, researchers have recently begun employing other forms of GaAs, such as NPs and NSs, in a variety of applications[53]. The characteristics of GaAs NPs and NSs differ significantly from those of bulk or thin film GaAs due to possible quantum confinement effects[54,55]. For particles smaller than 19 nm (Bohr exciton radius of GaAs)[56], this quantum confinement occurs. GaAs nanoparticles have several uses, including infrared light-emitting diodes, cost-effective radiation sources , and detectors[53,57]. Moreover, GaAs NPs/nanowires (NWs) have lately been utilized in applications including terahertz optoelectronics[58], nonlinear

optical research[59], solar cells, etc.[60]. Semiconducting Quantum dots (Particularly of CdSe, ZnS, and GaP) utilized in bio imaging, live cell labelling, etc., due to strong fluorescence, size/composition tunability, and photo stability[61,62]. Concerning GaAs NPs produced by laser ablation technique, it is still difficult to achieve high-quality particles devoid of oxidation and aggregation. Thus, direct applications of GaAs nanoparticles in the fields of biomedicine and bio sensing are yet to be achieved.

Even though the precise interaction processes that occur during the ablation of GaAs have not yet been explained, the impacts of laser parameters on GaAs have been examined in a few papers. The primary laser parameters are pulse duration ($\boldsymbol{\tau}$), wavelength ($\boldsymbol{\lambda}$), energy (**E**), and liquid media in which ablation is accomplished[63–66]. The cavitation bubble explosion time, as well as the physical and chemical characteristics of the ablated nanoparticles, are largely dependent on the length of the laser pulse[67–69]. De Bonis et al.[67] described the effects of pulse duration on the stoichiometry of GaAs nanoparticles. In nanosecond pulse ablation, Ga-rich spherical nanoparticles (Ga:As ratio of 1.4) were detected, whereas stoichiometric GaAs nanoparticles were observed during femtosecond pulse ablation. Borowiec et al.[70] examined the influence of single-shot laser energy on the morphology of the GaAs substrate and observed the creation of pit-like features on the surface upon ablation. In addition, they have discovered that the width and depth of the trenches increased as the energy is increased. Ganeev et al.[59,71] described the influence of liquid media on the nonlinear optical characteristics of GaAs and detected two-photon absorption, but they did not report any morphological or phase changes. Salminen et al.[56] have described the influence of liquid media on the stability of produced GaAs nanoparticles, finding that the NPs in ethanol are reddish-brown in color and have a long life (of about six months). Within 24 hours, NPs in water formed clusters and settled to the bottom. At lower ammonium sulphide concentrations, NPs in water plus ammonium sulphide solution were stable but at higher concentrations, stability decreased. However, there is no definite conclusion on the influence of the above-mentioned parameters/liquid media on the shape and phases of the generated GaAs nanoparticles based on the studies published so far. Table 3.4 summarizes the laser settings utilized by different authors and the results achieved. Even though there are a few reports in this area, the other possible phases that can be created during the high-power laser ablation of GaAs and the conditions that cause these other phases have yet to be identified. Due to liquid media effect, strong local heating, and extreme pressure created during laser ablation of GaAs, it is anticipated that a few compounds such as Ga_2O_3 or As_2O_3 etc. develop together with GaAs, which have not yet been described in the scientific

literature. In this study, we have investigated the effects of ultrafast laser ablation in various liquid media on the GaAs ablation products. In-depth investigation of the morphology and unique structural phases of ablated colloidal solutions are presented.

Table 3.4 Literature survey of laser ablated GaAs NPs

Substrate	Liquid media	Laser parameters	Results and remarks	Reference
GaAs	Water, Ethanol, Ethylene glycol,	Nd:YAG, 532 nm, 9 ns, 10 Hz, 30 mJ.	Non-linear optical properties studied. There was no discussion on the stoichiometry of NPs.	R. A. Ganeev et al.[72,71]
GaAs	Acetone	Nd:YAG 532 nm, 7 ns, 10 Hz, 30 mJ.	Non-stoichiometric, Ga–rich (13 nm).	A. De Bonis et al.[67]
GaAs	Acetone	Nd:glass 527 nm, 250 fs, 10 Hz, 3 mJ.	Stoichiometric (9 nm).	A. De Bonis et al.[67]
GaAs	De-ionized water	Fiber laser 1060 nm, 20 ps, 1 MHz, 1.6 µJ	GaAs nanocrystals & amorphous material are formed. There was no description of the amorphous material.	T. Salminen et al.[56]

3.2.1 Experimental details

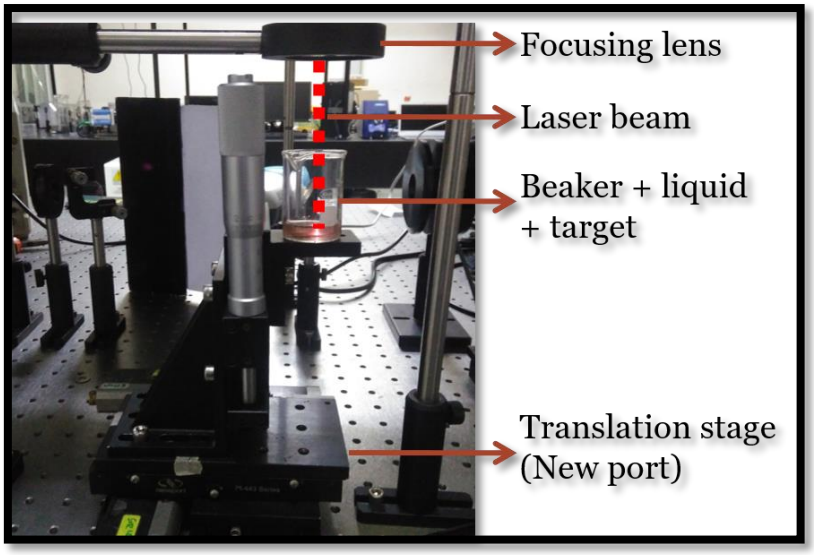

Fig. 3.7 Image of laser ablation set up taken during the experiment.

From a semi-insulating GaAs wafer with an orientation of <100>, 1 cm × 1 cm samples were cut. Afterwards, these samples were cleaned utilizing conventional method. After immersing the cleaned GaAs substrate in DW containing glass beaker, laser ablation was performed using a femtosecond amplifier (50 fs, 1 kHz, 800 nm) with different input pulse energies (100 µJ, 200 µJ, and 500 µJ). A 5 mm height was maintained between the liquid level (DW) in the beaker and the surface of the GaAs substrate. The experiment was conducted for ~40 minutes. After the ablation, NPs were collected in sealed 5 ml glass vials. The liquid NPs were

characterized using various spectroscopic and microscopic techniques. The Fig. 3.7 displays image of the experimental set up used.

3.2.2 Effects of Laser Energy on GaAs NPs produced by fs LAL

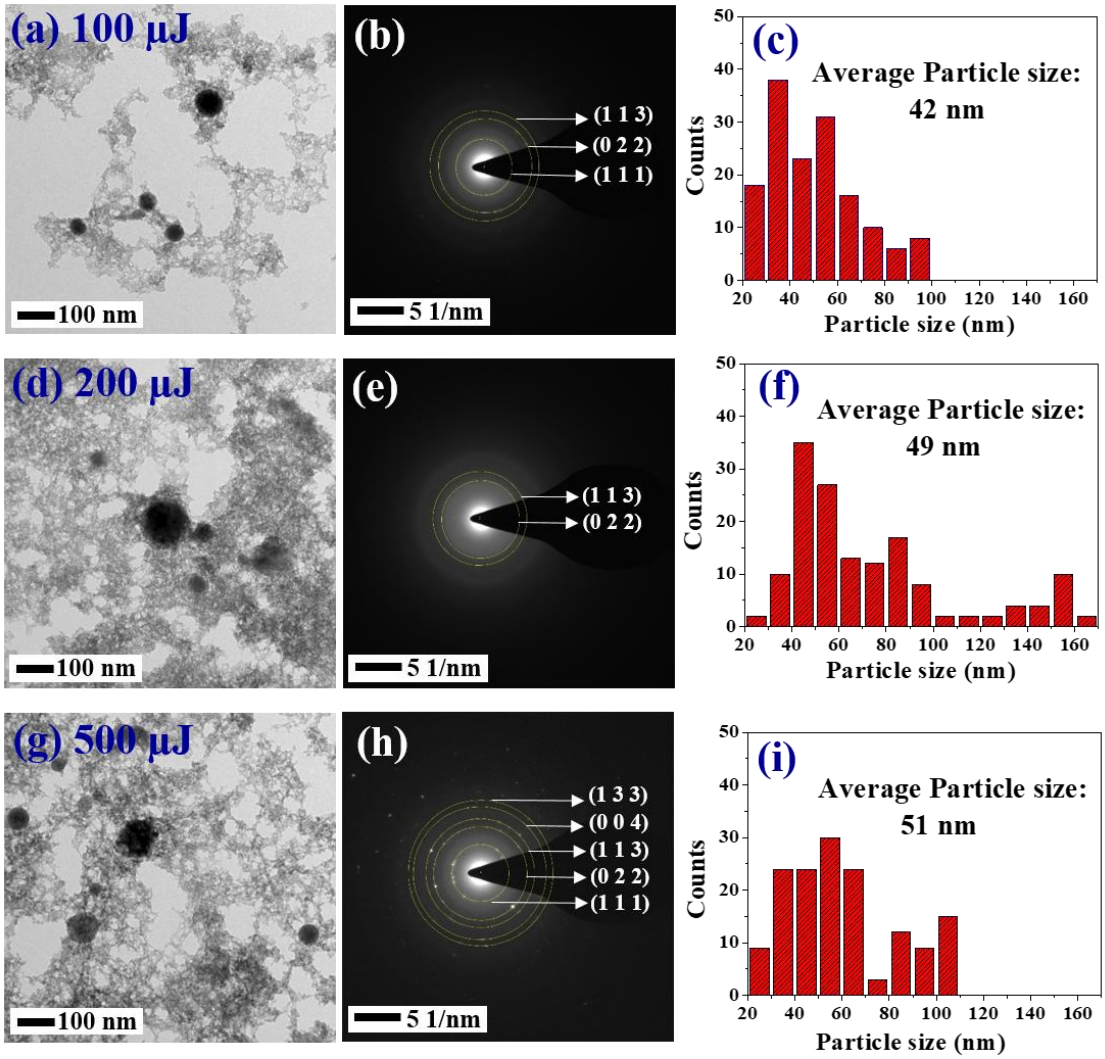

Fig. 3.8 TEM image, SAED pattern, and corresponding particle size distribution of GaAs NPs ablated in DW at laser energies of (a-c) 100 µJ, (d-f) 200 µJ, and (g-i) 500 µJ, respectively.

GaAs nanoparticles were effectively produced by femtosecond laser ablation of a GaAs single crystal wafer in DW at energies ranging from 100 µJ to 500 µJ. Figure 3.8 depicts TEM images showing the generation of GaAs NPs in DW at different energies and their associated SAED patterns, and size distributions (a-c) at 100 µJ, (d-f) at 200 µJ, and (g-i) at 500 µJ. Along with the spherical NPs, there is a formation of amorphous background material in all these samples. The spherical GaAs particles with an average size of ~33 nm were found when ablated at 100 µJ, whereas ~51 nm at 200 µJ, and ~58 nm at 500 µJ. The GaAs NPs created at 200 µJ exhibited a wide range of particle size distribution. The SAED patterns [in Fig. 3.8 (b, e, h)] show the existence of polycrystalline GaAs NPs, and the planes (1 1 1), (2 0 0), (2 2 0), and (3 1 1) are

consistent with cubic zinc blende GaAs. Due to quantum confinement effects and the high surface-to-volume ratio of NPs, it is well known that when a material is changed from bulk to nano size, there will be various changes in its optical and structural characteristics. UV-Vis-NIR spectroscopy was used to examine the optical characteristics of laser-ablated GaAs samples. GaAs nanoparticles have an absorption peak between 264 and 274 nm, as seen in Fig. 3.9 (a). Figure 3.9 (b) depicts the PL emission spectra with peaks at 411 nm and 439 nm when excited with a 355 nm wavelength.

Figure 3.10 depicts the XRD patterns for the GaAs peaks at 2θ values of 28.06 (1 1 1), 46.51 (0 2 2), 55.13 (1 1 3), 56.35 (1 1 4), and 57.70 (2 2 2) for the samples ablated at 500 µJ, a few peaks are observed in the samples ablated at 200 µJ, and no peaks are observed in the samples ablated at 100 µJ. These peaks are in good accord with the cubic zinc blende structure of GaAs and the results of selective area electron diffraction [SAED data shown in Fig. 3.8] analysis. The reason for the rise in the number of peaks in XRD spectra when the laser energy is increased may be related to the generation of greater yield/efficiency, which indirectly results in a higher concentration of NPs on the drop casted Si for XRD measurements. Figure 3.11 demonstrates the Raman spectrum of GaAs NPs generated in DW and drop-casted onto a Si substrate. The peaks detected at 266 cm^{-1} and 288 cm^{-1} correspond to the TO and LO modes of GaAs, which exhibit a little shift from the bulk GaAs [267 cm^{-1} and 292 cm^{-1}]. This minor shift may be caused by stress created during the ablation process. Particularly, the prominence of TO mode indicates, as expected, the loss of symmetry in nanoparticles as compared to that of the bulk GaAs. The Si substrate has a peak at 518 cm^{-1}.

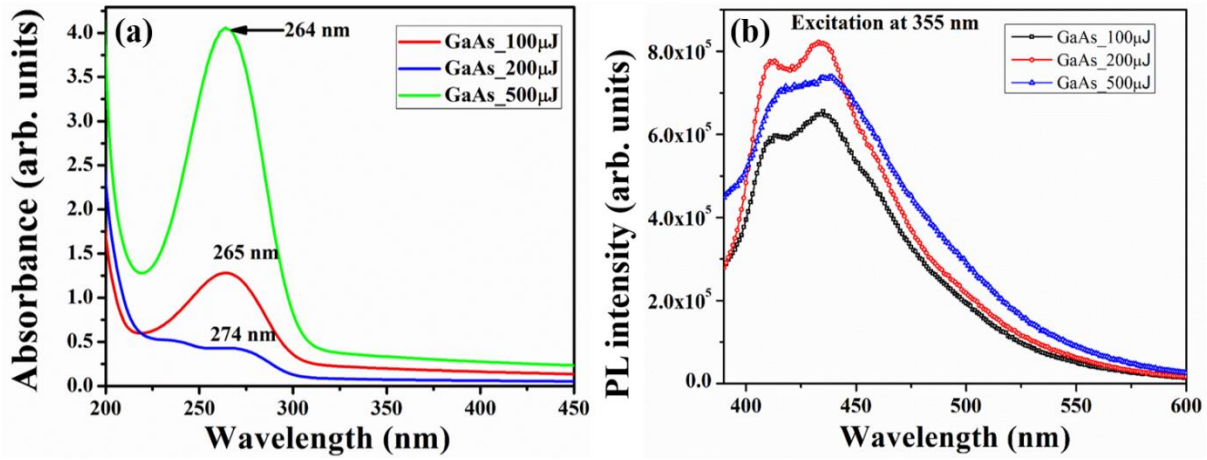

Fig. 3.9 (a) UV-Visible-NIR spectra and (b) Photoluminescence emission spectra of GaAs NPs Produced at different laser energies as depicted in the legends.

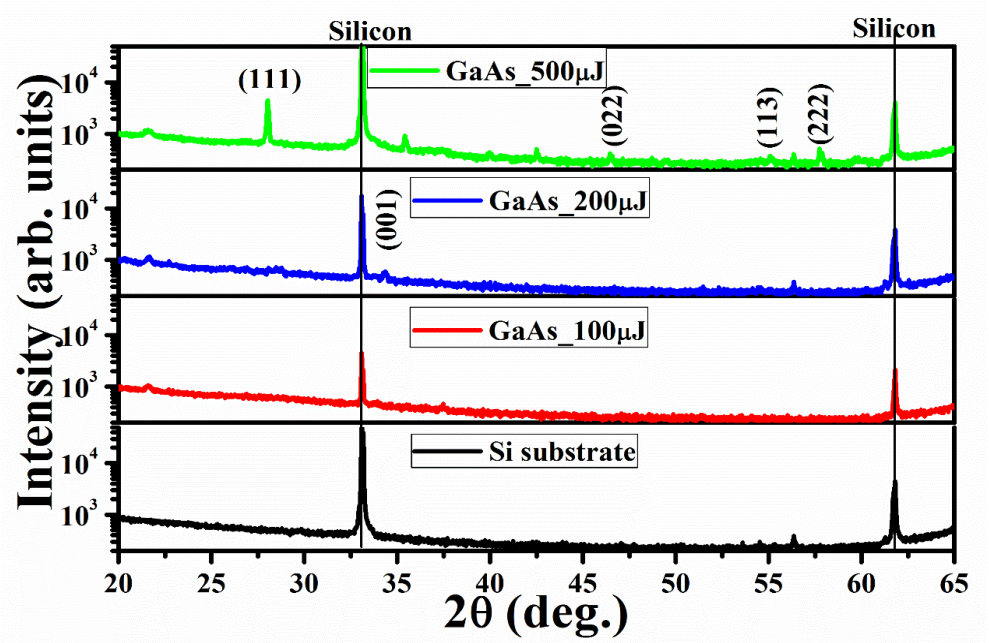

Fig. 3.10 XRD patterns of a Si substrate (black line) and GaAs NPs (Red, blue, and green lines) drop casted on Si substrate.

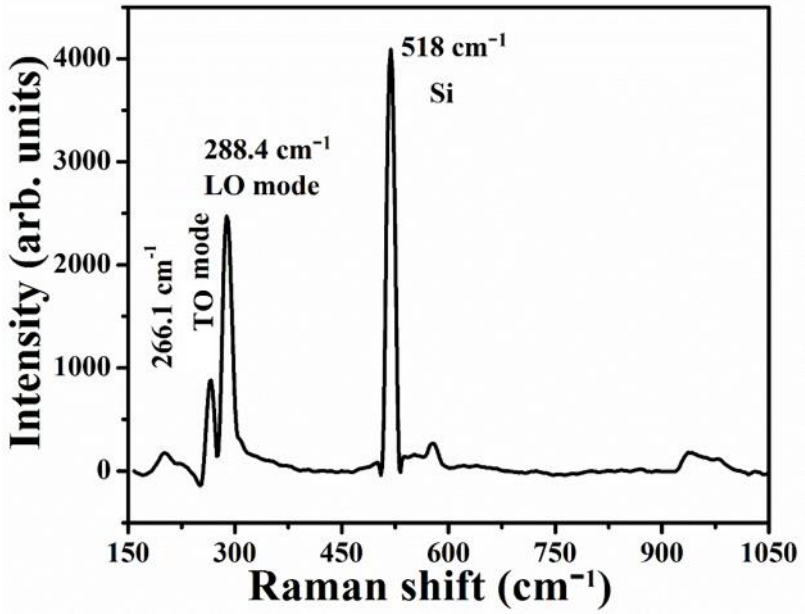

Fig 3.11 Raman spectra of GaAs nanoparticles (ablated at 500 μJ) that were drop-cast on a Si substrate.

Overall, in this energy dependent fs LAL, it is evident that spherical NPs with a size distribution of around 10-200 nm are produced. The average particle size is found to rise as the laser energy is increased. SAED patterns demonstrated that the planes (1 1 1), (2 0 0), (2 2 0), and (3 1 1) correspond to cubic GaAs. The presence of LO and TO modes in GaAs is observed in Raman spectra. Compared to its usual bulk substrate, GaAs is discovered to have a small shift in its Raman modes. This change might be attributable to the stress caused by the laser ablation procedure. XRD spectra confirmed this information further. Excited by a source emitting 355

nm, it is also shown that these NPs exhibit absorption and emission in the ranges of 264-274 nm and 411-439 nm, respectively.

3.2.3 Effects of liquid medium on GaAs NPs by fs LAL

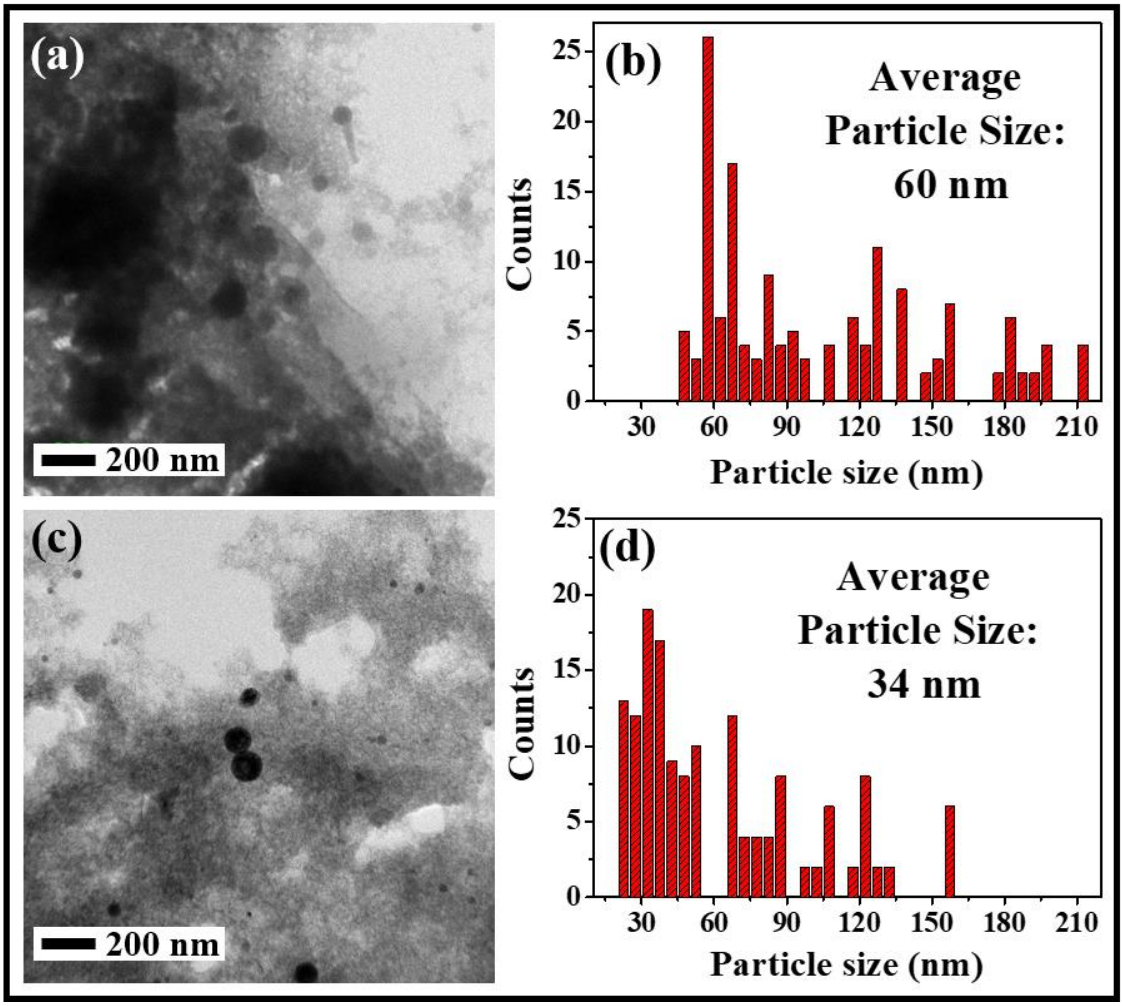

Fig. 3.12 TEM image and its corresponding particle size distribution of GaAs NPs ablated (a,b) in DW and (c,d) in ethanol.

There is a formation of background mesh like structure along with the ablated spherical GaAs NPs in the previous study performed at different laser energies (section 3.2.2). Hence, in this section, the effects of liquid medium is investigated by ablating the GaAs in both DW and ethanol. All other laser parameters were maintained same as the previous study (50 fs, 1 kHz, 800 nm, and an optimized laser energy of 500 µJ). It is noticed that irrespective of the difference in liquids, the mesh like background and spherical NPs of GaAs are formed as shown in the Fig. 3.12 (a, c). However, the particle size is smaller for the NPs ablated in ethanol (34 nm) compared to that of the DW ablation (60 nm) [see Fig. 3.12 (b, d)]. Further to understand the composition of this background material, elemental composition mapping was performed by

using EDAX attached to the TEM instrument. As shown in the Fig. 3.13, the spherical particles are having a composition of Ga and As, whereas the background material contains uniformly distributed Ga, As, and O. Fig. 3.13 (a) displays TEM image overlaid with the EDAX mapping, (b-d) the individual elemental maps of Ga, As, and O, respectively. The presence of oxygen appears to be high in the background material. This study clearly revealed that the spherical NPs are of GaAs and the background material is enriched with oxygen corresponding to the formation of either the oxidized Ga or As or $GaAsO_x$.

In the following part, ablation is carried out with a picosecond laser in order to explore GaAs laser ablation in the picosecond regime.

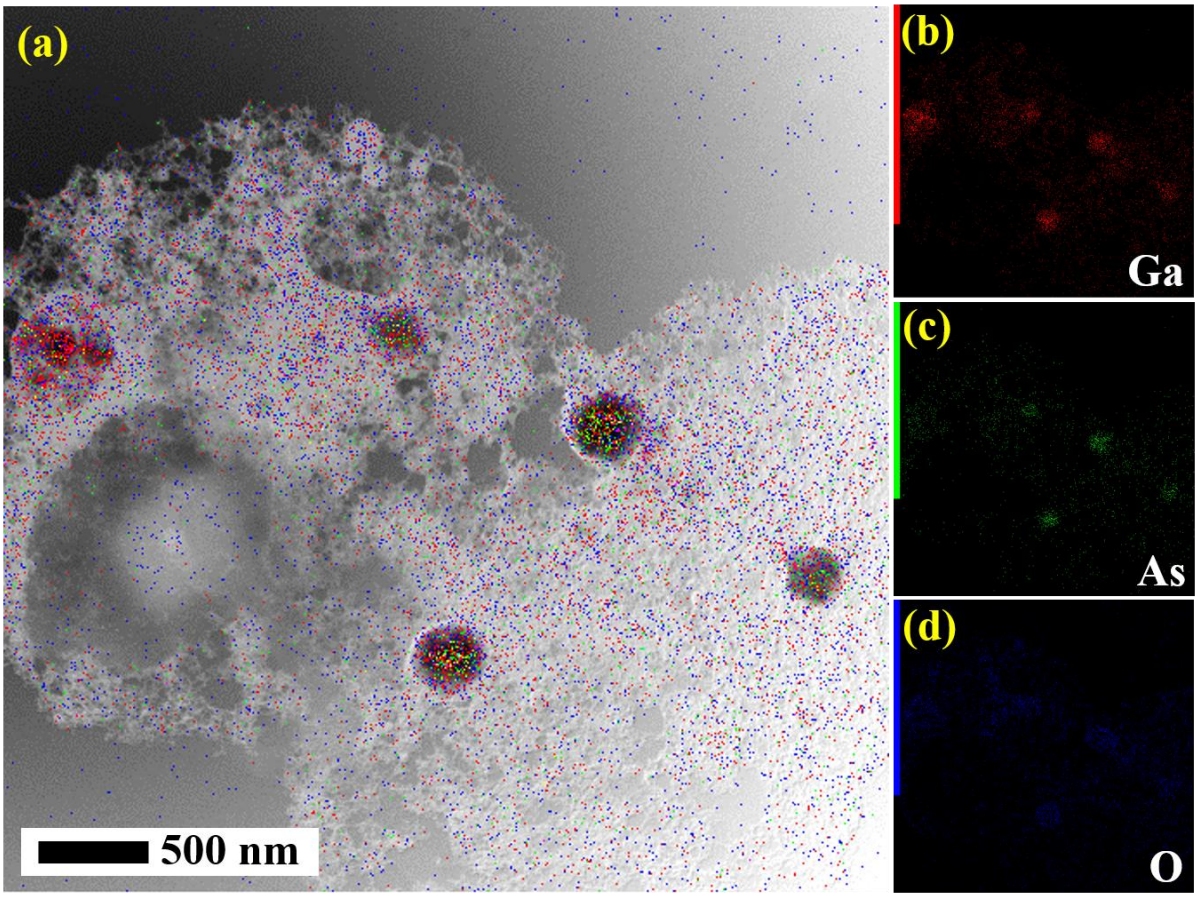

Fig. 3.13 (a) Composition mapping overlaid on TEM image, (b)-(d) individual elemental maps of Ga As and O, respectively.

3.2.4 Structural Studies of Picosecond Laser Ablated GaAs Nanoparticles in Various liquids

Further to understand the role of pulse duration as well as liquid medium on the GaAs laser ablated products, in this section GaAs was ablated with a picosecond laser in various liquid media such as deionized water (DW), ethanol, toluene, and chloroform. The produced colloidal

solutions had similar morphology with both particle-like and mesh-like features, and the particle-like structures were abundant in Ga and As, whereas mesh-like structures were abundant in Ga and O. Interestingly, a few micron-sized hexagonal, pentagonal, and cuboid crystals composed of As and O were also seen to have formed. The Raman spectra confirmed that β-Ga_2O_3 is the predominant phase in the colloidal solution generated in DW, GaAs and As_2O_3 as significant phases in ethanol and chloroform. However, in the case of toluene the presence of GaAs and GaO are noticed. All the non-equilibrium, exotic, and high-pressure phases of technologically significant NPs produced by ps laser ablation of GaAs were presented in this section.

3.2.4 (a) Experimental Details

In this study, a single spot ablation on the GaAs sample is conducted using an Nd:YAG, laser with 30 ps pulse duration, 532 nm wavelength, and 10 Hz repetition rate. Four different liquids such as DW, ethanol, toluene, and chloroform were used as surrounding ablation medium. The notations/names GAPS D15, GAPS E15, GAPS T15, and GAPS C15 denote GaAs ablated in DW, ethanol, toluene, and chloroform, respectively, at an input energy of 15 mJ. The Fig. 3.14 below is the image taken during the laser ablation process.

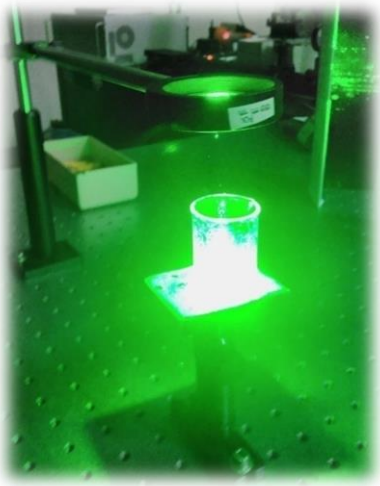

Fig. 3.14 Experimental setup for GaAs ablation using a picosecond laser (Wavelength: 532 nm).

3.2.4 (b) Results

Figure 3.15 (a) depicts the particle-like and mesh-like structures for GaAs ablated in DW (GAPS D15). Figure 3.15 (b) depicts the SAED pattern of the particle seen in Figure 3.15 (a). In addition, the crystal planes derived from SAED analysis, (0 0 2) and (1 1 0), are in good agreement with the polycrystalline hexagonal phase of GaAs. The SAED pattern recorded at the mesh-like structures had amorphous characteristics, which may include gallium oxide

(JCPDS No: GaAs-01-080-0003 and $GaAsO_4$-00-061-0383). Figure 3.15 (c) depicts the HRTEM image of the particle seen in Fig. 3.15 (a), whereas Fig. 3.15 (d) the inverse FFT of

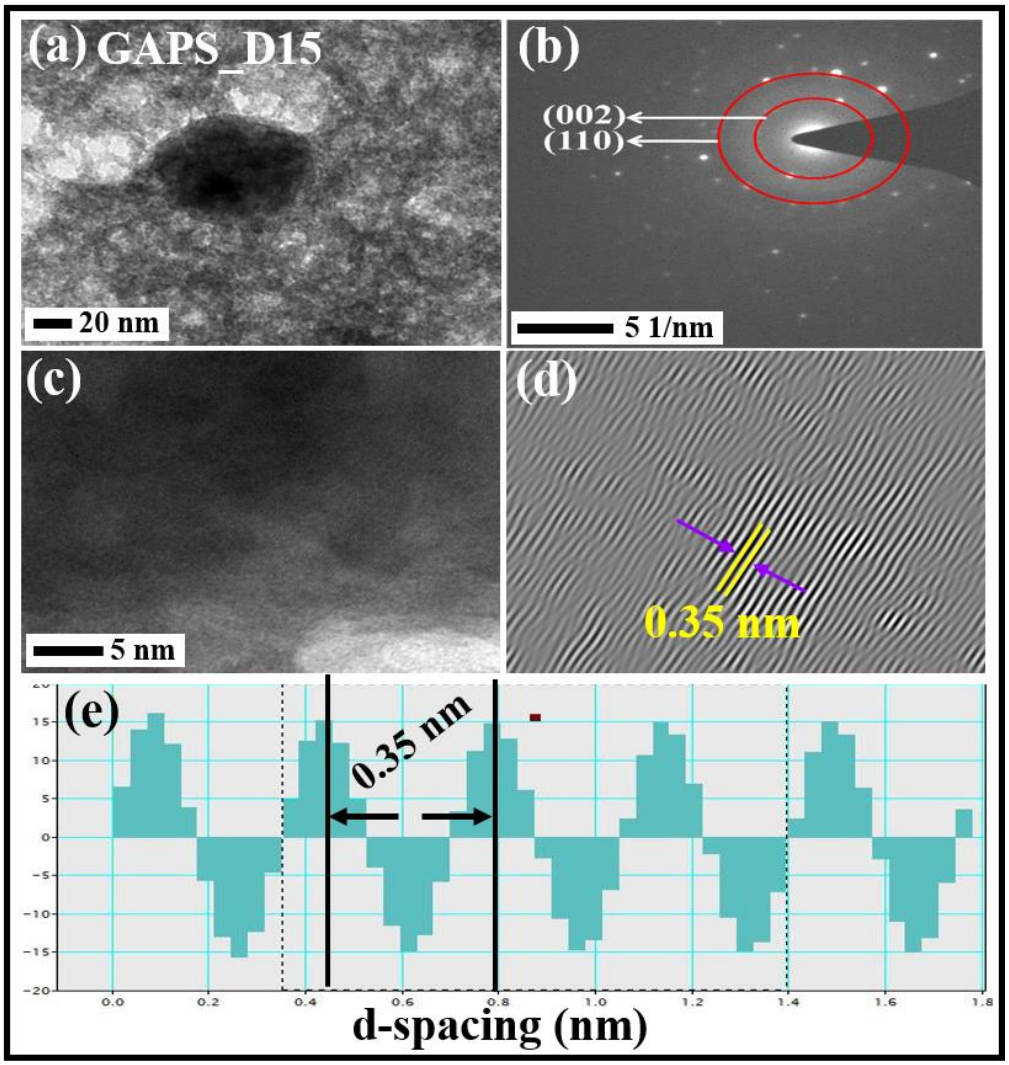

Fig. 3.15 (a) TEM image of GaAs substrate ablated in DW with 15 mJ energy, (b) SAED pattern of particle shown in (a), (c) HRTEM image for the same particle shown, (d) inverse FFT obtained from Gatan software, and (e) profile of lattice spacing obtained from (d).

HRTEM data and Fig. 3.15 (e) depicts the inverse FFT profile to compute the d-spacing. The inverse FFT profile calculated the d-spacing to be 0.35 nm, which is consistent with the (1 0 0) plane of hexagonal GaAs. Figure 3.16 depicts a similar study (as described above) for the ethanol-ablated GAPS E15 sample. Figure 3.16 (a) depicts spherical particles present in the mesh-like background, whereas Fig. 3.16 (b) illustrates the equivalent SAED pattern. Figures 3.16 (c, d) exhibit, respectively, the HRTEM picture and the inverse FFT. Figure 3.16 (e) depicts the d-spacing profile with a 0.37 nm spacing, which is consistent with the (011) plane of hexagonal $GaAsO_4$. Figure 3.17 (a) depicts TEM images of the toluene-ablated GAPS T15

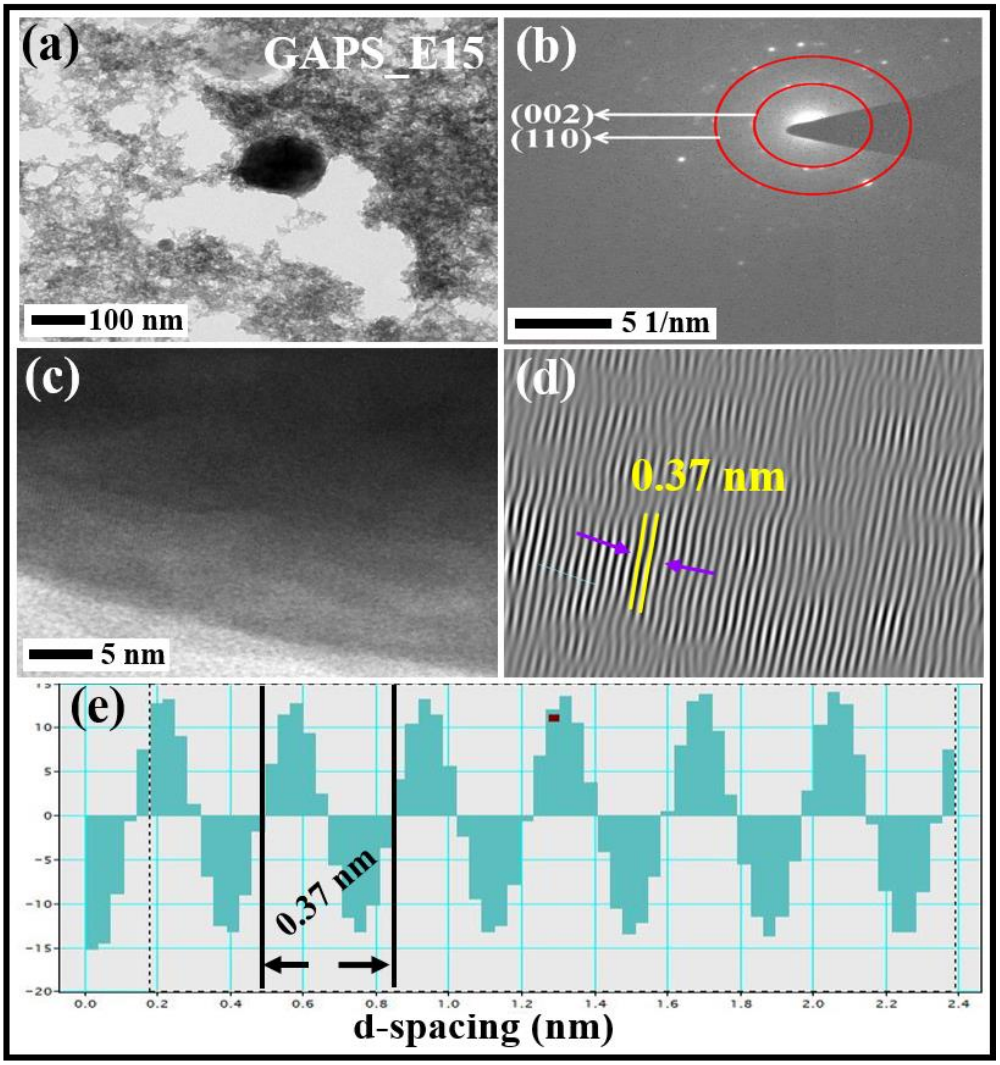

Fig. 3.16 (a) shows TEM image of GaAs substrate ablated in ethanol with 15 mJ energy, (b) SAED pattern of particles shown in (a). (c) HRTEM image for the same particle, (d) inverse FFT obtained from Gatan software for (c), and (e) is the profile of lattice spacing obtained from (d).

sample, whereas Fig. 3.17 (b) depicts the equivalent SAED pattern. Figure 3.17 (c) depicts the TEM image of GAPS C15 (ablated in chloroform), whereas Fig. 3.17 (d) illustrates its SAED pattern. It was noticed that the particle-like structures present in toluene [Fig. 3.17 (a)] were polycrystalline in nature, but the crystallinity was low and, as a result, HRTEM could not be achieved, whereas in the chloroform [Fig. 3.17 (c)], extremely fine particles that were amorphous in nature are noticed. De Bonis et al.[67] have previously documented the creation of particle-like GaAs structures together with the presence of amorphous domains, which is in excellent accord with the results of the current investigation. In contrast, for particle-like structures, the lattice planes obtained from SAED are (0 0 2), (1 1 0) and (0 0 4), and the d-spacing calculated from HRTEM data are 0.35 nm and 0.37 nm for different samples, which

are in good agreement with the hexagonal phase of GaAs, as confirmed by the JCPDS files [GaAs-01-080-0003 and $GaAsO_4$-00-061-0383]. The production of hexagonal phase GaAs may be due to the high temperatures and pressures generated by the picosecond laser during ablation.

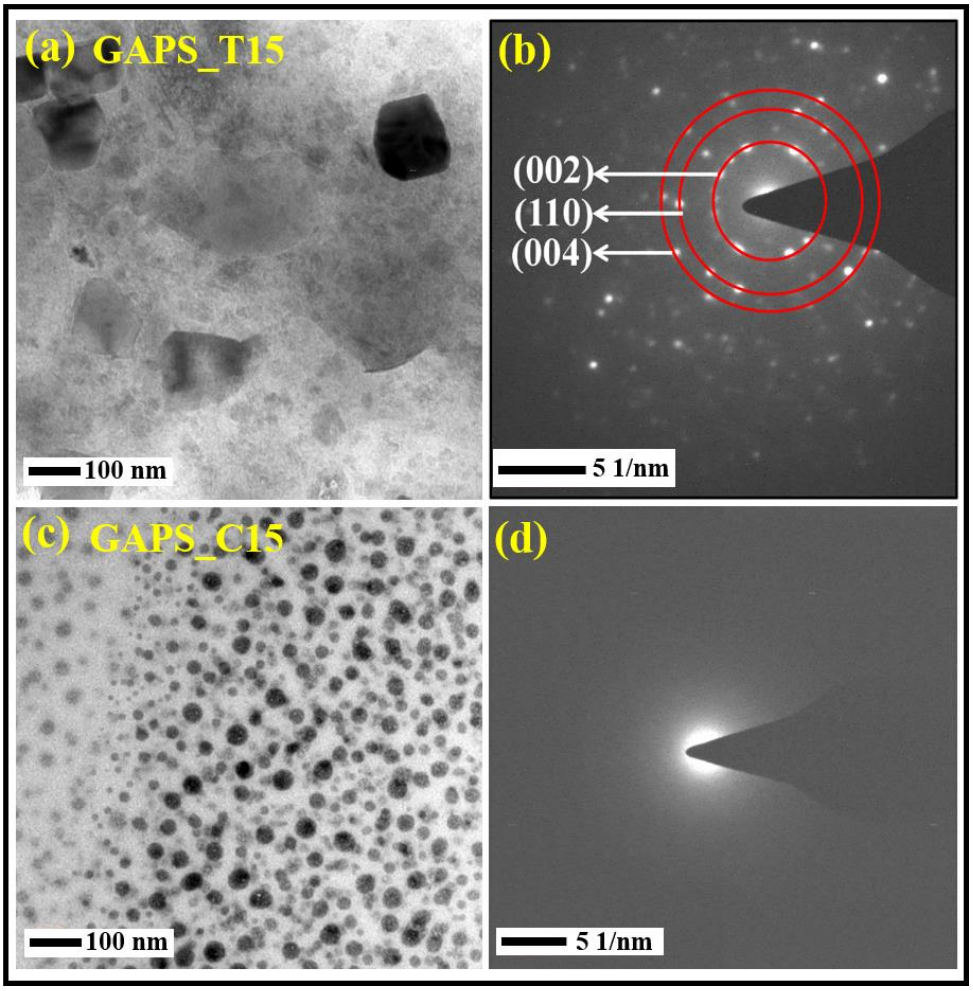

Fig. 3.17 (a) shows TEM image of GaAs substrate ablated in Toluene with 15 mJ energy (b) shows SAED pattern of particle shown in (a), (c) shows TEM image for the GaAs ablated in chloroform, and (d) shows SAED pattern on one of the particles shown in (c).

Figures 3.18 (a-d) illustrate the SEM images of ablated GaAs NPs in various liquids, including DW, ethanol, toluene, and chloroform, respectively. For each sample, the morphology consists of spherical particles and mesh-like structures. According to the EDAX of GAPS D15 sample illustrated in Fig. 3.19 (a) the spherical particles are composed of Ga, As, and O, whereas the mesh-like structures Fig. 3.19 (b) have only Ga and O. EDAX spectra for GAPS E15, GAPS T15, and GAPS C15 samples are depicted in Figs. 3.19 (c-e), respectively. Ga, As, and O were proven to exist in each of these samples.

A few locations on the samples had hexagons, pentagons, and cuboids, as seen in Figs. 3.20 (a, b), containing solely As and O. As illustrated in Figs. 3.20 (c, d) the mesh-like background structure is composed of Ga, As, and O. The production of arsenic oxide particles may be the result of agglomeration or the heat used to evaporate the DW during drop casting. The Raman data (shown in Fig. 3.21) supports the EDAX and demonstrates the presence of As_2O_3 in samples GAPS E15 and GAPS C15.

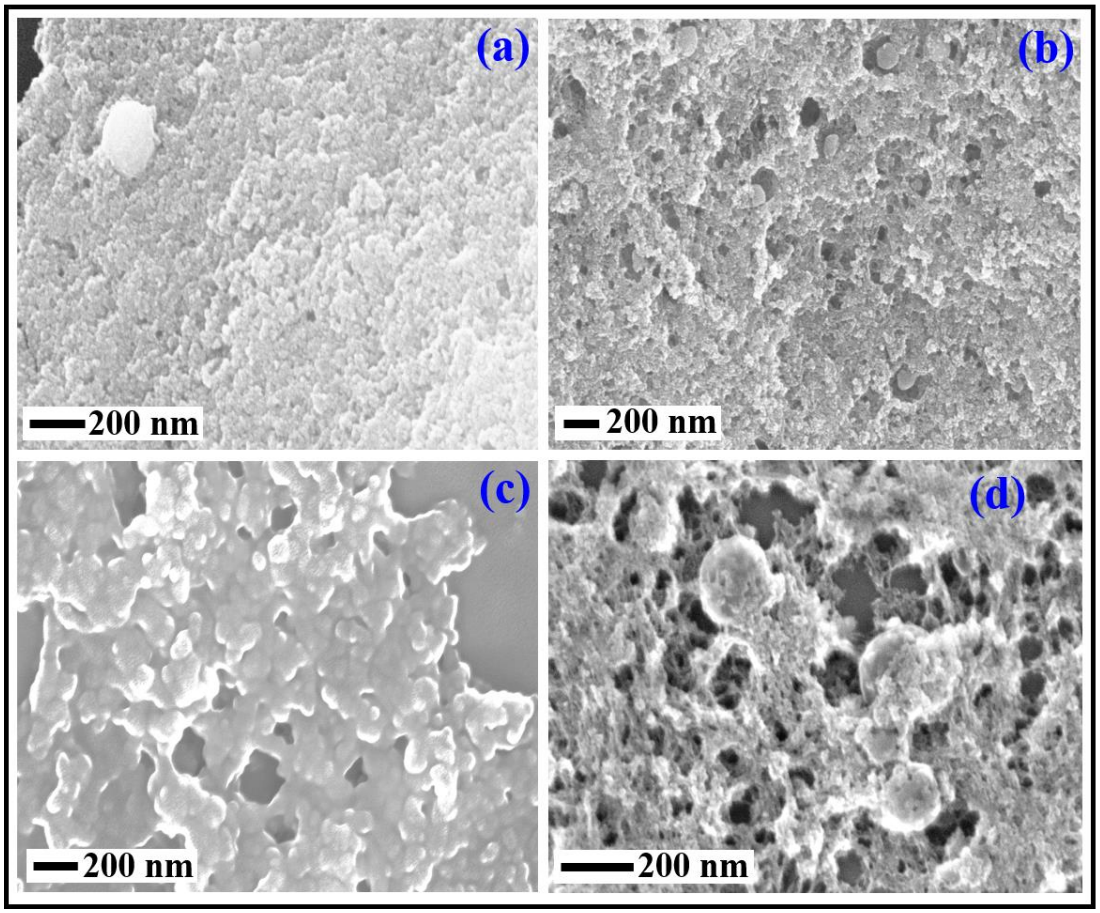

Fig. 3.18 FESEM images of GaAs ablated in (a) DW (b) ethanol (c) toluene and (d) chloroform.

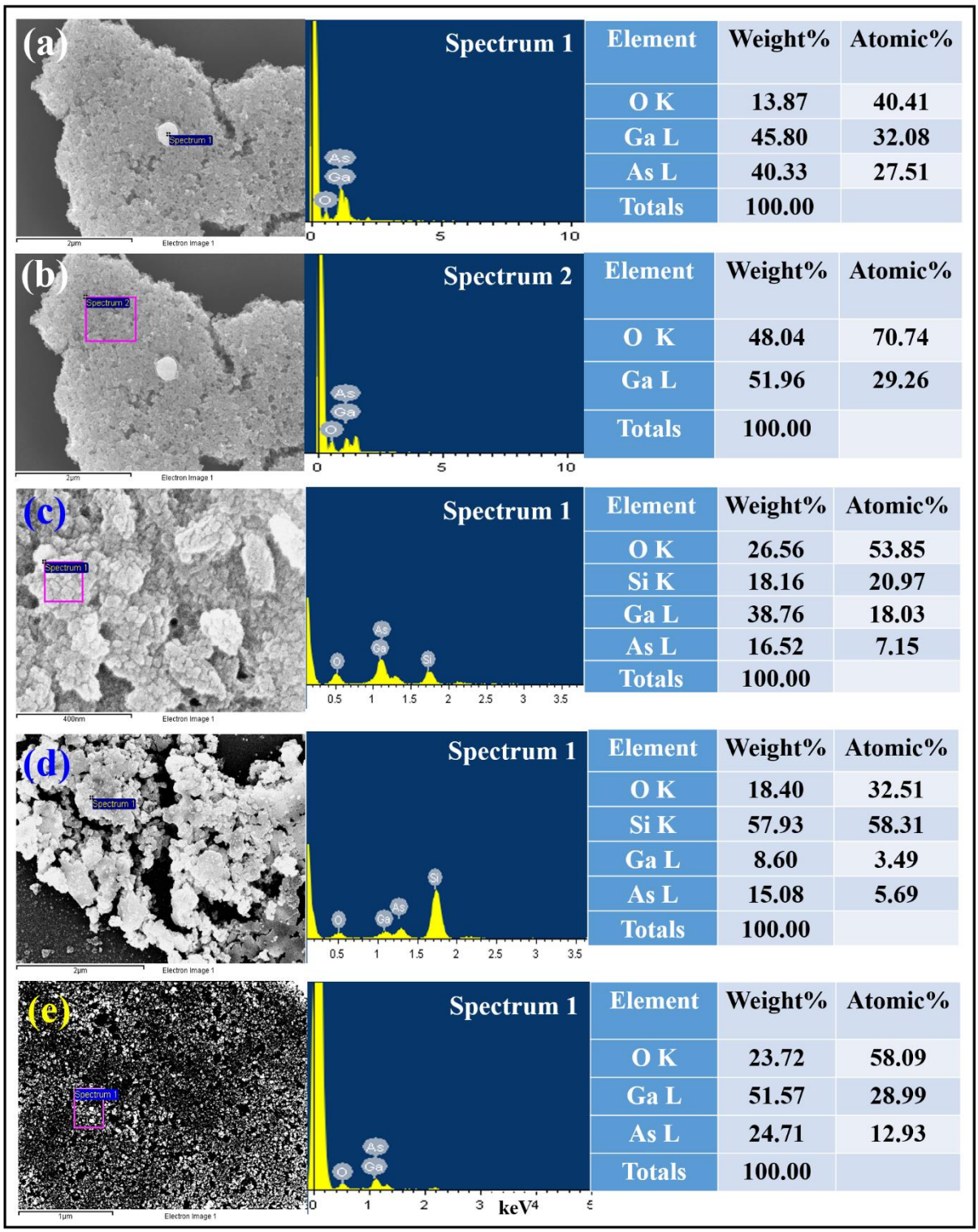

Fig. 3.19 EDAX analysis of GAPS_D15 (a, b), GAPS_E15 (c), GAPS_T15 (d), and GAPS_C15 (e) samples drop casted on Si.

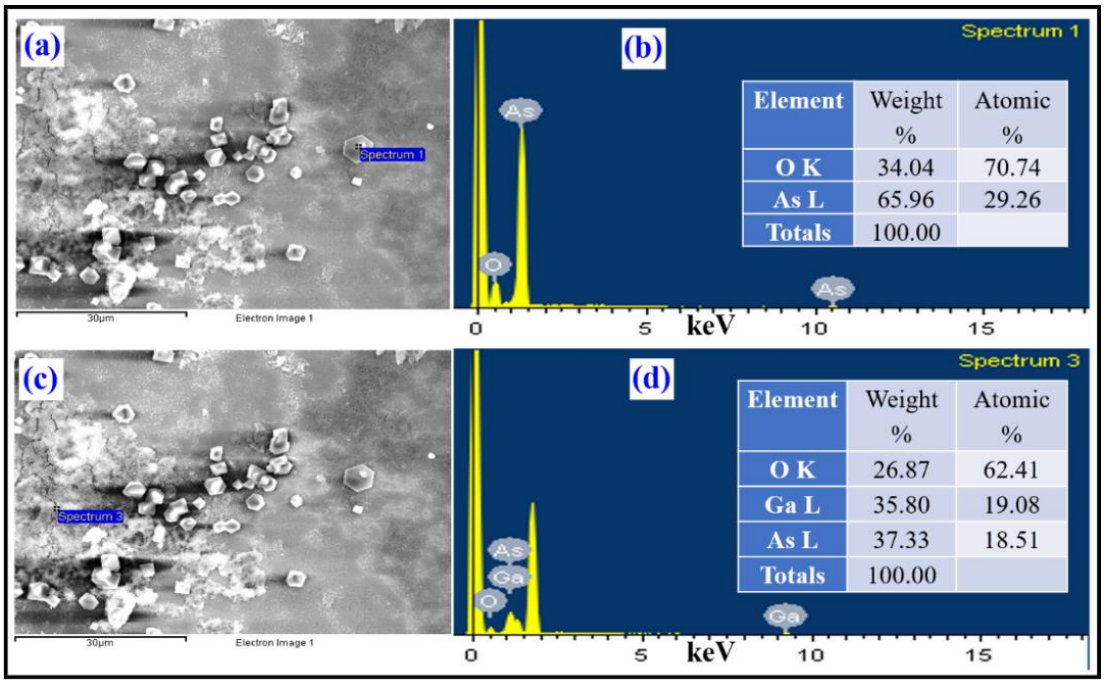

Fig. 3.20 (a, b) EDAX performed on hexagonal particle and (c, d) on the background mesh like structure**.**

It is obvious from Figure 3.21 (a) that the Raman spectrum of bulk GaAs comprises two Raman active modes, transverse optical (TO) at 267 cm^{-1} and longitudinal optical (LO) at 292 cm^{-1} (ref [73,74]). Figure 3.21 (b) depicts the Raman spectra of GAPS D15 (ablated in DW), in which the LO and TO modes of GaAs are missing yet the peaks in this spectrum perfectly match with those of the β-Ga_2O_3 phase[75,76]. This observation is consistent with the EDAX data presented in the earlier section. For the samples GAPS E15 (ablated in ethanol) and GAPS C15 (ablated in chloroform) shown in Figures 3.21 (c, d), respectively, there is only the TO (267 cm^{-1}) mode, which corresponds to GaAs, along with several additional peaks at 181 cm^{-1}, 369 cm^{-1}, 466 cm^{-1}, 558 cm^{-1}, and 778 cm^{-1}. Recently, Quaglianor et al.[77] explored As_2O_3 on the surface of GaAs substrates using Raman spectroscopy and got the As_2O_3 Raman spectrum, which matches our results precisely. This gives strong evidence that these samples include As_2O_3 particles. The peak at 267 cm^{-1} is close to one of the peaks attributed to As_2O_3 in reference[77]. This peak appears to have a greater intensity than the TO mode of GaAs alone. As indicated in a previous paper[77], it is probable that this strong and powerful peak of As_2O_3 obscured the TO mode of GaAs, which is comprised of both As_2O_3 and GaAs. Small variations in wavenumbers are anticipated as a result of stresses induced on the NPs. The Raman signal could not be obtained for GaAsT15 sample, a detailed study may be required to understand the ablation of GaAs in toluene. Consequently, the Raman analysis demonstrates explicitly that several phases,

including β-Ga_2O_3, GaAs, and As_2O_3, are present in the colloidal solution of GaAs ablated in various liquids.

From aforementioned results, we can deduce that the circumstances of GaAs ablated in DW promote the development of β-Ga_2O_3 together with other phases such as GaAs but for the other samples, GaAs and As_2O_3 are the predominant phases.

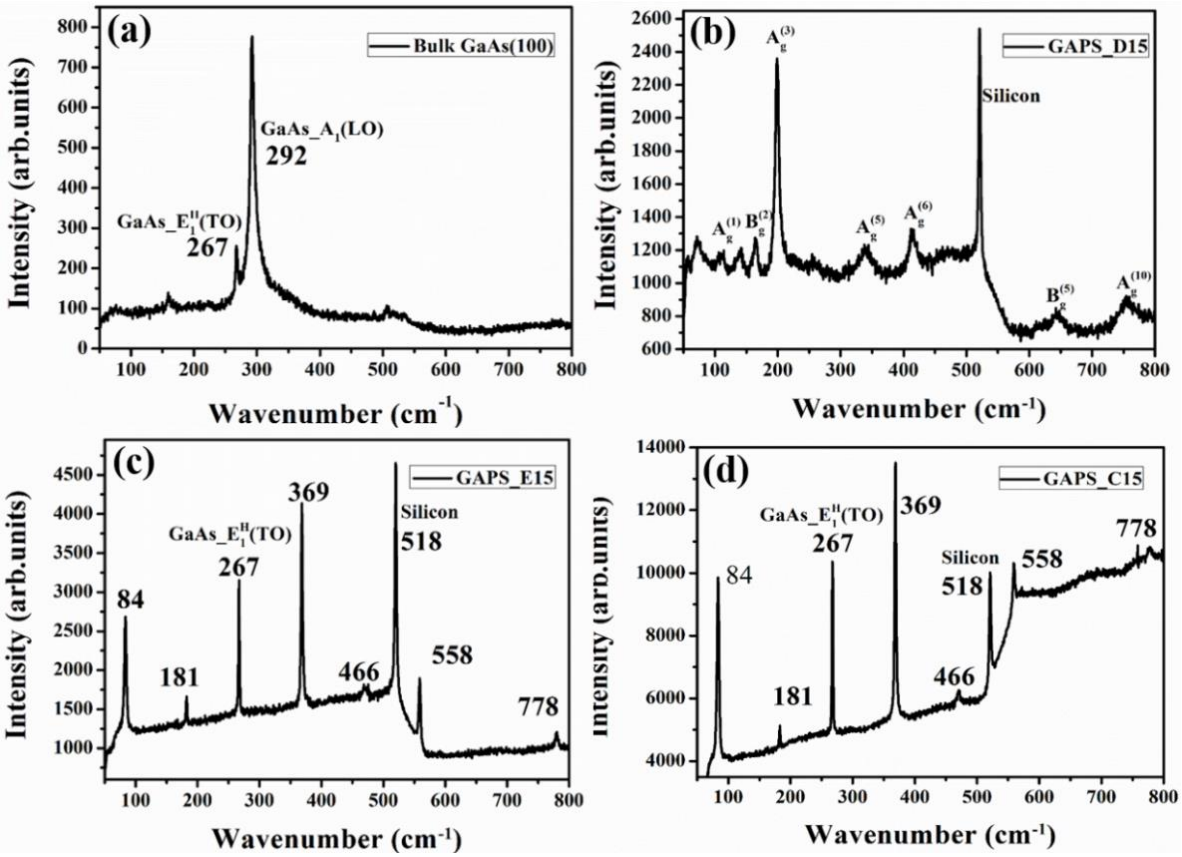

Fig. 3.21 Raman spectra of (a) bulk GaAs substrate measured for reference, and GaAs particles ablated (b) in DW, (c) in ethanol, and (d) in chloroform. The LO and TO modes are indicated wherever appropriate.

3.2.4 (c) Influence of temperature on the morphology of drop-casted GaAs colloidal nanoparticles on Si

As noted, before in Fig.3.20, the sample contains trace amounts of hexagons, pentagons of As_2O_3 crystals. This was may be due to the agglomeration effects caused when heating the Si substrates after drop-casting the NPs onto its surface. Hence, we conducted a temperature dependent drop casting study to examine the cause of this observation. On Si substrates, samples were drop-casted and then heated to three distinct temperatures: room temperature (RT), 75 °C, and 150 °C. Figure 3.22 (a-b) depicts FESEM images of GaAs that has been ablated in ethanol and then drop casted onto Si at room temperature (GAPS E15 RT). The

majority of the sample is found to include GaAs and GaO. A small number of As_2O_3 aggregates are also generated, as seen in EDAX data Fig. 3.22 (c). Figure 3.22 (d-e) depicts GaAs that has been ablated in ethanol, drop casted onto Si, and heated to 75 °C. In addition to the GaAs and GaO nanoparticles, a substantial number of As_2O_3 crystals have likely begun to develop due to the temperature impact. Flower-like and flake-like formations arise at 75 °C heat treatment. These flower-like formations are composed of As_2O_3 rods, as seen in Fig. 3.22 (f). Figure 3.22 (g-h) depicts GaAs ablated in ethanol, drop cast on Si, and heated to a temperature of 150 °C. In this instance, As_2O_3 crystals are completely produced and equally distributed across the whole sample. The number density of As_2O_3 crystals is much higher than that of samples treated at 75 °C and RT.

These agglomeration and oxidation are seen in all samples; however, if drop-casted samples are heated to temperatures higher than the room temperature, oxidation due to heating increases, resulting an increase in the generation of As_2O_3. Malik et al.[78] synthesized GaAs by chemical means and anticipated the production of Ga_2O_3, As_2O_3, and $GaAsO_4$ phases by evaluating the X-ray diffraction pattern and the broadening of corresponding peaks upon heating.

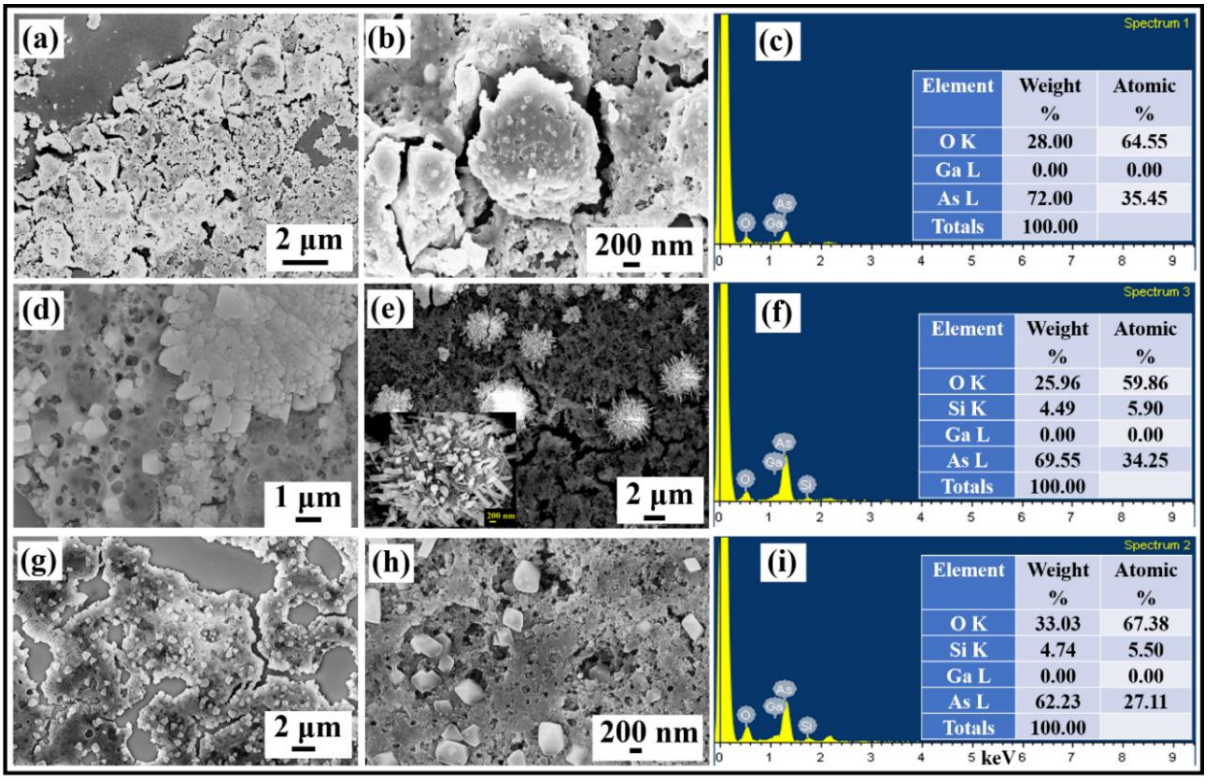

Fig. 3.22 FESEM images (two different regions), EDAX spectra and table of composition of GAPS E15 sample drop casted on Si and treated at (a-c) RT, (d-f) at 75 °C, and (g-i) at 150 °C, respectively.

3.2.5 Overall discussion of GaAs laser ablation results

From a detailed analysis of the laser ablated colloidal solutions of GaAs, it is shown that the femtosecond laser ablation has led to the formation of cubic-zinc blende structure of GaAs, which is a room temperature stable phase of GaAs. Upon increasing the laser energy, it is noticed that there is an increase in the average particle size of the GaAs NPs. Along with the spherical GaAs NPs, formation of mesh-like background structure is observed, which is amorphous and oxide rich Ga/As/GaAs. The EDAX mapping equipped to TEM instrument has revealed a clear distribution of O, Ga, and As in the background material, whereas mainly Ga and As in the particle like structures.

Further, in the picosecond LAL also there is a formation of particle like structures and mesh-like background material. However, in this case, the spherical polycrystalline GaAs NPs formed were in high temperature/high pressure phase of GaAs (i.e., Hexagonal GaAs). The background material again consists of oxide materials of Ga/As/GaAs. Varying the liquid environment during the ps LAL has led to the formation of different exotic compounds along with the GaAs NPs. For the ablation performed in DW the existence of β-Ga_2O_3 is dominant whereas As_2O_3 and GaAs are major compounds in ethanol and chloroform. A composition of GaAs/GaO are observed in toluene. Table 3.5 provides a summary of the liquids employed in this investigation and their additional significant features. In high viscous solvents such as DW (0.89×10^{-3} N s/m^2) and ethanol (1.09×10^{-3} N s/m^2), interestingly, polycrystalline GaAs NPs with good crystallinity are observed, whereas in relatively less viscous solvents such as toluene (0.55×10^{-3} N s/m^2), polycrystalline particles with less crystallinity are observed. Further, liquids with relatively low viscosity, chloroform (0.53×10^{-3} N s/m^2) contains totally amorphous nanoparticles. Hence, viscosity could be one reason for the observed differences in the crystallinity and composition of the ablated NPs. Further, the liquid's refractive index and polarity could also affect the amorphous material. It appears that even minute variations in the physical characteristics of liquids can significantly alter the LAL process by influencing the cavitation bubble's collapse time and internal dynamics. Hence, systematic study by varying only one parameter of the same solvent may be required to understand effect of liquid parameters.

Table 3.5 Different physical properties of the solvents used in this work.
[Below information is obtained from (1) https://www.sigmaaldrich.com/chemistry/stockroom-reagents/learning-center/technical-library/solvent-properties.html, (2) https://wiki.anton-paar.com/in-en/water/, (3) https://wiki.anton-paar.com/in-en/ethanol/, (4) https://wiki.anton-paar.com/in-en/chloroform/, and (5) https://wiki.anton-paar.com/in-en/toluene/.]

Liquid	**Density (gm/cc)**	**Refractive index (at 587 nm)**	**Viscosity (Ns/m^2) × 10^{-3}**	**Polarity**	**Results**
DW	1.00	1.33	0.89	Polar	Along with hex- GaAs polycrystalline particles, β-Ga_2O_3 was dominating phase.
Ethanol	0.78	1.36	1.09	Polar	Along with Hex GaAsO4 polycrystalline particles, GaO, As_2O_3 are dominating phases.
Chloroform	1.47	1.44	0.53	Mild polar	Along with GaAs very fine amorphous particles, GaO, As_2O_3 are dominating phases
Toluene	0.86	1.49	0.55	Non-polar	GaAs non-spherical particles are observed along with GaO.

Overall (see Fig. 3.23), the fs LAL with lower laser fluence has led to the pure/room temperature stable cubic GaAs NPs and the ps LAL performed at much higher fluence has led to the exotic hexagonal GaAs NPs and other compounds like As_2O_3 and Ga_2O_3. The high fluence there by the high pressures and temperatures created on the surface of GaAs are the primary cause of these exotic phases. Recently, Samuel et al.[45] showed that the cubic zinc blende structure of GaAs is stable at 300 K and ambient pressure, and that when the pressure

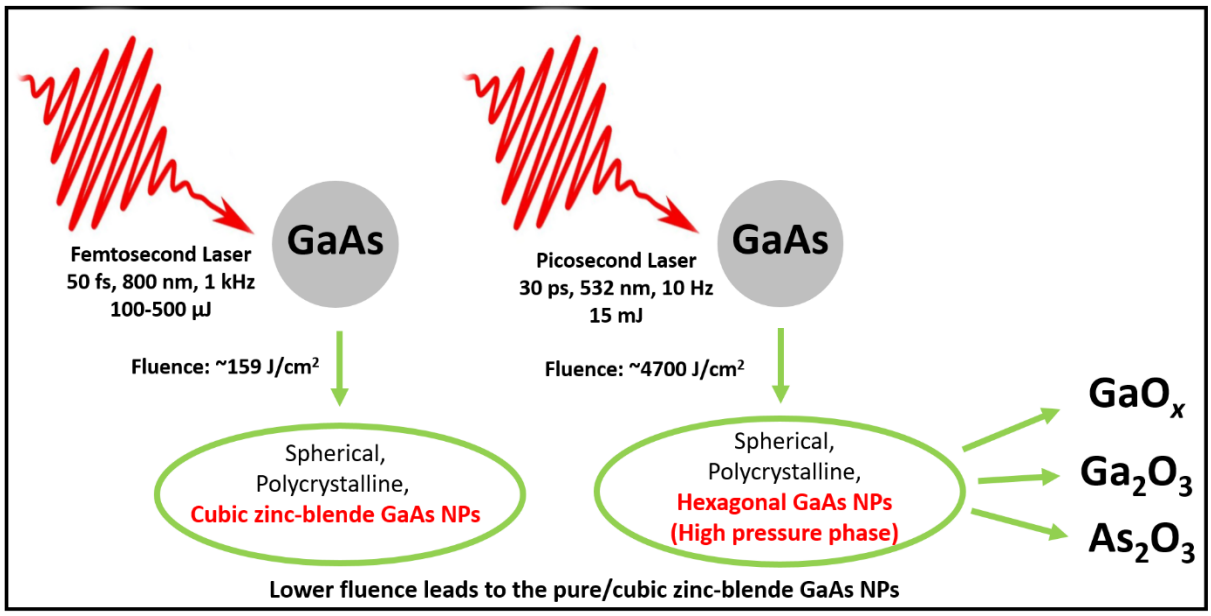

Fig. 3.23 schematic representation of the femtosecond and picosecond laser ablation parameters and their remarkable outcomes (Laser fluence is estimated using equation 4.4, given in chapter 4).

increases, the orthorhombic phase develops at 16.6 GPa and stays until 22.9 GPa. When the pressure reaches 28.1 GPa, the disordered simple hexagonal phase arises, and at 65.5 GPa, the ordered simple hexagonal phase appears, and so on up to 108 GPa. In addition, a number of theoretical and experimental experiments revealed comparable behaviour. Thus, rapid laser ablation of solids in liquid environments makes it feasible to create nanoparticles in their non-equilibrium and/or exotic phases [35].

3.2.6 Conclusion

In the first part of this study, HfO_2 pellets with two distinct initial grain sizes were achieved by ball-milling process and were ablated using fs laser pulses in DW and ethanol. The NPs were discovered to be polycrystalline, while the fiber-like structures were discovered to be amorphous. In addition, the formation of high-temperature and high-pressure phases of HfO_x NPs (tetragonal /cubic HfO_x) was observed along with the formation of ambient monoclinic HfO_2. The combination of ball milling and femtosecond laser ablation appears to be the most effective technique for synthesizing smaller NPs of exotic non-equilibrium phases.

In the second part of this study, in-depth research on the ultrafast laser ablation of GaAs in various liquids, and at various laser parameters is presented. When the GaAs target was ablated at higher fluence, exotic high temperature/high pressure stable phases like hexagonal GaAs and other compounds like As_2O_3 and Ga_2O_3 were created. In contrast, when GaAs was ablated at lower fluences, stable cubic (zinc blende) GaAs NPs were created. Accordingly, this study develops a method for selectively producing pure cubic-GaAs particles or high-temperature / high-pressure hexagonal particles, depending on the need.

References

(1) Rewari, S.; Nath, V.; Haldar, S.; Deswal, S. S.; Gupta, R. S. Hafnium Oxide Based Cylindrical Junctionless Double Surrounding Gate (CJLDSG) MOSFET for High Speed, High Frequency Digital and Analog Applications. *Microsyst. Technol.* **2019**, *25* (5), 1527–1536. https://doi.org/10.1007/s00542-017-3436-3.

(2) Pugachevskii, M. A.; Panfilov, V. I. Stabilization of the High-Temperature Phases of HfO2 by Pulsed Laser Irradiation. *Inorg. Mater.* **2014**, *50* (6), 582–585. https://doi.org/10.1134/S0020168514060144.

(3) Park, P. K.; Kang, S.-W. Enhancement of Dielectric Constant in HfO2 Thin Films by the Addition of Al2O3. *Appl. Phys. Lett.* **2006**, *89* (19), 192905. https://doi.org/10.1063/1.2387126.

(4) Quan, Y. C.; Lee, J. E.; Kang, H.; Roh, Y.; Jung, D.; Yang, C.-W. Formation of Reliable HfO 2 /HfSi x O y Gate-Dielectric for Metal-Oxide-Semiconductor Devices. *Jpn. J. Appl. Phys.* **2002**, *41* (Part 1, No. 11B), 6904–6907. https://doi.org/10.1143/JJAP.41.6904.

(5) Manikanthababu, N.; Basu, T.; Vajandar, S.; Nageswara Rao, S. V. S.; Panigrahi, B. K.; Osipowicz, T.; Pathak, A. P. Radiation Tolerance, Charge Trapping, and Defect Dynamics Studies of ALD-Grown Al/HfO2/Si NMOSCAPs. *J. Mater. Sci. Mater. Electron.* **2020**, *31* (4), 3312–3322. https://doi.org/10.1007/s10854-020-02879-w.

(6) Manikanthababu, N.; Arun, N.; Dhanunjaya, M.; Nageswara Rao, S. V. S.; Pathak, A. P. Gamma Irradiation-Induced Effects on the Electrical Properties of HfO 2 -Based MOS Devices. *Radiat. Eff. Defects Solids* **2016**, *171* (1–2), 77–86. https://doi.org/10.1080/10420150.2015.1135152.

(7) Choi, J. H.; Mao, Y.; Chang, J. P. Development of Hafnium Based High-k Materials—A Review. *Mater. Sci. Eng. R Reports* **2011**, *72* (6), 97–136. https://doi.org/10.1016/j.mser.2010.12.001.

(8) Vescio, G.; López-Vidrier, J.; Leghrib, R.; Cornet, A.; Cirera, A. Flexible Inkjet Printed High-k HfO 2 -Based MIM Capacitors. *J. Mater. Chem. C* **2016**, *4* (9), 1804–1812. https://doi.org/10.1039/C5TC03307A.

(9) Arun, N.; Vinod Kumar, K.; Mangababu, A.; Nageswara Rao, S. V. S.; Pathak, A. P. Influence of the Bottom Metal Electrode and Gamma Irradiation Effects on the Performance of HfO 2 -Based RRAM Devices. *Radiat. Eff. Defects Solids* **2019**, *174* (1–2), 66–75. https://doi.org/10.1080/10420150.2019.1579213.

(10) Al-Kuhaili, M. Optical Properties of Hafnium Oxide Thin Films and Their Application in Energy-Efficient Windows. *Opt. Mater. (Amst).* **2004**, *27*, 383–387. https://doi.org/10.1016/j.optmat.2004.04.014.

(11) Mangababu, A.; Sarang Dev, G.; Chandu, B.; Bharati, M. S. S.; Venugopal Rao, S.; Nageswara Rao, S. V. S. Structural Investigations of Picosecond Laser Ablated GaAs Nanoparticles in Different Liquids. *Nano-Structures & Nano-Objects* **2020**, *23*, 100509. https://doi.org/10.1016/j.nanoso.2020.100509.

(12) Lee, M.; Baraket, A.; Zine, N.; Zabala, M.; Campabadal, F.; Jaffrezic-renault, N.; Errachid, A. Impedance Characterization of the Capacitive Field-Effect PH-Sensor Based on a Thin-Layer Hafnium Oxide Formed by Atomic Layer Deposition. *Sens. Transducers* **2014**, *27* (May), 233–238.

(13) Zhang, X.; Tu, H.; Wang, X.; Xiong, Y.; Yang, M.; Wang, L.; Du, J. Hetero-Epitaxial Growth of the Cubic Single Crystalline HfO2 Film as High k Materials by Pulsed Laser Ablation. *J. Cryst. Growth* **2010**, *312* (20), 2928–2930. https://doi.org/10.1016/j.jcrysgro.2010.07.015.

(14) Tongpeng, S.; Makbun, K.; Janphuang, P.; Wannapaiboon, S.; Pattanakul, R.; Pojprapai, S.; Jiansirisomboon, S. Synthesis and Characterization of La-Doped Hafnium Oxide Thin Films by Sol–Gel Method. *Integr. Ferroelectr.* **2022**, *222* (1), 102–115. https://doi.org/10.1080/10584587.2021.1961520.

(15) Kumar, N.; George, B. P. A.; Abrahamse, H.; Parashar, V.; Ray, S. S.; Ngila, J. C. A Novel Approach to Low-Temperature Synthesis of Cubic HfO2 Nanostructures and Their Cytotoxicity. *Sci. Rep.* **2017**, *7* (1), 9351. https://doi.org/10.1038/s41598-017-07753-0.

(16) Cojocaru, B.; Avram, D.; Negrea, R.; Ghica, C.; Kessler, V. G.; Seisenbaeva, G. A.; Parvulescu, V. I.; Tiseanu, C. Phase Control in Hafnia: New Synthesis Approach and Convergence of Average and Local Structure Properties. *ACS Omega* **2019**, *4* (5), 8881–8891. https://doi.org/10.1021/acsomega.9b00580.

(17) Manory, R. R.; Mori, T.; Shimizu, I.; Miyake, S.; Kimmel, G. Growth and Structure Control of HfO2−x Films with Cubic and Tetragonal Structures Obtained by Ion Beam Assisted Deposition. *J. Vac. Sci. Technol. A Vacuum, Surfaces, Film.* **2002**, *20* (2), 549–554. https://doi.org/10.1116/1.1453453.

(18) Pugachevskii, M. A.; Panfilov, V. I. Effect of the Pulse Laser Radiation on the Stabilization of the ZrO_2 and HFO_2 High-Temperature Phases. *Solid State Phenom.* **2015**, *245*, 200–203. https://doi.org/10.4028/www.scientific.net/SSP.245.200.

(19) Pugachevskii, M. A.; Panfilov, V. I. Optical Properties of HfO2 Nanoparticles Produced by Laser Ablation. *J. Appl. Spectrosc.* **2014**, *81* (4), 640–643. https://doi.org/10.1007/s10812-014-9982-x.

(20) Daubert, J. S.; Hill, G. T.; Gotsch, H. N.; Gremaud, A. P.; Ovental, J. S.; Williams, P. S.; Oldham, C. J.; Parsons, G. N. Corrosion Protection of Copper Using Al 2 O 3 , TiO 2 , ZnO, HfO 2 , and ZrO 2 Atomic Layer Deposition. *ACS Appl. Mater. Interfaces* **2017**, *9* (4), 4192–4201. https://doi.org/10.1021/acsami.6b13571.

(21) Vyas, S. A Short Review on Properties and Applications of Zinc Oxide Based Thin Films and Devices : ZnO as a Promising Material for Applications in Electronics, Optoelectronics, Biomedical and Sensors. *Johnson Matthey Technol. Rev.* **2020**, *64* (2), 202–218. https://doi.org/10.1595/205651320X15694993568524.

(22) Wang, S.; Zou, Y.; Shan, Q.; Xue, J.; Dong, Y.; Gu, Y.; Song, J. Nanowire Network-Based

Photodetectors with Imaging Performance for Omnidirectional Photodetecting through a Wire-Shaped Structure. *RSC Adv.* **2018**, *8* (59), 33666–33673. https://doi.org/10.1039/C8RA06555A.

(23) Das, B. K.; Verma, S. K.; Das, T.; Panda, P. K.; Parashar, K.; Suar, M.; Parashar, S. K. S. Altered Electrical Properties with Controlled Copper Doping in ZnO Nanoparticles Infers Their Cytotoxicity in Macrophages by ROS Induction and Apoptosis. *Chem. Biol. Interact.* **2019**, *297*, 141–154. https://doi.org/10.1016/j.cbi.2018.11.004.

(24) Das, B. K.; Das, T.; Parashar, K.; Parashar, S. K. S.; Kumar, R.; Choudhary, H. K.; Khopkar, V. B.; Anupama, A. V.; Sahoo, B. Investigation of Structural, Morphological and NTCR Behaviour of Cu-Doped ZnO Nanoceramics Synthesized by High Energy Ball Milling. *Mater. Chem. Phys.* **2019**, *221* (September 2018), 419–429. https://doi.org/10.1016/j.matchemphys.2018.09.056.

(25) Das, B. K.; Das, T.; Parashar, K.; Parashar, S. K. S.; Kumar, R.; Anupama, A. V.; Sahoo, B. Effect of Cr Doping on Structural, Optical and Dielectric Properties of ZnO Nanoceramics Synthesized by Mechanical Alloying. *Electron. Mater. Lett.* **2020**, *16* (3), 255–263. https://doi.org/10.1007/s13391-020-00209-0.

(26) Das, T.; Das, B. K.; Parashar, K.; Kumar, R.; Choudhary, H. K.; Anupama, A. V.; Sahoo, B.; Sahoo, P. K.; Parashar, S. K. S. Effect of Sr-Doping on Sinterability, Morphology, Structure, Photocatalytic Activity and AC Conductivity of ZnO Ceramics. *J. Mater. Sci. Mater. Electron.* **2017**, *28* (18), 13587–13595. https://doi.org/10.1007/s10854-017-7198-6.

(27) Jayaraman, V.; Sagadevan, S.; Sudhakar, R. Studies on Optical and Electrical Properties of Hafnium Oxide Nanoparticles. *J. Electron. Mater.* **2017**, *46* (7), 4392–4397. https://doi.org/10.1007/s11664-017-5432-x.

(28) Zhang, Y.; Lu, H.-L.; Wang, T.; Ren, Q.-H.; Gu, Y.-Z.; Li, D.-H.; Zhang, D. W. Facile Synthesis and Enhanced Luminescent Properties of ZnO/HfO 2 Core–Shell Nanowires. *Nanoscale* **2015**, *7* (37), 15462–15468. https://doi.org/10.1039/C5NR03656A.

(29) Lee, M.; Zine, N.; Baraket, A.; Zabala, M.; Campabadal, F.; Caruso, R.; Trivella, M. G.; Jaffrezic-Renault, N.; Errachid, A. A Novel Biosensor Based on Hafnium Oxide: Application for Early Stage Detection of Human Interleukin-10. *Sensors Actuators B Chem.* **2012**, *175*, 201–207. https://doi.org/10.1016/j.snb.2012.04.090.

(30) Bayda, S.; Hadla, M.; Palazzolo, S.; Riello, P.; Corona, G.; Toffoli, G.; Rizzolio, F. Inorganic Nanoparticles for Cancer Therapy: A Transition from Lab to Clinic. *Curr. Med. Chem.* **2018**, *25* (34), 4269–4303. https://doi.org/10.2174/0929867325666171229141156.

(31) Lee, M.; Zine, N.; Baraket, A.; Zabala, M.; Campabadal, F.; Trivella, M. G.; Jaffrezic-Renault, N.; Errachid, A. Novel Capacitance Biosensor Based on Hafnium Oxide for Interleukin-10 Protein Detection. *Procedia Eng.* **2011**, *25*, 972–975. https://doi.org/10.1016/j.proeng.2011.12.239.

(32) Jayaraman, V.; Bhavesh, G.; Chinnathambi, S.; Ganesan, S.; Aruna, P. Synthesis and Characterization of Hafnium Oxide Nanoparticles for Bio-Safety. *Mater. Express* **2014**, *4* (5), 375–

383. https://doi.org/10.1166/mex.2014.1190.

(33) McGinnity, T. L.; Dominguez, O.; Curtis, T. E.; Nallathamby, P. D.; Hoffman, A. J.; Roeder, R. K. Hafnia (HfO 2) Nanoparticles as an X-Ray Contrast Agent and Mid-Infrared Biosensor. *Nanoscale* **2016**, *8* (28), 13627–13637. https://doi.org/10.1039/C6NR03217F.

(34) Sekar, N.; Ganesan, B.; Sahib, H. R. A.; Krishnamurthy, K.; Aruna, P.; Ga, S. Evalution of Dosimetric Properties of Hafnium Oxide Nanoparticles for Radiotherapy Applications. *J. Med. Phys.* **2018**, *43* (suppl1), 102–103.

(35) Dhanunjaya, M.; Byram, C.; Vendamani, V. S.; Rao, S. V.; Pathak, A. P.; Rao, S. V. S. N. Hafnium Oxide Nanoparticles Fabricated by Femtosecond Laser Ablation in Water. *Appl. Phys. A* **2019**, *125* (1), 74. https://doi.org/10.1007/s00339-018-2366-y.

(36) Zhou, Y. C.; Rahaman, M. N. Hydrothermal Synthesis and Sintering of Ultrafine CeO 2 Powders. *J. Mater. Res.* **1993**, *8* (7), 1680–1686. https://doi.org/10.1557/JMR.1993.1680.

(37) Vendamani, V. S.; Tripathi, A.; Pathak, A. P.; Rao, S. V.; Tiwari, A. Laser Ablation of Natural Micas: Synthesis of MgO and Mg(OH)2 Nanoparticles and Nanochains. *Mater. Lett.* **2017**, *192*, 29–32. https://doi.org/10.1016/j.matlet.2017.01.068.

(38) Van Overschelde, O.; Dervaux, J.; Yonge, L.; Thiry, D.; Snyders, R. Screening Effect in Gold Nanoparticles Generated in Liquid by KrF Ablation. *Laser Phys.* **2013**, *23* (5), 055901. https://doi.org/10.1088/1054-660X/23/5/055901.

(39) Phuoc, T. X. Complete Green Synthesis of Gold Nanoparticles Using Laser Ablation in Deionized Water Containing Chitosan and Starch. *J. Mater. Sci. Nanotechnol.* **2014**, *1* (4), 1–7. https://doi.org/10.15744/2348-9812.1.401.

(40) Wan, Y.; Zhou, X. Formation Mechanism of Hafnium Oxide Nanoparticles by a Hydrothermal Route. *RSC Adv.* **2017**, *7* (13), 7763–7773. https://doi.org/10.1039/c6ra26663k.

(41) Zhou, B.; Shi, H.; Zhang, X. D.; Su, Q.; Jiang, Z. Y. The Simulated Vibrational Spectra of HfO 2 Polymorphs. *J. Phys. D. Appl. Phys.* **2014**, *47* (11), 115502. https://doi.org/10.1088/0022-3727/47/11/115502.

(42) Wu, R.; Zhou, B.; Li, Q.; Jiang, Z.; Wang, W.; Ma, W.; Zhang, X. Elastic and Vibrational Properties of Monoclinic HfO 2 from First-Principles Study. *J. Phys. D. Appl. Phys.* **2012**, *45* (12), 125304. https://doi.org/10.1088/0022-3727/45/12/125304.

(43) Zhao, X.; Vanderbilt, D. First-Principles Study of Structural, Vibrational, and Lattice Dielectric Properties of Hafnium Oxide. *Phys. Rev. B - Condens. Matter Mater. Phys.* **2002**, *65* (23), 1–4. https://doi.org/10.1103/PhysRevB.65.233106.

(44) Jain, D.; Mangla, O.; Roy, S. Wide Band Gap Gallium Arsenide Nanoparticles Fabricated Using Plasma Method. In *AIP Conference Proceedings*; 2016; Vol. 1731, p 050143. https://doi.org/10.1063/1.4947797.

(45) Weir, S. T.; Vohra, Y. K.; Vanderborgh, C. A.; Ruoff, A. L. Structural Phase Transitions in GaAs

to 108 GPa. *Phys. Rev. B* **1989**, *39* (2), 1280–1285. https://doi.org/10.1103/PhysRevB.39.1280.

(46) Li, S. S. High-Speed III–V Semiconductor Devices. In *Semiconductor Physical Electronics*; Springer US: Boston, MA, 1993; pp 455–502. https://doi.org/10.1007/978-1-4613-0489-0_15.

(47) Wang, Z. J.; Kim, E. S.; Liang, J. G.; Qiang, T.; Kim, N. Y. A High-Frequency-Compatible Miniaturized Bandpass Filter with Air-Bridge Structures Using GaAs-Based Integrated Passive Device Technology. *Micromachines* **2018**, *9* (9), 463. https://doi.org/10.3390/mi9090463.

(48) Dumke, W. P.; Woodall, J. M.; Rideout, V. L. GaAs□GaAlAs Heterojunction Transistor for High Frequency Operation. *Solid. State. Electron.* **1972**, *15* (12), 1339–1343. https://doi.org/10.1016/0038-1101(72)90127-X.

(49) Ho, W.; Liu, J.; Chen, X.; Xiao, H. Light-trapping and Spectral Modulation to Increase the Conversion Efficiency of Triple-junction <scp>GaAs</Scp> Solar Cells Using Antireflective Coating Comprising a Periodic Array of Cone-shaped <scp> TiO_2 </Scp> Structures. *Int. J. Energy Res.* **2022**, *46* (8), 10157–10168. https://doi.org/10.1002/er.7240.

(50) Zhang, S. J.; Lin, S. S.; Li, X. Q.; Liu, X. Y.; Wu, H. A.; Xu, W. L.; Wang, P.; Wu, Z. Q.; Zhong, H. K.; Xu, Z. J. Opening the Band Gap of Graphene through Silicon Doping for the Improved Performance of Graphene/GaAs Heterojunction Solar Cells. *Nanoscale* **2016**, *8* (1), 226–232. https://doi.org/10.1039/C5NR06345K.

(51) Eberhardt, J. E.; Ryan, R. D.; Tavendale, A. J. High-Resolution Nuclear Radiation Detectors from Epitaxial n-Gas. *Appl. Phys. Lett.* **1970**, *17* (10), 427–429. https://doi.org/10.1063/1.1653257.

(52) Glinka, Y. D.; Shahbazyan, T. V.; Perakis, I. E.; Tolk, N. H.; Liu, X.; Sasaki, Y.; Furdyna, J. K. Ultrafast Spin Dynamics in GaAs/GaSb/InAs Heterostructures Probed by Second Harmonic Generation. *Appl. Phys. Lett.* **2002**, *81* (2), 220–222. https://doi.org/10.1063/1.1494107.

(53) Lin, F.; Cui, J.; Zhang, Z.; Wei, Z.; Hou, X.; Meng, B.; Liu, Y.; Tang, J.; Li, K.; Liao, L.; Hao, Q. GaAs Nanowire Photodetectors Based on Au Nanoparticles Modification. *Materials (Basel).* **2023**, *16* (4), 1735. https://doi.org/10.3390/ma16041735.

(54) Jiang, J.; Gao, B.; Han, T. T.; Fu, Y. Ab Initio Study of Energy Band Structures of GaAs Nanoclusters. *Appl. Phys. Lett.* **2009**, *94* (9), 10–13. https://doi.org/10.1063/1.3094914.

(55) Yan, X.; Zhang, X.; Li, J.; Wu, Y.; Cui, J.; Ren, X. Fabrication and Optical Properties of GaAs/InGaAs/GaAs Nanowire Core-Multishell Quantum Well Heterostructures. *Nanoscale* **2015**, *7* (3), 1110–1115. https://doi.org/10.1039/c4nr05486e.

(56) Salminen, T.; Dahl, J.; Tuominen, M.; Laukkanen, P.; Arola, E.; Niemi, T. Single-Step Fabrication of Luminescent GaAs Nanocrystals by Pulsed Laser Ablation in Liquids. *Opt. Mater. Express* **2012**, *2* (6), 799. https://doi.org/10.1364/OME.2.000799.

(57) Huang, H.; Trotta, R.; Huo, Y.; Lettner, T.; Wildmann, J. S.; Martín-Sánchez, J.; Huber, D.; Reindl, M.; Zhang, J.; Zallo, E.; Schmidt, O. G.; Rastelli, A. Electrically-Pumped Wavelength-Tunable GaAs Quantum Dots Interfaced with Rubidium Atoms. *ACS Photonics* **2017**, *4* (4), 868–872.

https://doi.org/10.1021/acsphotonics.6b00935.

(58) Adéo, J. U. M.; Argiolakis, A. T. M.; Hao, Z. H. E. N. U. Z.; Ale, P. E. J. H.; An, M. I. K. L. M.; Hao, Q. U. A. N. H. Z.; Eng, W. E. I. P.; Hi, W. A. N. G. H. O. U. S.; Ani, K. E. M. D. Madeo-Ultrafast Properties of Femtosecond-Laser-Ablated. **2015**, *40* (14), 3388–3391.

(59) Ganeev, R. A.; Ryasnyanskiy, A. I.; Usmanov, T. Optical and Nonlinear Optical Characteristics of the Ge and GaAs Nanoparticle Suspensions Prepared by Laser Ablation. *Opt. Commun.* **2007**, *272* (1), 242–246. https://doi.org/10.1016/j.optcom.2006.11.009.

(60) Hong, L.; Rusli; Yu, H.; Wang, X.; Wang, H.; Zheng, H. Surface Nanostructure Optimization for GaAs Solar Cell Application. *Jpn. J. Appl. Phys.* **2012**, *51* (10 PART 2), 13–16. https://doi.org/10.1143/JJAP.51.10ND13.

(61) Chan, W. C. .; Maxwell, D. J.; Gao, X.; Bailey, R. E.; Han, M.; Nie, S. Luminescent Quantum Dots for Multiplexed Biological Detection and Imaging. *Curr. Opin. Biotechnol.* **2002**, *13* (1), 40–46. https://doi.org/10.1016/S0958-1669(02)00282-3.

(62) Xing, Y.; Rao, J. Quantum Dot Bioconjugates for in Vitro Diagnostics & in Vivo Imaging. *Cancer Biomarkers* **2008**, *4* (6), 307–319. https://doi.org/10.3233/CBM-2008-4603.

(63) Kanitz, A.; Kalus, M.-R.; Gurevich, E. L.; Ostendorf, A.; Barcikowski, S.; Amans, D. Review on Experimental and Theoretical Investigations of the Early Stage, Femtoseconds to Microseconds Processes during Laser Ablation in Liquid-Phase for the Synthesis of Colloidal Nanoparticles. *Plasma Sources Sci. Technol.* **2019**, *28* (10), 103001. https://doi.org/10.1088/1361-6595/ab3dbe.

(64) Zhang, D.; Gökce, B.; Barcikowski, S. Laser Synthesis and Processing of Colloids: Fundamentals and Applications. *Chem. Rev.* **2017**, *117* (5), 3990–4103. https://doi.org/10.1021/acs.chemrev.6b00468.

(65) Tsuji, T. Preparation of Silver Nanoparticles by Laser Ablation in Solution.Pdf. *Appl. Surf. Sci.* **2002**, *202*, 80.

(66) Oseguera-Galindo, D. O.; Martínez-Benítez, A.; Chávez-Chávez, A.; Gómez-Rosas, G.; Pérez-Centeno, A.; Santana-Aranda, M. A. Effects of the Confining Solvent on the Size Distribution of Silver NPs by Laser Ablation. *J. Nanoparticle Res.* **2012**, *14* (9). https://doi.org/10.1007/s11051-012-1133-9.

(67) De Bonis, A.; Galasso, A.; Santagata, A.; Teghil, R. Laser Ablation of GaAs in Liquid: The Role of Laser Pulse Duration. *J. Phys. D. Appl. Phys.* **2016**, *49* (3), 035301. https://doi.org/10.1088/0022-3727/49/3/035301.

(68) Yan, Z.; Chrisey, D. B. Pulsed Laser Ablation in Liquid for Micro-/Nanostructure Generation. *J. Photochem. Photobiol. C Photochem. Rev.* **2012**, *13* (3), 204–223. https://doi.org/10.1016/j.jphotochemrev.2012.04.004.

(69) Byram, C.; Moram, S. S. B.; Soma, V. R. SERS Based Detection of Multiple Analytes from Dye/Explosive Mixtures Using Picosecond Laser Fabricated Gold Nanoparticles and

Nanostructures. *Analyst* **2019**, *144* (7), 2327–2336. https://doi.org/10.1039/C8AN01276H.

(70) Borowiec, A.; MacKenzie, M.; Weatherly, G. C.; Haugen, H. K. Femtosecond Laser Pulse Ablation of GaAs and InP: Studies Utilizing Scanning and Transmission Electron Microscopy. *Appl. Phys. A* **2003**, *77* (3–4), 411–417. https://doi.org/10.1007/s00339-002-1949-8.

(71) Ganeev, R. A.; Ryasnyanskii, A. I.; Kuroda, H. Laser Ablation of Gallium Arsenide in Different Solutions. *Opt. Spectrosc.* **2005**, *99* (6), 1006–1011. https://doi.org/10.1134/1.2149427.

(72) Ganeev, R. A.; Baba, M.; Ryasnyansky, A. I.; Suzuki, M.; Kuroda, H. Laser Ablation of GaAs in Liquids: Structural, Optical, and Nonlinear Optical Characteristics of Colloidal Solutions. *Appl. Phys. B* **2005**, *80* (4–5), 595–601. https://doi.org/10.1007/s00340-004-1734-9.

(73) Silva, S. W. da; Galzerani, J. C.; Lubyshev, D. I.; Basmaji, P. Surface Phonon Observed in GaAs Wire Crystals Grown on Porous Si. *J. Phys. Condens. Matter* **1998**, *10* (43), 9687–9690. https://doi.org/10.1088/0953-8984/10/43/011.

(74) Volodin, V. A.; Sinyukov, M. P. Anisotropy of Long-Wavelength Optical Phonons in GaAs/AlAs Superlattices. *JETP Lett.* **2014**, *99* (7), 396–399. https://doi.org/10.1134/S0021364014070121.

(75) Onuma, T.; Fujioka, S.; Yamaguchi, T.; Itoh, Y.; Higashiwaki, M.; Sasaki, K.; Masui, T.; Honda, T. Polarized Raman Spectra in β-Ga2O3single Crystals. *J. Cryst. Growth* **2014**, *401*, 330–333. https://doi.org/10.1016/j.jcrysgro.2013.12.061.

(76) Dohy, D.; Lucazeau, G.; Revcolevschi, A. Raman Spectra and Valence Force Field of Single-Crystalline β Ga2O3. *J. Solid State Chem.* **1982**, *45* (2), 180–192. https://doi.org/10.1016/0022-4596(82)90274-2.

(77) Quagliano, L. G. Detection of As2O3 Arsenic Oxide on GaAs Surface by Raman Scattering. *Appl. Surf. Sci.* **2000**, *153* (4), 240–244. https://doi.org/10.1016/S0169-4332(99)00355-4.

(78) Malik, M. A.; O'Brien, P.; Norager, S.; Smith, J. Gallium Arsenide Nanoparticles: Synthesis and Characterisation. *J. Mater. Chem.* **2003**, *13* (10), 2591. https://doi.org/10.1039/b305860n.

Chapter 4

Multi-functional Gallium Arsenide Nanoparticles and Nanostructures Fabricated Using Picosecond Laser Ablation

This chapter describes the fabrication of GaAs nanoparticles (NPs) and nanostructures (NSs) using picosecond laser ablation technique. Different surrounding liquid media and other laser parameters are tuned for obtaining better quality NPs and NSs.

Simultaneous fabrication of GaAs NPs and NSs and their possible applications are explored in part-A of this chapter. While a comparative study for the creation of surface structures in air and DW media was presented in part-B of this chapter.

Graphical abstract

Publications from this chapter

1. **A Mangababu**, R. Sai Prasad Goud, Chandu Byram, Jagannath Rathod, Dipanjan Banerjee, Venugopal Rao Soma, S.V.S. Nageswara Rao, Multi-functional gallium arsenide nanoparticles and nanostructures fabricated using picosecond laser ablation, ***Appl. Surf. Sci***. **589** (2022) 152802. https://doi.org/10.1016/j.apsusc.2022.152802.
2. **A Mangababu**, Dipanjan Banerjee, Kanaka Ravi Kumar, R. Sai Prasad Goud, Venugopal Rao Soma, and S. V. S. Nageswara Rao, Comparative study of GaAs nanostructures synthesized in air and distilled water by picosecond pulsed laser ablation and application in hazardous molecules detection. ***Journal of Laser Applications*** **34** (2022) 032014. https://doi.org/10.2351/7.0000750.

Chapter 4 (Part-A)

Simultaneous Fabrication of GaAs NPs and NSs for Photonic and SERS applications

This section presents a detailed study on the fabrication of GaAs nanoparticles (NPs) and nanostructures (NSs) simultaneously in a single experiment. It demonstrates the versatility and multi functionality of ablation products (GaAs NPs, NSs). NPs and NSs are synthesized in three different liquids: distilled water (DW), ethanol, and polyvinyl alcohol (PVA). Various characterization techniques are used to examine the morphology and compositions of these NPs and NSs. Optical and nonlinear optical (NLO) studies were performed on colloidal NPs, which revealed the presence of two-photon absorption. Furthermore, the ablated GaAs substrates exhibited quasi-periodic surface structures with wide angle anti-reflection and hydrophobic properties. These NSs coated with a 25 nm gold served as surface-enhanced Raman scattering (SERS) substrates for detecting trace level hazardous materials. Overall, this work demonstrates multifunctional applications for laser ablated GaAs NPs and NSs.

4.1.0 Introduction

The current effort of scientific communities all over the world is to meet the needs of the rapidly growing population by delivering energy-efficient, high-speed, and cost-effective devices[1]. This has attracted the interest of researchers working in the fields of nanomaterials and nano-devices, prompting the development of various techniques for the synthesis and characterization of these devices, as well as the resources used to create them[2]. Gallium arsenide is a compound semiconductor with promising and proven applications in electronic and optoelectronic devices due to its high and direct bandgap[3,4]. Because of its high electron mobility, it is also a proven substrate material for high-speed and high-frequency electronic applications[5,6]. At room temperature and ambient pressures, GaAs typically exists in the cubic (zinc blende) phase, but at high pressures, it has hexagonal and orthorhombic structures[7,8]. The properties of GaAs in bulk and thin-film form are well understood. However, GaAs-based three-dimensional nano-materials (NPs and NSs) have only recently gained prominence and are currently being thoroughly investigated for their potential in the fabrication of various functional devices[9]. Some of the current research interests for GaAs NPs include quantum LEDs, solar cells, and nonlinear optical (NLO) studies. The kHz and MHz fs pulses probed NLO studies of various NPs have been extensively accomplished in recent years[10–12]. Our

group has also looked into the prominent NLO properties of intriguing plasmonic/non-plasmonic NPs[13–15]. However, to the best of our knowledge, only a few studies on the NLO properties of GaAs NPs have been conducted [16,17]. As a result, researchers are very much interested in contributing to this unexplored area of broadband femtosecond (fs), MHz NLO for GaAs NPs. Sub-wavelength periodic surface NSs of GaAs, on the other hand, have a wide range of applications in optoelectronics, solar cells, antireflective devices/coatings, terahertz antennas, SERS, and so on[18–21].

SERS is a versatile technique for detecting trace amounts of elements and compounds. It enhances the traditional Raman signal with a specially designed surfaces[22–24]. Metal NPs and NSs, particularly Au, Ag, and others, are currently used to enhance SERS signals[25–28]. Based on the detection requirements, various types of SERS substrates employing various materials are now being developed[24,29–34]. Numerous predictions and a few experimental analyses have revealed that cleverly structured semiconductor materials can be used to improve SERS signals[35,36]. As a result, fabricating novel SERS substrates with a combination of Au NPs and GaAs NSs is of great interest in order to achieve portable devices for practical uses. Similarly, the antireflective characteristics of GaAs NSs hold great promise in solar cells and heat mirrors, while its hydrophobic/hydrophilic properties can be employed in self-cleaning, antifogging, and biomedical applications[37,38]. For the synthesis of these nano-entities, various techniques were established[39–46], wherein we used the technique of pulsed laser ablation in liquids (PLAL), which is a simple and quick approach for the fabrication of a variety of NPs[47]. When compared to other available techniques for synthesizing NPs, this established technique has many advantages[47–49]. These advantages and detailed ablation mechanisms are discussed in references[50–52]. Despite the fact that ablation processes are well studied and used in the synthesis of NPs, the underlying mechanisms that govern the formation of GaAs and related NPs remain unknown. PLAL is also known to be a one-of-a-kind fabrication process for producing NPs and NSs in a single experiment/exposure. However, obtaining pure GaAs NPs and NSs without forming amorphous/oxide materials is extremely difficult. To the best of our knowledge, no reports have been published in which GaAs NPs and NSs have been produced in a single exposure, particularly using picosecond lasers. Several previous studies[53,54] demonstrated the synthesis of semiconductor NSs in air using femtosecond lasers. Ionin et al.[37,55,56] recently demonstrated the antireflection properties of GaAs NSs synthesized using femtosecond (fs) laser pulses. Controlling stoichiometry and avoiding material oxidation are major challenges in all of these experiments. Similarly, Salminen et al.[57] recently demonstrated

the formation of amorphous materials alongside crystalline GaAs NPs using PLAL. In chapter 3, we also reported on the fabrication of GaAs NPs using picosecond (ps) laser ablation (Wavelength λ= 532 nm, pulse width 30 ps, repetition rate 10 Hz, and input laser energy of 15 mJ). We discovered minor amounts of oxide materials such as As_2O_3 and Ga_2O_3 coexisting with the obtained GaAs NPs[50,51]. The formation of such oxide and/or amorphous materials may have been caused by higher laser energy and certain liquid media. As a result, in order to produce simultaneously the NSs without oxidation and the NPs without amorphous materials and other phases, we performed picosecond PLAL experiments in three different liquids with a reduced laser pulse energy of 5 mJ and an input wavelength of 1064 nm. Various well-established techniques have been used to characterize these NPs and NSs in order to investigate their potential multifunctional applications in various fields.

4.1.1 Experimental Details

GaAs wafers are usually cut into 1×1 cm^2 pieces, cleaned up using normal acid cleaning processes[58], and then affixed to the bottom of a borosilicate glass beaker. Beaker containing sample was filled with 5 ml of liquid, placed on X-Y motion controller, and translated at an optimal speed of 0.1 mm/s in both X and Y directions. A raster scan of 5×5 mm^2 area is performed for each sample during the ablation (~ 40 minutes). Picosecond (ps) laser [Nd:YAG, M/s EKSPLA] ablation parameters are 30 ps pulse duration, 10 Hz repetition rate, 1064 nm wavelength, and 5 mJ laser energy. As previously indicated, the liquid medium varied, which include the distilled water (DW), ethanol, and PVA (10 mM). Figure 4.1 depicts more details about the experimental setup used in this study.

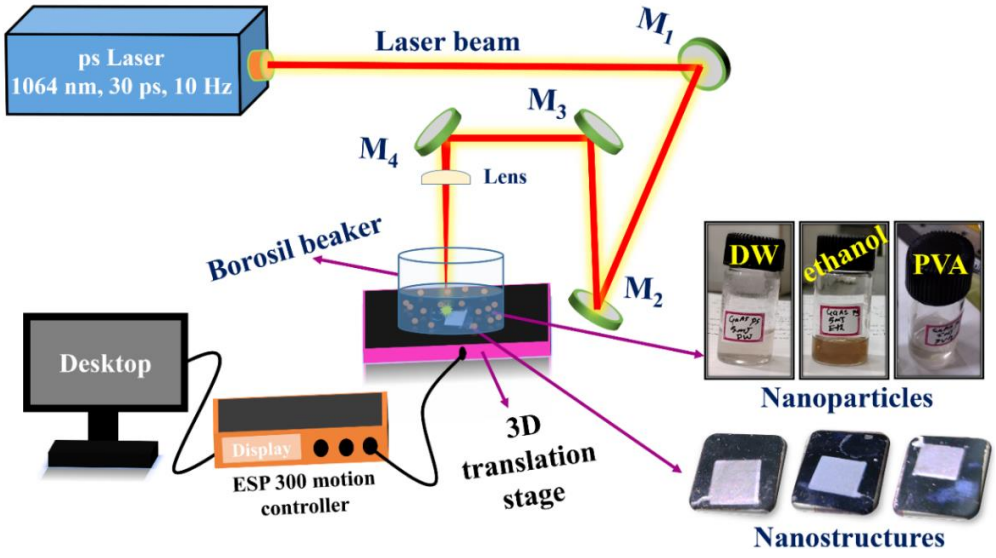

Fig. 4.1 Schematic of the laser ablation process used for the fabrication of GaAs NPs and NSs in a single experiment.

4.1.2 Results

4.1.2 (a) Morphology/Compositional analysis of GaAs NPs

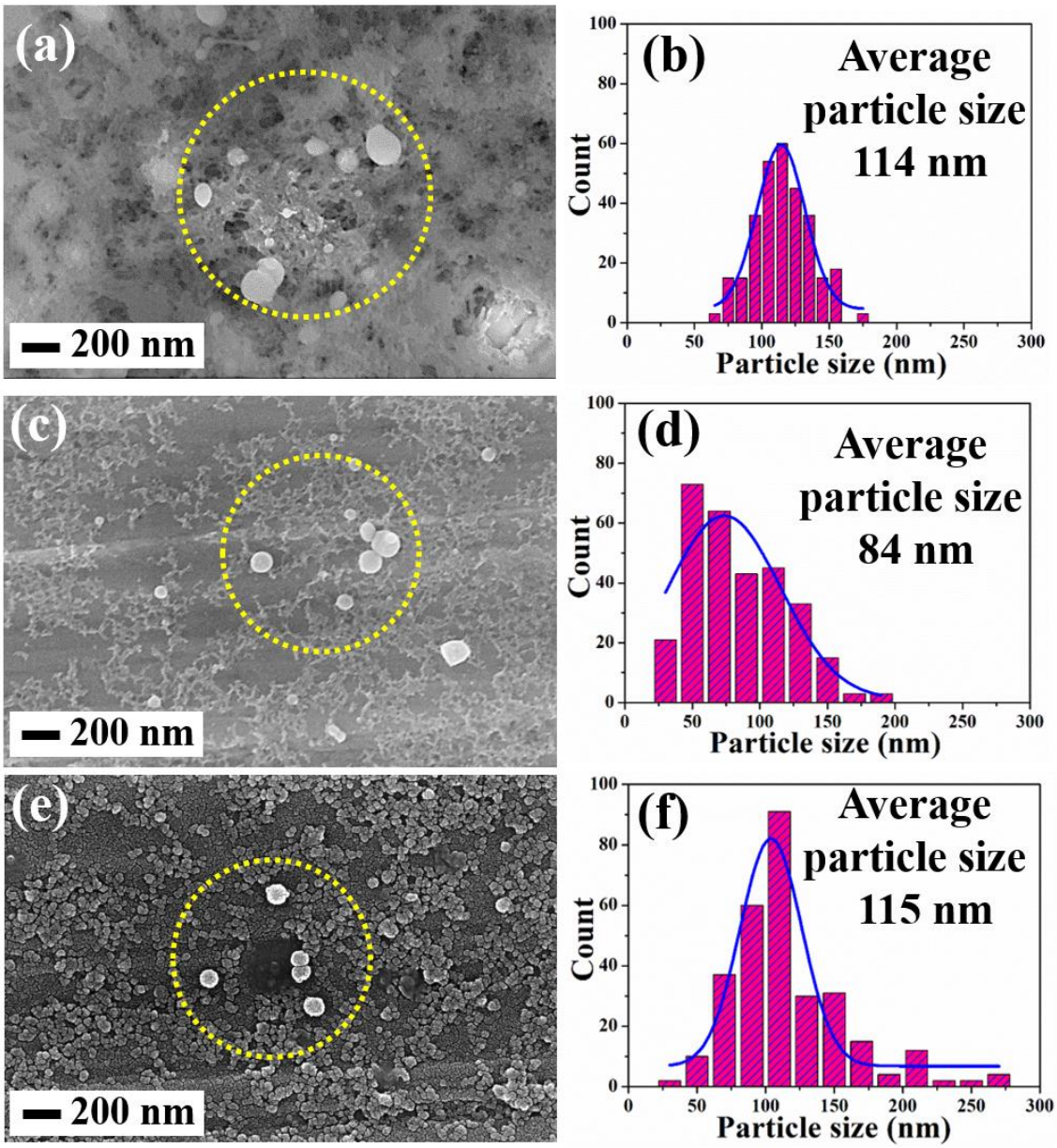

Fig. 4.2 FESEM image and their corresponding particle size distribution for GaAs NPs ablated (a, b) in DW, (c, d) in ethanol, and (e, f) in PVA, respectively. The dotted yellow circles marked in (a), (c), and (e) depict well formed, spherical GaAs NPs.

After the ablation procedure, the colloidal GaAs NPs were collected and a few milliliters of them were drop-cast onto a copper tape to prevent charging effects during the FESEM imaging; the measurements were then conducted. GaAs NPs generated in DW were depicted in Fig. 4.2 (a) and its particle size distribution was depicted in Fig. 4.2 (b). Figure 4.2 (c) depict the produced NPs in ethanol, whereas Fig. 4.2 (d) depicts the particle size distribution. The

generated NPs in PVA were displayed in Fig. 4.2 (e), with their matching particle size distribution depicted in Fig. 4.2 (f). All the dotted yellow circles in Figs. 4.2 (a), 4.2 (c), and 4.2 (e) are spherical GaAs NPs that were properly formed. With a little amount of background material, the average size of the NPs in DW was 114 nm. The average particle size of NPs produced in ethanol and PVA was 84 nm and 115 nm, respectively, with little background material. Figures 4.3 (a-c) display the spectra for the GaAs NPs and 4.3 (d-f) for the background material ablated in DW, respectively. Here, the yellow annotations on the FESEM pictures in the first column indicate the region at which EDAX was recorded, the second column displays the associated EDAX spectra, and the third column displays the quantitative findings. Figures 4.3 (g-l) and 4.3 (m-r) demonstrate the similar study performed on GaAs NPs produced in ethanol and PVA, respectively. The EDAX taken on spherical NPs produced in a colloidal solution of DW reveals the presence of entities such as Ga, As, O, and Cu, while the white background material has significant concentrations of Cu and tiny levels of As, O. As previously stated, we utilized a thick copper tape as the substrate material for drop-casting the GaAs NPs during FESEM experiments. Consequently, the presence of Cu is evident, but the presence of oxygen may be due to slight oxidation effects. Similar findings are achieved for GaAs nanoparticles generated in ethanol and PVA.

The investigation demonstrates that the spherical particles contain Cu, Ga, and As, whereas the background material has large concentrations of Cu and negligibly low concentrations of Ga/As. Therefore, it is thought that the spherical particles are GaAs nanoparticles and the white backdrop was composed of amorphous/oxide material. In ethanol, the amount of amorphous/oxide material was significantly lower than in DW, and the corresponding FESEM picture [Fig. 4.3 (j)] reveals the existence of nano-islands. In PVA, this type of background material was not detected, although minute particles can be seen in the background. However, EDAX study performed in this location did not reveal significant Ga and As concentrations. Consequently, these particles may be part of the sputtered gold covering [see Figs. 4.3 (p-r)] applied on this PVA sample to prevent charging effects during FESEM observations. It is important to highlight that other samples evaluated in this study do not require this gold coating.

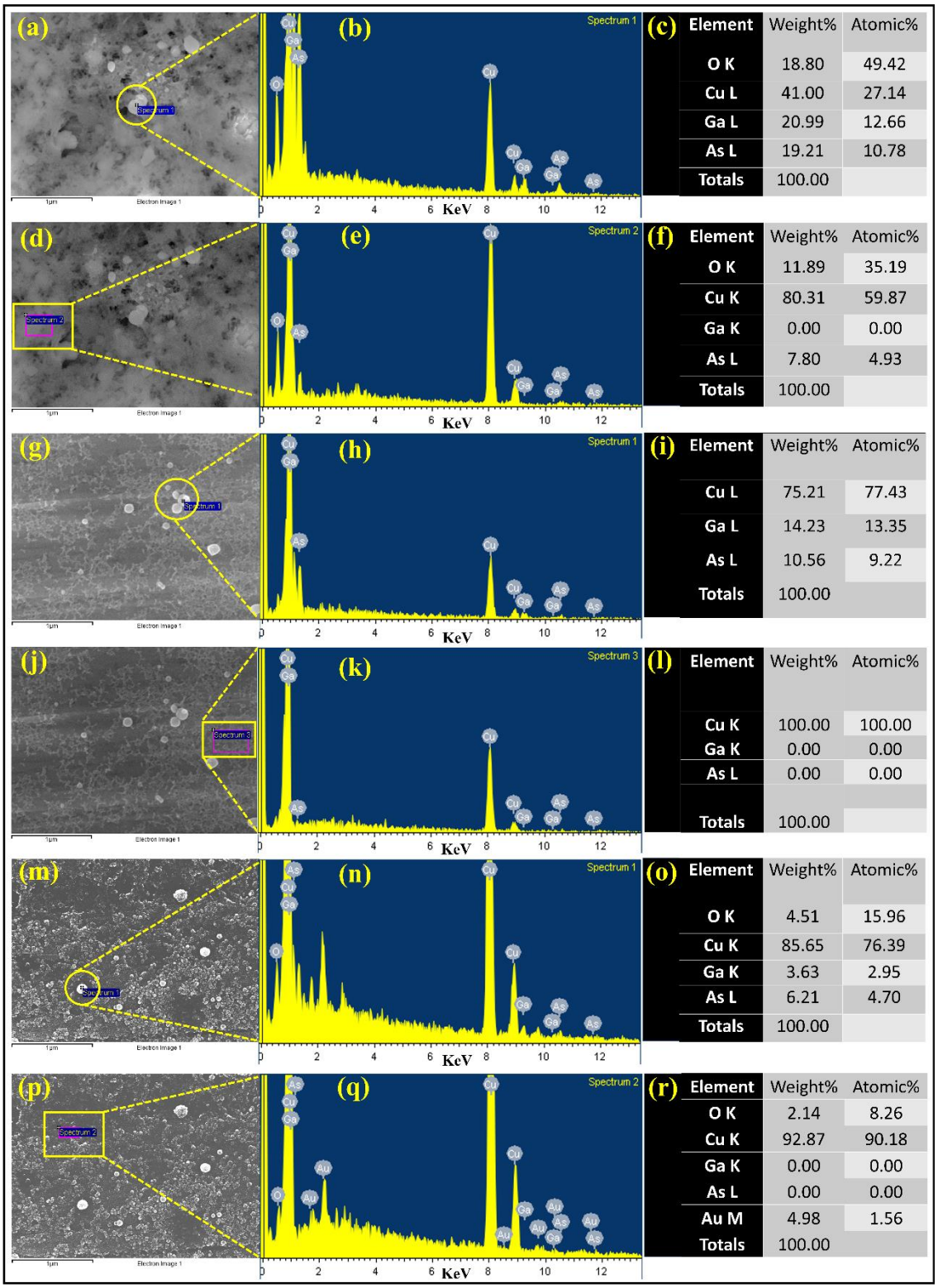

Fig. 4.3 (a-c) EDAX analysis of GaAs NPs produced in DW and (d-f) its background material (Yellow annotations on the FESEM images in first column represents location at which EDAX is recorded). Similarly, (g-l) for GaAs NPs and background material produced in ethanol, and (m-r) for GaAs NPs and background material produced in PVA.

Figures 4.4 (a, b) illustrate the TEM image and SAED pattern of GaAs NPs ablated in DW, respectively. While 4.4 (c, d) demonstrate the same for GaAs NPs obtained in ethanol and 4.4 (e, f) for GaAs NPs obtained in PVA. In comparison to DW, ethanol and PVA produced a higher density of particles. In addition to GaAs NPs, an amorphous background material was also found in these samples, with a greater concentration in DW and a quantitative reduction in ethanol and PVA. This matches with FESEM analysis. The SAED study presented in Fig. 4.4 clearly reveals that the generated particles belong to the polycrystalline ambient stable phase of GaAs. The cubic (Zinc blend) phase of GaAs comprises the crystalline planes (4 2 2), (5 1 1) for NPs created in DW, (1 1 1), (2 2 0), and (3 1 1) for NPs produced in ethanol, and (1 1 1), (2 2 0), and (3 1 1) for NPs produced in PVA (ICDD: 00-014-0450 and ICDD: 01-079-0614). Figure 4.5 (a) depicts the Raman study done on the bulk GaAs wafer. Further, the generated GaAs NPs are drop-casted onto a copper strip to perform Raman measurements. The spectra depicting the Raman modes of NPs generated in DW [panel (b)], ethanol [panel (c)], and PVA [panel (d)] are presented in Figure 4.5. In each image, three curves depict the spectra acquired at three random positions on the same sample in order to evaluate the signal's consistency. As the spot size of the incoming 532 nm laser beam is ~ 0.72 µm ([see fig. 4.2 (b)]), we anticipate that the presence of a combination of a few NPs and the background material has been investigated in this work. The spectra obtained from three distinct places validate the accuracy of these findings. Observed spectra for NPs in DW have peaks at 190 cm^{-1}, 245 cm^{-1}, 264 cm^{-1}, and 286 cm^{-1} at all three locations on the sample. These peaks at 264 cm^{-1} and 286 cm^{-1} are assigned to the TO and LO modes of crystalline GaAs NPs, whereas the peaks seen at 245 cm^{-1} and 190 cm^{-1} are attributed to amorphous GaAs and amorphous 'As' present on the sample, respectively. Recent results published by Salminen et al.[57] are in perfect accord with this observation. In the majority of measurements taken at various places on the sample, the spectra for NPs produced in ethanol and PVA contain the TO (264 cm^{-1}) and LO (286 cm^{-1}) modes only; however, a few sites show peaks that correspond to oxide material. Therefore, it is evident that amorphous materials are more in the DW and that their concentration in ethanol and PVA solutions is negligible.

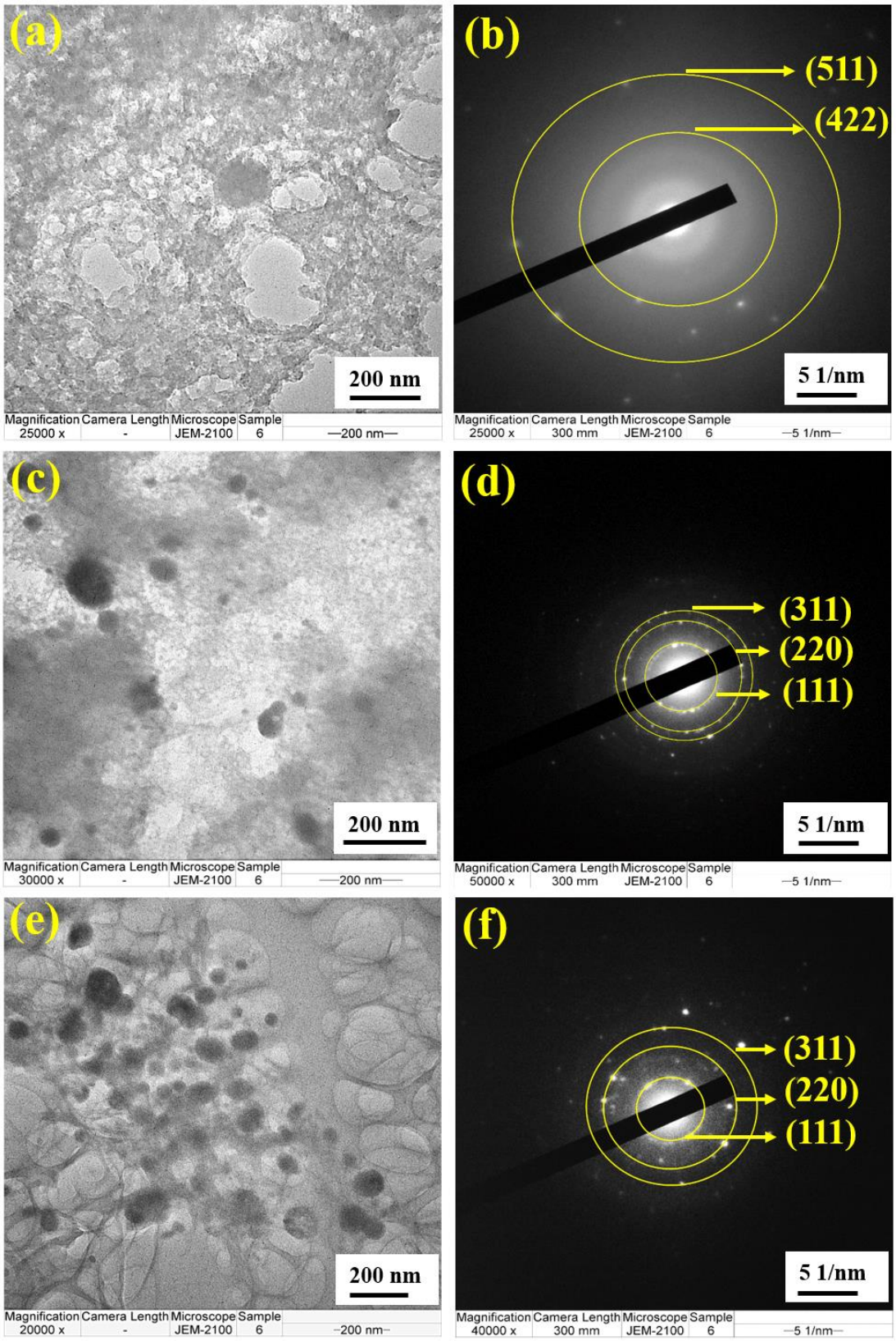

Fig. 4.4. TEM image, corresponding SEAD pattern of GaAs NPs ablated (a, b) in DW, (c, d) in ethanol, and (e, f) in PVA, respectively.

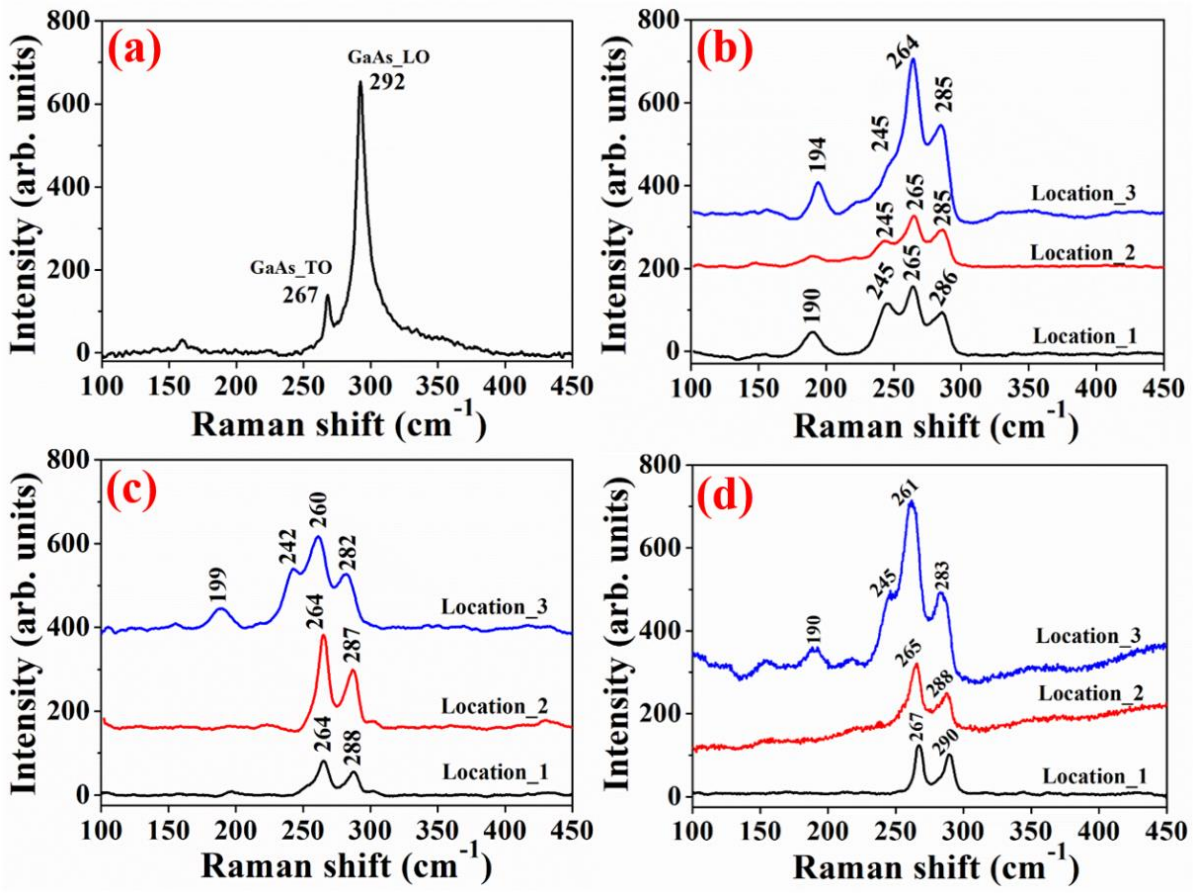

Fig. 4.5 Raman spectra of (a) bulk GaAs, (b) GaAs NPs produced in DW, (c) GaAs NPs produced in ethanol, (d) GaAs NPs produced in PVA. The legends given, i.e., location 1, 2, & 3 represent spectra recorded at three random locations on the same sample.

The TO and LO modes of the bulk GaAs substrate are 267 cm^{-1} and 292 cm^{-1}, respectively. The observed change in the TO and LO modes of NPs may be attributable to the stress caused by the ablation procedure. As shown in past works[59,60], this change in the Raman modes is well-known and understood for nano-entities and strained surfaces. Overall, the FESEM, TEM, and Raman results indicate that the colloidal solutions generated by ablation of GaAs in DW, ethanol, and PVA resulted in polycrystalline spherical GaAs NPs, although a small amount of amorphous material is visible in DW. PVA is the optimal solvent for the manufacture of GaAs nanoparticles without the formation of amorphous oxide. It has been shown that ethanol is preferred to DW in terms of high production yield of nanoparticles and lower yields of amorphous material. These observations are consistent with the microscopy analysis presented in previous section.

4.1.2 (b) Optical Studies of GaAs NPs

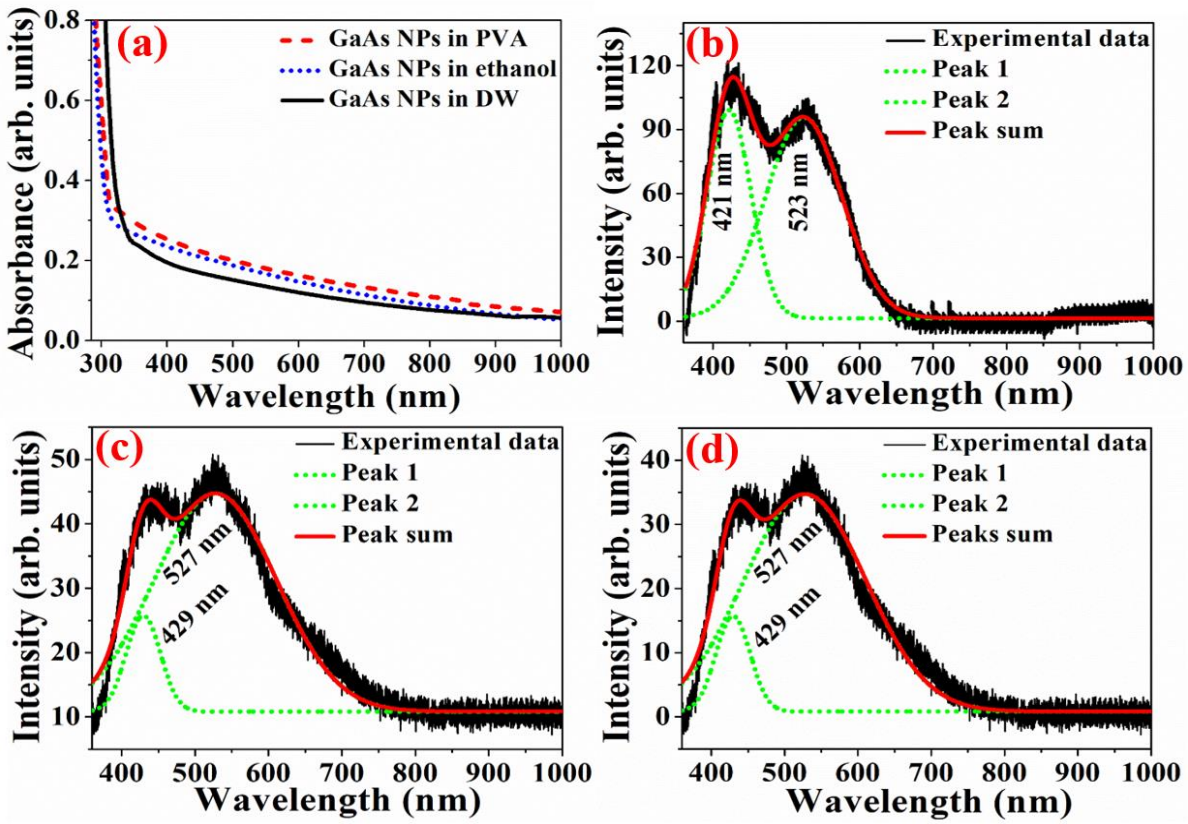

Fig. 4.6 (a) UV-Visible-NIR absorption spectra of GaAs NPs obtained in DW (solid black line), ethanol (dotted blue line), and PVA (dashed red line), (b-d) PL emission spectra of GaAs NPs ablated in DW, ethanol, and in PVA, respectively.

As shown in Fig. 4.6 (a), the generated colloidal solutions have an optical absorption edge at ~310 nm, which was in good agreement with our prior results[50] and published literature[61]. Comparing the absorption edge at shorter wavelengths to that of bulk GaAs absorption (as reported in the literature) demonstrates that the band gap of these NPs increases when they are transformed from bulk to nano-form. These colloidal solutions are drop-cast onto copper foils, and photoluminescence (PL) spectra are then recorded using a laser excitation of 325 nm. PL was observed in the range of 400-600 nm, two deconvoluted curves at 421 nm and 523 nm for GaAs NPs in DW, 429 nm and 527 nm for NPs in ethanol, and 429 nm, 527 nm for NPs in PVA, as depicted in Figs. 4.6 (b-d), respectively. The solid/black lines in the picture reflect the experimental data, the solid/red lines indicate the equivalent Gaussian fits, and the dotted/green lines represent the deconvoluted peaks derived from the experimental data. There are two possible causes for the two luminescence peaks observed here: (i) particles with different sizes, and (ii) emission from defect levels. These findings are consistent with those of Salminen et

al.[57] and Malik et al.[62]. Future systematic research employing time-resolved PL measurements will be designed to better study the specific origin of these PL peaks.

4.1.2 (c) Femtosecond NLO Studies

Z-scan is a promising NLO approach developed by Sheik Bahae and colleagues[63] for identifying the magnitude/sign of the real/imaginary components of the third order NLO susceptibility [$\chi^{(3)}$]. We have conducted our investigations using the two-photon absorption (TPA) model, where the transmittance of the output beam varies based on the following equations.

$$\boldsymbol{Transmittance, T_{OA(2PA)}} = \frac{\mathbf{1}}{\mathbf{1}+\boldsymbol{\beta L_{eff}}\left(\frac{\boldsymbol{I_{00}}}{\mathbf{1}+\left(\frac{\boldsymbol{z}}{\boldsymbol{z_0}}\right)^{\mathbf{2}}}\right)} \qquad \text{..... [4.1]}$$

In case of closed aperture configuration, it is as follows

$$\boldsymbol{Transmittance, T_{CA(2PA)}} = \left(\mathbf{1} \pm \left(\frac{\mathbf{4}\left(\frac{\boldsymbol{z}}{\boldsymbol{z_0}}\right)\boldsymbol{\Delta\Phi}}{\left[\mathbf{9}+\left(\frac{\boldsymbol{z}}{\boldsymbol{z_0}}\right)^{\mathbf{2}}\right]\left[\mathbf{1}+\left(\frac{\boldsymbol{z}}{\boldsymbol{z_0}}\right)^{\mathbf{2}}\right]}\right)\right) \qquad \text{..... [4.2]}$$

Here, Beam waist at (z=0) focal point $\omega_0(mm) = \frac{f.\lambda}{\pi.d}$, the sample effective length is calculated by $L_{eff}(cm^{-1}) = \frac{1-e^{-\alpha L}}{\alpha}$ (TPA), the Rayleigh Range $z_0(mm) = \frac{\pi\omega_0^2}{\lambda}$, where 'd' is the laser beam waist at lens and 'λ' is the wavelength. Precisely, the intensity dependent NLO refractive index part, extracted out from the fitted data, is related to the phase-shift, $as\ n_2(\frac{cm^2}{W}) = \frac{\Delta\Phi}{I_{0.}\,L_{eff.}\,k} = \frac{\Delta\Phi.\lambda}{I_{0.}L_{eff.}\,2\pi}$. Finally, we get an estimation about both real and imaginary parts of NLO susceptibility, $\chi^{(3)}$, from the following mathematical correlations as $Im\left|\chi^{(3)}\right|(m^2/V^2) = \frac{c\epsilon_0\lambda n_0^2\alpha_2(m/W)}{2\pi}$, $Re\left|\chi^{(3)}\right|(m^2/V^2) = 2c\epsilon_0 n_0^2 n_2\,(m^2/W)$.

In the current investigation, the fs NLO measurements were performed on three distinct colloidal samples containing GaAs NPs those were ablated in DW, ethanol, and PVA. Corresponding data is shown in Figs. 4.7, 4.8, and 4.9, respectively, for GaAs NPs in DW, ethanol, and PVA. By fitting the experimental data with theory, we were able to extract the magnitudes of various NLO coefficients, including the two-photon absorption coefficient [β (cmW^{-1})], nonlinear refractive index n_2 (cm^2W^{-1}), two-photon absorption cross section σ_{TPA} (GM), and third-order NLO susceptibility [$\chi^{(3)}$]. All colloidal forms of NPs exhibited the reverse saturable absorption (RSA) response, which corresponds to two-photon absorption in

the case of an open aperture configuration. In the case of Z-scan data with a closed aperture, we found peak-valley transmittance curves, revealing a negative NLO refractive index.

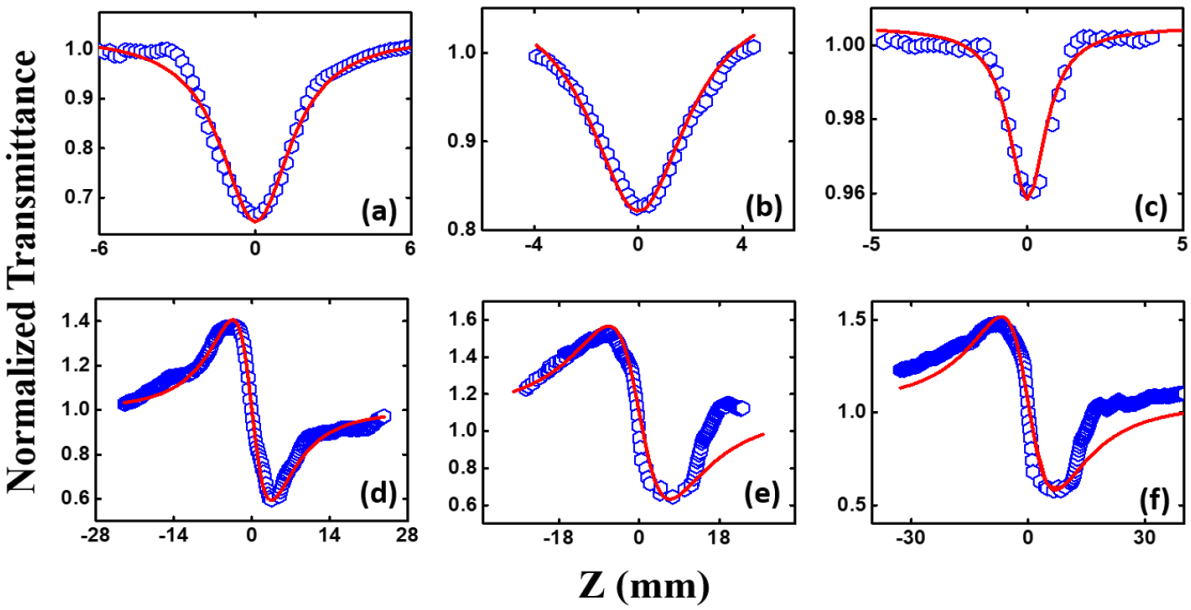

Fig. 4.7 Z-scan data of GaAs NPs in DW recorded at wavelengths 800 nm, 850 nm, 900 nm, (a-c) in OA mode & (d-f) in CA mode, respectively. The hexagonal (blue) bubble curves represent the experimental data and solid red curves represent theoretically fitted data.

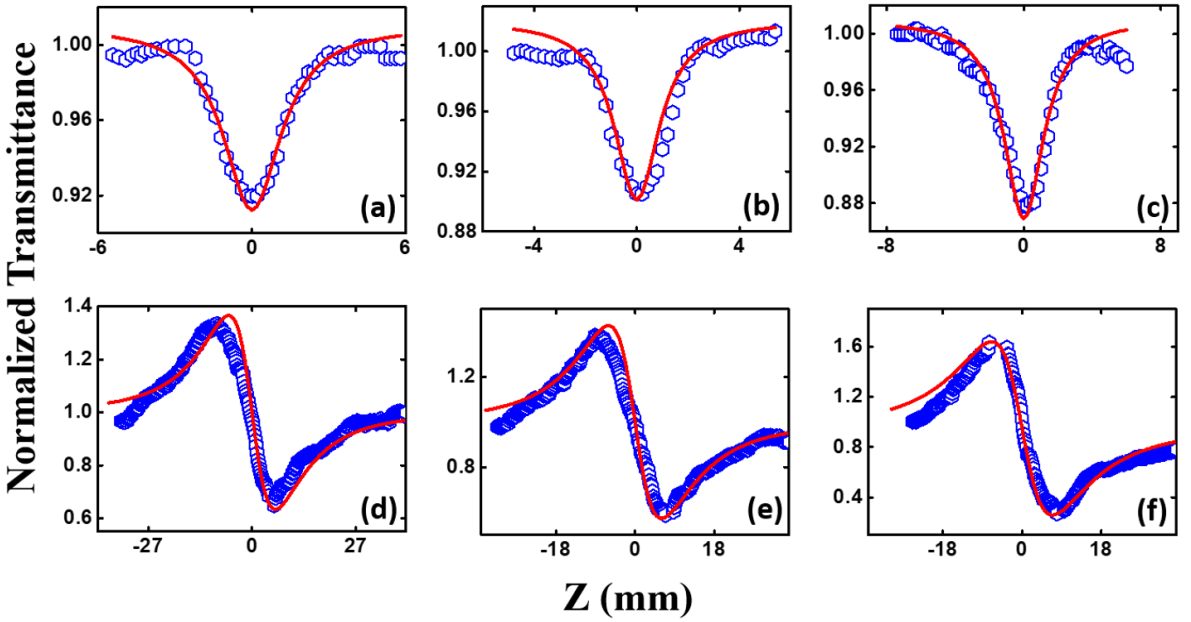

Fig. 4.8 Z-scan data of GaAs NPs in ethanol recorded at wavelengths 800 nm, 850 nm, 900 nm, (a-c) in OA mode & (d-f) in CA mode respectively. The hexagonal (blue) bubble curves represent the experimental data and solid red curves represent theoretically fitted data.

Table 4.1 Nonlinear optical parameters calculated from the experimental data, where (λ) wavelength of the laser, (β) two photon absorption coefficients, (σ_2) two photon absorption cross section, [$\chi^{(3)}$] nonlinear susceptibility, and (n_2) nonlinear refractive index.

Sample Name	λ (nm)	β×10^{-8} (cmW^{-1})	σ_2 (GM) ×10^6	Im ($\chi^{(3)}$) ×10^{-11} (e.s.u.)	n_2×10^{-11} (cm^{2}W^{-1})	Re ($\chi^{(3)}$) ×10^{-10} (e.s.u.)	Total ($\chi^{(3)}$) × 10^{-10} (e.s.u.)
GaAs NPs in DW	800	2.8	2.3	1.2	1.1	7.1	7.2
	850	13	10.1	5.7	1.5	9.8	9.8
	900	25	18.3	11.5	1.9	12.1	12.2
DW	-	0.7	-	-	-	-	-
GaAs NPs in Ethanol	800	4.5	3.7	1.9	1.1	6.4	6.4
	850	5.5	4.3	2.4	1.4	8.9	9
	900	6.8	5	3.1	2.6	16.6	17.1
Ethanol	-	0.4	-	-	-	-	-
GaAs NPs in PVA	800	40	33	16.4	0.6	4	4.3
	850	130	101	56.6	1.13	7.2	9.2
	900	280	205	129	1.65	10.6	16.7
PVA	-	5.5	-	-	-	-	-

Figures 4.7 (a-c) depict the Z-scan results acquired in open aperture mode for the GaAs NPs in DW. By adjusting the input wavelength (800-900 nm) in the near-infrared region, the values were observed to increase from 2.8×10^{-8} cmW^{-1} to 25×10^{-8} cmW^{-1}. These NPs have demonstrated much improved nonlinearity at longer wavelengths, making them a possible contender for photonic applications in the near-infrared range. The two-photon absorption cross sections (σ_2) have been computed to be in the region of 10^6 GM and are observed to rise with increasing IR wavelength. At 900 nm, it is observed to be the greatest with a value of 18.3×10^6 GM. Similarly, the NLO refractive index data are depicted in figures 4.7 (d-f), revealing an obvious negative tendency and the extracted n_2 magnitudes are tabulated in table 4.1. The NLO susceptibilities with respect to probe wavelength have been calculated and are listed in Table 4.1. We estimate that the NLO coefficients and cross-sections reported here

have a deviation of 5%. Mostly, the deviation in NLO coefficients may arise due to (a) input laser intensity variations (b) estimation of input peak intensities (c) fitting procedures etc.

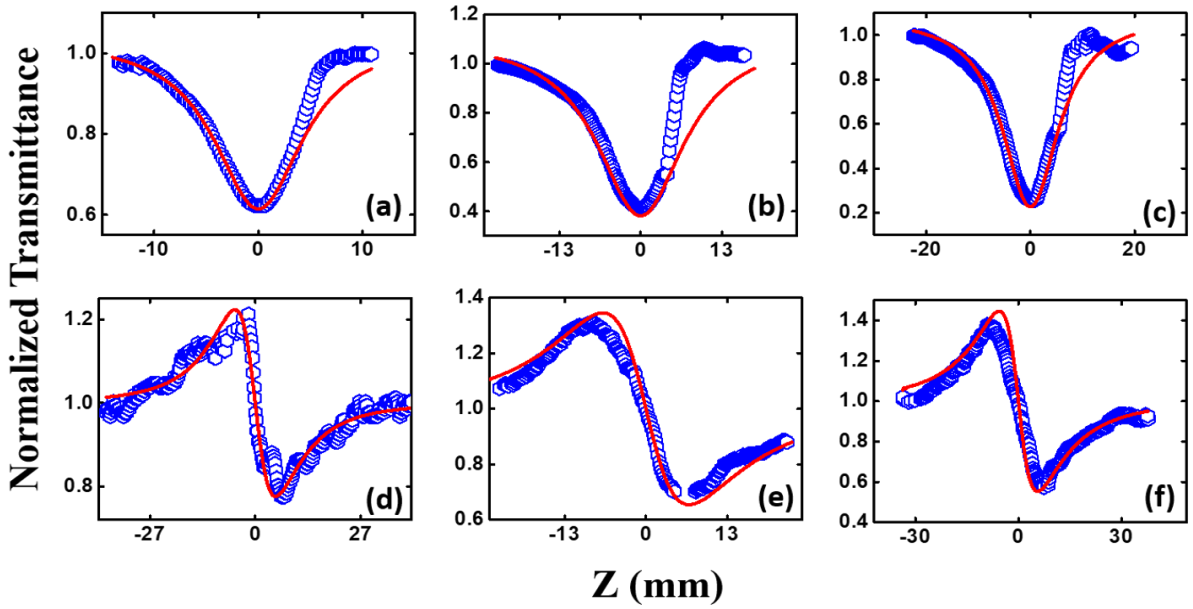

Fig. 4.9 Z-scan data of GaAs NPs in PVA recorded at wavelengths 800 nm, 850 nm, 900 nm, (a-c) in OA mode & (d-f) in CA mode respectively. The hexagonal (blue) bubble curves represent the experimental data and solid red curves represent theoretically fitted data.

Figure 4.8 depicts the entire NLO data for GaAs NPs colloids in ethanol solvent. Specifically, figures 4.8 (a-c) depict the Z-scan data collected in open aperture mode. β values have varied from 4.5×10^{-8} cmW^{-1} to 6.8×10^{-8} cmW^{-1} in response to diverse excitation wavelengths between 800 nm and 900 nm. The computed two-photon absorption cross sections (σ_2) found to be in the region of 10^6 GM. The greatest value of σ_2, 5×10^6 GM, corresponds to an excitation wavelength of 900 nm. The magnitudes of the retrieved n_2 data are determined to be 10^{-11} cm^{2}W^{-1} after fitting the NLO curves depicted in figures 4.8(d-f). Calculated NLO susceptibilities for each excitation wavelength are reported in Table 4.1. Furthermore, the entire open aperture data for the GaAs colloidal sample in PVA is shown in figures 4.9 (a-c). Correspondingly, values have been reported to vary from 40×10^{-8} cmW^{-1} to 280×10^{-8} cmW^{-1}, and σ_2 values have been recorded to increase from (33–205) $\times10^6$ GM. Figures 4.9 (d-f) depict the entire closed aperture NLO data for the GaAs in PVA sample. The measured n_2 values are of the order ~10^{-11} cm^{2}W^{-1}. The coefficients and cross-sections derived from a comprehensive data analysis have been included in Table 4.1. To elucidate the minor contribution of the various solvents utilized, the equivalent NLO data for pure solvents have been recorded and their magnitude has been elucidated in the same Table 4.1. GaAs nanoparticles have

demonstrated intriguing NLO behavior in terms of a greatly increased NLO response with a red-shifted pump beam, making them promising candidates for optical limiters and photonic devices operating in the near-infrared zone. The NLO coefficients of GaAs NPs in PVA were found to be at least 1-2 orders of magnitude greater than those of Ag-TiO_2 NPs generated by femtosecond ablation and investigated using the same experimental setup[15].

4.1.3 Summary of GaAs NPs

In this study, PLAL was utilized to produce GaAs NPs in three distinct liquids: DW, ethanol, and PVA. Using FESEM, TEM, and Raman spectroscopic studies, their shape and composition are comprehensively analyzed. According to FESEM (Fig. 4.2) and EDAX (Fig. 4.3) observations, the spherical particles in each sample are composed of 'Ga' and 'As'. For NPs generated in a colloidal solution of DW, the presence of background material and oxygen is noticed, but it is negligible in the other two samples. According to the TEM results depicted in Fig. 4.4, NPs in the colloidal solution of DW have a more amorphous background that is successively decreased in ethanol and PVA. Raman investigation [Fig. 4.5] demonstrates that the NPs in DW (spectra collected at three random positions on the sample) display Raman modes corresponding to the amorphous oxide material (194 cm^{-1} and 245 cm^{-1}) in addition to the TO (267 cm^{-1}) and LO (292 cm^{-1}) modes of GaAs. In contrast, for NPs in ethanol and PVA, just a few of locations exhibit modes matching to amorphous material. In the GaAs PLAL, in addition to the spherical GaAs NPs, more amorphous background material is generated in the colloidal solution of DW than in the colloidal solutions of ethanol and PVA. Due to the presence of polymer chains in the PVA solvent the laser intensity may not be adequate to disrupt polymer chain bonds, hence the formation of amorphous/oxide material in PVA solvent is minimal. The most important finding obtained (NLO data) demonstrates that colloidal GaAs NPs exhibit a definite two-photon absorption in the aforementioned solvents, with the two-photon absorption coefficient (β) increasing with increasing irradiance wavelength. These NLO characteristics and coefficients of the generated GaAs NPs can be used for applications in second harmonic generation (SHG), Terahertz generation (THz), optical communications, and integrated photonic circuits, among others.

Now, as part of this laser ablation process to create NPs, there is a formation of surface structures on the ablated GaAs target material. These surface structures are thoroughly analyzed and presented in the next sections of this thesis.

4.1.4 Morphology and compositional analysis of GaAs NSs

Intriguingly, GaAs substrates exhibit quasiperiodic NSs following ablation in the aforementioned three solvents for the formation of NPs. Figure 4.10 depicts three different magnifications of the concurrently created NSs on GaAs substrates ablated in (a-c) DW, (d-f) ethanol, and (g-i) PVA. The periodicity/quality of structures ablated in DW appears to be superior to that of other samples [see Figure 4.10 (c)], although a large number of self-decorated particles are observed on NSs generated in PVA solvent [see Fig. 4.10 (i)].

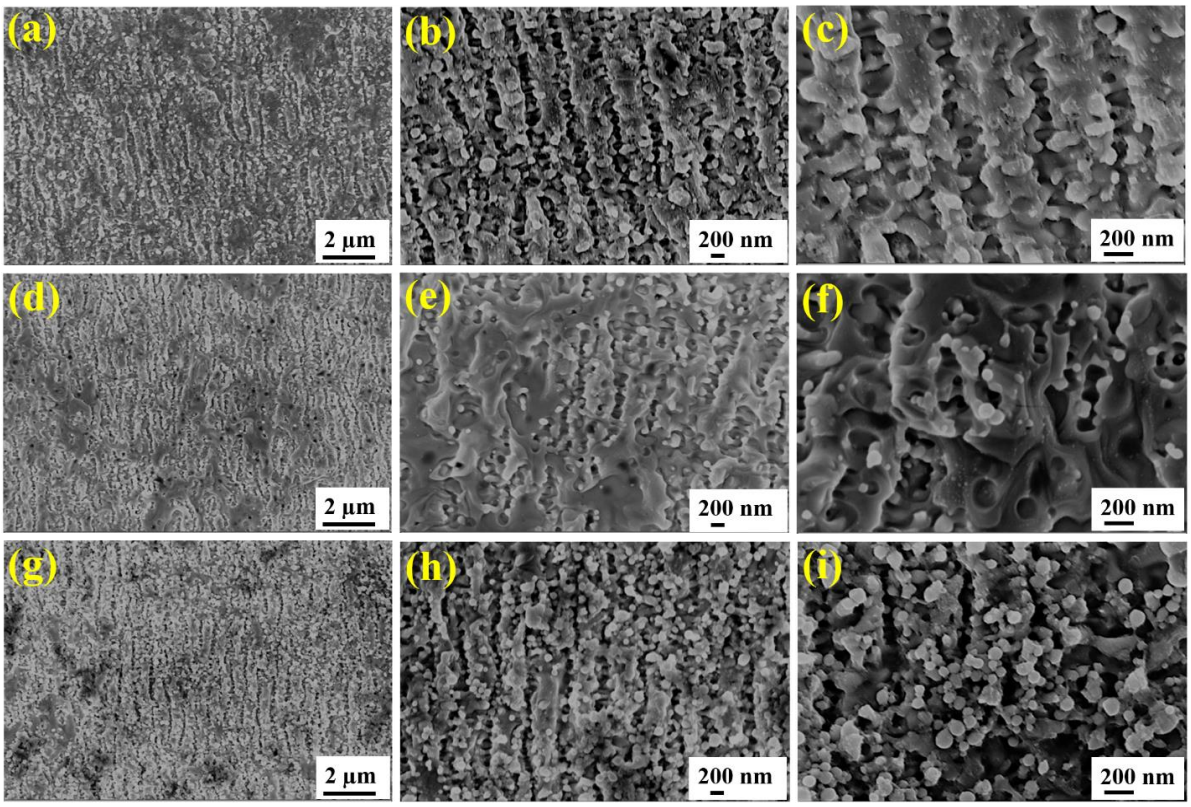

Fig. 4.10 FESEM images recorded at three different magnifications (a-c) for GaAs NSs synthesized in DW, (d-f) for GaAs NSs synthesized in ethanol, and (g-i) for GaAs NSs synthesized in PVA.

The composition of Ga and As in all three samples is depicted by the EDAX data displayed in Fig. 4.11. Figure 4.11 (a) depicts the spot on the FESEM picture where EDAX is captured, whereas Fig. 4.11 (b) depicts the EDAX spectrum, with the inset of (b) displaying the composition table for NSs formed in DW. Similarly, the FESEM image and EDAX spectra for NSs created in ethanol and in PVA are depicted in Fig. 4.11 (c-d) and Fig. 4.11 (e-f), respectively. Ga to As ratios are about 1.12, 1.05, and 1.10 for GaAs NSs in DW, ethanol, and PVA, respectively. Interestingly, no hints of an oxide are found in these samples, this may be attributed to a fact that the ablation is done in liquid media. The formation of these

quasiperiodic NSs on GaAs substrate may be explained by analyzing the laser-matter interaction between the picosecond pulses and the GaAs material in great detail.

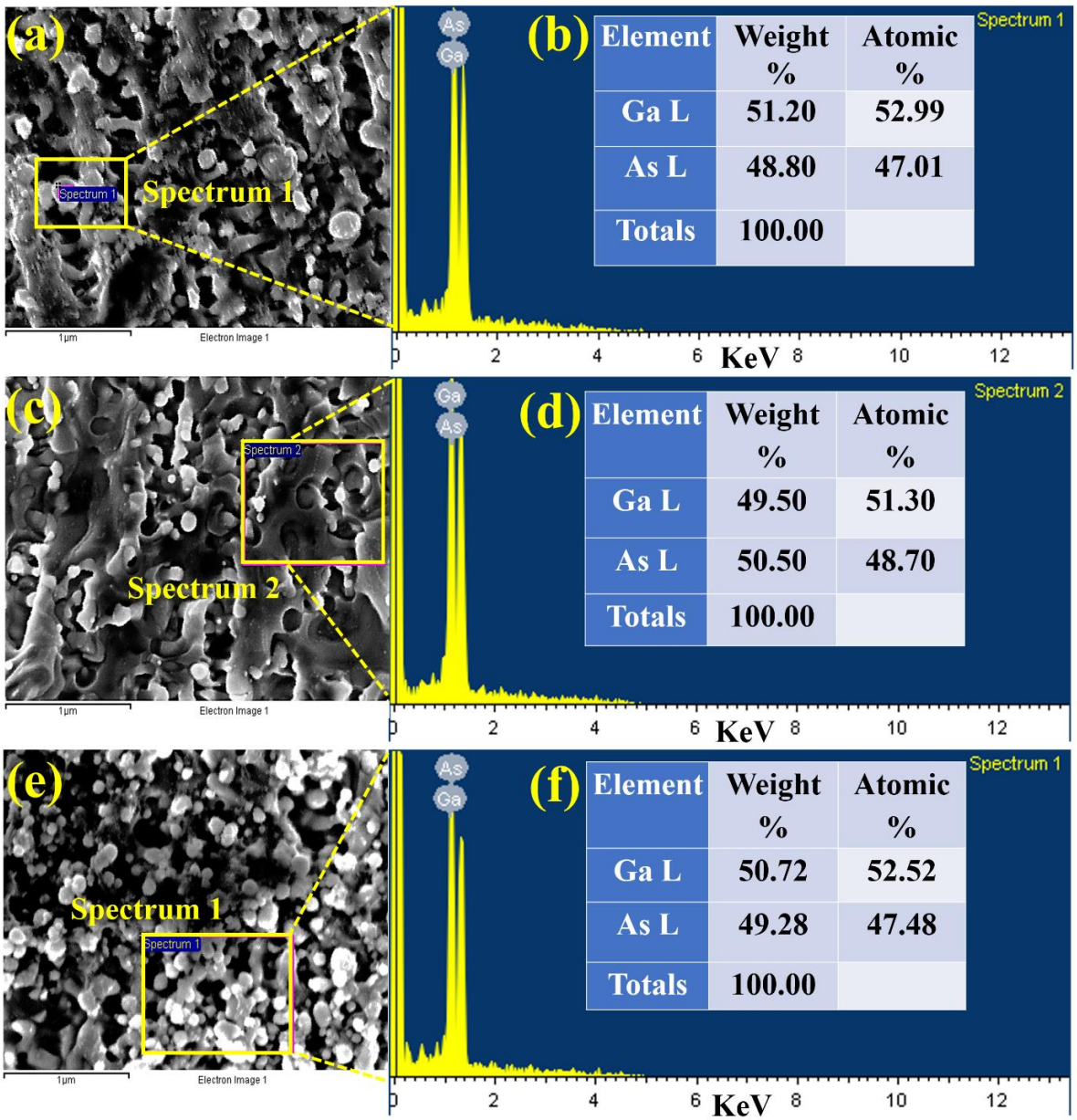

Fig. 4.11 (a) FESEM image, the rectangular yellow box indicates the location at which EDAX is recorded, (b) its corresponding EDAX spectrum and the inset of (b) shows the table of composition for GaAs NSs synthesized in DW. Similarly, (c, d) EDAX analysis for GaAs NSs synthesized in ethanol, and (e, f) EDAX analysis for GaAs NSs synthesized in PVA.

Existing theories for explaining laser-induced periodic surface structures (LIPSS) on metals, semiconductors, and dielectrics come into two broad categories: (1) matter reorganization models and (2) electromagnetic field models. For the matter rearrangement effects, even longer timescales are required for the material to melt and move away from the produced grooves.

Bonse et al.[64] have published the time scale necessary to transfer material over a molten layer radially across a distance of L (accounting for the Marangoni effect given in ref [64]) and it is given as

$$\tau_M = (\mu \times L^2)/(|\gamma_T| \times T_m \times h_m) \quad \ldots\ldots [4.3]$$

Where, L, μ, $|\gamma_T|$, T_m, and h_m represent, respectively, the radial distance, dynamic viscosity, absolute temperature coefficient of surface tension, the melting temperature, and the melt depth (of the molten material), respectively. We have estimated the value of τ_M for the GaAs NSs created in this work by using L ~160 nm (half of the periodicity), μ ~2.5×10^{-3} Nsm^{-2}, $|\gamma_T|$ ~0.18×10^{-3} Nm^{-1}, T_m ~1511 K, and h_m ~80 nm (depth of the molten layer is considered as RMS roughness of the NSs formed)[65–67]. The obtained value of τ_M is 2.9 ns, but the laser utilized in the current experiment generates ps pulses (30 ps), which are at least two orders of magnitude shorter than the time necessary to move molten material (τ_M) assuming material reorganization theory is applicable to these structures. Hence, material reorganization models alone don't explain for our structures. Consequently, the production processes of these GaAs NSs may be described by electromagnetic effects such as surface electromagnetic waves (SEWs)/surface plasmon polaritons (SPPs), which can exactly explain the generation and direction of NSs. The laser's incoming electromagnetic field interacts (interferes) with fields dispersed by surface roughness or emitted by SPPs, resulting in the periodic loss of laser energy[64,68]. In turn, this results in the creation of sub-wavelength periodic surface patterns with significantly lower periodicity than the laser's wavelength. In this study, the created NSs had an average periodicity (∧) of 320 nm, which is much shorter than the laser's wavelength (i.e., ∧ <λ/3, where λ ~1064 nm). In addition, the orientation of the ripples depends up on the polarization of the laser. On the basis of the periodicity and direction of the produced NSs, the LIPSS can be either LSFL or HSFL. Periodicity (∧) larger than λ/2 results in LSFL, whereas periodicity less than λ /2 results in HSFL. Therefore, the GaAs NSs created in this study can be referred to be quasi-periodicity HSFL structures. This is the first study to our knowledge on the simultaneous production of GaAs NPs and NSs using picosecond laser pulses. Using adequate laser settings and solvent refractive index, the quality of NSs may be further tweaked and refined.

Figure 4.12 (a) depicts the existence of both the TO and LO modes of GaAs at 263 cm^{-1} and 286 cm^{-1}, respectively, for NSs manufactured in DW (black line, curve I). Similarly, similar modes were found at 264 cm^{-1} and 287 cm^{-1} for GaAs NSs in ethanol (red line, curve II), and at 265 cm^{-1} and 288 cm^{-1} for NSs generated in PVA (blue line, curve III) [figure 11(b)]. The laser-induced damage on the surface of the NSs may account for the difference between the

LO and TO modes of bulk GaAs and those of NSs. Within the ablated NSs themselves, a minor shift of 1 cm^{-1} is seen from sample to sample, which may be attributable to the difference in stress across samples.

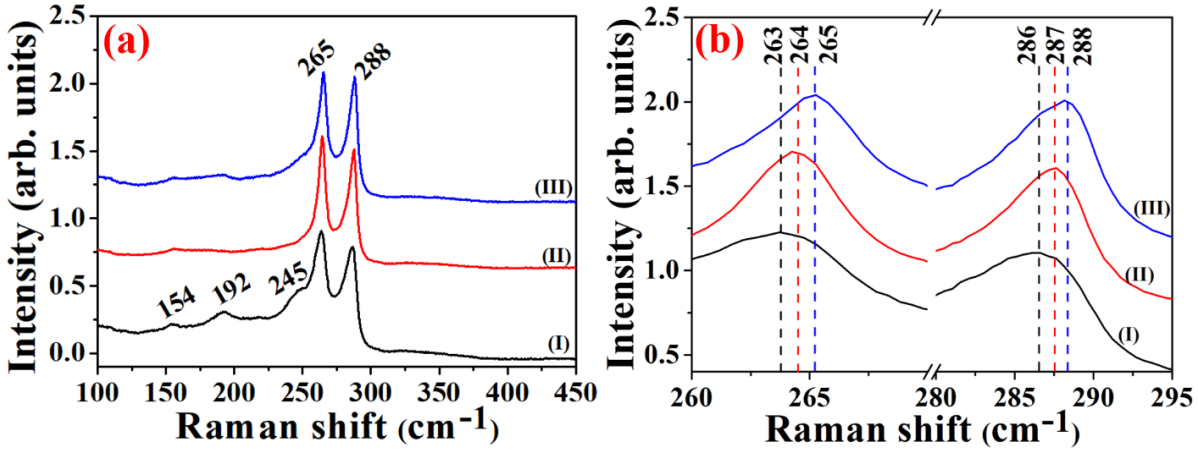

Fig. 4.12 (a) Raman spectra of GaAs NSs formed in DW, ethanol, and PVA represented in solid black line (curve I), solid red line (curve II), and solid blue line (curve III), respectively. (b) Magnified view of (a) shown in the range from 255 cm^{-1} to 300 cm^{-1}.

4.1.5 Wettability study on GaAs NSs

Figure 4.13 (a) depicts the results acquired from contact angle measurements done on the pure GaAs sample, whereas Figs. 4.13 (b-d) exhibit contact angles on the structures generated in DW, ethanol, and PVA, respectively. The pure GaAs sample exhibits a contact angle of 88.5º, which is consistent with Rajan et al.[69] finding. The NSs created in DW exhibited an increase in contact angle of about 9º (i.e., 97.5 º), but the NSs produced in ethanol exhibited no change compared to the pristine sample (i.e., 88.5 º), and the NSs produced in PVA exhibited a further decrease of 14º (i.e., 74.5 º). Here, the nature of the GaAs NSs in PVA changed from hydrophobic to hydrophilic, whilst the other two NSs exhibited no change. The high quantity of NPs self-decorated on GaAs NSs generated in PVA may be associated with this phenomenon [see Fig. 4.10 (i)]. According to the Wengel model[70], surface wettability is assumed to rely on the sample's shape and roughness. Consistent with the Wengel model, it is discovered that GaAs NSs with greater number of decorated NPs/roughness are hydrophilic in nature.

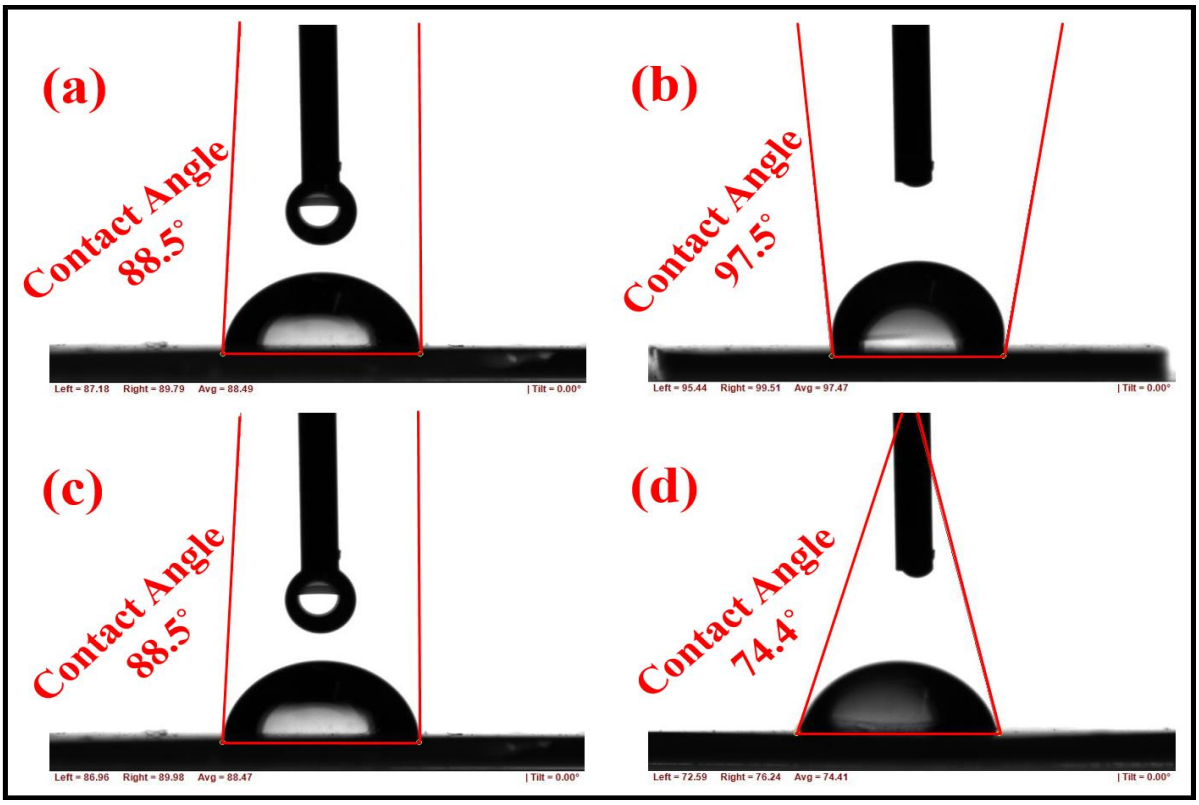

Fig. 4.13 Contact angle measurements of (a) GaAs bulk substrate, (b) GaAs NSs formed in DW, (c) GaAs NSs formed in ethanol, and (d) GaAs NSs formed in PVA.

4.1.6 Broad band and wide-angle anti-reflective nature of GaAs NSs

Figure 4.14 (a) depicts the reflectance spectra recorded at an incidence angle of 30° (detector positioned at 60°) for the pristine GaAs substrate (black line, curve 1), GaAs NSs in DW (red line, curve 2), GaAs NSs in ethanol (blue line, curve 3), and GaAs NSs in PVA (green line, curve 4). Figure 4.14 (b) depicts reflectance measured at an incidence angle of 45° (detector positioned at 90°), whereas Figure 4.14 (c) depicts reflectance recorded at an incidence angle of 60° (detector positioned at 120°). The reflectance of the pristine sample is generally 50-60% at all incidence angles, but the reflectance of the structured surfaces is 0-5% at 30° incidence, 5-10% at 45° incidence, and 10-20% at 60° incidence. The signature of the reflectance spectra of a pure GaAs sample matches the findings provided by Kim et al.[71] precisely. Our results are likewise in good accord with the computational and experimental data provided by Lee et al.[72] for GaAs NSs made by ion etching followed by lithography. When the substrate is structured, the reflectance decreases, and hence these substrates may be employed for antireflection

applications in the construction of optoelectronic devices. There have been previous experimental indications that GaAs NPs and NSs can be used in optoelectronics[73].

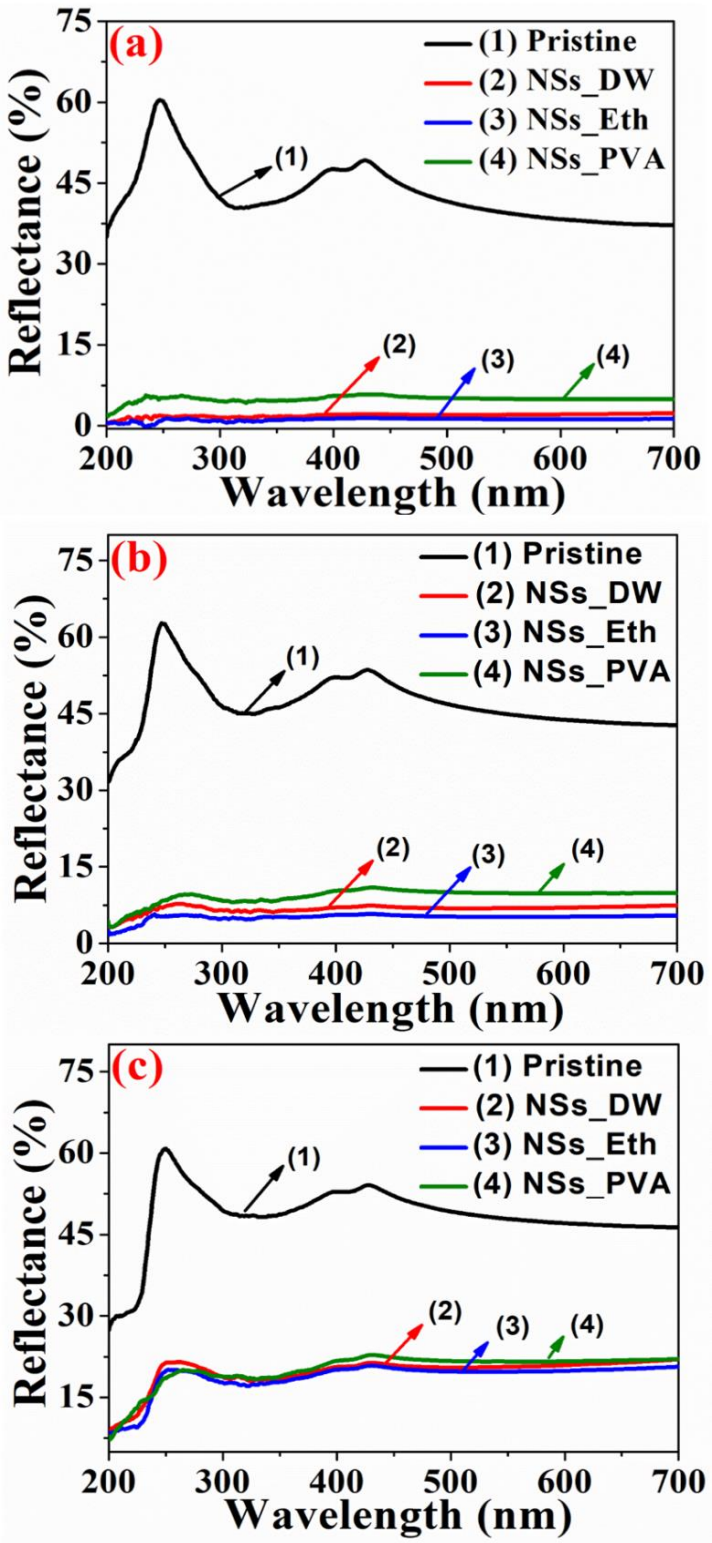

Fig. 4.14 Reflectance spectra with source incident angles at (a) 30°, (b) 45°, and (c) 60°, respectively. The spectra corresponding to GaAs pristine wafer, NSs formed in DW, NSs formed in ethanol, and NSs formed in PVA are represented with solid black line, red line, blue line, and green line, respectively.

4.1.7 SERS analysis of GaAs NSs

To investigate SERS response, the GaAs NSs were coated with a thin coating of gold (nominal thickness ~25 nm) utilizing thermal evaporation. The conditions of deposition were described in chapter 2 [Section 2.4.2 (a)]. The morphology/composition were examined using FESEM and EDAX measurements respectively to validate gold deposition. Using Gwyddion software, the periodicity and roughness of one of the samples (i.e., GaAs NSs generated in DW) were estimated before and after the deposition of a gold layer, and the resulting data was displayed in Fig. 4.15. The FESEM images displayed in Figure 4.15 (a) [unablated region] and Fig. 4.15 (b) [ablated region] for GaAs NSs were captured prior to gold deposition, as shown by the optical image inset. Figures 4.15 (c-d) depict, respectively, unablated and ablated areas following the gold coating. The grey scale vs distance spectra shown in figures 4.15 (e-h) correspond to those shown in Figs. 4.15 (a-d). Figure 4.15 (i) illustrates the EDAX spectra recorded before the gold deposition, indicating the presence of just 'Ga' and 'As,' whereas Fig. 4.15 (j) exhibits the EDAX spectra recorded after gold deposition on the same sample, indicating the presence of Au in addition to Ga and As. Consequently, it is evident from both optical insets and EDAX data that a thin gold coating has been deposited. It is also evident that the periodicity (0.32 μm) does not alter with deposition, however the roughness (grey value) has decreased in the sample's structured part and increased in its unstructured portion (at the corner of the same sample). Therefore, it is projected that the deposited gold has filled the NSs' grooves, hence reducing their roughness. On the smooth, unstructured surface, gold was subsequently deposited as a rough layer, indicating an increase in surface roughness. These gold-coated GaAs NSs were able to detect up to 500 nM of malachite green (MG), a dye molecule. For SERS measurements a portable Raman spectrometer (iRaman plus) is used (details are given in chapter 2), the obtained spectra are baseline corrected using the origin software for clear presentation.

Figure 4.16 (a) illustrates the SERS data for 500 nM MG drop-casted on three distinct GaAs NSs generated in DW, ethanol, and PVA. All of the Raman modes of MG shown in the SERS spectrum are in excellent agreement with the values published in the literature[74]. Figure 4.16 (b) illustrates the associated enhancement factor (EF): [EF was calculated using equation 2.1 (presented in chapter 2)], which is 1×10^5 for PVA, 5×10^4 for ethanol, and 3×10^4 for the DW sample. Among these three samples, the NSs generated in PVA exhibited the highest enhancement factor. Figure 4.16 (c) illustrates the SERS reproducibility data collected at

different locations on the same sample, whereas Fig. 4.16 (d) represents the SERS data recorded at various analyte concentrations. Figures 4.16 (e, f) depict the linear relationship between log (I) and log (C) for the two primary modes of the MG [1170 cm^{-1} and 1616 cm^{-1}, respectively]. These structures have shown high repeatability [see Fig. 4.16 (c)] with relative standard deviation (RSD) values of 10% for the mode at 1170 cm^{-1} [see Fig. 4.16 (g)] and 11% for the mode at 1616 cm^{-1} [see Fig. 4.16 (h)]. Figure 4.17 demonstrates that the generated NSs have a high reusability, which is confirmed by sonicating the NSs in distilled water to remove the MG analyte, then reusing them for SERS experiments to detect another molecule (Thiram, a pesticide). Figure 4.17 (a) depicts the molecular structure and SERS spectra of the thiram molecule, which agreed well with previous results[26,27,75]. Figure 4.17 (b) depicts the SERS data at various thiram concentrations, whereas Fig. 4.17 (c) depicts its log (I) vs log (C) dependency (c). Again, these substrates exhibited a high level of repeatability [see Figure 4.17 (d)] with RSD values of 16.13% for their 1141 cm^{-1} mode [see Fig. 4.17 (e)] and 16.74% for its 1374 cm^{-1} mode [Fig. 4.17 (f)], respectively.

In this work, 25 nm gold-coated GaAs nanostructures (NSs) proved to be effective and reusable SERS substrates for detecting MG and thiram, and these structures gave a greater enhancement than gold-coated pure GaAs wafers.

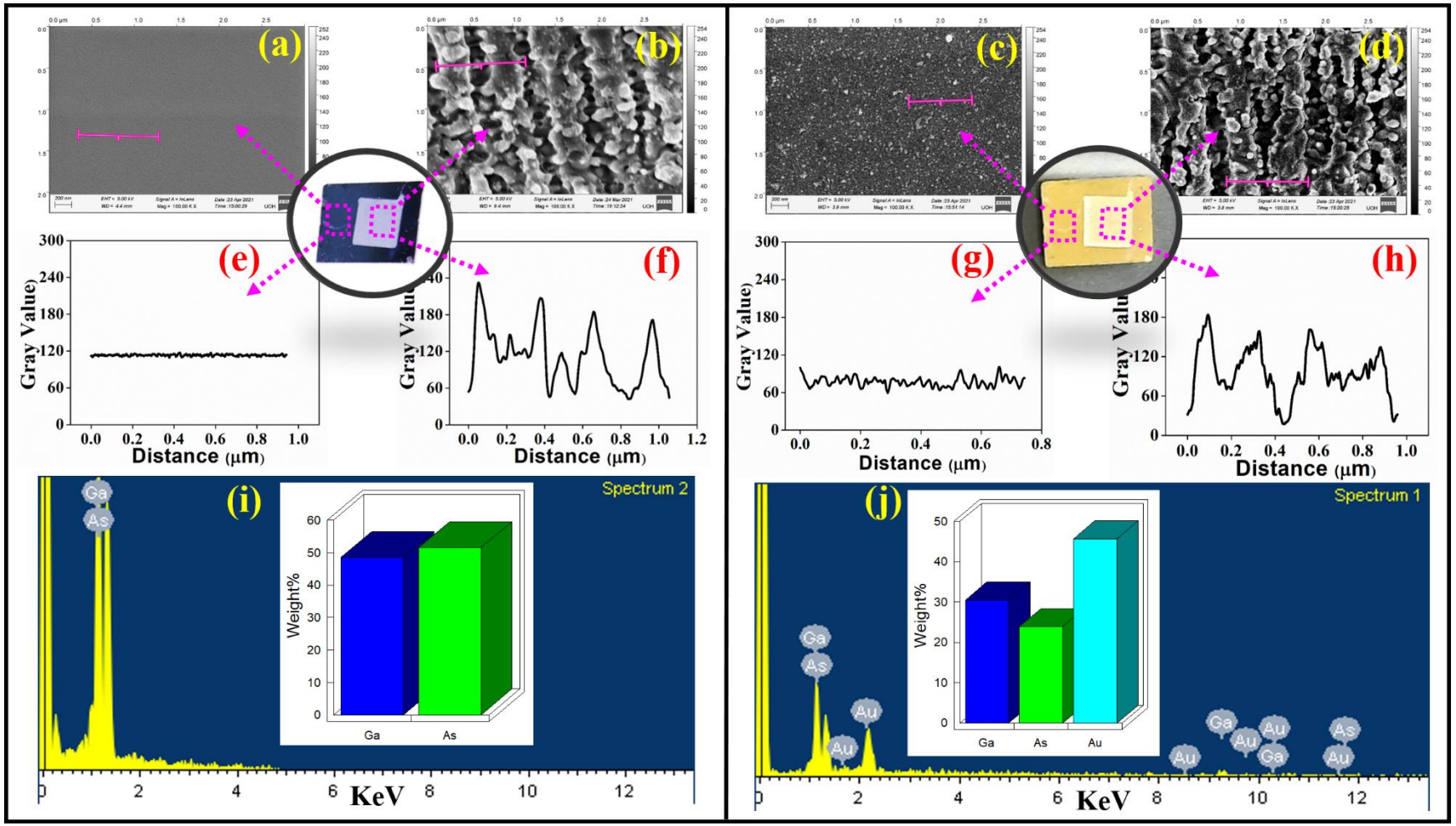

Fig. 4.15 FESEM images of GaAs NSs at unablated and ablated regions (a, b) as such, (c, d) gold coated, respectively as shown in the optical images (insets). In the same order (e-h) represents their corresponding periodicity (Gray value Vs Distance) curves, (i, j) EDAX spectra of bare and gold coated NSs, respectively. Insets of (i, j) depicts composition bar charts.

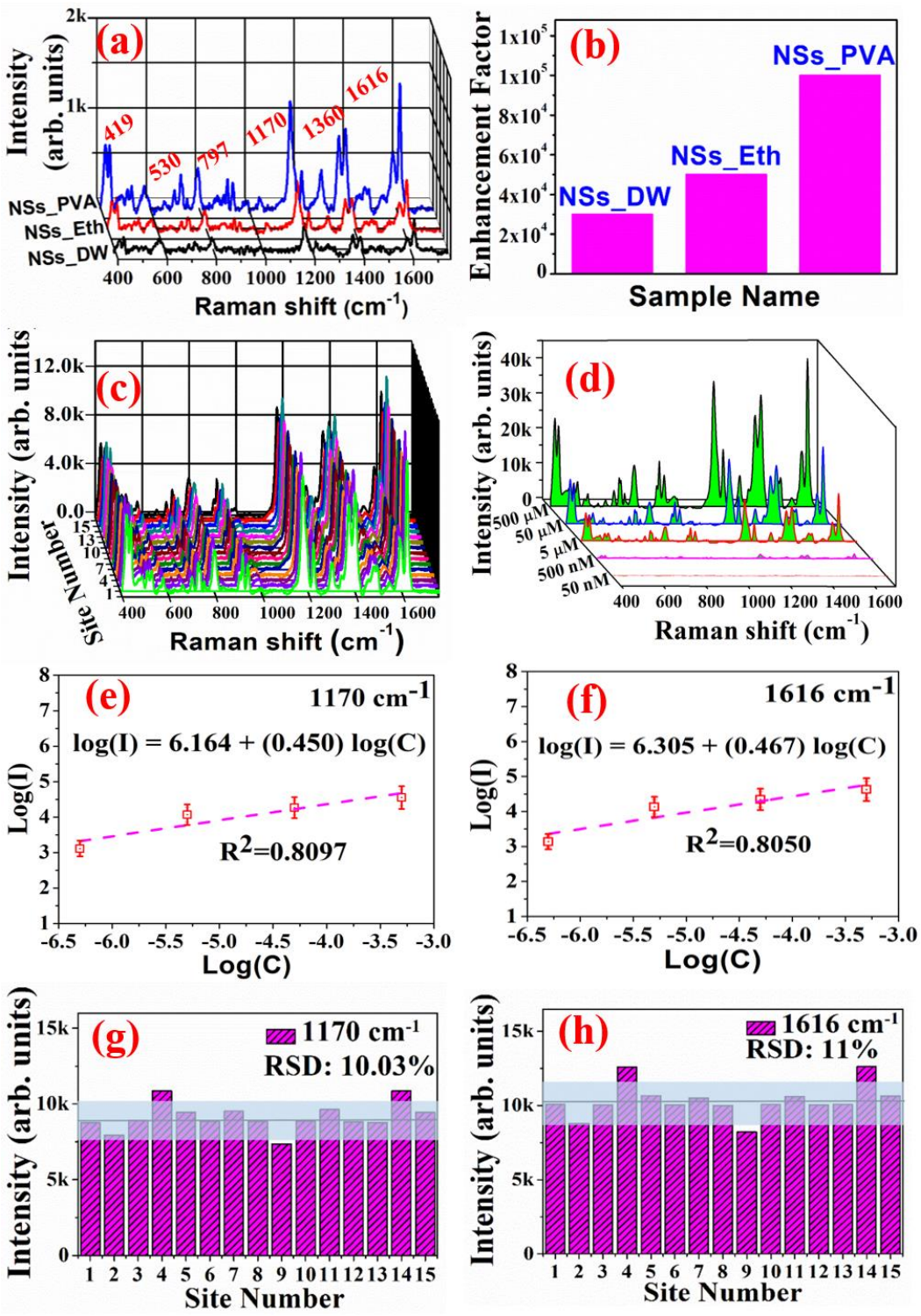

Fig. 4.16. SERS of GaAs NSs (a) 0.5 μM MG detected on three different GaAs NSs produced in DW, ethanol, and PVA, (b) enhancement factor calculated for the same three NSs, (c) reproducibility of SERS signal recorded at different locations on the sample, (d) concentration spectra of MG, (e, f) log(I) vs log(C) graphs of 1170 and 1616 cm^{-1} modes respectively, and (g, h) RSD plots of 1170 and 1616 cm^{-1} modes of analyte.

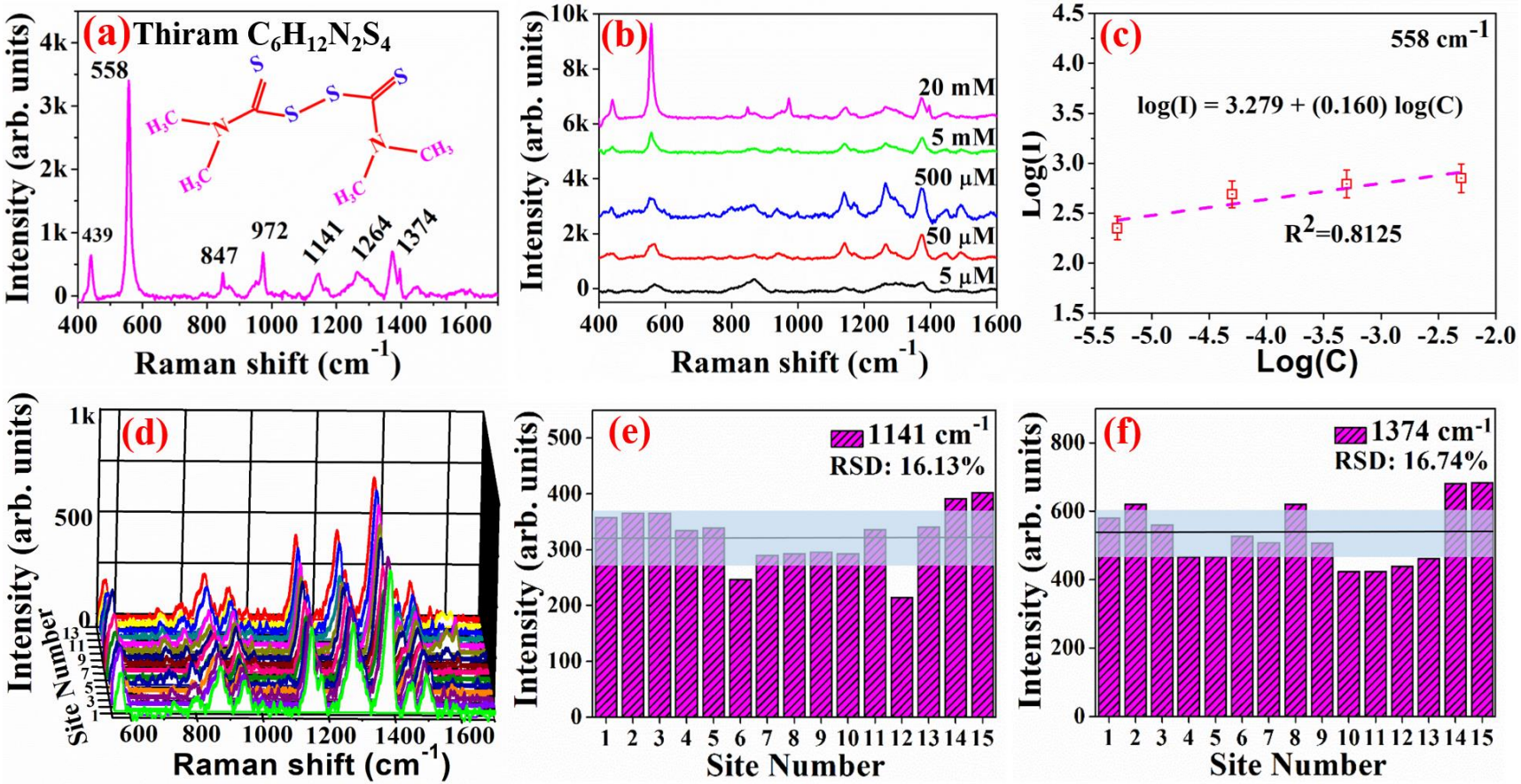

Fig. 4.17 SERS of GaAs NSs (a) structure of thiram molecule used as analyte in the study and its SERS spectrum (b) SERS spectra recorded with different concentrations of analyte (c) log (I) vs log (C) for the 558 cm^{-1} peak (d) SERS spectra recorded at 15 locations on the sample, (e, f) shows RSD plots of 1141 cm$^{-1,}$ 1374 cm^{-1} modes of the analyte molecule.

4.1.8 Summary of GaAs NSs

A thorough examination of the data pertaining to GaAs NSs enables us to comprehend the relationship between the morphology and its influence on the applications described in this article. It is evident from the FESEM images in Fig. 4.10 that GaAs NPs self-decorated on the GaAs NSs in the ablation process. The number of these self-decorated GaAs NPs is greater for the NSs generated in PVA solvent than for the other two NSs. Figure 4.13 demonstrates that the same structures had a smaller contact angle than the other two NSs; in fact, they turned hydrophilic while being hydrophobic before the ablation. As demonstrated in Figure 4.16 (b), the largest enhancement factor is again seen for the same GaAs NSs in PVA following Au coating, compared to the other two NSs. Figure 4.18 provides a graphic summary and visual representation of all the aforementioned observations. Using Gwydion software, the RMS roughness was determined from FESEM pictures. The values of the contact angle, reflectance, and enhancement factors were derived from the data shown in Figs. 4.13, 4.14, and 4.16, respectively.

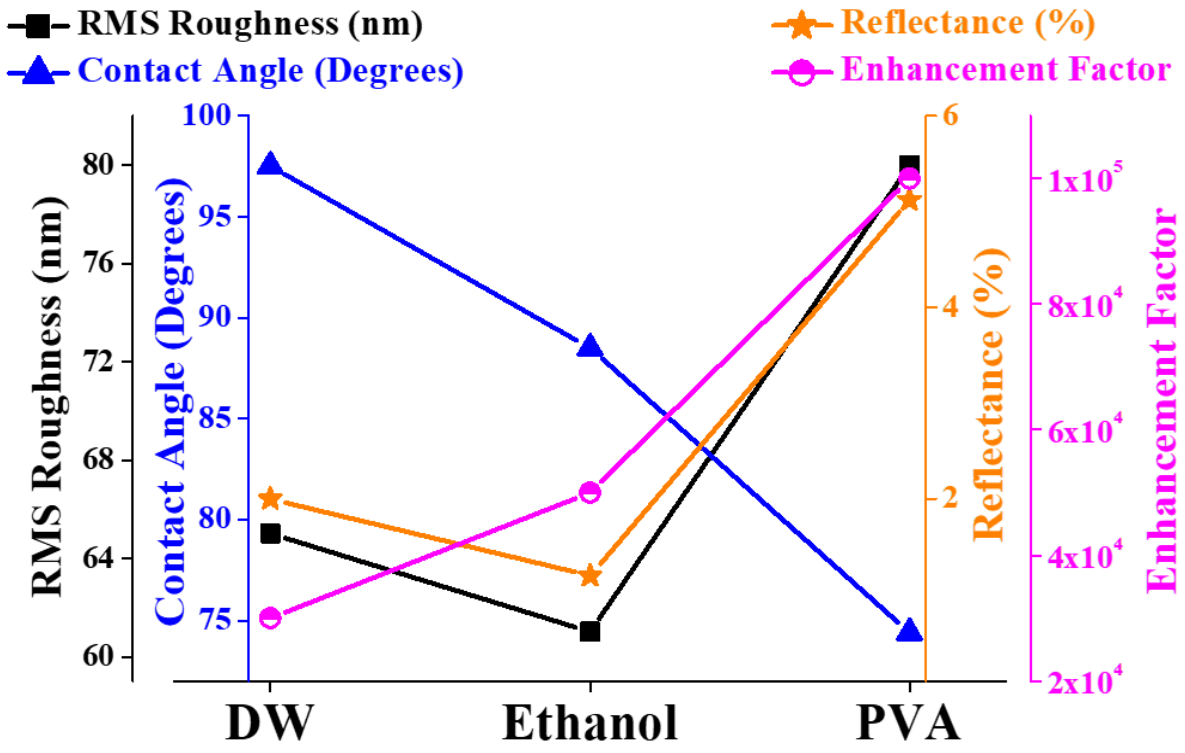

Fig. 4.18 GaAs NSs in DW, ethanol, and PVA on X-axis, variation of its properties on multiple Y-axes. RMS roughness (black rectangles), contact angle (blue triangles), reflectance (orange stars), and enhancement factor (magenta semi-solid circles).

The GaAs NSs created in DW and ethanol have a smaller number of GaAs NPs on the surface, but the GaAs NSs produced in PVA have a larger number of GaAs NPs that seem to be self-

decorated on the surface. NSs with a larger number of NPs (i.e., NSs generated in PVA) have a high roughness, resulting in a decreased contact angle. In addition, these particles coated with a thin layer of gold may operate as active plasmonic sources (hotspots), which may account for the found higher enhancement factors in NSs generated in PVA compared to NSs produced in DW and ethanol. According to Pilot et al. [76], the distance between the plasmonic hotspots and the analyte molecules is crucial for SERS amplification. Since the GaAs NSs in PVA are adorned with a greater number of NPs, this might have resulted to a reduction in the effective distance between the nano-entities, allowing for a greater number of plasmonic hotspots. Additionally, the distance between analyte molecules and hotspots minimized, which may explain why this sample's enhancement factor is greater than the other two.

The SERS response of plasmonic metal NPs have been widely researched. However, when these substrates are irradiated with laser light for SERS measurements, their electrical (No band gap) and thermal characteristics cause them to emit heat. This can ruin samples that are sensitive to such a little amount of heat (as in biological samples). Specifically for this reason, semiconductors are currently being investigated as SERS substrates[77,78]. Consequently, this type of pristine and a thin metal coated NSs generated on semiconductors, particularly compound semiconductors (GaAs NSs), with extra bio-compatibility must be further investigated and optimized to be competitive with pure plasmonic NPs based SERS substrates. It is important to note that creation/modification of surface structures on GaAs is easy compared to other semiconductors, and highly promising for fabrication of various devices and sensors. Hence, the subsequent sections of this thesis concentrate on optimizing better surface structures on GaAs and their formation mechanisms.

Chapter 4 (Part-B)

A Comparative study of GaAs Nanostructures Fabricated in Air and Distilled Water by Picosecond Pulsed Laser Ablation

4.2.0 Introduction

As depicted in the part-A of this chapter, GaAs quasi-periodic surface structures can be utilized in various fields. Hence, it is interesting to tune the quality of these surface structures there by tuning their properties. Researchers are trying to fabricate these surface structures with least possible periodicity and good quality. However, the GaAs periodic structures produced by ultrafast lasers in air face a formidable obstacle in preventing oxidation and sustaining stability. Laser patterning in DW might be a viable option for preventing these oxidations. Exploring GaAs laser ablation/writing in DW and comparing it to ablation in air is crucial for the development of novel and useful technologies. This study used GaAs laser ablation in both ambient (air) and distilled water media. First set of samples were fabricated by varying the scan speed and next set of samples by varying scan spacing, keeping all other parameters constant throughout the experiment. Detailed comparisons of the surface morphologies seen in both air and DW are presented below.

4.2.1. Experimental Details

GaAs wafer with (100) orientation and resistivity of 10^6 Ohm-cm was sliced into 1 cm × 1 cm squares. These samples were then cleaned and ablated in both air and DW using an Nd:YAG laser (30 ps, 10 Hz, 1064 nm, and energy: 2 mJ.

1. Varying laser scan speeds of 0.05, 0.15, 0.25, 0.5, and 1.0 mm/s.
2. Varying raster scan spacing of 0.05, 0.15, 0.25, and 0.35 mm.

Throughout the experiment, all other laser parameters were kept constant. A 10 cm focal length plano-convex lens was used to focus the laser beam onto the sample. An X-Y motion controller, on which the samples were positioned, was used to regulate the scan gaps and speeds.

4.2.2. Results and Discussion

4.2.2 (a) Morphology of GaAs NSs at different scan speeds

The GaAs NSs created in DW at different scan speeds such as 0.05, 0.15, 0.25, 0.5, and 1.0 mm/s were shown in Fig. 4.19 (a-e), it was noticed that the structures quality/appearance was good at lower scan speed (i.e., at 0.05 mm/s, see Fig. 4.19 (a)). Increase in scan speed in DW decreases the ablation of material led to weak structure at highest scan speed (i.e., at 1.0 mm/s, see Fig. 4.19 (e)). Further, these structures have not shown any significant oxygen levels as indicated in Fig. 4.19 (f). Next, the NSs formed in air have shown a completely different morphology than that of NSs created in DW. At lower scan speeds, the structure formation was not noticed [see Fig. 4.20 (a-c)] may be due to re-deposition of the ablated nanomaterial on the surface of the NSs. For the higher scan speeds, quasiperiodic NSs are noticed here and there on the samples [see Fig. 4.20 (d-e)]. Another noteworthy point was the presence of the oxygen in the NSs formed in the air, which was not observed for NSs formed in DW. Since the ablation was occurring below the liquid, where there was less dissolved oxygen, hence, there may not be any noticeable oxygen levels in the ablated GaAs NSs.

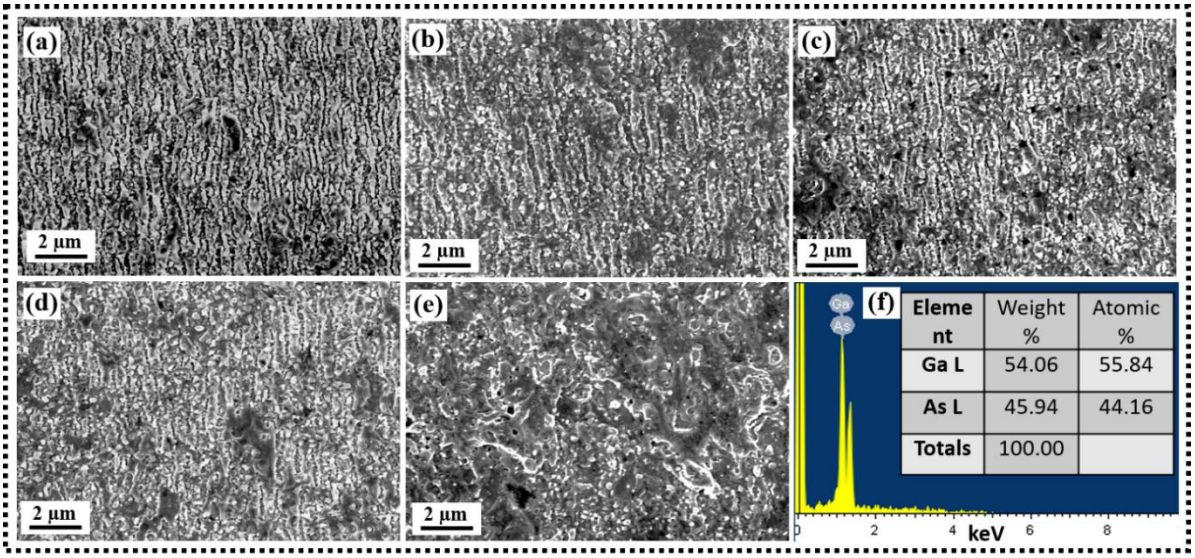

Element	Weight %	Atomic %
Ga L	54.06	55.84
As L	45.94	44.16
Totals	100.00	

Fig. 4.19 (a-e) FESEM images of GaAs NSs produced in DW at scan speeds 0.05, 0.1, 0.25, 0.5, and 1.0 mm/s, respectively and the image (f) represents composition of these structures (All these structures have similar composition, hence, the spectra of one of the samples was shown).

The Raman spectra recorded on the GaAs NSs produced in DW is shown in Fig. 4.21 (a), the curves 1-5 show the NSs produced in DW at different scan speeds such as 0.05, 0.1, 0.25, 0.5, and 1.0 mm/s, respectively. The Raman active modes at 265 cm^{-1} and 289 cm^{-1} correspond to the TO and LO modes of GaAs. The intensity of 265 cm^{-1} is higher than that of the 289 cm^{-1} mode in laser interacted regions, indicating the loss of crystal symmetry mostly due to the formation of nanostructures. With decreasing the scan speed, the irradiance will increase as the

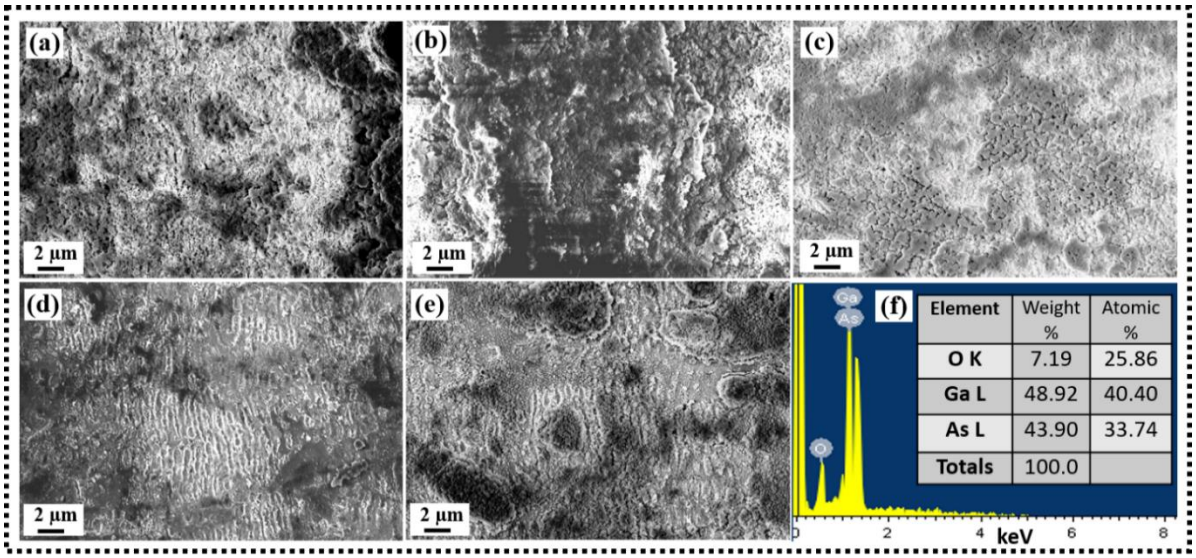

Fig. 4.20 (a-e) FESEM images of GaAs NSs produced in air at scan speeds 0.05, 0.1, 0.25, 0.5, and 1.0 mm/s, respectively and the image (f) represents composition of these structures (All these structures have similar composition, hence, the spectra of one of the samples was shown).

number of pulses hitting at each spot increase. This leads to the increase in the TO mode intensity as well the TO/LO ratio as depicted in the Fig. 4.22. The GaAs NSs produced in air also contain the Raman active modes around the same positions that is 265 cm^{-1} and 289 cm^{-1} [See Fig. 4.21 (b)]. In this case also a similar observation is noticed revealing higher damage at lower scan speed leading to an increase in the TO mode intensity.

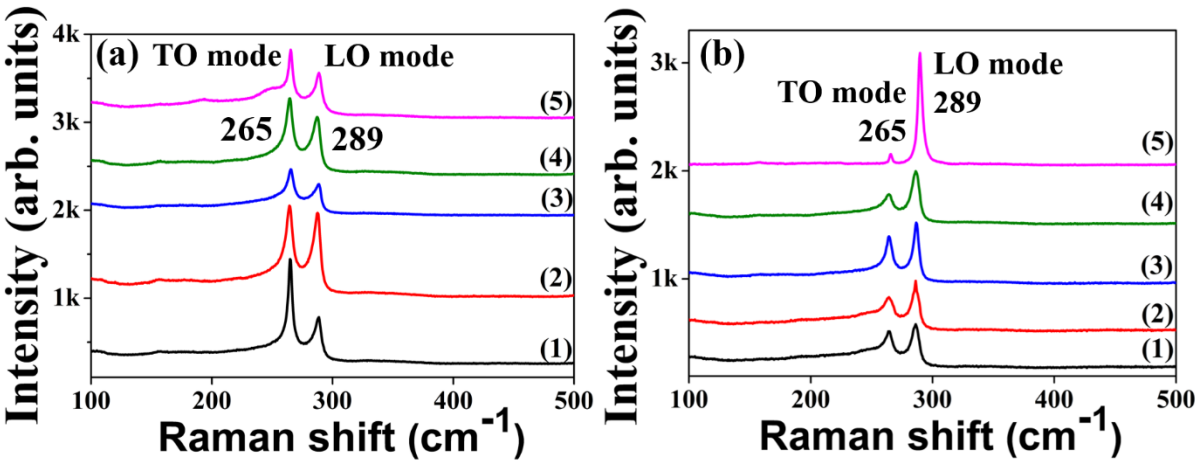

Fig. 4.21 Raman spectra of GaAs NSs ablated (a) in DW, (b) in air. Curves 1-5, represents NSs produced at scan speeds 0.05, 0.1, 0.25, 0.5, and 1.0 mm/s, respectively.

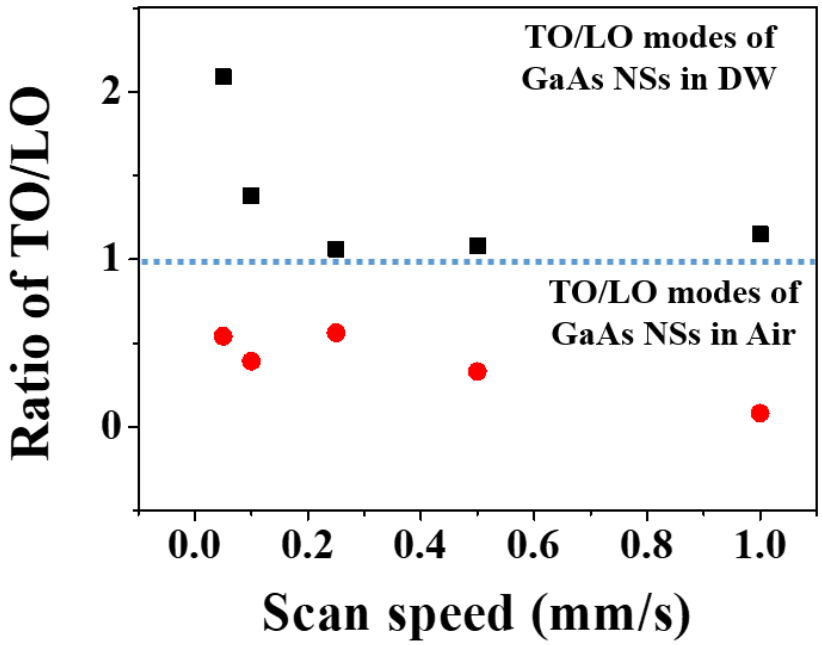

Fig. 4.22 Ratio of TO and LO modes of GaAs NSs ablated in DW (black rectangles) and air (red circles) are plotted against the scan speed of the ablation process.

4.2.2 (b) Morphology of GaAs NSs at different scan spacing

Figures 4.23 (a_1-a_4) depict the optical images of GaAs NSs generated in air for scan spacing of 0.05, 0.15, 0.25, and 0.35 mm, whereas Figs. 4.23 (a_5-a_8) depict their FESEM images. For raster scan spacing of 0.05 mm and 0.15 mm, it is obvious that there is no substantial separation between the GaAs NSs produced in air [see Figure 4.23 (a_1, a_2, a_5, a_6)]. Owing to the fact that the spacing between the lines (0.05 and 0.15 mm) is lower than the laser spot size/line width (0.2 mm) formed on the GaAs surface, the lines became overlapping, resulting in the absence of space. For the remaining scan spacing of 0.25 mm and 0.35 mm, both optical and FESEM images reveal a considerable separation [Figs. 4.23 (a_3, a_4, a_7, a_8)].

Similar analysis was done for the NSs generated in DW [Figs. 4.23 (b_1-b_4) are optical images and Figs. 4.23 (b_5-b_8) are FESEM images] at the same spacing as before 0.05, 0.15, 0.25, and 0.35 mm. The most intriguing conclusion is that, given the identical line spacing of 0.05, 0.15, 0.25, and 0.35 mm, none of the GaAs NSs generated in DW have any separation between the lines. It might be related to the increase in laser spot size on the GaAs surface, which will cause the overlap between the scan lines to increase. The formation of a dense plasma and a cavitation bubble in the water-confined regime when a picosecond laser strikes a GaAs substrate placed in DW (see Fig. 4.24, row 2) may have played a significant role in diverging/absorbing the laser beam[79]. As noted by Besner et al.[80], it is also widely known that the refractive index of

the DW (1.33), which is greater than that of air (1.0), causes the focus plane to move. Consequently, an increase in laser spot size may result from either divergence from a strong plasma and dense cavitation bubble or a change in the focal plane [81]. This increase in spot size explains the observed overlap between lines generated on GaAs NSs in DW, as seen in Fig. 4.24, row 2. This type of plasma plume creation and laser beam refraction is not achievable in the case of GaAs ablation in air medium, as shown in Fig. 4.24, row 1.

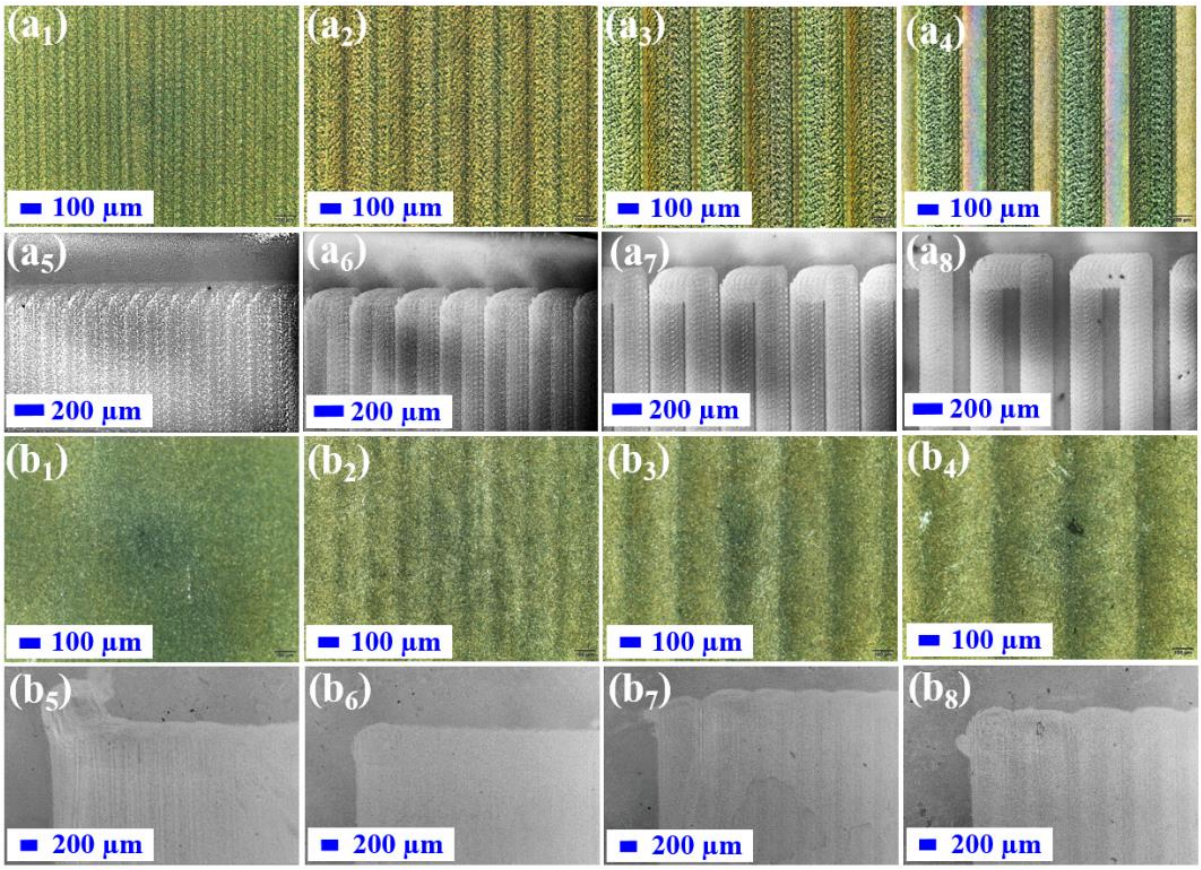

Fig. 4.23 (a1-a4) shows optical microscopic images and (a5-a8) FESEM images of GaAs NSs produced in air at various raster scan spacings of 0.05, 0.15, 0.25, and 0.35 mm, respectively. Similarly, (b1-b4) optical microscopic images and (b5-b8) FESEM images of GaAs NSs generated in DW at raster scan spacings of 0.05, 0.15, 0.25, and 0.35 mm.

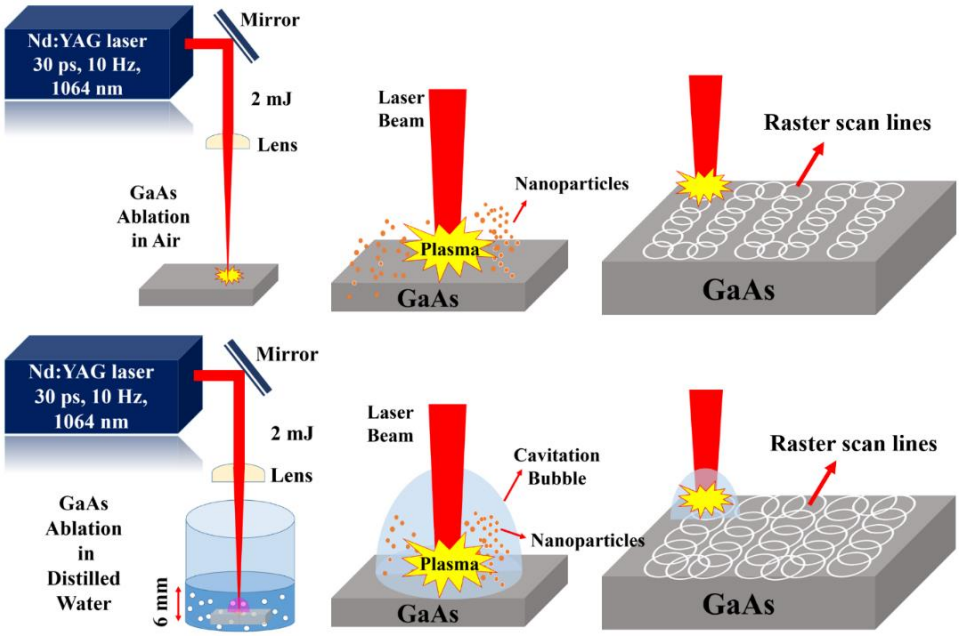

Fig. 4.24 Schematic representation of picosecond laser ablation in air and DW.

Moreover, debris-filled NSs are created inside the raster scan lines for all samples ablated in air, whereas quasi-periodic NSs are formed for all samples ablated in DW. The distance between the raster scan lines had no influence on the GaAs NSs created inside the lines; hence, all of the samples ablated in air had identical debris-like structures and all of the samples ablated in DW had quasi-periodic NSs. Figure 4.25 depicts pictures at a greater magnification for only one sample of GaAs NSs generated in air [4.25 (a)] and one sample of GaAs NSs created in DW [4.25 (c)]. The EDAX data indicates the presence of Ga, As, and O in the NSs generated in air, as seen in Fig. 4.25 (b), and the composition table is presented in the inset. The NSs generated in the DW include solely Ga and As, as seen in Fig. 4.25 (d), and the composition table is presented in the picture's inset. The Fig. 4.24 explains why the production of surface periodic NSs in air and DW is so drastically different. The laser energy utilized in this investigation is 2 mJ, and the spot size/scan width seen on the GaAs is 200 µm. Therefore, using the formula, the laser fluence given to the GaAs surface in air is estimated.

$$F = \frac{E}{\pi\left(\frac{D}{2}\right)^2} \qquad J/cm^2 \qquad \text{.....4.4}$$

Where E is the laser pulse energy and D is the focal point diameter of the laser spot. In this instance, the calculated fluence is 6.4 J/cm^2. This number is significantly greater than the laser ablation thresholds reported for GaAs (0.1 J/cm^2)[82]. Therefore, there is full destruction to the GaAs, resulting to the production of debris on the GaAs's surface. This enormous energy deposition in the ambient environment causes the oxidation of Ga, As, and O containing debris,

as seen in Fig. 4.26 (a, b). The same laser pulse energy of 2 mJ is employed in DW (the height of the DW was 6 mm), but the energy supplied to the surface of the GaAs may be greatly reduced due to the energy loss happening in the dense DW medium compared to the air medium[79]. Therefore, the laser fluence may fall under the ablation threshold value range for GaAs, resulting in the creation of quasi-periodic surface NSs in DW. The observed variations in laser scan spacing between GaAs NSs in air and DW are a consequence of (I) divergence of the laser beam owing to the thick plasma plume/cavitation bubble and (II) a shift in the focus plane due to the refractive index of the DW. Similarly, the debris created in air and quasi-periodic NSs formed on the GaAs surface are attributable to the effective laser fluence given to its surface.

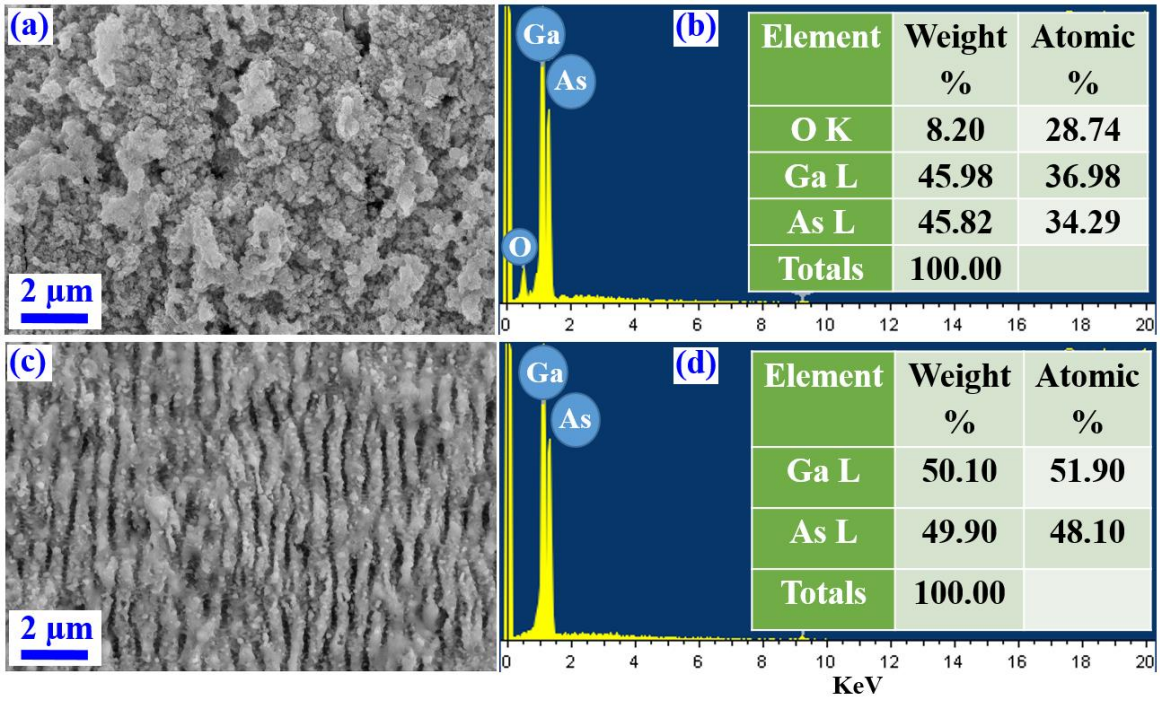

Fig. 4.25 (a) is a higher magnification FESEM image of the GaAs NSs generated in air, (b) EDAX spectrum, and a table of composition. Similarly, (c) is a higher magnification FESEM image of the GaAs NSs generated in DW, (d) EDAX spectrum and inset illustrates its composition table.

4.2.3. SERS study of Au/GaAs NSs produced by ps laser ablation

Now, these quasi-periodic GaAs nanostructures have been coated with a thin coating of gold and employed as SERS substrates for detecting tiny levels of hazardous chemicals. In the present work, gold coating is done using a thermal evaporation technique, and these samples are subsequently annealed at 400 °C to create evenly ornamented hotspots on these NSs, as seen in figure 4.26 (a, b). The EDAX conducted on these NSs revealed the presence of Ga, As, and Au, as shown in 4.26 (c), and the composition table shown in 4.26 (d) verified the existence

of gold coating. These substrates were then utilized to identify the methylene blue and thiram. All of these NSs created in DW exhibited comparable detection levels; hence, SERS data is only shown for one of the samples, namely GaAs NSs produced in DW with a scan spacing of 0.25 mm. Figure 4.26 (e) depicts the SERS spectra of MB recorded at various concentrations, including 5 nM, 50 nM, 500 nM, 5 µM, 50 µM, 500 µM, and 5 mM, as shown by curves I-VII, respectively. For data legibility, the curves I-III are multiplied by 3, and Fig. 4.26 (f) displays repeatability data obtained at random sites on the same sample. The smallest amount of MB molecule that could be detected was 5 nM, and the RSD values for the two most prominent Raman modes, 446 cm^{-1} and 1621 cm^{-1}, are 9.5% and 12.7%, respectively. The calculated enhancement factor is 10^5. These structures are re-used for the detection of thiram molecule after cleaning with acetone, and the corresponding SERS spectra are depicted in Fig. 4.26 (g), which depicts the SERS spectra for various concentrations of the pesticide (thiram) molecule (Curves I-VI in Fig. 4.26 (g) correspond to 500 nM, 5 µM, 50 µM, 500 µM, 5 mM. Figure 4.27 (h) displays the reproducibility data obtained from random sites on the same sample. The lowest observed concentration of thiram was 500 nM, with an enhancement factor of 10^4 and relative standard deviations of 17.2% and 12.4% for the main modes 561 cm^{-1} and 1374 cm^{-1}, respectively.

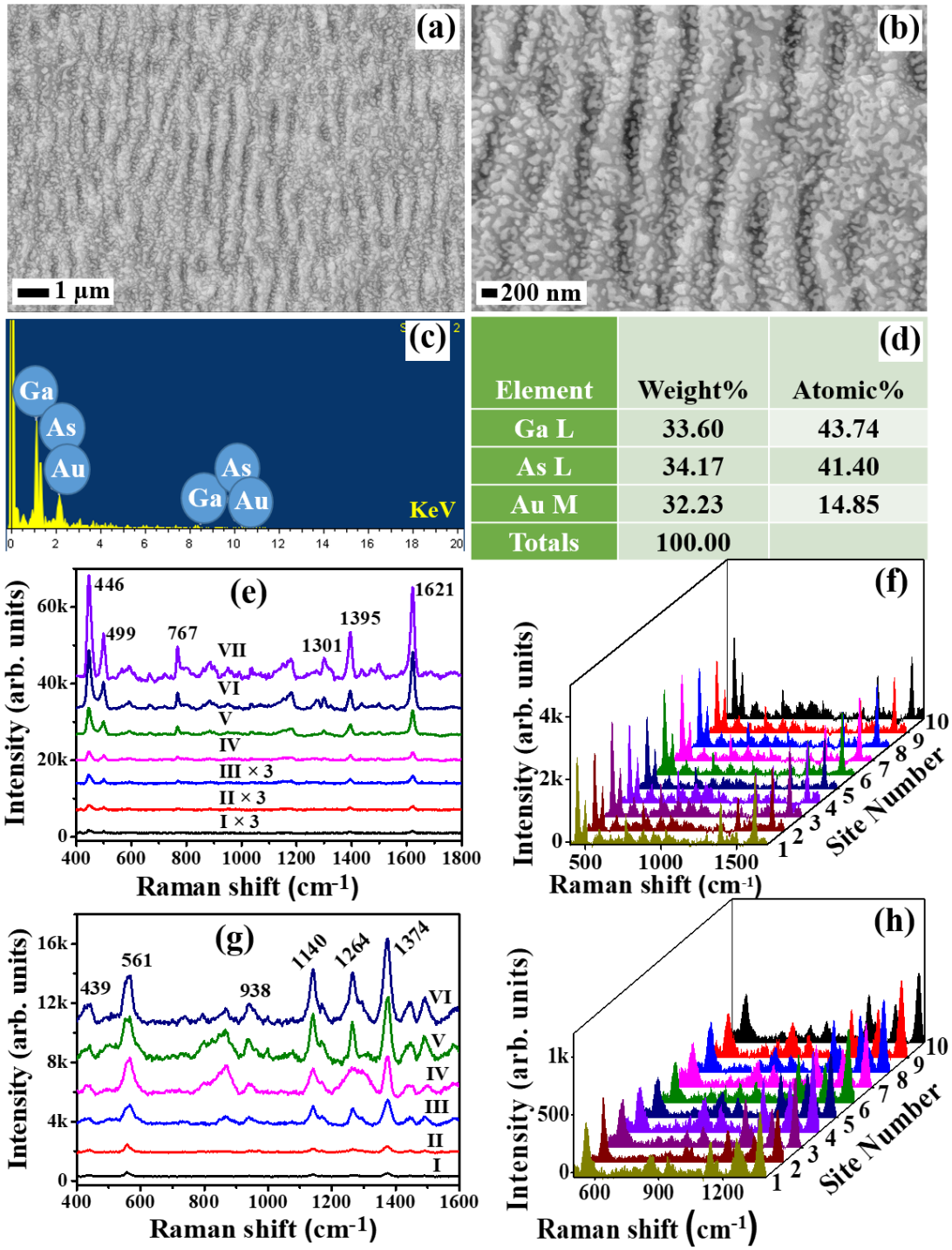

Fig. 4.26 (a, b) Two FESEM images of annealed Au/GaAs NSs at different magnifications, (c) an EDAX spectra, and (d) a table of composition. The graphs (e, f) SERS concentration spectra and reproducibility data of the dye molecule MB on Au/GaAs NSs (Curves I-VII in (e) correspond to 5 nM, 50 nM, 500 nM, 5 M, 50 M, 500 M, and 5 mM, respectively; curves I-III are multiplied by three for data legibility). Graphs (g, h) SERS concentration spectra and reproducibility for the pesticide thiram on Au/GaAs NSs (Curves I-VI (g) correspond to 500 nM, 5 M, 50 M, 500 M, 5 mM, and 50 mM, respectively).

4.2.4 Conclusion

First part of this chapter describes the outcomes of the simultaneous production of GaAs NPs and NSs utilizing picosecond PLAL in a single exposure. The produced NPs are polycrystalline, spherical, and have a size distribution between 50 and 120 nm. The fs NLO studies demonstrated the existence of two-photon absorption for the GaAs NPs. The GaAs quasiperiodic HSFL structures have a periodicity of 320 nm, with anti-reflection and wettability properties. In addition, after coating these NSs with a thin layer of gold, they have been proved to be effective hybrid SERS substrates. In addition, the current research shows that the laser parameters of 5 mJ, 30 ps, 1064 nm, and 10 kHz are optimal for the production of GaAs NPs and NSs by ps PLAL. Ethanol is a superior solvent and PVA is the best solvent compared to DW as a liquid medium for the synthesis of GaAs NPs with less amorphous/oxide formation.

The second part presents a comparative study of GaAs NSs generated by picosecond laser ablation in air and DW media. The influence of raster scan speed and spacing on the formation of GaAs NSs is investigated. Lower scan speed is better for structuring in the DW medium whereas comparatively higher speed is necessary for the creation of structures in air medium. The scan spacing has no significant effect on the quality of NSs created. However quasi-periodic structures are produced in DW and debris like structures in air. Overall, this work demonstrates that the laser ablation in DW is the optimal method for producing GaAs NSs without oxidation, and it illustrates the basic distinctions between the ablation mechanisms occurring in DW and air. These kinds of investigations might aid in the advancement of GaAs periodic surface nanostructures with smaller feature sizes and their applications in a variety of domains, including SERS.

References

(1) Li, S. S. High-Speed III–V Semiconductor Devices. In *Semiconductor Physical Electronics*; Springer US: Boston, MA, 1993; pp 455–502. https://doi.org/10.1007/978-1-4613-0489-0_15.

(2) Terry L. Alford , Leonard C. Feldman, J. W. M. *Fundamentals of Nanoscale Film Analysis*; Springer US: Boston, MA, 2007. https://doi.org/10.1007/978-0-387-29261-8.

(3) Higo, A.; Kiba, T.; Tamura, Y.; Thomas, C.; Takayama, J.; Wang, Y.; Sodabanlu, H.; Sugiyama, M.; Nakano, Y.; Yamashita, I.; Murayama, A.; Samukawa, S. Light-Emitting Devices Based on Top-down Fabricated GaAs Quantum Nanodisks. *Sci. Rep.* **2015**, *5* (1), 9371. https://doi.org/10.1038/srep09371.

(4) Yang, L.; Pillai, S.; Green, M. A. Can Plasmonic Al Nanoparticles Improve Absorption in Triple Junction Solar Cells? *Sci. Rep.* **2015**, *5* (1), 11852. https://doi.org/10.1038/srep11852.

(5) Wang, Z. J.; Kim, E. S.; Liang, J. G.; Qiang, T.; Kim, N. Y. A High-Frequency-Compatible Miniaturized Bandpass Filter with Air-Bridge Structures Using GaAs-Based Integrated Passive Device Technology. *Micromachines* **2018**, *9* (9), 463. https://doi.org/10.3390/mi9090463.

(6) Dumke, W. P.; Woodall, J. M.; Rideout, V. L. GaAs□GaAlAs Heterojunction Transistor for High Frequency Operation. *Solid. State. Electron.* **1972**, *15* (12), 1339–1343. https://doi.org/10.1016/0038-1101(72)90127-X.

(7) Weir, S. T.; Vohra, Y. K.; Vanderborgh, C. A.; Ruoff, A. L. Structural Phase Transitions in GaAs to 108 GPa. *Phys. Rev. B* **1989**, *39* (2), 1280–1285. https://doi.org/10.1103/PhysRevB.39.1280.

(8) Besson, J. M.; Weill, G.; Mansot, J. L.; Gonzalez, J. Phase Diagram of GaAs. *High Press. Res.* **1990**, *4* (1–6), 312–314. https://doi.org/10.1080/08957959008246106.

(9) Leahu, G.; Petronijevic, E.; Belardini, A.; Centini, M.; Voti, R. L.; Hakkarainen, T.; Koivusalo, E.; Guina, M.; Sibilia, C. Photo-Acoustic Spectroscopy Revealing Resonant Absorption of Self-Assembled GaAs-Based Nanowires. *Sci. Rep.* **2017**, *7* (1), 1–9. https://doi.org/10.1038/s41598-017-02839-1.

(10) Rathi, P.; Ekta; Kumar, S.; Banerjee, D.; Soma, V. R.; Sankar, M. Unsymmetrical β-Functionalized 'Push–Pull' Porphyrins: Synthesis and Photophysical, Electrochemical and Nonlinear Optical Properties. *Dalt. Trans.* **2020**, *49* (10), 3198–3208. https://doi.org/10.1039/C9DT04252K.

(11) Bharati, M. S. S.; Bhattacharya, S.; Suman Krishna, J. V.; Giribabu, L.; Venugopal Rao, S. Femtosecond, Broadband Nonlinear Optical Studies of a Zinc Porphyrin and Zinc Phthalocyanine. *Opt. Laser Technol.* **2018**, *108*, 418–425. https://doi.org/10.1016/j.optlastec.2018.07.008.

(12) Ahmed, M. S.; Sireesha, L.; Nayak, S. K.; Bakthavatsalam, R.; Banerjee, D.; Soma, V. R.; Kundu, J.; Raavi, S. S. K. Tunable Near-Infrared Emission and Three-Photon Absorption in Lanthanide-Doped Double Perovskite Nanocrystals. *Nanoscale* **2023**, *15* (21), 9372–9389. https://doi.org/10.1039/d3nr00988b.

(13) Allu, R.; Banerjee, D.; Avasarala, R.; Hamad, S.; Rao, S. V.; Podagatlapalli, G. K. Broadband

Femtosecond Nonlinear Optical Properties of Silver Nanowire Films. *Opt. Mater. (Amst).* **2019**, *96* (September), 109305. https://doi.org/10.1016/j.optmat.2019.109305.

(14) Venkatram, N.; Narayana Rao, D.; Giribabu, L.; Venugopal Rao, S. Femtosecond Nonlinear Optical Properties of Alkoxy Phthalocyanines at 800 Nm Studied Using Z-Scan Technique. *Chem. Phys. Lett.* **2008**, *464* (4–6), 211–215. https://doi.org/10.1016/j.cplett.2008.09.029.

(15) Banerjee, D.; Moram, S. S. B.; Byram, C.; Rathod, J.; Jena, T.; Podagatlapalli, G. K.; Soma, V. R. Plasmon-Enhanced Ultrafast and Tunable Thermo-Optic Nonlinear Optical Properties of Femtosecond Laser Ablated TiO2 and Silver-Doped TiO2 Nanoparticles. *Appl. Surf. Sci.* **2021**, *569*, 151070. https://doi.org/10.1016/j.apsusc.2021.151070.

(16) Ganeev, R. A.; Ryasnyanskiy, A. I.; Usmanov, T. Optical and Nonlinear Optical Characteristics of the Ge and GaAs Nanoparticle Suspensions Prepared by Laser Ablation. *Opt. Commun.* **2007**, *272* (1), 242–246. https://doi.org/10.1016/j.optcom.2006.11.009.

(17) Ganeev, R. A.; Ryasnyanskii, A. I.; Kuroda, H. Laser Ablation of Gallium Arsenide in Different Solutions. *Opt. Spectrosc.* **2005**, *99* (6), 1006–1011. https://doi.org/10.1134/1.2149427.

(18) Sun, X.; Zhou, F.; Dong, X.; Zhang, F.; Liang, C.; Duan, L.; Hu, Y.; Duan, J. Fabrication of GaAs Micro-Optical Components Using Wet Etching Assisted Femtosecond Laser Ablation. *J. Mod. Opt.* **2020**, *67* (20), 1516–1523. https://doi.org/10.1080/09500340.2020.1869849.

(19) Huang, M.; Zhao, F.; Cheng, Y.; Xu, N.; Xu, Z. The Morphological and Optical Characteristics of Femtosecond Laser-Induced Large-Area Micro/Nanostructures on GaAs, Si, and Brass. *Opt. Express* **2010**, *18* (S4), A600. https://doi.org/10.1364/oe.18.00a600.

(20) Zhang, W.; Shi, Z.; Chen, C.; Yang, X.; Yang, L.; Zeng, Z.; Zhang, B.; Liu, Q. Super-Resolution GaAs Nano-Structures Fabricated by Laser Direct Writing. *Mater. Sci. Semicond. Process.* **2018**, *84* (March), 119–123. https://doi.org/10.1016/j.mssp.2018.05.016.

(21) Hu, Y.; LaPierre, R. R.; Li, M.; Chen, K.; He, J.-J. Optical Characteristics of GaAs Nanowire Solar Cells. *J. Appl. Phys.* **2012**, *112* (10), 104311. https://doi.org/10.1063/1.4764927.

(22) Bharati, M. S. S.; Byram, C.; Soma, V. R. Femtosecond Laser Fabricated Ag@Au and Cu@Au Alloy Nanoparticles for Surface Enhanced Raman Spectroscopy Based Trace Explosives Detection. *Front. Phys.* **2018**, *6* (March), 1–13. https://doi.org/10.3389/fphy.2018.00028.

(23) Yadav, S.; Senapati, S.; Desai, D.; Gahlaut, S.; Kulkarni, S.; Singh, J. P. Portable and Sensitive Ag Nanorods Based SERS Platform for Rapid HIV-1 Detection and Tropism Determination. *Colloids Surfaces B Biointerfaces* **2021**, *198* (September 2020), 111477. https://doi.org/10.1016/j.colsurfb.2020.111477.

(24) Saad, N. A.; Ramya, E.; Saikiran, V.; Naraharisetty, S. R. G.; Narayana Rao, D. Novel Synthesis and Study of Nonlinear Absorption and Surface-Enhanced Raman Scattering of Carbon Nanotubes Decorated with Silver Nanoparticles. *Chem. Phys.* **2020**, *533* (October 2019), 110703. https://doi.org/10.1016/j.chemphys.2020.110703.

(25) Moram, S. S. B.; Byram, C.; Soma, V. R. Gold-Nanoparticle- and Nanostar-Loaded Paper-Based SERS Substrates for Sensing Nanogram-Level Picric Acid with a Portable Raman Spectrometer. *Bull. Mater. Sci.* **2020**, *43* (1), 53. https://doi.org/10.1007/s12034-019-2017-8.

(26) Haidar, I.; Day, A.; Martino, U.; Chevillot-Biraud, A.; Félidj, N.; Boubekeur-Lecaque, L. Bottom-up Assembly of Au@Ag Plasmonic Nanocrystals: Issues to Be Addressed to Achieve a Good SERS Substrate. *Appl. Mater. Today* **2019**, *15*, 462–471. https://doi.org/10.1016/j.apmt.2019.02.015.

(27) Tegegne, W. A.; Su, W.-N.; Tsai, M.-C.; Beyene, A. B.; Hwang, B.-J. Ag Nanocubes Decorated 1T-MoS2 Nanosheets SERS Substrate for Reliable and Ultrasensitive Detection of Pesticides. *Appl. Mater. Today* **2020**, *21*, 100871. https://doi.org/10.1016/j.apmt.2020.100871.

(28) Verma, A. K.; Soni, R. K. Laser Ablation Synthesis of Bimetallic Gold-Palladium Core@shell Nanoparticles for Trace Detection of Explosives. *Opt. Laser Technol.* **2023**, *163* (August 2022), 109429. https://doi.org/10.1016/j.optlastec.2023.109429.

(29) Moram, S. S. B.; Shaik, A. K.; Byram, C.; Hamad, S.; Soma, V. R. Instantaneous Trace Detection of Nitro-Explosives and Mixtures with Nanotextured Silicon Decorated with Ag–Au Alloy Nanoparticles Using the SERS Technique. *Anal. Chim. Acta* **2020**, *1101* (xxxx), 157–168. https://doi.org/10.1016/j.aca.2019.12.026.

(30) Lin, Y.; Zhang, Y.-J.; Yang, W.-M.; Dong, J.-C.; Fan, F.-R.; Zhao, Y.; Zhang, H.; Bodappa, N.; Tian, X.-D.; Yang, Z.-L.; Stucky, G. D.; Tian, Z.-Q.; Li, J.-F. Size and Dimension Dependent Surface-Enhanced Raman Scattering Properties of Well-Defined Ag Nanocubes. *Appl. Mater. Today* **2019**, *14*, 224–232. https://doi.org/10.1016/j.apmt.2018.12.012.

(31) Dharmalingam, P.; Venkatakrishnan, K.; Tan, B. An Atomic-Defect Enhanced Raman Scattering (DERS) Quantum Probe for Molecular Level Detection – Breaking the SERS Barrier. *Appl. Mater. Today* **2019**, *16*, 28–41. https://doi.org/10.1016/j.apmt.2019.04.016.

(32) Inci, F.; Saylan, Y.; Kojouri, A. M.; Ogut, M. G.; Denizli, A.; Demirci, U. A Disposable Microfluidic-Integrated Hand-Held Plasmonic Platform for Protein Detection. *Appl. Mater. Today* **2020**, *18* (xxxx), 100478. https://doi.org/10.1016/j.apmt.2019.100478.

(33) Perales-Rondon, J. V.; Colina, A.; González, M. C.; Escarpa, A. Roughened Silver Microtubes for Reproducible and Quantitative SERS Using a Template-Assisted Electrosynthesis Approach. *Appl. Mater. Today* **2020**, *20*, 100710. https://doi.org/10.1016/j.apmt.2020.100710.

(34) Botta, R.; Rajanikanth, A.; Bansal, C. Silver Nanocluster Films for Glucose Sensing by Surface Enhanced Raman Scattering (SERS). *Sens. Bio-Sensing Res.* **2016**, *9*, 13–16. https://doi.org/10.1016/j.sbsr.2016.05.001.

(35) Han, X. X.; Ji, W.; Zhao, B.; Ozaki, Y. Semiconductor-Enhanced Raman Scattering: Active Nanomaterials and Applications. *Nanoscale* **2017**, *9* (15), 4847–4861. https://doi.org/10.1039/C6NR08693D.

(36) Ma, Y.; Du, Y.; Chen, Y.; Gu, C.; Jiang, T.; Wei, G.; Zhou, J. Intrinsic Raman Signal of Polymer Matrix Induced Quantitative Multiphase SERS Analysis Based on Stretched PDMS Film with Anchored Ag Nanoparticles/Au Nanowires. *Chem. Eng. J.* **2020**, *381* (September 2019), 122710. https://doi.org/10.1016/j.cej.2019.122710.

(37) Ionin, A. A.; Klimachev, Y. M.; Kozlov, A. Y.; Kudryashov, S. I.; Ligachev, A. E.; Makarov, S. V.; Seleznev, L. V.; Sinitsyn, D. V.; Rudenko, A. A.; Khmelnitsky, R. A. Direct Femtosecond Laser Fabrication of Antireflective Layer on GaAs Surface. *Appl. Phys. B* **2013**, *111* (3), 419–423. https://doi.org/10.1007/s00340-013-5350-4.

(38) Choi, K.; Kim, K.; Moon, I. K.; Bang, J.; Oh, J. Subwavelength Photocathodes via Metal-Assisted Chemical Etching of GaAs for Solar Hydrogen Generation. *Nanoscale* **2019**, *11* (32), 15367–15373. https://doi.org/10.1039/c9nr03870a.

(39) Dunaev, A. V.; Barabanov, D. V.; Zhukova, T. A. Nanoscale Structuring of Gallium Arsenide in High-Frequency and Glow Discharge Plasma. *Russ. Microelectron.* **2021**, *50* (4), 246–252. https://doi.org/10.1134/S1063739721040041.

(40) Dejarld, M.; Shin, J. C.; Chern, W.; Chanda, D.; Balasundaram, K.; Rogers, J. A.; Li, X. Formation of High Aspect Ratio GaAs Nanostructures with Metal-Assisted Chemical Etching. *Nano Lett.* **2011**, *11* (12), 5259–5263. https://doi.org/10.1021/nl202708d.

(41) Li, X. Metal Assisted Chemical Etching for High Aspect Ratio Nanostructures: A Review of Characteristics and Applications in Photovoltaics. *Curr. Opin. Solid State Mater. Sci.* **2012**, *16* (2), 71–81. https://doi.org/10.1016/j.cossms.2011.11.002.

(42) Zhao, Y.; Ye, D.; Wang, G.-C.; Lu, T.-M. Designing Nanostructures by Glancing Angle Deposition. In *Nanotubes and Nanowires*; Lakhtakia, A., Maksimenko, S., Eds.; 2003; Vol. 5219, p 59. https://doi.org/10.1117/12.505253.

(43) Trynkiewicz, E.; Jany, B. R.; Janas, A.; Krok, F. Recent Developments in Ion Beam-Induced Nanostructures on AIII-BV Compound Semiconductors. *J. Phys. Condens. Matter* **2018**, *30* (30), 304005. https://doi.org/10.1088/1361-648X/aacc45.

(44) Golosov, E. V.; Ioninb, A. A.; Kolobov, Y. R.; Kudryashov, S. I.; Ligachev, A. E.; Novoselov, Y. N.; Seleznev, L. V.; Sinitsyn, D. V. Ultrafast Changes in the Optical Properties of a Titanium Surface and Femtosecond Laser Writing of One-Dimensional Quasi-Periodic Nanogratings of Its Relief. *J. Exp. Theor. Phys.* **2011**, *113* (1), 14–26. https://doi.org/10.1134/S1063776111050025.

(45) Fu, Y. Q.; Colli, A.; Fasoli, A.; Luo, J. K.; Flewitt, A. J.; Ferrari, A. C.; Milne, W. I. Deep Reactive Ion Etching as a Tool for Nanostructure Fabrication. *J. Vac. Sci. Technol. B Microelectron. Nanom. Struct.* **2009**, *27* (3), 1520. https://doi.org/10.1116/1.3065991.

(46) Mohanta, S. K.; Soni, R. K.; Gosvami, N.; Tripathy, S.; Kanjilal, D. Morphological and Micro-Raman Investigations on Ar + -Ion Irradiated Nanostructured GaAs Surface. *Appl. Surf. Sci.* **2007**, *253* (10), 4531–4536. https://doi.org/10.1016/j.apsusc.2006.10.020.

(47) Zhang, D.; Li, Z.; Sugioka, K. Laser Ablation in Liquids for Nanomaterial Synthesis: Diversities of Targets and Liquids. *J. Phys. Photonics* **2021**, *3* (4), 042002. https://doi.org/10.1088/2515-7647/ac0bfd.

(48) Fazio, E.; Gökce, B.; De Giacomo, A.; Meneghetti, M.; Compagnini, G.; Tommasini, M.; Waag, F.; Lucotti, A.; Zanchi, C. G.; Ossi, P. M.; Dell'Aglio, M.; D'Urso, L.; Condorelli, M.; Scardaci, V.; Biscaglia, F.; Litti, L.; Gobbo, M.; Gallo, G.; Santoro, M.; Trusso, S.; Neri, F. Nanoparticles Engineering by Pulsed Laser Ablation in Liquids: Concepts and Applications. *Nanomaterials* **2020**, *10* (11), 2317. https://doi.org/10.3390/nano10112317.

(49) Hamad, S.; Podagatlapalli, G. K.; Vendamani, V. S.; Nageswara Rao, S. V. S.; Pathak, A. P.; Tewari, S. P.; Venugopal Rao, S. Femtosecond Ablation of Silicon in Acetone: Tunable Photoluminescence from Generated Nanoparticles and Fabrication of Surface Nanostructures. *J. Phys. Chem. C* **2014**, *118* (13), 7139–7151. https://doi.org/10.1021/jp501152x.

(50) Mangababu, A.; Sarang Dev, G.; Chandu, B.; Bharati, M. S. S.; Venugopal Rao, S.; Nageswara Rao, S. V. S. Structural Investigations of Picosecond Laser Ablated GaAs Nanoparticles in Different Liquids. *Nano-Structures & Nano-Objects* **2020**, *23*, 100509. https://doi.org/10.1016/j.nanoso.2020.100509.

(51) Mangababu, A.; Sarang Dev, G.; Chandu, B.; Bharati, M. S. S.; Debashish, P.; Venugopal Rao, S.; Nageswara Rao, S. V. S. Fabrication and Characterization of GaAs Nanoparticles Achieved Using Femtosecond Laser Ablation. *Mater. Today Proc.* **2020**, *33* (5), 2385–2389. https://doi.org/10.1016/j.matpr.2020.05.727.

(52) Byram, C.; Soma, V. R. 2,4-Dinitrotoluene Detected Using Portable Raman Spectrometer and Femtosecond Laser Fabricated Au–Ag Nanoparticles and Nanostructures. *Nano-Structures and Nano-Objects* **2017**, *12*, 121–129. https://doi.org/10.1016/j.nanoso.2017.09.019.

(53) Dostovalov, A.; Bronnikov, K.; Korolkov, V.; Babin, S.; Mitsai, E.; Mironenko, A.; Tutov, M.; Zhang, D.; Sugioka, K.; Maksimovic, J.; Katkus, T.; Juodkazis, S.; Zhizhchenko, A.; Kuchmizhak, A. Hierarchical Anti-Reflective Laser-Induced Periodic Surface Structures (LIPSSs) on Amorphous Si Films for Sensing Applications. *Nanoscale* **2020**, *12* (25), 13431–13441. https://doi.org/10.1039/d0nr02182b.

(54) Zhang, D. S.; Sugioka, K. Hierarchical Microstructures with High Spatial Frequency Laser Induced Periodic Surface Structures Possessing Different Orientations Created by Femtosecond Laser Ablation of Silicon in Liquids. *Opto-Electronic Adv.* **2019**, *2* (3), 1–19. https://doi.org/10.29026/oea.2019.190002.

(55) Ionin, A. A.; Kudryashov, S. I.; Makarov, S. V. Femtosecond Laser-Induced Periodical Nanomodification of Surface Composition. *Semiconductors* **2019**, *53* (16), 2094–2099. https://doi.org/10.1134/S106378261912011X.

(56) Ionin, A. A.; Kudryashov, S. I.; Seleznev, L. V.; Sinitsyn, D. V. Dynamics of the Spallative

Ablation of a GaAs Surface Irradiated by Femtosecond Laser Pulses. *JETP Lett.* **2012**, *94* (10), 753–758. https://doi.org/10.1134/S002136401122005X.

(57) Salminen, T.; Dahl, J.; Tuominen, M.; Laukkanen, P.; Arola, E.; Niemi, T. Single-Step Fabrication of Luminescent GaAs Nanocrystals by Pulsed Laser Ablation in Liquids. *Opt. Mater. Express* **2012**, *2* (6), 799. https://doi.org/10.1364/OME.2.000799.

(58) Song, J. S.; Choi, Y. C.; Seo, S. H.; Oh, D. C.; Cho, M. W.; Yao, T.; Oh, M. H. Wet Chemical Cleaning Process of GaAs Substrate for Ready-to-Use. *J. Cryst. Growth* **2004**, *264* (1–3), 98–103. https://doi.org/10.1016/j.jcrysgro.2003.12.063.

(59) Zhou, W.; Chen, X. J.; Zhang, J. B.; Li, X. H.; Wang, Y. Q.; Goncharov, A. F. Vibrational, Electronic and Structural Properties of Wurtzite GaAs Nanowires under Hydrostatic Pressure. *Sci. Rep.* **2014**, *4*, 1–5. https://doi.org/10.1038/srep06472.

(60) Im, H. S.; Park, K.; Kim, J.; Kim, D.; Lee, J.; Lee, J. A.; Park, J.; Ahn, J. P. Strain Mapping and Raman Spectroscopy of Bent GaP and GaAs Nanowires. *ACS Omega* **2018**, *3* (3), 3129–3135. https://doi.org/10.1021/acsomega.8b00063.

(61) Sharifi, T.; Dorranian, D.; Torkamany, M. J. Optimisation of GaAs Nanocrystals Synthesis by Laser Ablation in Water. *J. Exp. Nanosci.* **2013**, *8* (6), 808–817. https://doi.org/10.1080/17458080.2011.608729.

(62) Malik, M. A.; O'Brien, P.; Norager, S.; Smith, J. Gallium Arsenide Nanoparticles: Synthesis and Characterisation. *J. Mater. Chem.* **2003**, *13* (10), 2591. https://doi.org/10.1039/b305860n.

(63) Sheik-Bahae, M.; Said, A. A.; Wei, T. H.; Hagan, D. J.; Van Stryland, E. W. Sensitive Measurement of Optical Nonlinearities Using a Single Beam. *IEEE J. Quantum Electron.* **1990**, *26* (4), 760–769. https://doi.org/10.1109/3.53394.

(64) Bonse, J.; Gräf, S. Maxwell Meets Marangoni—A Review of Theories on Laser-Induced Periodic Surface Structures. *Laser Photon. Rev.* **2020**, *14* (10), 2000215. https://doi.org/10.1002/lpor.202000215.

(65) Nakamura, S.; Hibiya, T. Thermophysical Properties Data on Molten Semiconductors. *Int. J. Thermophys.* **1992**, *13* (6), 1061–1084. https://doi.org/10.1007/BF01141216.

(66) Ozawa, S.; Eguchi, M.; Fujii, T.; Fukuda, T. Increase of Effective Viscosity of Molten GaAs and InSb under an Axial Magnetic Field. *Appl. Phys. Lett.* **1987**, *51* (3), 197–199. https://doi.org/10.1063/1.98921.

(67) Rupp, R.; Müller, G. Experimental Study of the Surface Tension of Molten GaAs and Its Temperature Dependence under Controlled As-Vapor Pressure. *J. Cryst. Growth* **1991**, *113* (1–2), 131–139. https://doi.org/10.1016/0022-0248(91)90018-Z.

(68) Ionin, A. A.; Kudryashov, S. I.; Ligachev, A. E.; Makarov, S. V; Mel'nik, N. N.; Rudenko, A. A.; Seleznev, L. V; Sinitsyn, D. V; Khmelnitskii, R. A. Local Field Enhancement on Metallic Periodic Surface Structures Produced by Femtosecond Laser Pulses. *Quantum Electron.* **2013**, *43* (4), 304–

307. https://doi.org/10.1070/qe2013v043n04abeh015105.

(69) Rajan, R. A.; Ngo, C. V.; Yang, J.; Liu, Y.; Rao, K. S.; Guo, C. Femtosecond and Picosecond Laser Fabrication for Long-Term Superhydrophilic Metal Surfaces. *Opt. Laser Technol.* **2021**, *143* (April), 107241. https://doi.org/10.1016/j.optlastec.2021.107241.

(70) Ahmad, D.; van den Boogaert, I.; Miller, J.; Presswell, R.; Jouhara, H. Hydrophilic and Hydrophobic Materials and Their Applications. *Energy Sources, Part A Recover. Util. Environ. Eff.* **2018**, *40* (22), 2686–2725. https://doi.org/10.1080/15567036.2018.1511642.

(71) Kim, B.-J.; Kim, J. Fabrication of GaAs Subwavelength Structure (SWS) for Solar Cell Applications. *Opt. Express* **2011**, *19* (S3), A326. https://doi.org/10.1364/oe.19.00a326.

(72) Lee, Y.-C.; Chang, C.-C.; Chou, Y.-Y. Experimental and Simulation Studies of Anti-Reflection Sub-Micron Conical Structures on a GaAs Substrate. *Opt. Express* **2013**, *21* (S1), A36. https://doi.org/10.1364/oe.21.000a36.

(73) Madéo, J.; Margiolakis, A.; Zhao, Z.-Y.; Hale, P. J.; Man, M. K. L.; Zhao, Q.-Z.; Peng, W.; Shi, W.-Z.; Dani, K. M. Ultrafast Properties of Femtosecond-Laser-Ablated GaAs and Its Application to Terahertz Optoelectronics. *Opt. Lett.* **2015**, *40* (14), 3388. https://doi.org/10.1364/OL.40.003388.

(74) Nguyen, T. B.; Nguyen, N. A.; Ngo, G. L. A Simple and Rapid Method to Produce SERS Substrates Using Au Nanoparticles Prepared by Laser Ablation and DVD Template. *J. Electron. Mater.* **2020**, *49* (1), 311–317. https://doi.org/10.1007/s11664-019-07754-x.

(75) Naqvi, T. K.; Bajpai, A.; Dwivedi, S.; Bhaiyya, M.; Goel, S.; Dwivedi, P. K. Flexible, Label Free and Low-Cost Paper Based Microfluidic SERS Substrates for Thiram Detection. *Sensors Actuators A Phys.* **2023**, *356* (January), 114341. https://doi.org/10.1016/j.sna.2023.114341.

(76) Pilot, R.; Signorini, R.; Durante, C.; Orian, L.; Bhamidipati, M.; Fabris, L. A Review on Surface-Enhanced Raman Scattering. *Biosensors*. April 17, 2019, p 57. https://doi.org/10.3390/bios9020057.

(77) Zhang, X.; Lei, Z.; Pan, Z.; Hu, J.; Tao, L.; Zheng, Z.; Feng, X.; Xue, J.; Tao, L.; Zhao, Y. A General Approach to Hybrid Platform of Au Nanoparticles on Monolayer Semiconductor for Ultrasensitive Raman Enhancement of 2D Materials and Molecule Detection. *J. Alloys Compd.* **2023**, *938*, 168468. https://doi.org/10.1016/j.jallcom.2022.168468.

(78) Guselnikova, O.; Lim, H.; Kim, H.; Kim, S. H.; Gorbunova, A.; Eguchi, M.; Postnikov, P.; Nakanishi, T.; Asahi, T.; Na, J.; Yamauchi, Y. New Trends in Nanoarchitectured SERS Substrates: Nanospaces, 2D Materials, and Organic Heterostructures. *Small* **2022**, *18* (25), 2107182. https://doi.org/10.1002/smll.202107182.

(79) Hamad, A. H.; Khashan, K. S.; Hadi, A. A. Laser Ablation in Different Environments and Generation of Nanoparticles. In *Applications of Laser Ablation - Thin Film Deposition, Nanomaterial Synthesis and Surface Modification*; InTech, 2016. https://doi.org/10.5772/65241.

(80) Besner, S.; Degorce, J.-Y.; Kabashin, A. V.; Meunier, M. Surface Modifications during Femtosecond Laser Ablation in Vacuum, Air, and Water. *Photonics North 2004 Photonic Appl. Astron. Biomed. Imaging, Mater. Process. Educ.* **2004**, *5578* (February 2014), 554. https://doi.org/10.1117/12.567746.

(81) Zhu, S.; Lu, Y. F.; Hong, M. H.; Chen, X. Y. Laser Ablation of Solid Substrates in Water and Ambient Air. *J. Appl. Phys.* **2001**, *89* (4), 2400–2403. https://doi.org/10.1063/1.1342200.

(82) Abere, M. J.; Torralva, B.; Yalisove, S. M. Periodic Surface Structure Bifurcation Induced by Ultrafast Laser Generated Point Defect Diffusion in GaAs. *Appl. Phys. Lett.* **2016**, *108* (15), 153110. https://doi.org/10.1063/1.4946861.

Chapter 5

Effects of Laser fluence on the GaAs periodic surface structures achieved by femtosecond laser ablation in Air and Distilled Water

In this chapter, fabrication of periodic surface structures on GaAs is presented. At various laser energies, single line scans are performed in air and DW media, the morphology is thoroughly analyzed and the corresponding mechanisms are predicted. Once the energy of the laser is optimized for the formation of good quality LIPSS, the large area structures are made with the optimized energy, coated with the plasmonic Au thin film, then its SERS based sensing applications are explored. Structures produced in air medium are presented in the Part-A of this chapter and structures produced in DW are presented in Part-B.

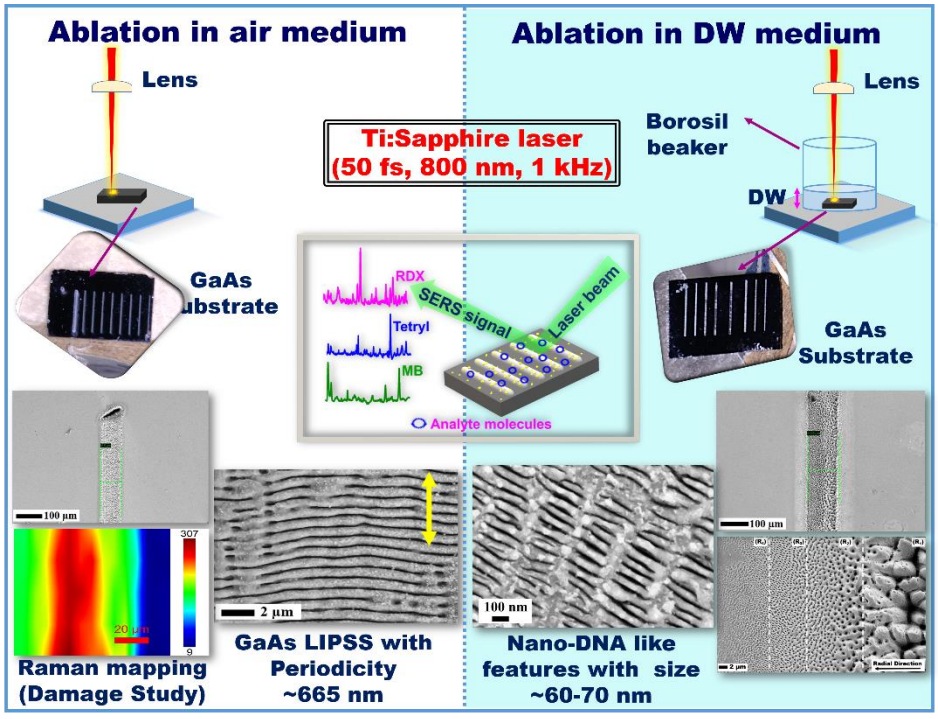

Graphical abstract

Publications from this chapter

1. Mangababu Akkanaboina, Dipanjan Banerjee, Kanaka Ravi Kumar, R. Sai Prasad Goud, Venugopal Rao Soma, S. V. S. Nageswara Rao, Gold nanoparticles coated LIPSS on GaAs for trace detection of RDX and Tetryl, Surfaces and Interfaces 36 (2023) 102563. DOI; 10.1016/j.surfin.2022.102563.
2. Mangababu Akkanaboina, Dipanjan Banerjee, Kanaka Ravi Kumar, R. Sai Prasad Goud, Venugopal Rao Soma, S. V. S. Nageswara Rao, Sub-100 nm DNA-like Surface Structures on Femtosecond Laser Irradiated GaAs in Distilled Water for Sensing Application, Optics Letters (under review).

Chapter 5 (Part-A)

Gold nanoparticles coated LIPSS on GaAs for trace detection of RDX and Tetryl

In this work, by varying the input pulse energy from 5 µJ to 100 µJ, single laser scan lines were drawn. The sub-wavelength LIPSS produced inside each line were thoroughly examined, and the origin of LIPSS formation was attributed to the electromagnetic interactions between the incident laser light and the surface plasmon polaritons (especially, SIPE-Drude model). The periodicity (663±16 nm) was nearly same for all energies in the range of 5 µJ to 100 µJ, indicating that these GaAs-LIPSS have acceptable quality throughout vast ablation energies. However, with the increase in laser energy there is an increase in the oxidation of LIPSS. Hence, at an optimized energy of 5 µJ, a set of GaAs-LIPSS was created in a 2×2 mm^2 region. To investigate the laser-induced damage on these structures, photoluminescence and Raman investigations were carried out.

Further, these samples were coated with a 25 nm gold layer and annealed at 400 °C in ambient conditions. The plasmonic Au nanoparticles coated GaAs-LIPSS that resulted were employed as SERS substrates for sensing dye (MB) and explosives (RDX, Tetryl) molecules. Enhancement factors of 10^5 and 10^4 (lowest observed concentrations of 10^{-9} M and 10^{-5} M) were observed, respectively, for dye and explosive molecules. These findings, we hope, will aid in the development of GaAs-LIPSS with lower feature sizes for enhanced sensing and optoelectronic applications.

5.1.0. Introduction

Understanding the device applications of subwavelength periodic surface structures in areas like photonics, electronics, optoelectronics, etc. is crucial[1–4]. The possibility to develop highly effective, quick, and affordable devices has increased the significance of synthesizing novel periodic surface structures on many technologically significant materials[5–7]. In some particular applications, these periodic surface patterns in nano-dimensions provide improved characteristics compared to their smooth, bulk substrates[8–10]. The increased capabilities of these nano-dimensional periodic surface structures may be due to a variety of factors, including higher surface-to-volume ratios, dangling or open bonds on the surfaces, and periodic distribution of surface features/fields[11–15]. The synthesis of the aforementioned periodic surface structures can be accomplished using a variety of manufacturing techniques. Some of them

include hydrothermal synthesis[16], wet chemical etching[17,18], selective reactive ion etching[19,20], ion radiation[21], laser radiation[14,22], etc. When compared to the other available methods, laser irradiation is a quick and versatile production method with its own advantages, hence it is used as the synthesis method in the current work[23,24]. LIPSS are already being created on a variety of materials[25], including dielectrics (ZrO_2, HfO_2, fused silica, etc.)[26,27], semiconductors (Si, Ge, GaAs, GaN, etc.)[15,28], and metals (Fe, Ag, Au, W, stainless steel, etc.)[29–32]. The nature of the material as well as the input laser parameters such as wavelength, fluence, polarization, and incident angle determine the size, shape, and orientation of these LIPSS[11,25,33,34].

The periodicity of the LIPSS can be changed by varying the laser wavelengths, fluences, and number of pulses[34]. LIPSS orientation is mostly determined by the laser polarisation direction and incident angle[35]. In the case of normal incidence, however, the ripples/LIPSS will be either parallel or perpendicular to the laser polarization direction. The exact reliance of this orientation is linked to the interplay of incident and scattered laser light from the ablating material's surface[36]. Nanostructured metallic surfaces have been extensively studied in research and industrial applications during the last two decades[37–39]. Nanostructured semiconductors, as compared to metal counterparts, have enormous potential in a variety of disciplines due to their tunable optical and electrical properties. GaAs, in particular, has a wide range of applications in electronics, optoelectronics, solar cell studies, radiation sensors, quantum LEDs, etc.[40]. As a result, studying GaAs subwavelength surface patterns is critical for understanding their characteristics and potential applications[41]. Using an ultrashort laser (744 nm, 100 fs), Ionin and co-workers[42–44] recently created GaAs LIPSS and investigated the variations in chemical composition along the grooves and ridges of the nano-ripples. They also used fs pulses to create a large-scale diffractive nano-grating on a GaAs surface for antireflection applications. Margiolakis et al.[41] studied the ultrafast dynamics that occur when a femtosecond laser interacts with GaAs. The main responsible process for the creation of LIPSS in GaAs was demonstrated to be surface plasmon polaritons (SPP) excitation. Previously, our group demonstrated the simultaneous manufacturing of GaAs NPs and NSs in a single experiment using a picosecond laser, and demonstrated their potential in photonic, antireflective, and surface enhanced Raman scattering/spectroscopy (SERS) applications (This work is presented in previous chapter).

According to the majority of findings in the literature, the SIPE-Drude model is well accepted in explaining the creation of LIPSS in semiconductors[34]. The initial few laser pulses hit the smooth surface, causing some roughness. Its roughened surface aids in the stimulation of SPPs

along the sample's surface that interacts with the laser's electromagnetic field, resulting in the periodic dissipation of laser energy. This periodic dissipation of energy modifies the surface, creating periodic ripples. Despite the fact that this is a well-known phenomenon for the production of ripples in semiconductors, particularly GaAs, there are a few claims that the creation of ripples is associated with material reorganization / diffusion of defects. For example, Michael et al.[45] employed fs laser irradiation to create GaAs LIPSS and claimed that the generation of high spatial frequency LIPSS was related to defect diffusion-induced bifurcation of the low spatial frequency LIPSS. Alex et al.[46] determined from their extensive analyses that surface defect creation and atomic constituent desorption are the potential mechanisms in the formation of the LIPSS. These experiments also demonstrated that the ablation surroundings and laser fluence have an effect on the mechanisms of LIPSS development. As a result, comprehensive experimentation is required to have a concise understanding of the GaAs LIPSS creation mechanisms. Hence, in this study, a GaAs (100) wafer was utilized to generate LIPSS using the fs ablation in air and varying the input laser energy from 5 µJ to 100 µJ while maintaining all other laser parameters constant throughout the experiment. FESEM, Raman, and PL studies were used to examine the morphology and basic physicochemical characteristics. Additionally, plasmonic Au deposition on these GaAs LIPSS accompanied by thermal annealing resulted in the development of SERS substrates, which were employed for sensing a dye molecule [Methylene blue (MB)] and explosive molecules (RDX and Tetryl).

5.1.1 Experimental Details

5.1.1 (a) Laser ablation

For the synthesis of GaAs LIPSS, a femtosecond amplifier with pulse duration ~50 fs, repetition rate ~1 kHz, central wavelength ~800 nm, and varying input laser energies from 5 µJ to 100 µJ were employed. Laser beam was focused onto the sample mounted on a 2D translational stage using a plano-convex lens (focal length ~10 cm). Single laser scan patterns of 5 mm long were initially drawn using varying laser energies (5, 10, 15, 20, 25, 30, 40, 50, and 100 µJ), as shown in the schematic Fig.5.1. For drawing these lines, the stage was moved at an optimized scan speed of 0.25 mm/s in 1D (i.e., let us say Y-direction). After thorough understanding of the scan lines drawn at different laser energies, a laser energy of 5 µJ was chosen for making full structures of area 2×2 mm^2 for realizing SERS based sensing applications. For drawing these structures, stage is moved at 0.25 mm/s in 2D (i.e., both in X and Y-directions).

5.1.1 (b) Synthesis of decorated Au NPs on GaAs LIPSS

Thermal evaporation was used to coat Au film (25 nm) on the aforementioned GaAs LIPSS samples. After attaining a vacuum of ~10^{-6} mbar, deposition was started at a rate of ~1 Å/s. During the deposition a vacuum of ~10^{-5} mbar was noticed. Additionally, to decorated Au NPs on the ridges of the LIPSS, these gold-coated GaAs LIPSS samples were annealed at a temperature of 400 °C in a tubular furnace.

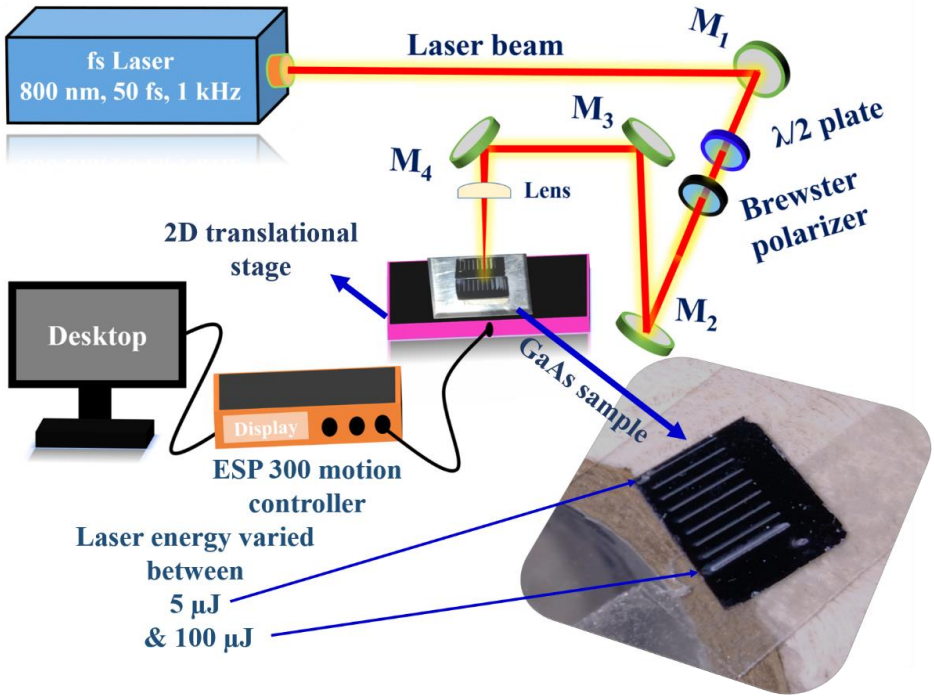

Fig. 5.1 Schematic of femtosecond laser ablation setup.

5.1.2 Results and Discussion

Production and understanding of GaAs LIPSS with the smallest feasible feature sizes is critical for optoelectronics and sensing applications. Despite a few investigations in this area, the mechanics of GaAs LIPSS production are still debated[34,41–46]. To understand the ultrafast phenomena that occur when a fs laser interacts with GaAs substrates, as well as the effect of laser pulse energy on GaAs LIPSS, single line laser scans are drawn at various laser energies ranging from 5 µJ to 100 µJ, as shown in Fig. 5.1. Figure 5.2 (a-i) show the FESEM images relating to these individual scan lines at laser energies of 5, 10, 15, 20, 25, 30, 35, 40, 50, and 100 µJ, respectively.

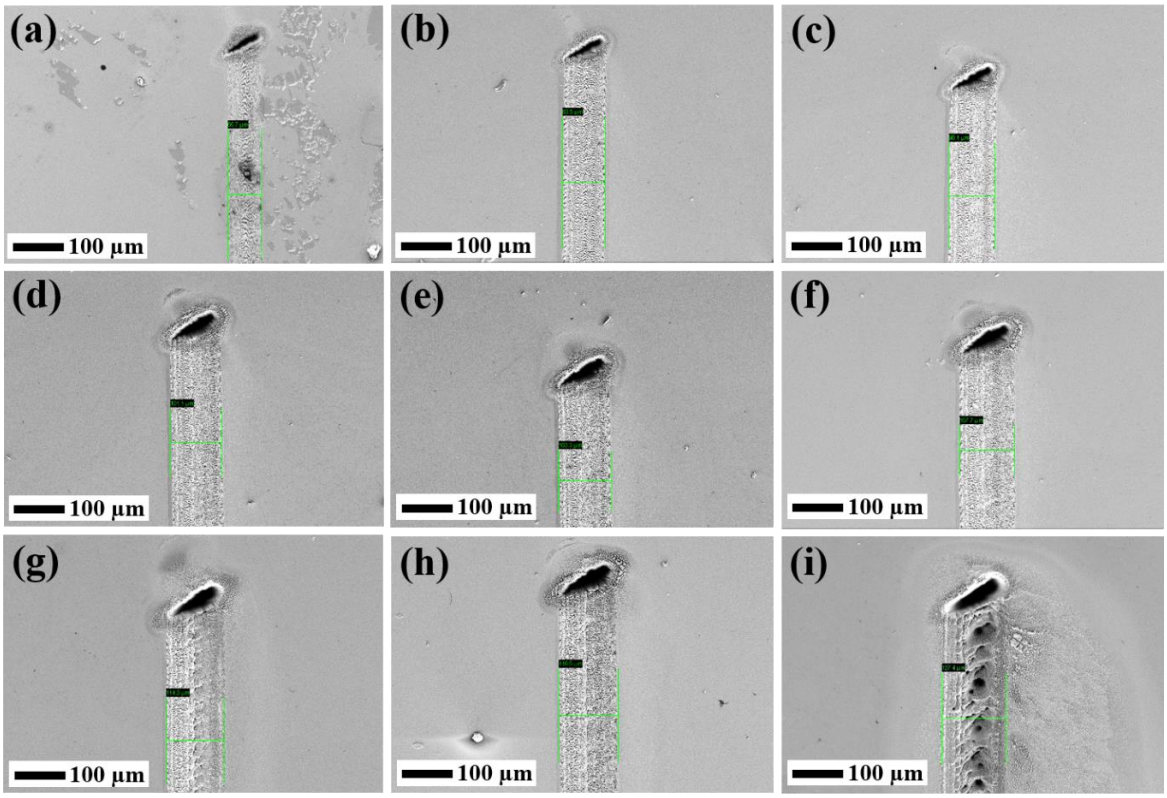

Fig. 5.2 FESEM images of the laser ablated tracks on GaAs substrate at various laser energies (a) 5 µJ, (b) 10 µJ, (c) 15 µJ, (d) 20 µJ, (e) 25 µJ, (f) 30 µJ, (g) 40 µJ, (h) 50 µJ, and (i) 100 µJ.

The width of the resulting scan lines varies from 60 µm to 130 µm as the laser energy increases from 5 µJ to 100 µJ. The creation of crater-like formations at the scan starting position for each line is noticed, which could be caused by the larger number of pulses colliding when focusing the laser. The production of such craters when an ultrafast (plane polarized) laser interacts with semi-conductors is well-known and has been observed by Lenzner et al.[47] and others[48,49]. The experimentally measured structural widths were 3-4 times greater than the theoretically expected single pulse spot size (20 µm). We believe that the estimated/theoretical spot size is the ideal scenario, however the experiments may not have ideal optics. Furthermore, this theoretical spot size is the radial range where the intensity drops to $1/e^2$ of the peak intensity [i.e., when I drop to 13.6% of I_o, as illustrated in Section 5.1.3, Fig. 5.8 (b)]. The tail of the Gaussian beam, on the other hand, comprises light with a lower intensity [0.1-13.6% of I_o]. According to Abere et al.[50], the single pulse ablation threshold for GaAs is 0.1 J/cm^2, implying that the multi-pulse ablation threshold will be substantially lower. As a result, in our scenario, the tail of the laser beam will also ablate GaAs. Due to the imprecise stage motion during laser scanning, there may be extra ablation effects along both sides of the scan line, as documented in literature and well acknowledged in several researchers on laser

welding/machining[51,52]. Furthermore, experimental widths may also increase due to little spillover of hot plasma, overlap of laser pulses, and energy of each pulse etc.[53]. Borowiec et al.[53,54] reported on energy dependent laser ablated width variations. The most intriguing outcome is that the formation nano-dimensional GaAs LIPSS within each of the aforementioned laser scan lines. The FESEM imaging was used to conduct a complete investigation within these lines (shown in Fig. 5.2). For laser energy of 5 µJ, 10 µJ, 15 µJ, 20 µJ, 25 µJ, 30 µJ, 40 µJ, 50 µJ, and 100 µJ, respectively, the LIPSS on GaAs are shown in Fig. 5.3(a)-(i). Large area LIPSS were generated at all energies from 5 µJ to 50 µJ, and at an energy of 100 µJ, there was a re-deposition of debris or damage.

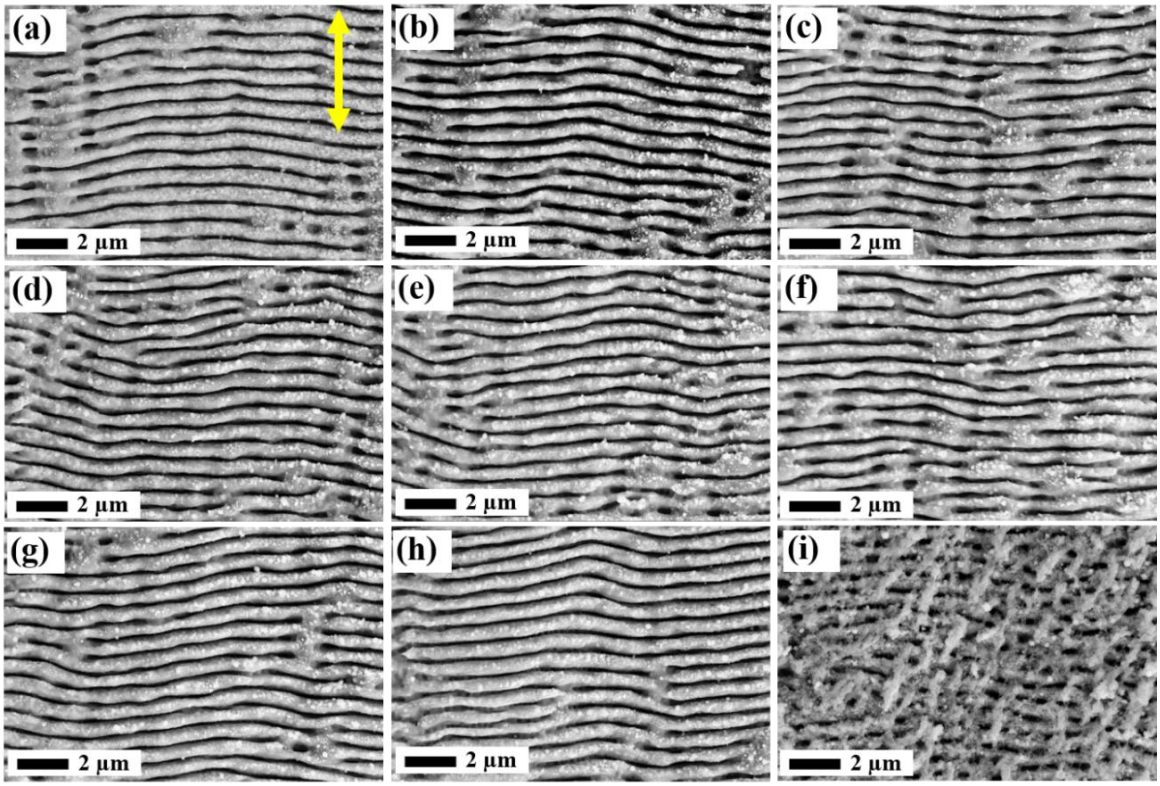

Fig. 5.3 FESEM images of GaAs LIPSS formed inside each laser scan lines shown in Fig. 5.2, at various laser input energies (a)-(i) 5 µJ, 10 µJ, 15 µJ, 20 µJ, 25 µJ, 30 µJ, 40 µJ, 50 µJ, and 100 µJ, respectively. Yellow colored double-sided arrow in (a) represents the laser polarization direction and the laser writing direction.

Now, for obtaining the periodicity, the grey value versus distance curves shown in Fig. 5.4 were computed using FESEM images [Fig. 5.3 (a-i)] and Gwydion software[55]. At input laser energy from 5 µJ, 10 µJ, 15 µJ, 20 µJ, 25 µJ, 30 µJ, 40 µJ, 50 µJ, and 100 µJ, respectively, the LIPSS have periodicities of 665 nm, 697 nm, 671 nm, 666 nm, 642 nm, 670 nm, 649 nm, 650 nm, and 660 nm. Regardless of laser energy, these LIPSS have nearly identical periodicity, with an average value of 663±16 nm.

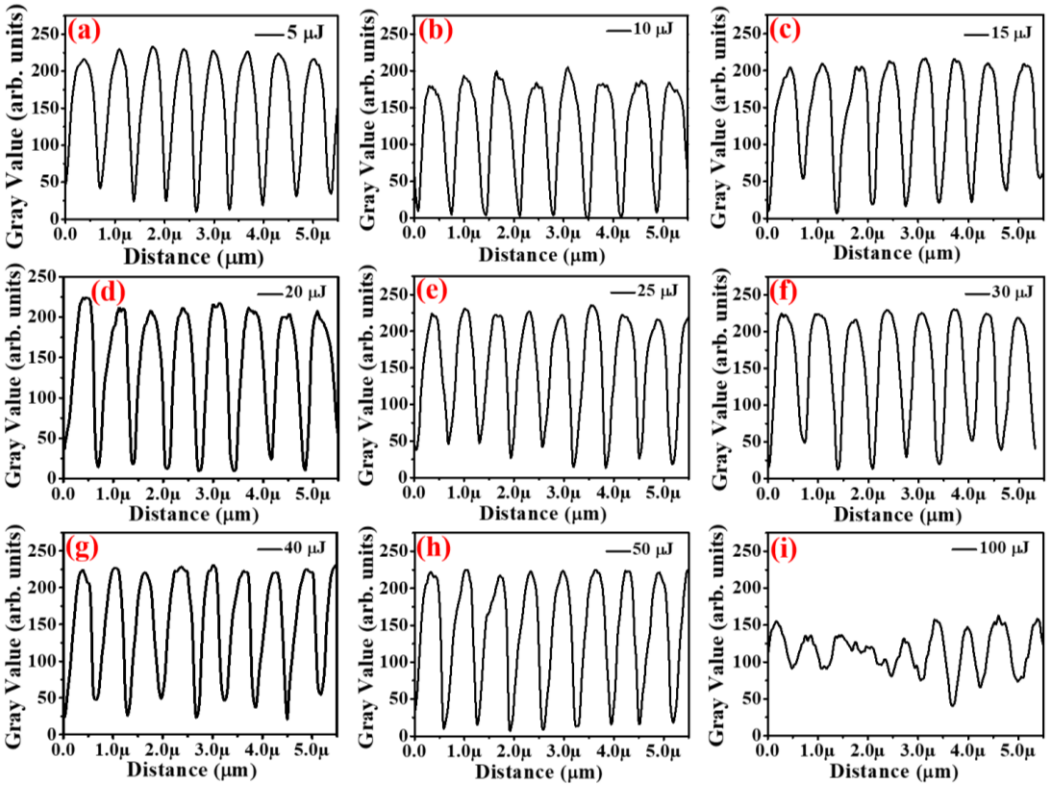

Fig. 5.4 Grey value vs distance spectra for LIPSS created on GaAs substrate at various energies (a) 5 μJ, (b) 10 μJ, (c) 15 μJ, (d) 20 μJ, (e) 25 μJ, (f) 30 μJ, (g) 40 μJ, (h) 50 μJ, and (i) 100 μJ, respectively.

These findings demonstrated that within a range of 5 μJ to 100 μJ, the GaAs LIPSS periodicity is independent of laser energy. Also, it was observed that the LIPSS orientation was perpendicular to the laser polarization direction [Fig. 5.3 (a), double-sided arrow denotes the polarization direction]. For the readers' convenience, Table 5.1 below summarizes the periodicity, laser energy, and laser fluence. Equation (5.1) was used to calculate the fluence supplied at the surface while taking into account the theoretical or estimated laser spot size (*D*) of 20 μm and the pulse energy (*E*).

$$F = \frac{E}{\pi\left(\frac{D}{2}\right)^2} \qquad J/cm^2 \ldots\ldots\ldots\ldots \textbf{(5.1)}$$

Table 5.1. Laser energy, fluence, and LIPSS periodicity.

S. No.	Laser energy (μJ)	Laser fluence (J/cm^2)	Periodicity (Λ) (nm)
1	5	1.59	665
2	10	3.18	697
3	15	4.77	671
4	20	6.36	666
5	25	7.96	642
6	30	9.55	670
7	40	12.73	649
8	50	15.92	650
9	100	31.84	660

5.1.3 GaAs LIPSS Formation mechanism

GaAs LIPSS produced inside each scan line was thoroughly examined to acquire more information about its formation mechanisms. Figure 5.5 (a) displays the FESEM image of the entire laser scan line created at 5 µJ. Figures 5.5 (b-d) depict broken/pore-like structures produced at the left edge of the ablated track drawn on GaAs, Figs. 5.5 (e-g) depict homogeneously created GaAs LIPSS at the middle of the laser scan track, and Figs. 5.5 (h-j) depict broken structures captured at the right edge of the track. Similar analysis was performed for the laser ablated track at 30 µJ [See Fig. 5.6 (a)]. At the middle region of the line, we saw GaAs LIPSS over a significant area, while at the central portion, there was a crack [as shown in Fig. 5.6 (e-g)], which may have been caused by the high energy/fluence that was deposited [30 µJ/9.55 J/cm^2]. As can be seen in Fig. 5.6 (b-d, h-j), broken structures were created at the outer edges. There was a total damage and re-deposition in the case of track drawn at an energy of 100 µJ (fluence ~31.84 J/cm^2) [See Fig. 5.7 (a)]. Figures 5.7 (b-d) exhibit the GaAs LIPSS loaded with debris at the left edge of the laser scan line (blue dotted box). Huge craters created in the center of the laser scan line were depicted in Fig. 5.7 (e-g) (yellow dotted rectangle). The images in Fig. 5.7 (h-j) were captured near the right edge of the laser scan line, which was indicated by the magenta dotted box.

This investigation makes it clear that the GaAs LIPSS were produced perpendicular to the scan direction and also to the laser polarization direction. These LIPSS were evenly created at the center of the track. They were observed to be immaturely growing or resembling broken constructions as we moved towards the edges. Within grooves (between LIPSS), small holes with typical sizes of 200-300 nm were also seen. These kinds of tiny holes were earlier observed by Santiago et al.[56]. Although the precise cause of the creation of these craters was unknown, they might have been caused by the effective laser fluence that was applied at various locations on the sample.

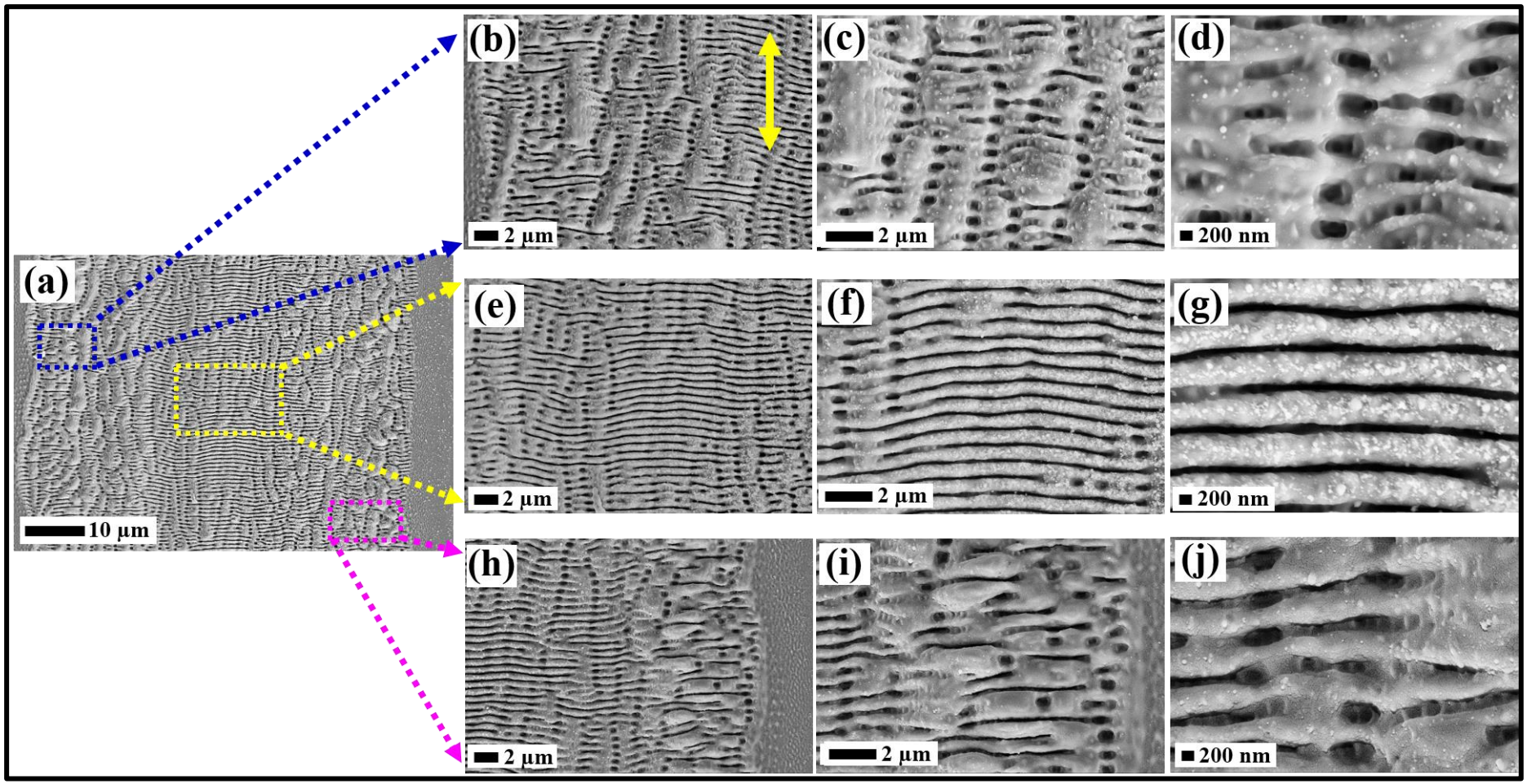

Fig. 5.5 (a) FESEM image of laser ablated track on GaAs at an energy of 5 µJ, three different magnification images recorded (b-d) at left edge of the laser scan line as marked by rectangular blue dotted lines, (e-g) at central part of the laser scan line as marked by rectangular yellow dotted lines, (h-j) at right edge of the laser scan line as marked by rectangular magenta dotted lines. The double-sided yellow arrow in (b) represents the laser polarization direction.

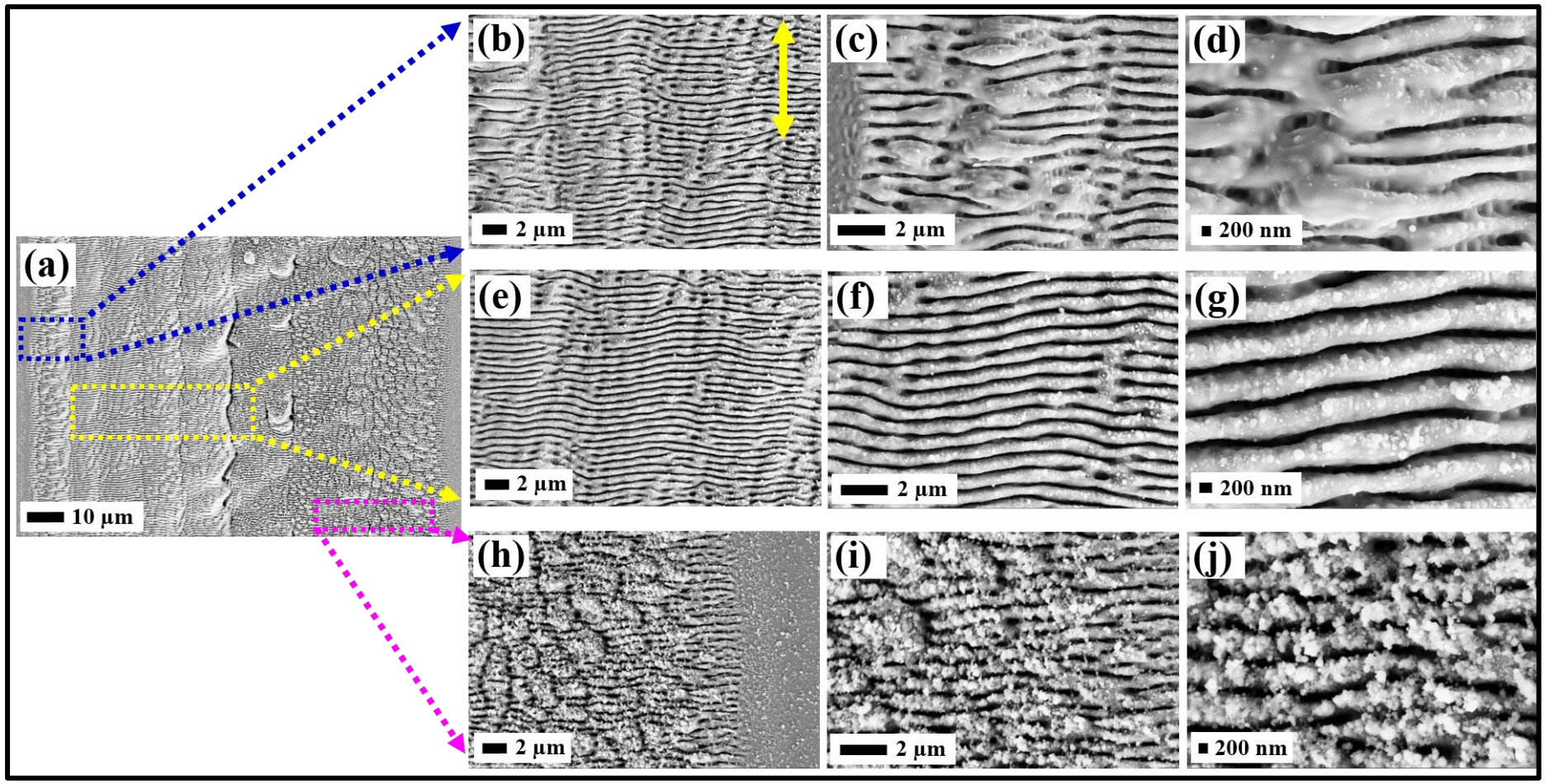

Fig. 5.6 (a) FESEM image of laser scan line drawn on GaAs at an energy of 30 µJ, three different magnification images recorded (b-d) at left edge of the laser scan line as marked by rectangular blue dotted lines, (e-g) at central part of the laser scan line as marked by rectangular yellow dotted lines, (h-j) at right edge of the laser scan line as marked by rectangular magenta dotted lines. The double-sided yellow arrow in (b) represents the laser polarization direction.

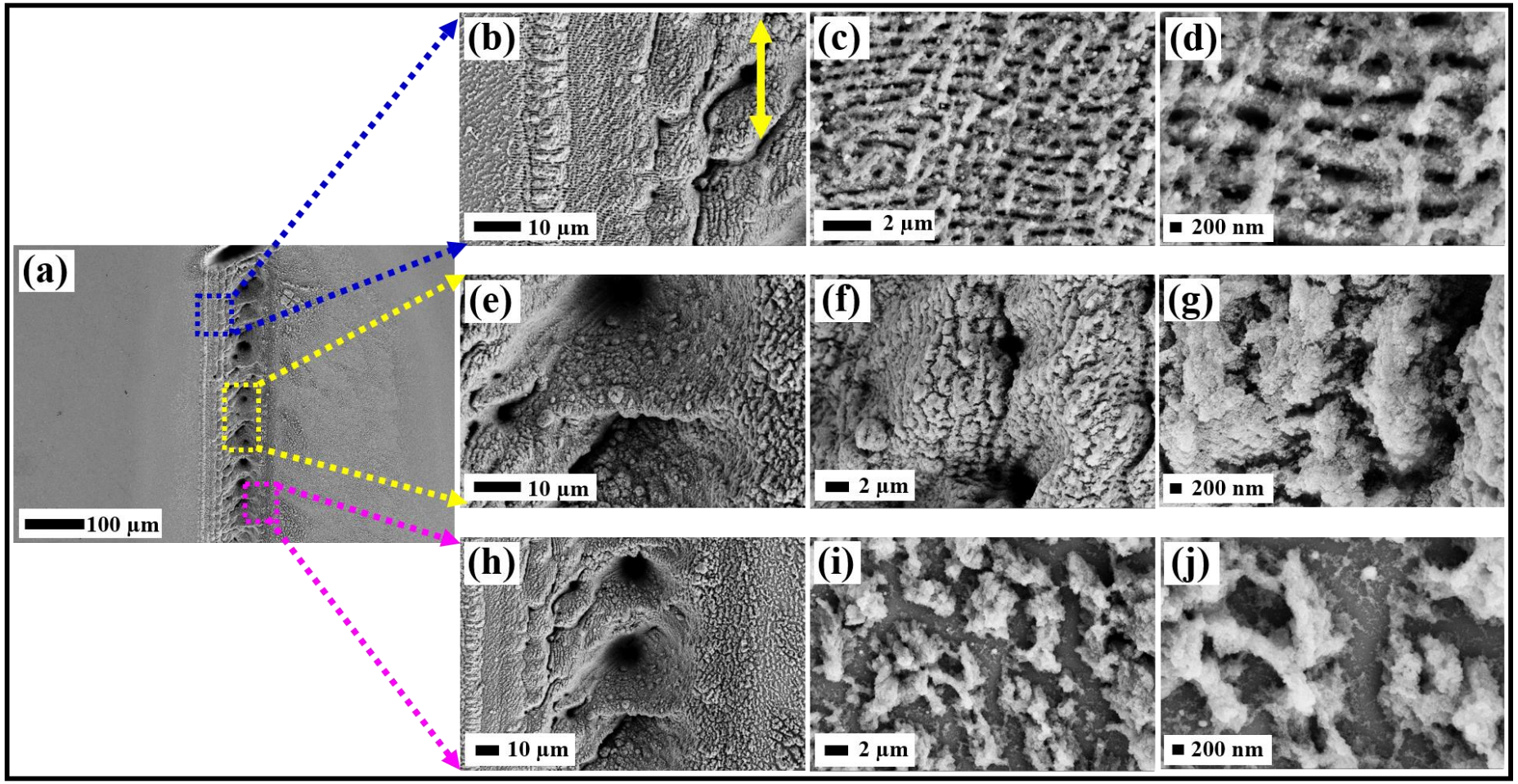

Fig. 5.7 (a) FESEM image of laser scan line drawn on GaAs at an energy of 100 µJ, three different magnification images recorded (b-d) at left edge of the laser scan line as marked by rectangular blue dotted lines, (e-g) at central part of the laser scan line as marked by rectangular yellow dotted lines, (h-j) at right edge of the laser scan line as marked by rectangular magenta dotted lines. The double-sided yellow arrow in (b) represents the laser polarization direction.

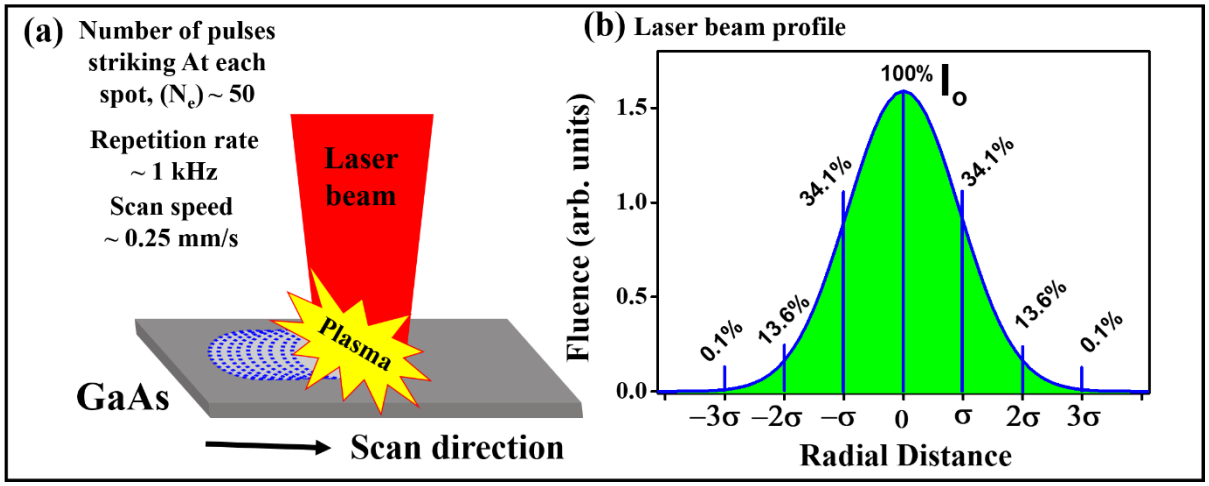

Fig. 5.8 (a) Schematic representation of effective number of pulses hitting GaAs in each spot before the laser moves to the next spot, (b) laser beam profile showing radial fluence variation from the center to tails.

As a result, the Gaussian beam's radial fluence variation [as depicted in Fig. 5.8 (b)] is the significant factor affecting LIPSS quality. For the GaAs LIPSS at 5 µJ laser irradiation, the higher irradiance at the middle of scan line would have resulted in fewer craters and high quality LIPSS, and lower fluence/other ablation processes at the edges could have supported the production of a larger number of craters. In order to fully comprehend the origin of such craters, more in-depth investigation is required in this direction. The periodicity of LIPSS (663 nm) and the laser wavelength employed (800 nm) are related as $\Lambda = 0.8\lambda$ (i.e., $\Lambda > \lambda/2$). So, these patterns belong to the category of low spatial frequency LIPSS (LSFL)[34].

Additionally, with a laser scanning rate of 0.25 mm/s, repetition rate of 1 kHz the effective number of pulses hitting the GaAs surface (N_{eff}) is calculated to be 50 inside a region defined by the theoretically estimated laser spot size (20 µm) (See equation. 5.2, adopted from ref.[57]).

$$N_{eff} = \sqrt{\pi/2}\,\frac{\omega f}{v} \ldots\ldots\ldots\ldots \textit{(5.2)},$$

Where, ω, f, and $\boldsymbol{v}$ are laser spot radius, repetition rate, and scan speed, respectively. Thus, these GaAs LIPSS are generated by multi-shot ablation process with an overlap of ~50 pulses impacting at each spot area before the beam passes to the next spot [As shown in Fig. 5.8 (a)]. The initial laser pulses interact with smooth surface of GaAs and create roughness, this roughened surface enables excitation of surface plasmon polaritons (SPPs) [see, ref. 65]. These SPPs provides intra-pulse feedback mechanism which helps the creation of periodic structures (LIPSS)[41]. Though the SPP model (or SIPE's theory) is well established for the metallic surfaces having enormous number of free charge carriers, it can also be used to explain the creation of LIPSS on semiconductors. According to Bonse et al.[58], the integration of the

SIPE theory with Drude model fits well for explaining the GaAs LIPSS. As per the Drude model, laser irradiation causes variations in the dielectric function and electron density in the conduction band. Because of the densely packed conduction band, semiconductors behave as metals (metallization)[59]. Furthermore, this metallic aspect, according to the SIPE theory, aids in the excitation of SPPs, which operate as intra-pulse feedback in the multi-pulse laser ablation. In some situations, regardless of the number of pulses used, a single pulse can excite SPPs and form immature structures that serve as a seed for the growth of LIPSS. This is experimentally verified and demonstrated in the context of Si, as mentioned in reference[58]. As a result, this will cause the creation of LIPSS with periodicity (∧) close to the SPP's wavelength (SPP). The SPP wavelength will rely on the wavelength of the laser, dielectric constants of air and GaAs, as governed by the following equation (5.3), adopted from ref [68].

$$\lambda_{SPP} = \lambda^* \sqrt{\frac{(\varepsilon_d + \varepsilon_m)}{(\varepsilon_d * \varepsilon_m)}} \quad \text{..... (5.3)}$$

Where ε_d (~1), ε_m are dielectric constants of air and GaAs, respectively.

According to the literature[60–62], the dielectric function of GaAs subjected to laser pulses (with fluence over the ablation thresholds) will be less than -1 under illumination. As a result, SPPs with wavelength in the range of λ/2 to λ (Where λ is ~800 nm, the wavelength of the laser used) will result. In our case, the experimentally observed GaAs LIPSS periodicity (∧) was 0.8λ, which falls within the previously specified SPP wavelength range (i.e., between λ /2 and λ), and so we assume that this GaAs LIPSS creation mechanism is electromagnetic in nature. It is applicable to both the SPP or SIPE-Drude models in particular. Mastellone et al.[27] reported similar findings in their extensive review. Shin et al.[63] investigated the impact of Gaussian beam radial distribution upon this formation of LIPSS in metal alloys. Further extensive experimental and theoretical research (such as, high-level molecular dynamics simulations) are required to precisely locate and elucidate the LIPSS creation mechanisms and pore-like/broken structures at the scan line's extreme edges.

5.1.4 Composition analysis of GaAs LIPSS

The composition of the GaAs LIPSS was examined at several sample locations. The FESEM picture of the evenly produced GaAs LIPSS is shown in Fig. 5.9 (a) overlaid with color mapping. The corresponding black rectangular box on the right side displays its EDAX spectra, table of composition, and individual color maps of Ga and As. It is clear that the uniformly generated GaAs LIPSS are not significantly oxidized and have almost precise stoichiometry,

with an atomic percentage of Ga approximately 50% and an atomic percentage of As approximately 50%.

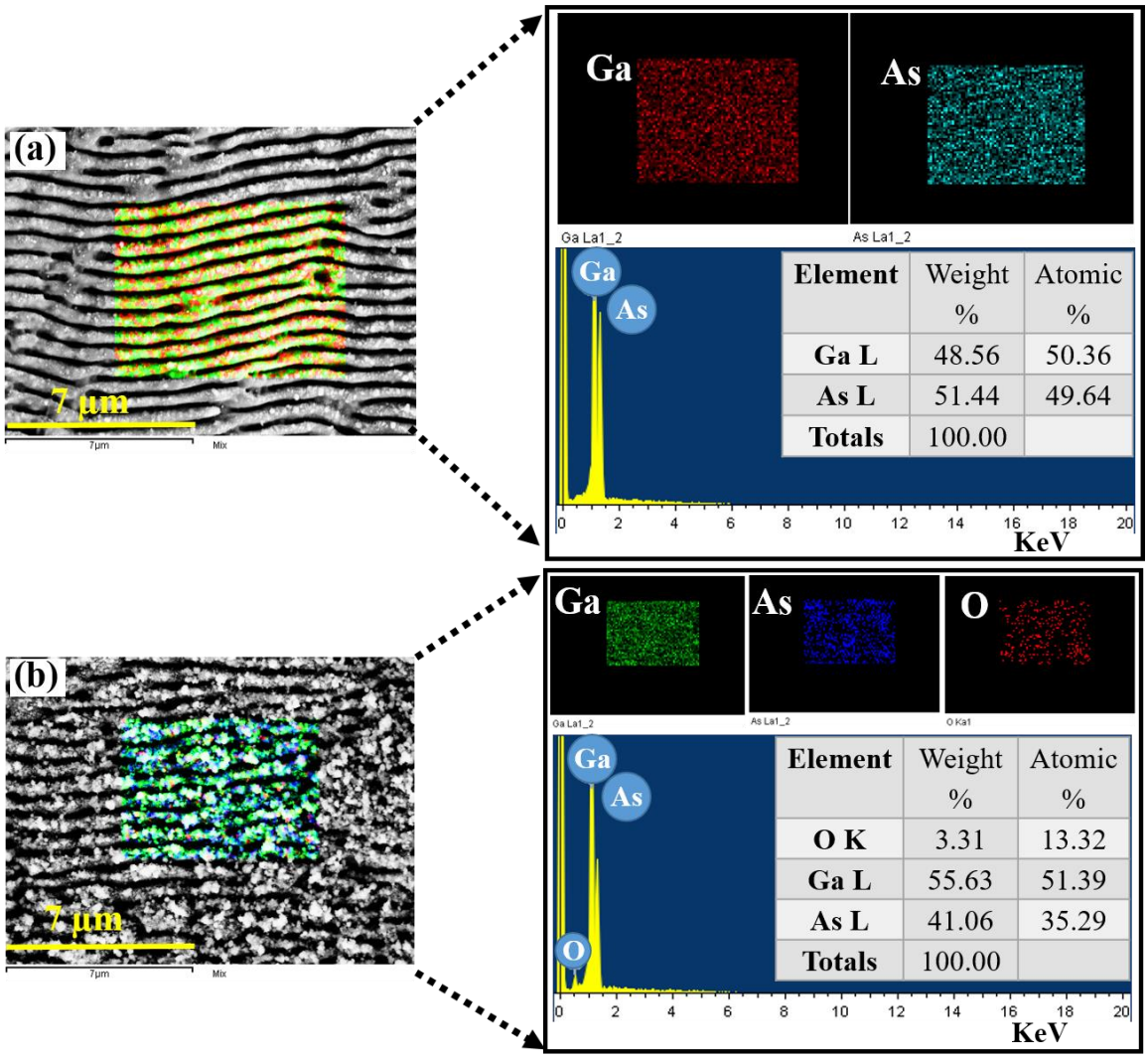

Fig. 5.9 FESEM image of (a) GaAs LIPSS, (b) GaAs LIPSS covered with debris. The red color rectangles on FESEM images shows the region at which EDAX mapping is performed, the black color rectangles on right side showing the corresponding elemental maps, EDAX spectra, and table of composition.

Further, at higher laser energy, some GaAs LIPSS regions underwent re-deposition, resulting in the development of debris-covered LIPSS, as seen in Fig. 5.9 (b). These regions were subjected to EDAX mapping, which revealed the presence of elements including Ga, As, and O [See the black color rectangular box on the right side of Fig. 5.9 (b)]. The amounts of oxygen (13%), Ga (51%), and As (35%) found clearly show that the ablation process results in debris with low oxygen levels on GaAs LIPSS when the laser energy exceeds a particular value. Overall, our study showed that the development of LSFL on GaAs results from the assistance of an electromagnetic field during the dissipation of laser energy. The creation of uniform GaAs

LIPSS with standard quality and no oxidation was discovered to be possible with an input laser energy of 5 µJ. Hence, these vast area structures created under an ideal experimental condition were investigated for studies and applications.

5.1.5 Synthesis of Large-area (2 × 2 mm^2) GaAs LIPSS and Defects/damage Studies

In this subsection, we demonstrate the 2 × 2 mm^2 GaAs LIPSS manufactured for use in technological applications. A set of three GaAs surface structures were created using an optimized laser energy ~5 µJ, an 800 nm wavelength, a 1 KHz repetition rate, and a 0.25 mm/s scan speed in both the X and Y directions, and depicted in Figs. 5.10 (a-c). The lines are spaced 0.08 mm apart. The photographs in the insets were taken with a mobile phone. Figures 5.10 (d-f) show the related higher magnification images (1 µm scale bar), whereas figures 5.10 (g-i) show images obtained at even higher magnifications (i.e., at 200 nm scale bar). As they were created under the identical experimental conditions, the morphology of all three samples is similar. Raman investigations, Raman mapping, and photoluminescence studies are performed on one of these samples to gather information about the strain/defects created on GaAs during the laser ablation process.

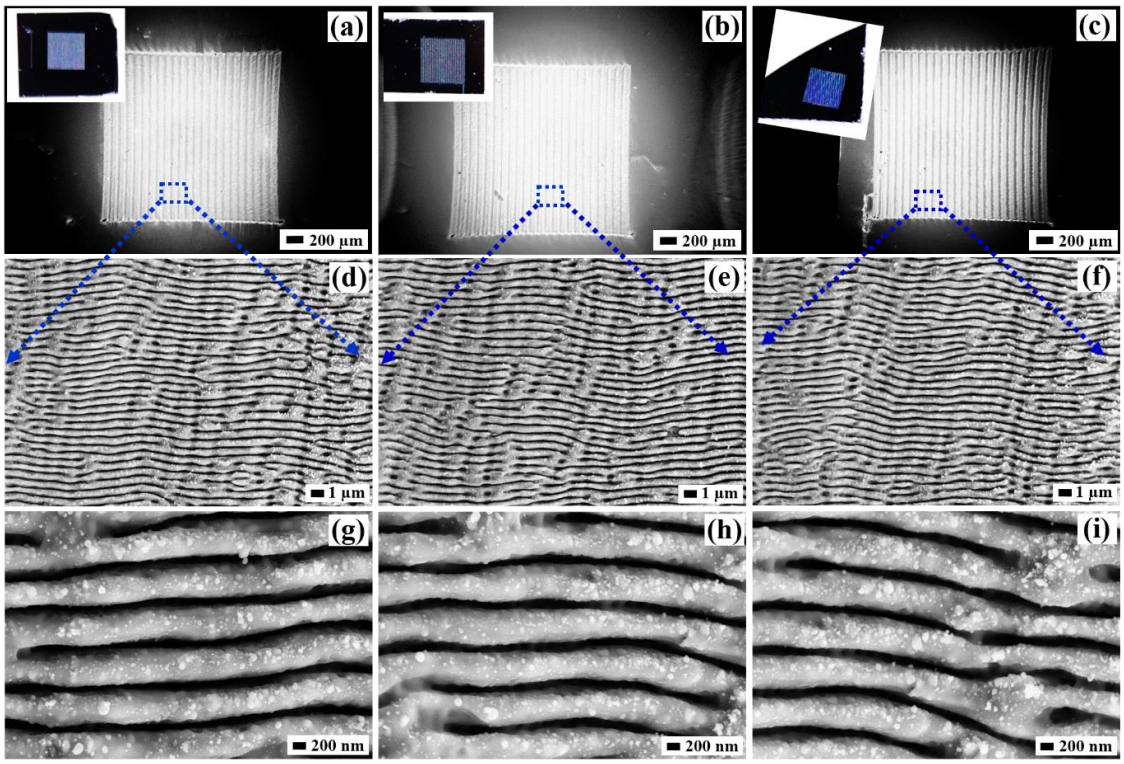

Fig. 5.10 (a-c) FESEM images obtained at lower magnification for a set of three laser ablated GaAs NSs (All these three samples were ablated in similar conditions with an optimized laser energy of 5 µJ over an area of 3 mm^2) with insets showing the optical images captured with a mobile phone. Row_2 (d-f) & Row_3 (g-i) present higher magnification FESEM images corresponding to (a-c), respectively.

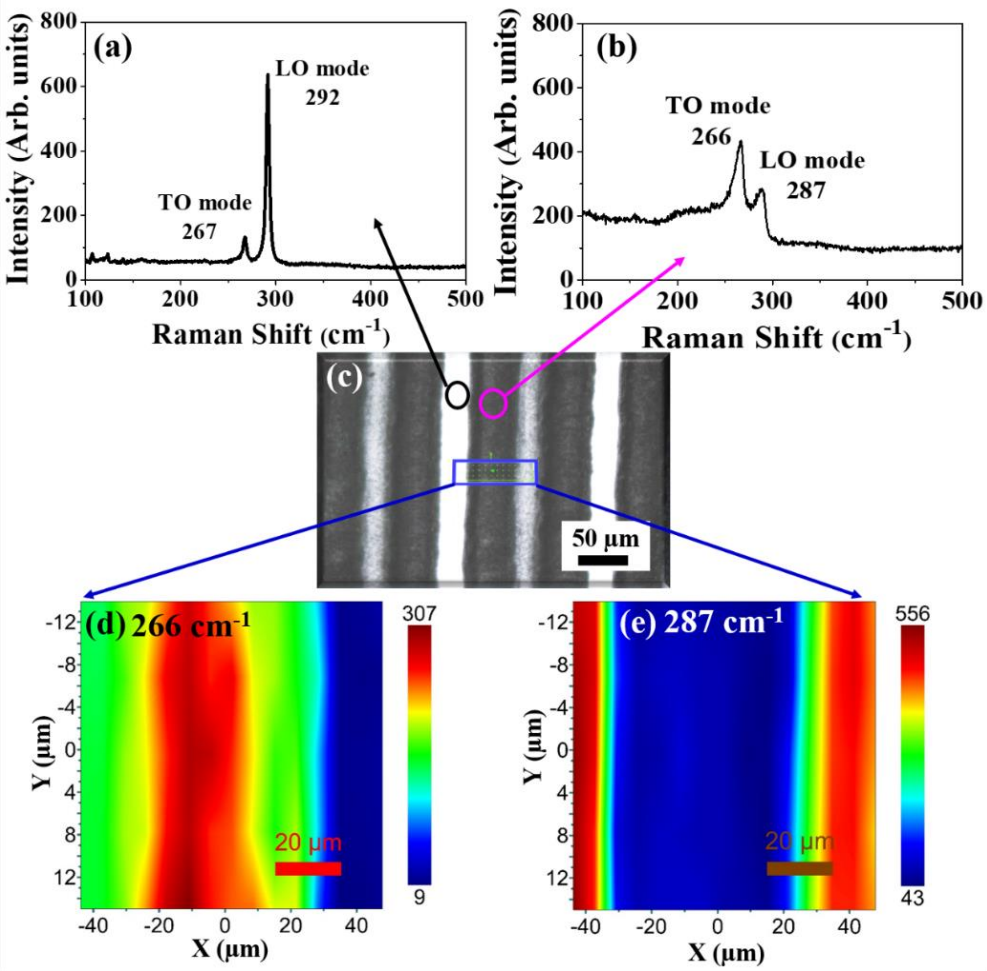

Fig. 5.11 (a) Raman spectra of GaAs in an un-irradiated area of the sample, (b) in irradiated area of the same sample, (c) Optical image showing ablated GaAs NSs on which Raman mapping was performed and presented in (d) for 267 cm^{-1} mode and (e) 292 cm^{-1} mode.

As seen in the optical image of Fig. 5.11 (c), Fig. 5.11 (a) and (b) show Raman spectra that were recorded at un-irradiated and irradiated locations on GaAs, respectively. In general, semi-insulating GaAs with an orientation of (111) allows both longitudinal optical (LO) and transverse optical (TO) phonon Raman scattering, while (110) GaAs's symmetry only allows TO mode and forbids LO[61,64]. In our context, laser ablation is performed on GaAs (100), which only permits LO mode scattering and forbids TO mode scattering[65]. However, the experimental data showed a weak TO mode at 267 cm^{-1}, which is consistent with other reports, alongside the very intensity LO mode (292 cm^{-1}).

Apart from the expected losses of symmetry in these structured samples, little deviations in the measurement's backscattering geometry may also cause the observed occurrence of the forbidden TO mode. The Raman spectra of a bulk GaAs wafer published in the literature[66,67] match the spectrum of GaAs in the un-irradiated region [see Fig. 5.11 (a)]. In order to synthesize LIPSS, a 5 µJ laser energy is applied to the surface of the GaAs. In this irradiated

area, the TO mode intensity increases while the LO mode intensity decreases [see Fig. 5.11 (b)], indicating a change in local symmetry. Semjonow et al.[68] and Raphael et al.[69] suggest that these modifications could be brought on by laser-induced damage, re-orientation, or recrystallization of the GaAs surface. According to Holtz et al.[70], a reduction in the correlation length of the optical phonons, which is constrained by a reduction in crystallite length for irradiated GaAs, is the cause of the fall in LO mode strength in particular. The strain/surface reorientation caused by the intense plasma produced during laser irradiation could be the reason of the rise in TO mode intensity. Amorphous As/GaAs may be present because it is observed that the signal background increases between 200 and 250 cm^{-1} [see Fig. 5.11 (b)].

Raman mapping was thus carried out on the sample at the location indicated by the rectangle green box displayed on Fig. 5.11 (c) in order to provide a more specific interpretation of this result. The entire GaAs irradiated scan line and a small area that is not irradiated surround the area that was chosen for mapping; the related mapping pictures are shown in Fig. 5.11 (d) for the TO mode and Fig. 5.11 (e) for the LO mode, respectively. It is evident that the TO mode [Fig. 5.11 (d)] intensity is greatest at the center of the irradiated scan line (red color on the map), and the intensity declines (appears in green and blue color) with distance from the center.

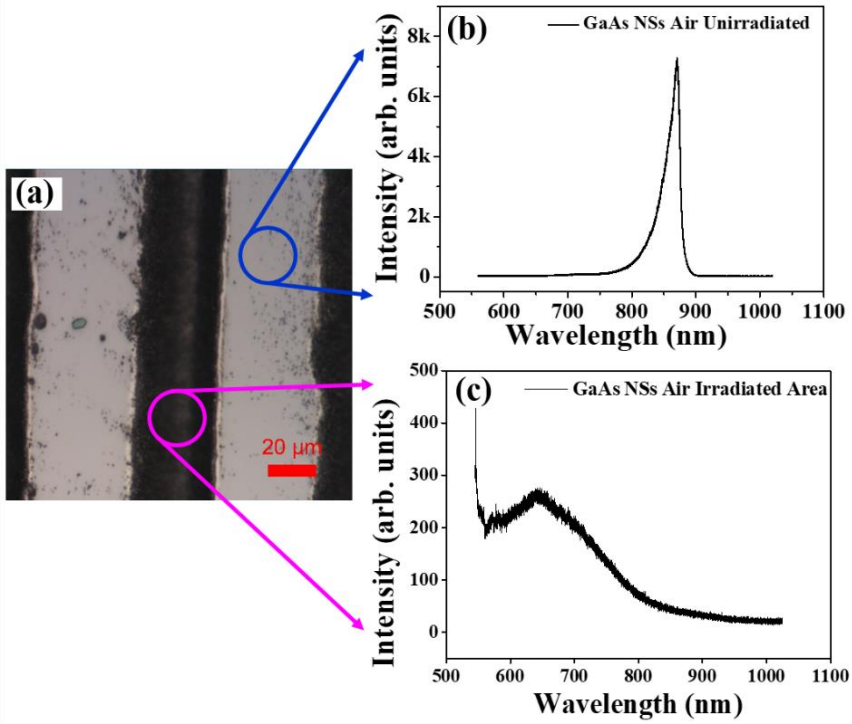

Fig. 5.12 (a) Optical image of laser ablated GaAs structure, (b and c) are the corresponding PL spectra recorded at un-irradiated and irradiated locations on GaAs structure as marked in Fig. (a), with blue and pink circles, respectively.

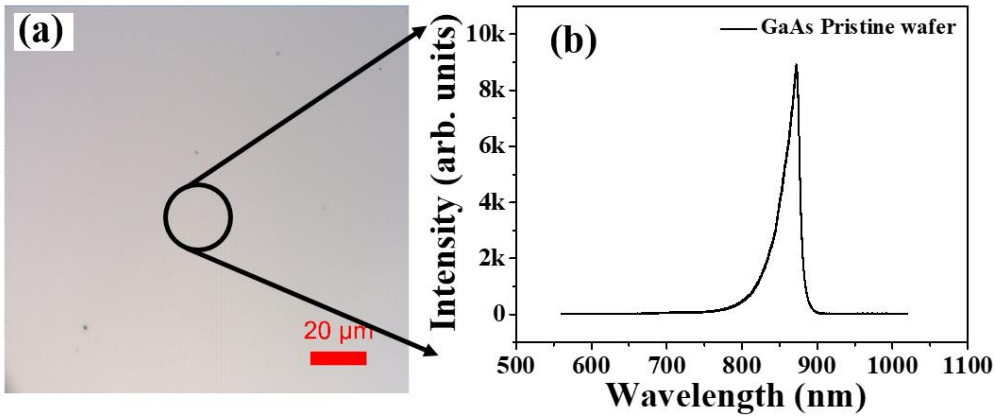

Fig. 5.13 (a) Optical image of GaAs pristine wafer, (b) the corresponding PL spectra recorded at the location marked in Fig. (a), with black circle.

The TO mode mapping demonstrated substantial damage in the center of the irradiated line, which reduces as one moves away from the center. As mentioned previously, the increase in TO mode intensity represents the damage/reorientation. Hence, the change of the Gaussian beam intensity from the center to the edges as indicated in the previous section [Fig. 5.8 (b)] precisely accounts for the damage/stress inflicted on the laser-irradiated GaAs scan line. The laser-induced damage is strong in the center of the irradiated scan line and reduces as we travel to the line's edges, which is further supported by the low intensity of LO mode [Fig. 5.11 (e)]. Overall, our Raman mapping study has provided a clear image of the variation of stress/strain in the laser-irradiated GaAs samples, which is strong near the center of the ablated track and gradually decreases with distance.

PL measurements were also performed to further understand the damage on the GaAs LIPSS. The PL spectra in Fig. 5.12 (b) correspond to the un-irradiated region on the GaAs sample at the location depicted in Fig. 5.12 (a). The sharp peak at ~880 nm corresponds to the band-gap emission of bulk GaAs[71–73]. To have a better understanding, the PL of a bulk GaAs wafer was measured and found to be at 880 nm (shown in the Fig. 5.13). Further, more importantly, the PL spectra [Fig. 5.12 (c)] revealed a less intense and broad PL peak in the range of 600-750 nm in the irradiated region of the sample. This data shows that there was a considerable quenching of the 880 nm PL peak intensity (peak suppression), which could be related to laser-induced damage/defects. The presence of minor amounts of NPs (with a greater bandgap) on the surface of the GaAs LIPSS may account the less intense broad peak around 600-750 nm. As a result, a systematic examination of Raman and PL data can be used to investigate the evolution of laser-induced damage on GaAs.

5.1.6 SERS response of Au decorated GaAs LIPSS

The SERS response of substrates is primarily determined by the size, shape, and distribution of plasmonic hotspots on the surface. Sharper/narrower hotspots create a stronger electro-magnetic field. Furthermore, the base surface structure on which the hotspots are located is important in the SERS response. According to the literature, periodicity, feature sizes, distance between structures, and structure alignment can all have a significant impact on localized surface plasmon resonance (LSPR) coupling[74,75]. Because LSPR is the primary parameter used to modify the SERS response, GaAs LIPSS were coated with gold (25 nm) and annealed at 400 °C for use as SERS active substrates in this investigation. The morphology of GaAs LIPSS produced with 5 µJ laser energy is shown in Fig. 5.14 (a) and 5.14 (b) [two different magnifications]. The same structures are shown in Fig. 5.14 (d) and 5.14 (e) after coating with a thin layer of gold, and after annealing the gold coated GaAs LIPSS at 400 °C for 1 hour in a tube furnace are shown in Fig. 5.14 (g) and 5.14 (h). The presence of gold on the surfaces is random prior to annealing [see Fig. 5.14 (d, e)]. After heat treatment, Au nanoparticles were observed to be equally adorned on the LIPSS [see Fig. 5.14 (g, h)]. It's also worth noting that annealing, as expected, also caused mild oxidation of the LIPSS. The EDAX analysis shown in Fig. 5.14 (c, f, and i) confirms the presence of 'Ga' and 'As' in the pristine GaAs LIPSS; Ga, As, and Au in the coated LIPSS; and Ga, As, Au, and O in the annealed Au coated LIPSS.

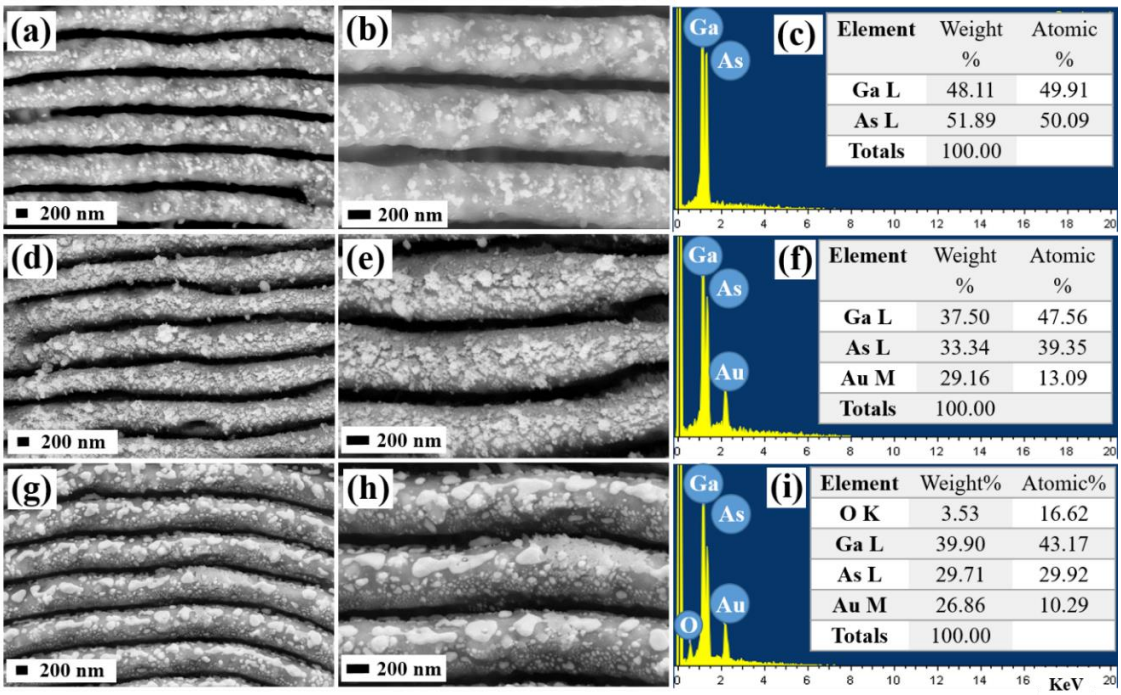

Fig. 5.14 (a-c) Two different magnification FESEM images and EDAX spectra of as ablated GaAs LIPSS (before Au deposition) produced with 5 µJ laser energy, (d-f) the same GaAs LIPSS after Au deposition, and (g-i) after annealing Au/GaAs LIPSS at an optimized temperature of 400 °C in an ambient atmosphere, respectively.

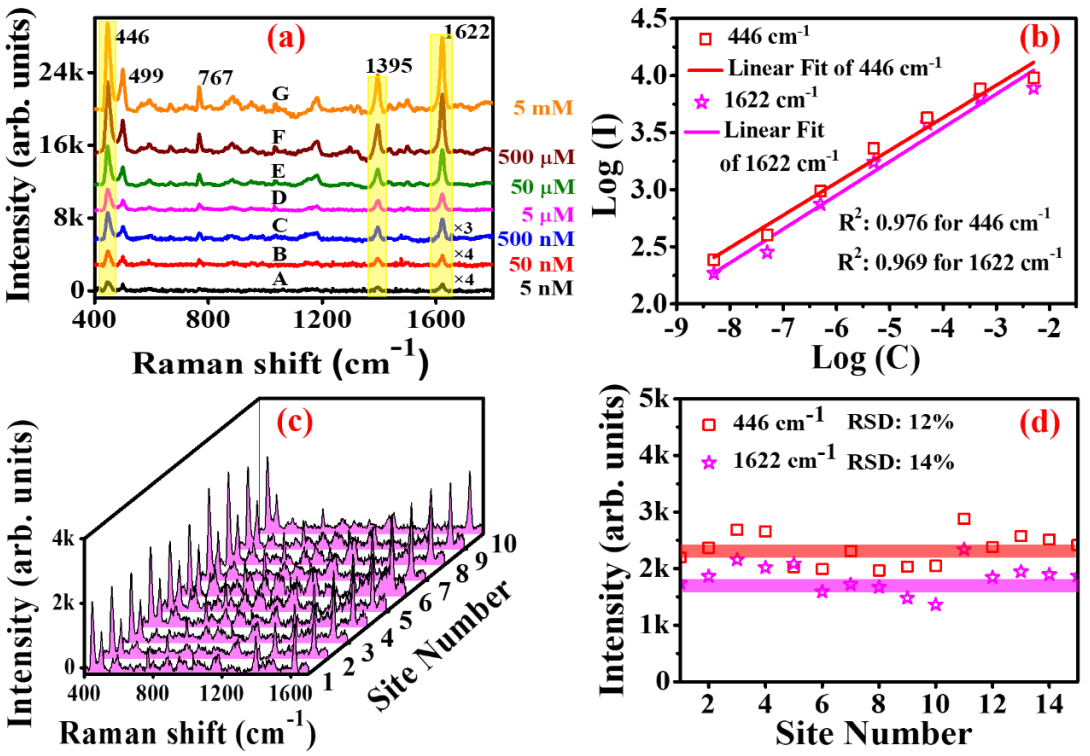

Fig. 5.15 (a) SERS spectra of MB molecule recorded at different concentrations (curves A, B, C, D, E, F, and G corresponds to 5 nM, 50 nM, 500 nM, 5 µM, 50 µM, 500 µM, and 5 mM, respectively as represented in legends), (b) corresponding log (I) vs log (C) graph, (c) SERS spectra recorded at 10 different locations on the same sample, and (d) intensity of the major Raman modes 446 cm^{-1} and 1622 cm^{-1} plotted against site number for calculating RSD values (RSD is calculated using 15 spectra but in Fig.5.15(c), we have shown only 10 spectra for an enhanced data legibility).

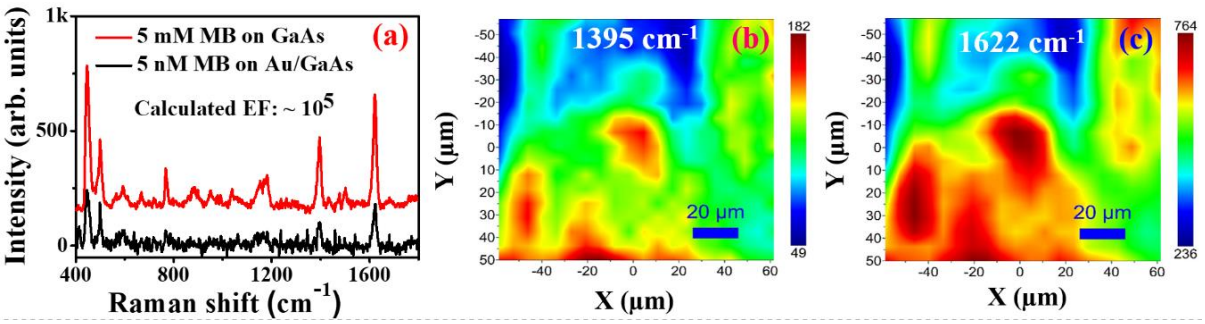

Fig. 5.16 (a) SERS spectra of 5 nM methylene blue (MB) recorded on annealed Au/GaAs LIPSS (black solid line) and Raman spectra of 5 mM MB recorded on GaAs LIPSS (red solid line), SERS mapping image of (b) 446 cm^{-1} mode, and (c) 1622 cm^{-1} mode, respectively.

The annealed Au adorned GaAs LIPSS were employed for the detection of dye molecules (MB) and explosive molecules (RDX and Tetryl). The SERS study of MB on Au NPs adorned GaAs LIPSS is shown in Fig. 5.15, where curves A, B, C, D, E, F, and G indicate the SERS spectra recorded for different concentrations of MB such as 5 nM, 50 nM, 500 nM, 5 µM, 50 µM, 500

μM, and 5 mM, respectively. The log (I) versus log (C) graph for the principal Raman modes of the MB 446 cm^{-1} and 1622 cm^{-1} is shown in Fig. 5.15 (b), and it reveals a linear relationship

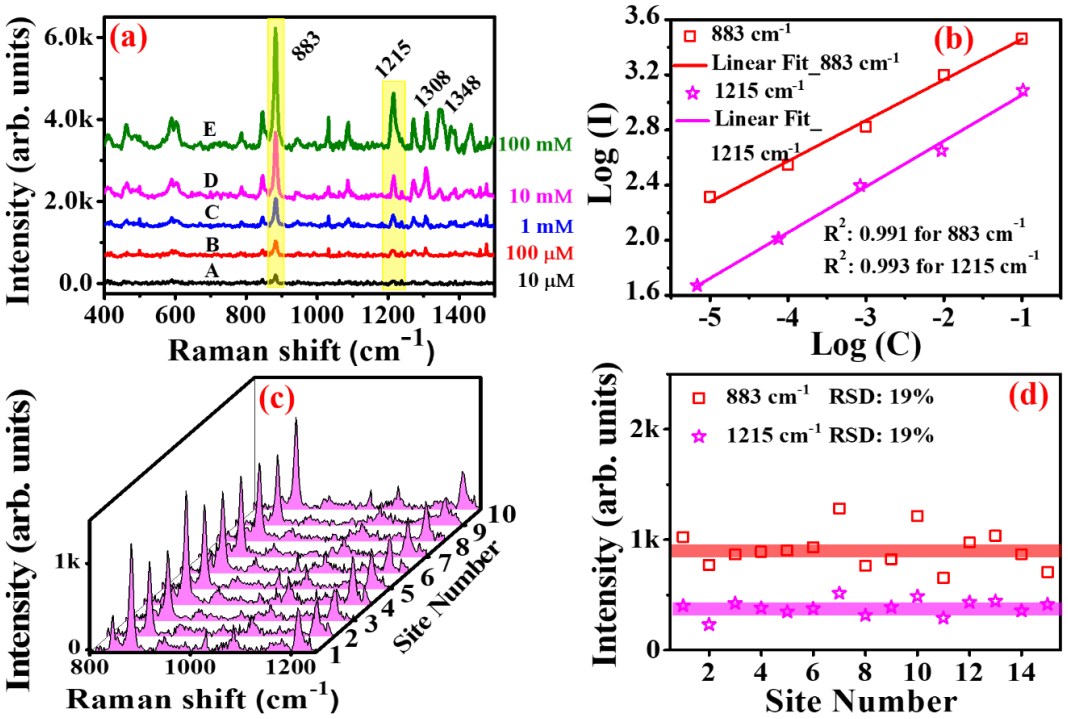

Fig. 5.17 (a) SERS spectra of RDX recorded at different concentrations (curves A, B, C, D, and E corresponds to 10 μM, 100 μM, 1 mM, 10 mM, and 100 mM, respectively as represented in legends), (b) corresponding log (I) vs log (C) graph, (c) SERS spectra recorded at 10 different locations on the same sample, and (d) intensity of the major Raman modes of 883 cm^{-1} and 1215 cm^{-1} plotted against site number for calculating RSD values (RSD is calculated using 15 spectra but in Fig.5.17(c), we have shown only 10 spectra for an enhanced data legibility).

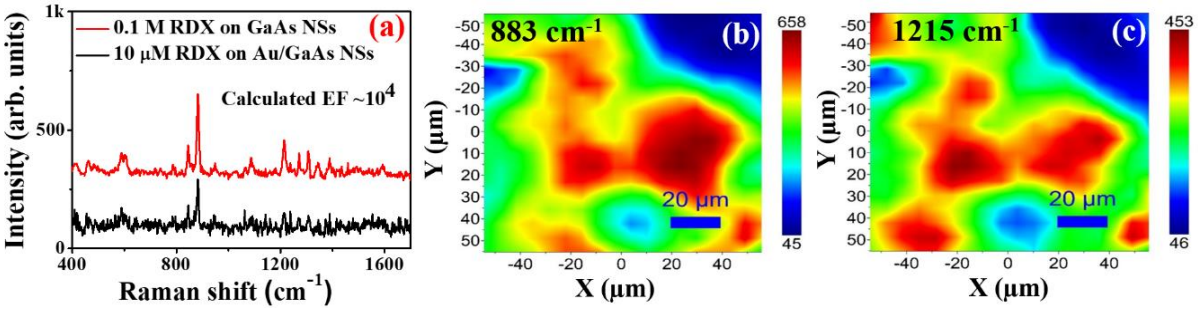

Fig. 5.18 (a) SERS spectra of 10 μM RDX recorded on annealed Au/GaAs LIPSS (black solid line) and Raman spectra of 0.1 M RDX recorded on GaAs LIPSS (red solid line), SERS mapping image of (b) 883 cm^{-1} mode, and (c) 1215 cm^{-1} mode, respectively.

between concentration and intensity. Spectra were measured at various locations on the sample to compute the relative standard deviation (RSD) in the signal, and the data is shown in Fig. 5.15 (c). Figure 5.15 (d) shows the intensity of the principal modes (446 cm^{-1} and 1622 cm^{-1}) plotted against site number. MB molecules up to a lower concentration of 5 nM were detected with a 12% RSD for the 446 cm^{-1} mode and a 14% RSD for the 1622 cm^{-1} mode. The EF was

calculated to be 10^5 using the SERS spectra of 5 nM MB on annealed Au/GaAs LIPSS and the Raman spectra of 5 mM MB on pristine GaAs LIPSS, as shown in Fig. 5.16 (a). SERS mapping images exhibiting variations in signal intensity on the surface of GaAs LIPSS across large areas are presented in Fig. 5.16 (b) for the 446 cm^{-1} mode and Fig. 5.16 (c) for the 1622 cm^{-1} mode. A similar examination was carried out on another sample from the same batch to sense RDX. Fig. 5.17 (a) shows the SERS spectra of RDX at concentrations of 10 µM, 100 µM, 1 mM, 10 mM, and 100 mM, as represented by curves A, B, C, D, and E, and Fig. 5.17 (b) shows the corresponding log (I) vs log (C) graph. On this annealed Au coated GaAs LIPSS, RDX explosive, up to a lower concentration of 10 µM was successfully detected. The SERS spectra collected at ten different sites on the same sample are shown in Fig. 5.17 (c). The intensity of the major modes 883 cm^{-1} and 1215 cm^{-1} is plotted against site number in Fig. 5.17 (d) to calculate RSD values. The computed RSD for both major modes, 883 cm^{-1} and 1215 cm^{-1}, was 19%. The RDX was determined to have an EF of 10^4 using these structures. Figure 5.18 shows the details of the EF calculation and accompanying SERS mapping data. The SERS spectra shown in Fig. 5.19 (a) were acquired using the explosive compound tetryl at various concentrations (10 µM, 100 µM, 1 mM, 10 mM, and 100 mM, indicated by curves A, B, C, D, and E, respectively) and its corresponding log (I) vs log (C) graph [Fig. 5.19 (b)] showing the lowest detection of 10 µM with a linear variation of signal intensity with analyte concentration. The computed RSD values were 25% for the 824 cm^{-1} mode and 17% for the 1357 cm^{-1} mode. The EF of the Tetryl explosive was similarly found to be 10^4. In Fig. 5.20, the EF calculation and SERS mapping for 824 cm^{-1} and 1357 cm^{-1} modes are displayed.

These SERS studies demonstrated that the Au NPs loaded GaAs LIPPS may easily be employed for the identification of trace level molecules. These substrates could detect dye molecules at nano molar (5 nM) concentrations and explosive molecules at micro molar (10 M) concentrations with good repeatability and decreased RSD values. The reported EFs of 10^5 and 10^4 for dye and explosive molecules on Au/GaAs LIPSS are somewhat lower than the EFs observed on pure Au NPs/NSs, but are comparable to the EFs observed on other hybrid SERS substrates. They do, however, have some advantages over traditional plasmonic NSs. Because these substrates are made up of metal NPs coated on a semi-conducting base material, the heat generated during SERS measurements will be far lower than on pure metallic substrates. As a result, Au/GaAs SERS platforms can be utilized to identify biomolecules or trace-level chemicals that are heat sensitive. Furthermore, the EF of the hybrid Au/GaAs LIPSS may be increased by adjusting many parameters such as morphology, roughness of the GaAs surface

structures, size, shape, distribution, number density, and separation between the Au NPs. As a consequence, experimenting with different Au thicknesses and LIPSS feature sizes is desirable

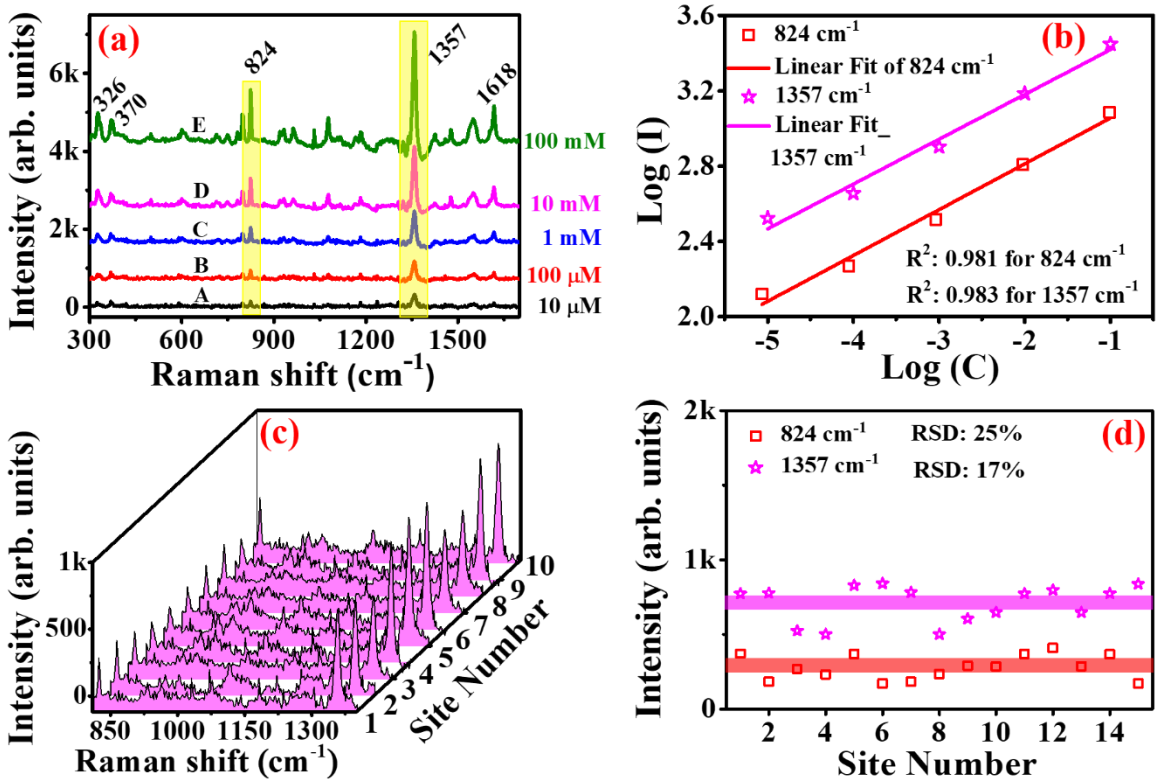

in the development of efficient, hybrid SERS substrates.

Fig. 5.19 (a) SERS spectra of Tetryl recorded at different concentrations (curves A, B, C, D, and E corresponds to 10 µM, 100 µM, 1 mM, 10 mM, and 100 mM, respectively as represented in legends), (b) corresponding log (I) vs log (C) graph, (c) SERS spectra recorded at 10 different locations on the same sample, and (d) intensity of the major Raman modes of 824 cm^{-1} and 1357 cm^{-1} plotted against site number for calculating RSD values (RSD is calculated using 15 spectra but in Fig.5.19 (c), we have shown only 10 spectra for an enhanced data legibility).

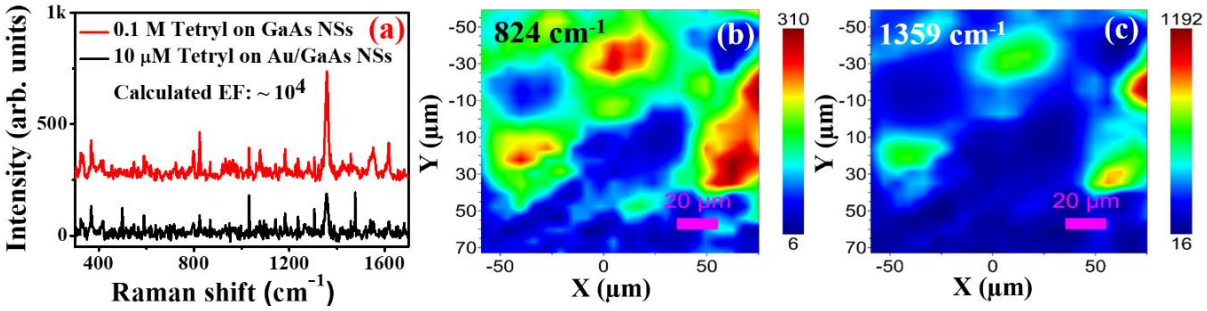

Fig. 5.20 (a) SERS spectra of 10 µM Tetryl recorded on annealed Au/GaAs LIPSS (solid black line) and Raman spectra of 0.1 M Tetryl recorded on GaAs LIPSS (solid red line), SERS mapping image of (b) 824 cm^{-1} mode, and (c) 1359 cm^{-1} mode, respectively.

5.1.7 Summary of fs laser structured GaAs LIPSS in air

This research found that GaAs is an excellent material for the creation of LIPSS over a wide range of laser energy ranging from 5 µJ to 100 µJ. More curiously, despite changing laser energy across the whole range indicated above, the periodicity of these LIPSS is nearly constant. These LIPSS were not oxidized at lower laser energies, but as laser energy increased, a few debris-like formations re-deposited over LIPSS containing tiny amounts of oxygen. As a result, reduced laser energy may be suitable for producing GaAs LIPSS without oxidation. The mechanisms of GaAs LIPSS creation were thoroughly examined using existing data and our expertise. The origin of LIPSS has been attributed to surface electromagnetic fields, particularly SPPs. The SIPE-Drude model worked well in our case for describing the creation of GaAs LIPSS. There were, however, broken LIPSS/pore-like structures at the borders of each scan line, which we attribute to radial fluctuations in laser fluence/other ablation effects. As a result, additional tests will be planned to determine the precise origin of such patterns in different locations of the same scan line. Furthermore, both Raman and PL studies confirmed a large number of defects/strain created on the surfaces of the laser-irradiated GaAs samples. When coated with Au and annealed, these GaAs LIPSS performed well as SERS substrates. MB molecules with a detection level of 5 nM, EF of 10^5, and explosive molecules (RDX and Tetryl) with a detection level of 10 M, EF of 10^4, were effectively detected in this work. We believe that these plasmonic NPs (Au NPs) decorated GaAs LIPSS are prospective hybrid SERS substrates for further improving detection limits, as well as candidates for other applications such as biomolecule detection. These plasmonic NPs coated GaAs LIPSS can also be investigated for other optoelectronic device applications.

Chapter 5 (Part-B)

Sub-70 nm Surface Structures on Femtosecond Laser Irradiated GaAs in Distilled Water and Sensing Applications

This study indicates the possibility of distinct ablation mechanisms at different radial locations of the ablated track on GaAs when ablated with femtosecond pulses in distilled water. Micron-sized cones, nano-pores, and nano-DNA-like deep sub-wavelength structures (average size of 60-70 nm) were observed in the ablated track. The need for simulations that take into account fluctuations in Gaussian fluence and the hydrodynamics of the melt flow/surrounding media is discussed. To our knowledge, this is the first time that sub-70 nm surface nanostructures on GaAs have been reported. Furthermore, after gold coating, these GaAs surface structures performed excellently as hybrid SERS platforms.

5.2.0 Introduction

Laser-induced periodic surface structures of GaAs, as well as several potential mechanisms driving their formation, are already being investigated using appropriate experimental evidence[41,42,45,46]. The majority of these investigations are conducted in the air, where avoiding oxidation is difficult[76]. We recently accomplished wide area uniform LIPSS on GaAs using femtosecond laser ablation in air, minor oxidation effects were observed at higher laser energies[77]. Laser irradiation in liquid media is a promising technology for preventing material oxidation. Irradiation beneath the liquid layer can result in an oxygen-free, polar environment with little dissolved oxygen. In a recent study[78], no oxidation effects were seen when the LIPSS (on GaAs) were created by a picosecond pulsed laser in several liquid environments, including distilled water, ethanol, and polyvinyl alcohol. The morphology, composition, and formation mechanisms of the ablated GaAs nanoparticles have recently gained much attention in pulsed laser ablation in liquids (PLAL)[79,80]. However, to the best of our knowledge, the underlying surface structures created on the ablated target, their reliance on the ablation medium (particularly liquids), and potential methods for producing diverse surface structures have not yet been thoroughly investigated. When a liquid is involved, the underlying mechanisms are fairly complex. As a result, we attempted to comprehend the effect of DW medium and laser energy on the surface structures generated on GaAs.

5.2.1 Experimental details

The Ti:Sapphire laser pulses (50 fs, 800 nm, and 1 kHz) were directed to a 1 cm^2 area GaAs sample immersed in the DW medium. A 5 ml DW beaker filled gives a liquid level of 8 mm above the GaAs surface. Different laser scan lines/tracks are drawn, with laser energies ranging from 50 µJ to 500 µJ. The glass beaker along with sample was placed on a 2D motion controller and translated at 0.05 mm/s in the X-direction to make 5 mm tracks. Full details about the experimental setup can be found in chapter 2 and elsewhere[77,81].

5.2.2 Results and discussion

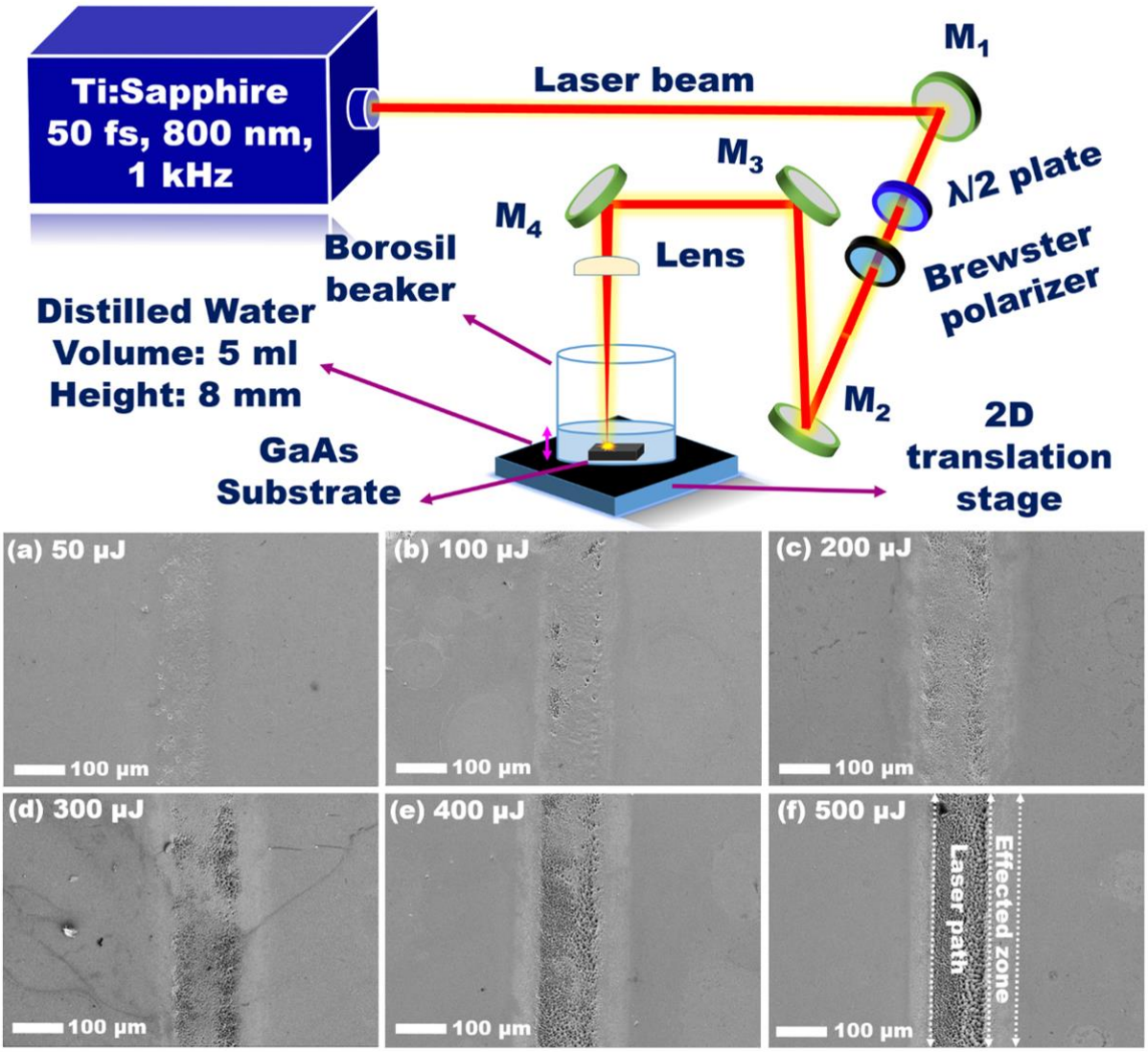

Fig. 5.21 Schematic of pulsed laser ablation in liquids (upper half), FESEM images of laser ablated tracks on the surface of GaAs immersed in DW at various laser energies (a) 50 µJ, (b) 100 µJ, (c) 200 µJ, (d) 300 µJ, (e) 400 µJ, and (f) 500 µJ, respectively. In Fig. 2 (f), dotted lines are drawn for guiding the eye about the laser path and affected zone outside the laser path.

Figures 5.21 (a-c) show that minor ablation was detected for input laser energy ranging from 50 µJ to 200 µJ. Figures 5.21 (d-f) demonstrate the formation of ablation/depth profiles when the energy (300-500 µJ) was increased further. When the laser intensity was increased, the width and depth of the ablated track structures appeared to increase. It is also discovered that there is an affected zone at the boundaries of the laser scan tracks; dotted lines are placed on Fig. 5.21 (f) for eye-guiding purposes. These various zones found on scan tracks drawn at energies of 100 µJ and 500 µJ were thoroughly investigated and are shown in Fig. 5.22 and Fig. 5.23, respectively.

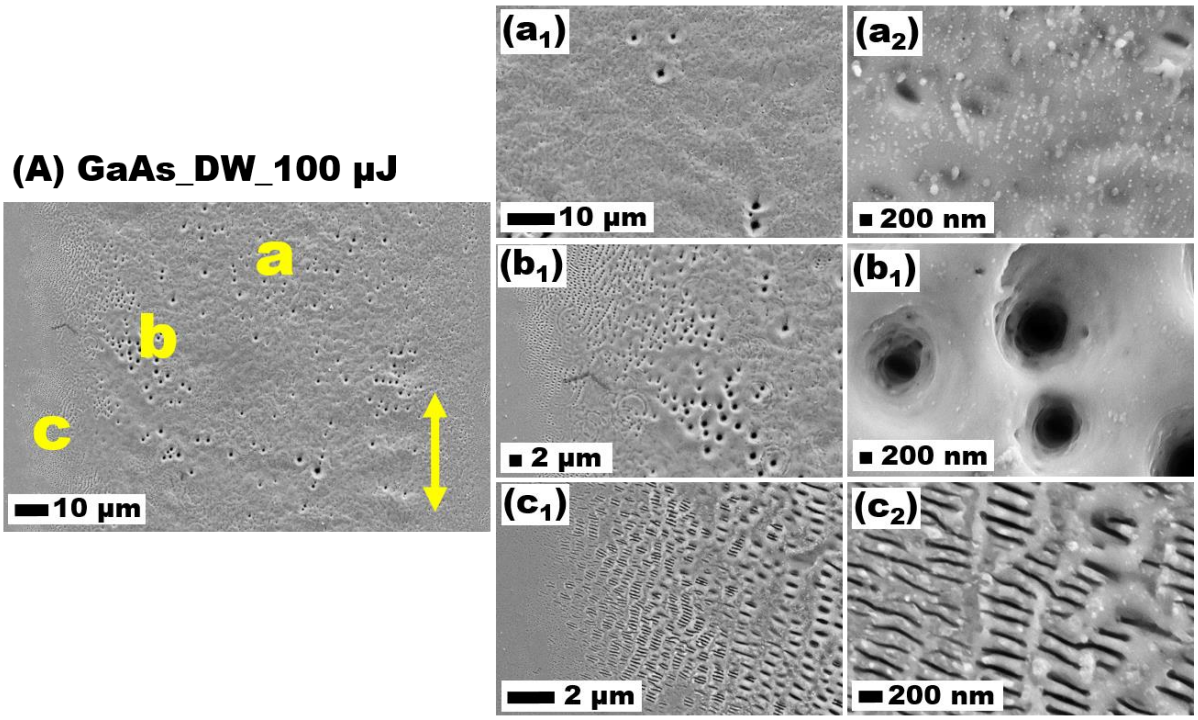

Fig. 5.22 (A) FESEM image of laser ablated GaAs line structure in DW medium at an energy of 100 µJ, the letters a, b, and c represent different regions on the scan line, the images recorded at these regions are shown in row-1 (a_1-a_2), row-2 (b_1-b_2), and row-3 (c_1-c_2), respectively.

Significant ablation was not detected for the track drawn at an energy of 100 µJ, despite the presence of pore-like structures in the center of the track and nano-DNA-like structures around edges. Figure 5.23 (A) depicts the FESEM image of the ablated track at 500 µJ laser energy. As demonstrated in row-3 (c1-c2), micron size cones were created in the center of the track [the region indicated with letter "c" in Fig. 5.23 (A), and their corresponding 2D FFT [see Fig. 5.23 (c3)] verified that these cones were randomly orientated with respective to laser polarization direction. Moving away from the track's center [i.e., to the region denoted by the letter "b" in fig. 5.23 (A)], nano-pore-like formations were detected [see Fig. 5.23 (b1-b2)], and their corresponding 2D FFT analysis [see Fig. 5.23 (b3)] revealed that these pores also does

not have any specific orientation with the laser polarization direction. Surprisingly, nano-dimensional DNA-like structures were detected along the track's extreme edges [regions denoted with the letters "a & d" in Fig. 5.23 (A)]. Figures 5.23 (a1-a3) show FESEM pictures and the corresponding 2D FFT of the nano DNA-like entities generated on the ablated track's left side. Figures 5.23 (d1-d3) represent the ones on the right side of the track in the same way. The average orientation of these DNA-like structures is approximately 29° with regard to the polarization direction, the laser polarization direction is depicted by a double-sided arrow in Fig 5.23 (A)]. Furthermore, the size distribution of cone-like structures was 2-5 µm, whereas that of pore-like structures was 300-400 nm. The observed feature sizes in the DNA-like structures are in the range of 60-70 nm.

When ablated with 50 µJ of energy, these DNA-like structures were not completely produced. These DNA-like structures were reported to be prominent at laser intensities ranging from 100 µJ to 500 µJ, with a comparable size distribution. The creation of this energy-dependent DNA-like structure is depicted in Fig. 5.24. The EDAX mapping, displayed in Fig. 5.25, revealed that the varied surface structures generated during the PLAL method had no noticeable oxidation impacts

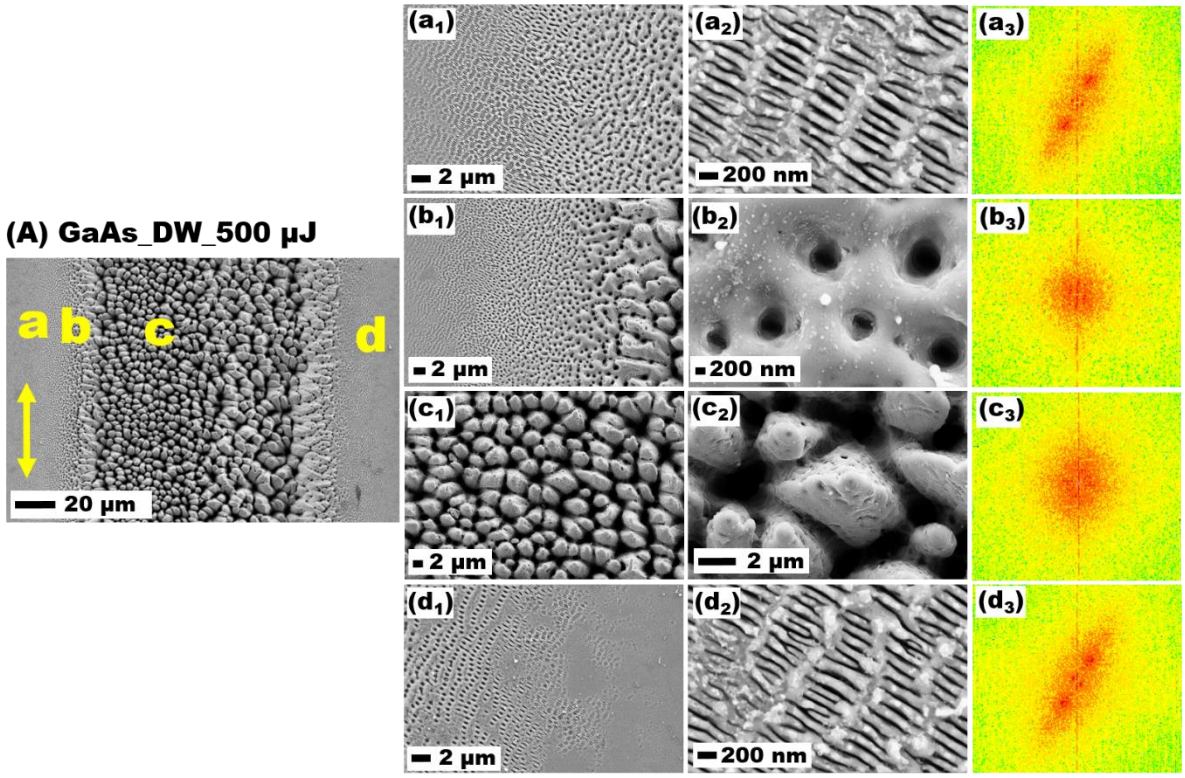

Fig. 5.23 (A) FESEM images of laser ablated GaAs track structure in DW medium at an energy of 500 µJ, the letters a, b, c, and d represent different regions on the scanned track, the images recorded at these regions and their corresponding 2D FFT are shown in row-1 (a_1-a_3), row-2 (b_1-b_3), row-3 (c_1-c_3), and row-4 (d_1-d_3), respectively.

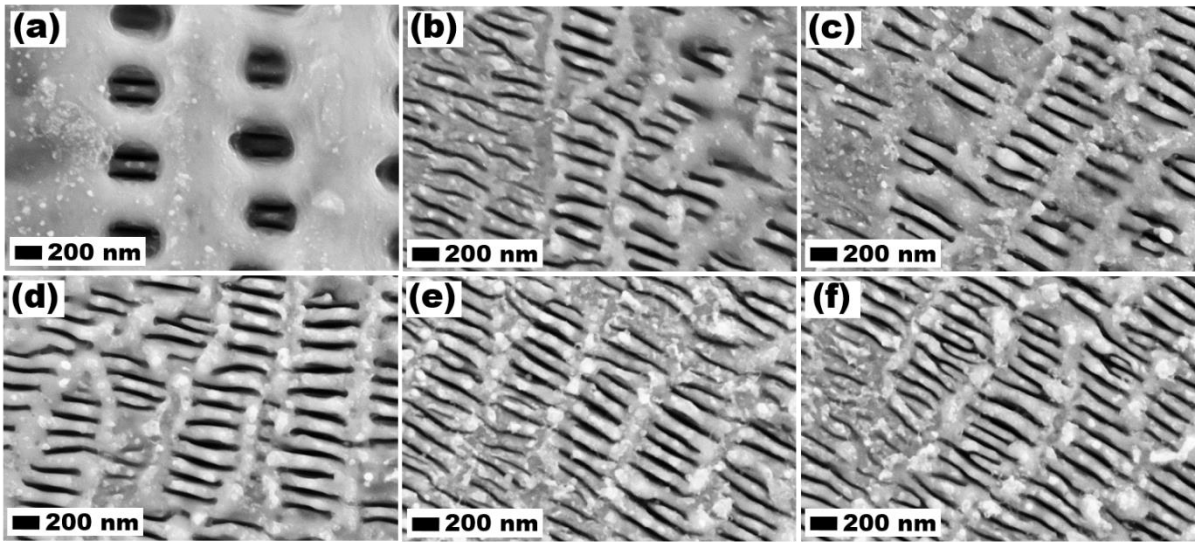

Fig. 5.24 FESEM images of nano-DNA like structures formed at different laser energies (a) 50 µJ, (b) 100 µJ, (c) 200 µJ, (d) 300 µJ, (e) 400 µJ, and (f) 500 µJ, respectively (These structures are observed around the edges of the ablated track on both sides).

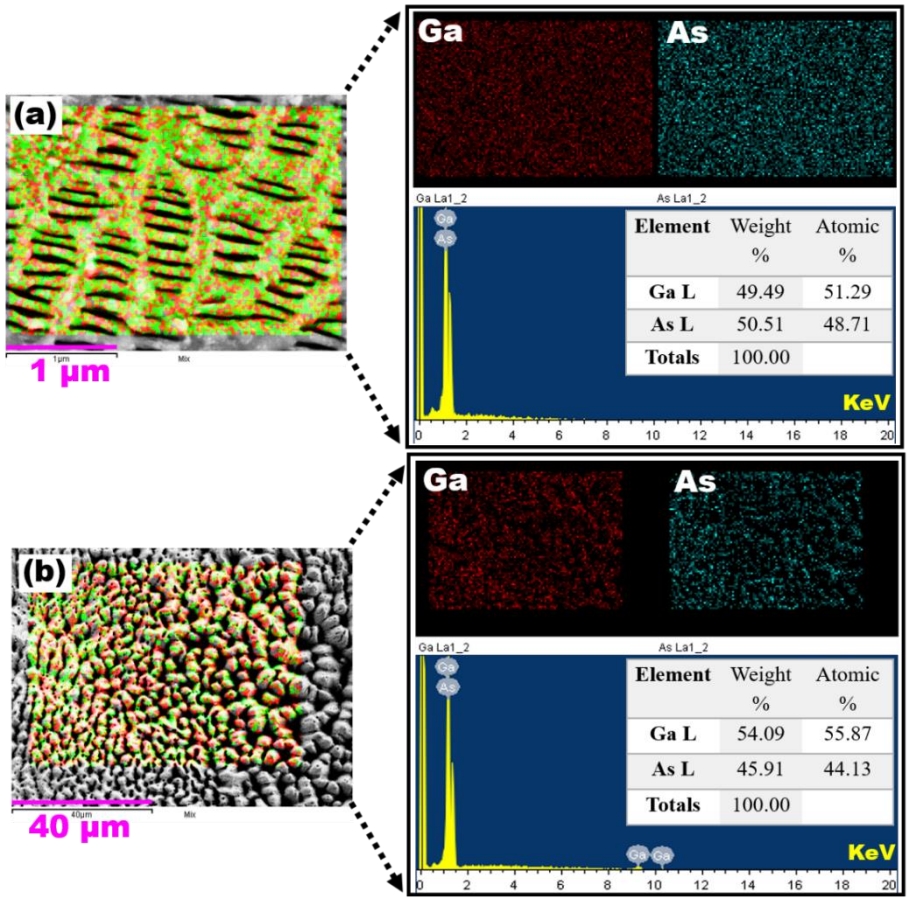

Fig. 5.25 Overlay image of the EDAX mapping recorded on (a) DNA like structures, (b) cone like structures. The corresponding individual elemental mappings and spectra are shown at the right side within a rectangular black box for each structure.

Figure 5.26 exhibits the magnified image at the structure's edge, which depicts several types of surface structures at various radial distances from the ablated track's center. There were micron-sized cones in the R1 region, spherical pores in R2, non-spherical pores in R3, and nano-DNA-like structures in R4. To the best of our knowledge, no perfect explanation exists for what caused distinct structures to emerge in different radial positions. In a few previous investigations, such as those by Ganeev et al.[82], the density of the surrounding media was interpreted as the reason of the production of various structures such as ripples, holes, and bump-like structures. Fluences over the laser ablation thresholds cause LSFL, while fluences slightly less than or equal to the threshold produce HSFL[46].

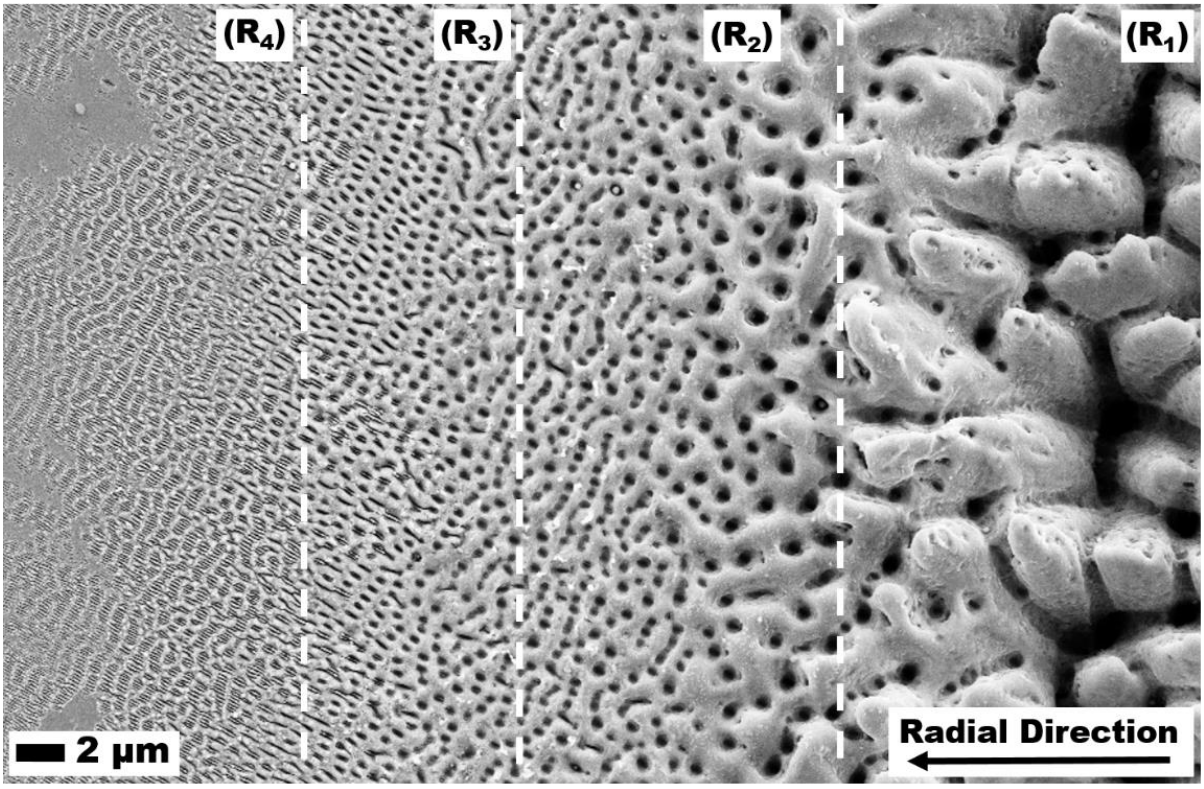

Fig. 5.26 FESEM image of GaAs ablated in DW, the regions R_1-R_4 represent four different kinds of GaAs surface structures formed (cones, spherical pores, non-spherical pores, and DNA like structures) from center to extreme edges of the ablated track, respectively.

On the other hand, extensive studies[83–85] have shown that LSFL structures form in the center of the laser path and HSFL structures form at the margins. Wang et al.[83] indicated that the creation of subwavelength and deep-subwavelength structures is caused by the imparted localized effective fluence (LEF). Other methods, such as two temperature model (TTM) simulations and finite-difference time-domain (FDTD) simulations, demonstrated the quasi-periodic, LSFL, and HSFL structures at different areas on the same irradiation spot. All of these models and simulations are appropriate for explaining the ripple-like features. However, in the

present study, other structures, such as cones, holes, and DNA-like structures, have also been observed within the same tracks. Following a careful examination of the experimental results, we propose the following feasible explanations for the production of such a diverse range of structures on the laser-ablated track on GaAs. The laser fluences are computed using equation 5.1 (given in the first section of this chapter). The table 5.2 displays fluences computed using a laser beam diameter of 100 μm (experimental ablation width).

Table 5.2 Laser energy and estimated laser fluences.

S. No.	Laser energy (μJ)	Laser fluence(J/cm^2)
1	50	0.64
2	100	1.27
3	200	2.54
4	300	3.82
5	400	5.09
6	500	6.36

The experimental data revealed that at initial low energy in the range of 50-200 μJ (F ~0.64-2.54 J/cm^2), nano-pores in the center of the track and nano-DNA-like structures around the margins were detected (See Fig. 5.22). By increasing the energy from 300 to 500 μJ, cone-like structures in the center, pores on the edges, and nano-DNA-like formations at the extreme edges were seen (see Fig. 5.26). When the maximal energy of 500 μJ was employed, the center area had a peak fluence of 6.36 J/cm^2; as one moved radially outside, the fluence decreased. The fluence in the tail of the Gaussian beam will be 1-13% of the peak fluence (i.e., 0.06-0.8 J/cm^2). When using the electromagnetic/surface plasmon polariton (SPP) model to explain the formation of surface structures, the SPP wavelength is determined by the real component of the dielectric function[86]. For semiconductors, this parameter is highly dependent on the input fluence; thus, variations in the laser fluence in the center and tails regions of the Gaussian beam may yield the observed variations in densities and wavelengths of SPPs, resulting in different surface topologies. In the present situation, instead of LSFL, micron-sized cones formed in the center of the beam, while nano-pores and nano-DNA-like structures were detected around the margins as HSFL. This is consistent with our observations that when the track was ablated at lower fluences, nano-pores appeared in the middle region (Fig. 5.22). Besides the effective laser fluence and dielectric function, the surrounding liquid medium may have additional impacts. The creation of nano-pores and nano-DNA-like formations at the margins may also

be caused by hydrodynamic melt flows/instabilities[87]. Because we employed 1000 pulses per second, the melt (plasma) is subjected to different forces at different times, which could have resulted in fast movement and settlement of the hot plasma (in the presence of liquid), resulting in such diversified structures. As a result, distinct ablation mechanisms are thought to exist to generate diverse shapes at varied radial distances from the center of the ablated track on the GaAs. The overall size and shape of the surface structures are influenced by the effective laser fluence supplied at different spatial locations, as well as the density, viscosity, refractive index, and dielectric function of the surrounding liquid medium. To fully explain the processes for forming various surface structures on laser ablated GaAs in liquids, theoretical simulations/studies involving radial fluence effects, electromagnetic field effects, melt flow hydrodynamics, and surrounding liquid properties must be considered, which will be the focus of our future research. We believe that the current study will be useful in exposing experimental findings that there may be more than one ablation process for the creation of distinct surface patterns on GaAs in DW medium.

5.2.3 SERS study of Au/GaAs NSs

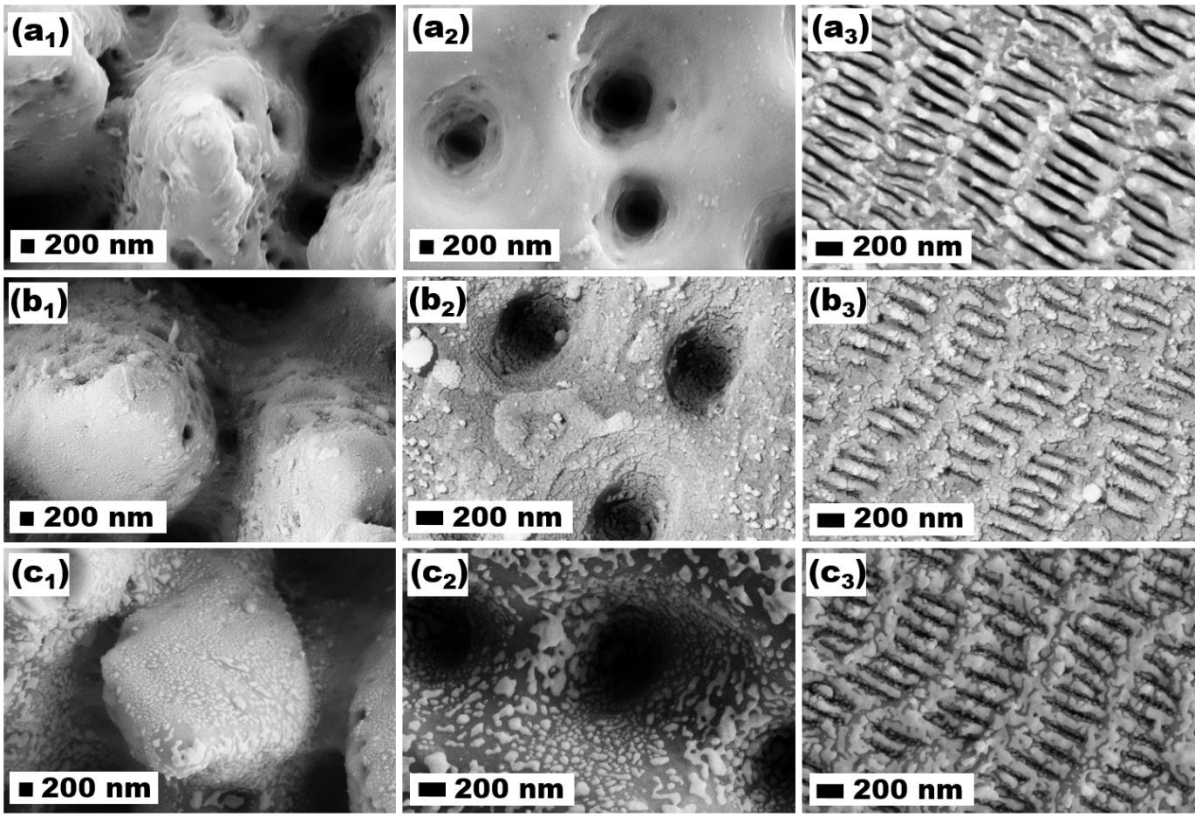

Fig. 5.27 FESEM images of micron size cones, nano-pores, and nano-DNA-like structures on (a_1-a_3) as ablated GaAs, (b_1-b_3) Au-coated GaAs, and (c_1-c_3) annealed Au/GaAs, respectively.

In addition, to evaluate these surface structures as hybrid SERS substrates, a set of GaAs structures were produced in DW at an optimum laser energy (500 µJ), then coated with a thin coating of gold and annealed at 400 °C. Figures 5.27 (a1-a3) depict images of various surface features on as ablated GaAs structures, whereas figures 5.27 (b1-b3) depict photos of Au-coated GaAs structures. The cone, pore, and DNA-like structures were observed to be decorated with Au NPs after annealing [as shown in Fig.5.27 (c1-c3]. These structures exhibited a substantial SERS response for detecting MB and RDX. The Raman (5 mM MB, curve A) and SERS (50 nM MB, curve B) spectra obtained on pristine GaAs and Au/GaAs NSs are shown in Fig. 5.28(a).

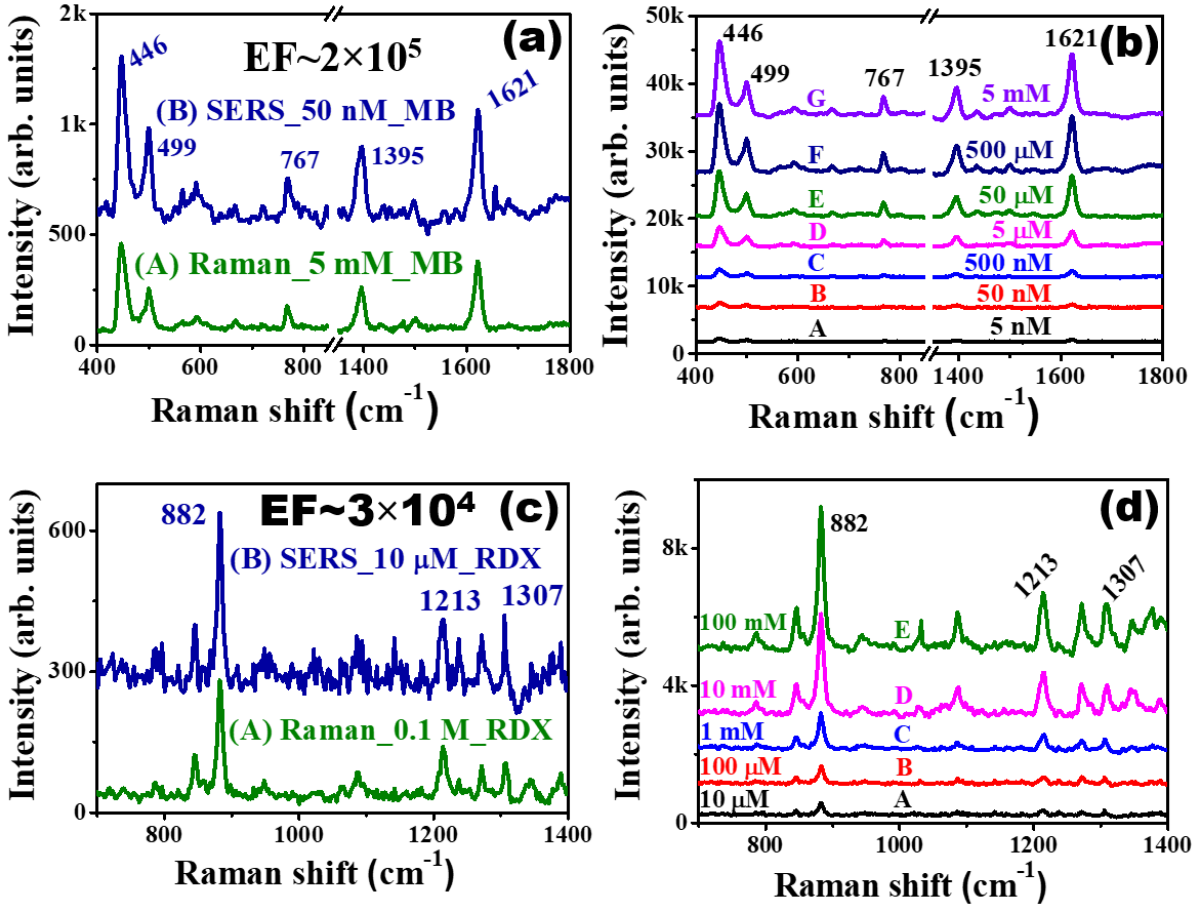

Fig. 5.28 (a) Raman spectra of 5 mM MB detected on GaAs (curve-A) and SERS spectra of 50 nM MB on Au/GaAs NSs (curve-B), (b) concentration dependent SERS spectra of MB on Au/GaAs NSs, (c) Raman spectra of 0.1 M RDX detected on GaAs (curve-A) and SERS spectra of 10 µM RDX on Au/GaAs NSs (curve-B), and (d) concentration dependent SERS spectra of RDX on Au/GaAs NSs.

These annealed Au/GaAs NSs had an enhancement factor of 2×10^5. According to the spectra in Fig 5.28 (b), the SERS signal increased with analyte MB concentration. As shown in Fig. 5.29 (a), these structures exhibit strong reproducibility with reduced RSD values (15% for 446 cm^{-1} modes and 11% for 1621 cm^{-1} modes, respectively). The data from a similar examination for

sensing RDX, an explosive chemical, is presented in Fig. 5.28 (c), where the Raman (0.1 M RDX, curve A) and SERS (10 µM RDX, curve B) spectra were recorded on pristine GaAs and Au/GaAs NSs, respectively. RDX could be identified at concentrations as low as 10 µM, with high signal repeatability. The RDX on Au/GaAs NSs had an EF of 3×10^4 and an RSD of 13% [see Fig. 5.29 (b)]. Because these structures featured a variety of surface characteristics within the same ablated track (micron size cones, nano-pores, and nano-DNA-like structures), we expect that when coated with Au, these structures will behave as plasmonic hotspots of various sizes and shapes. SERS measurements are performed using a portable Raman spectrometer (iRaman plus) with a spot size of 100 µm. As a result, the signal acquired in this study is the sum of the effects of all these surface structures. These annealed Au/GaAs structures have clearly proven their ability to detect MB and RDX at trace quantities.

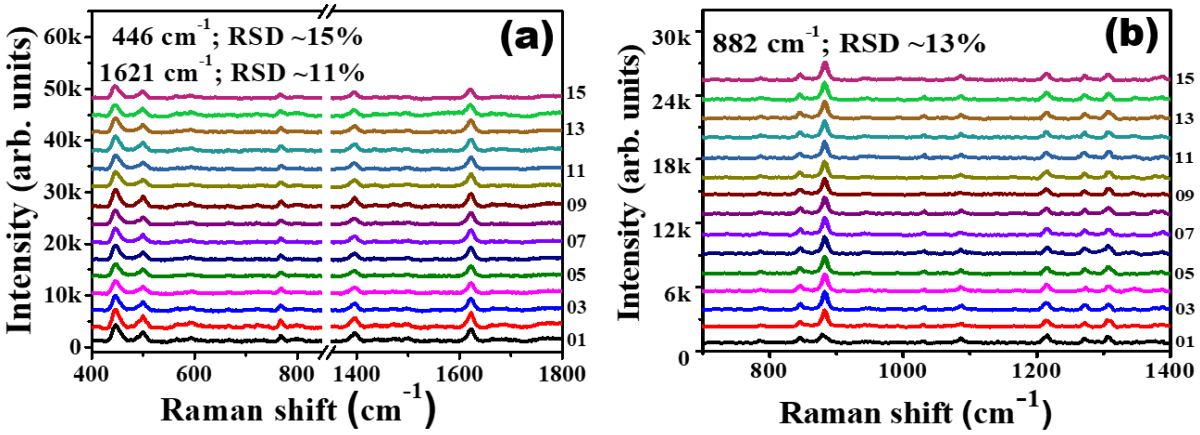

Fig. 5.29 SERS spectra recorded at 15 random locations on Au/GaAs NSs for analytes (a) MB and (b) RDX, respectively.

5.2.4 Summary of fs laser ablated GaAs surface structures in DW

This study demonstrates the creation of deep sub-wavelength structures on GaAs without surface oxidation. The key finding of this work is the formation of sub-70 nanometer DNA-like structures around the edges of the laser path. Furthermore, the presence of four distinct forms of surface structures on laser-ablated GaAs in DW demonstrated the possibility of diverse laser ablation mechanisms occurring at different spatial locations. The GaAs NSs coated with an Au layer were successfully employed as SERS substrates to detect MB and RDX traces. The lowest observed concentration, EF, for MB was calculated to be 50 nM, 2×10^5, while for RDX it was 10 µM, 3×10^4.

5.2.5. Conclusion

In this chapter, a variety of surface structures were created on GaAs. Initially, by performing single line scans at different laser energies in air medium, subwavelength LIPPS with periodicity ~665 nm were thoroughly understood. Effect of laser fluence on the quality and oxidation of these surface structures was investigated. Structures made at lower fluence have better quality with low/no oxidation effects. Further, the Raman and PL study revealed the damage/modification of GaAs that follows the signature of Gaussian beam used in this study. GaAs ablation in DW has led to the formation of cone-like, spherical pores, non-spherical pores, and nano-DNA-like structures at different radial positions from the center of the ablated track. The interesting result was the formation deep-sub wavelength (size ~60-70 nm) DNA like structures at the extreme edges/outside the track. The possibility of different ablation mechanisms at different spatial locations was proposed. Significance of involving dynamic melt flows in the models/theories to closely match the experimental structures was discussed. Finally, these GaAs surface structures were coated with Au NPs and utilized for trace detection of RDX, Tetryl, and MB. These hybrid SERS substrates successfully demonstrated an EF ~10^4 for explosives and 10^5 for dye molecules. Good signal reproducibility with lower RSD values revealed its capability of detection.

References

(1) Wang, W.; Wang, G.; Zhang, Y.; Sun, X.-C.; Yu, Y.; Lian, Y. Light Management With Grating Structures in Optoelectronic Devices. *Front. Chem.* **2021**, *9* (July), 2014–2019. https://doi.org/10.3389/fchem.2021.737679.

(2) Malik, P.; Acharyya, J. N.; Shanu, M.; Kuriakose, A.; Ghosh, S.; Srivastava, P.; Prakash, G. V. Studies on Femtosecond Laser Textured Broadband Anti-Reflective Hierarchical a-SiNx:H Thin Films for Photovoltaic Applications. *ACS Appl. Energy Mater.* **2023**, *6* (3), 2039–2048. https://doi.org/10.1021/acsaem.2c03984.

(3) Deepak, K. L. N.; Kumar, R. S. S.; Narayana Rao, D.; Venugopal Rao, S. Femtosecond Laser Written Microstructures in PMMA and PDMS at 800 Nm for Photonic Applications. *ICALEO 2009 - 28th Int. Congr. Appl. Lasers Electro-Optics, Congr. Proc.* **2009**, *102* (January 2021), 1499–1506. https://doi.org/10.2351/1.5061521.

(4) El-Ansary, Z.; Ram Kumar, H. P.; Brioual, B.; Petronijevic, E.; Cesca, T.; Scian, C.; Mattei, G.; El Hasnaoui, M.; Sibilia, C.; Belardini, A. Broadband, Angle-Dependent Optical Characterization of Asymmetric Self-Assembled Nanohole Arrays in Silver. *Opt. Quantum Electron.* **2023**, *55* (7), 627. https://doi.org/10.1007/s11082-023-04813-w.

(5) Paquin, F.; Rivnay, J.; Salleo, A.; Stingelin, N.; Silva, C. Multi-Phase Semicrystalline Microstructures Drive Exciton Dissociation in Neat Plastic Semiconductors. *J. Mater. Chem. C* **2015**, *3* (207890), 10715–10722. https://doi.org/10.1039/b000000x.

(6) D'Amico, C.; Martin, G.; Troles, J.; Cheng, G.; Stoian, R. Multiscale Laser Written Photonic Structures in Bulk Chalcogenide Glasses for Infrared Light Transport and Extraction. *Photonics* **2021**, *8* (6), 211. https://doi.org/10.3390/photonics8060211.

(7) Kobtsev, D.; Kolesnikova, I.; Redkin, R.; Sarkisov, S. A Comparison of Photoconductive Semiconductors with Long and Short Charge Carrier Lifetimes for Pulsed and CW Terahertz Generation and Detection. *Opt. InfoBase Conf. Pap.* **2019**, *Part F140-* (2014), 1.

(8) Zhang, Z. Y.; Oehler, A. E. H.; Resan, B.; Kurmulis, S.; Zhou, K. J.; Wang, Q.; Mangold, M.; Süedmeyer, T.; Keller, U.; Weingarten, K. J.; Hogg, R. A. 1.55 Mm InAs/GaAs Quantum Dots and High Repetition Rate Quantum Dot SESAM Mode-Locked Laser. *Sci. Rep.* **2012**, *2* (1), 477. https://doi.org/10.1038/srep00477.

(9) Zhang, W.; Shi, Z.; Chen, C.; Yang, X.; Yang, L.; Zeng, Z.; Zhang, B.; Liu, Q. Super-Resolution GaAs Nano-Structures Fabricated by Laser Direct Writing. *Mater. Sci. Semicond. Process.* **2018**, *84* (March), 119–123. https://doi.org/10.1016/j.mssp.2018.05.016.

(10) Sarbada, S.; Huang, Z.; Shin, Y. C.; Ruan, X. Low-Reflectance Laser-Induced Surface Nanostructures Created with a Picosecond Laser. *Appl. Phys. A Mater. Sci. Process.* **2016**, *122* (4), 1–10. https://doi.org/10.1007/s00339-016-0004-0.

(11) Van Driel, H. M.; Sipe, J. E.; Young, J. F. Laser-Induced Periodic Surface Structure on Solids: A

Universal Phenomenon. *Phys. Rev. Lett.* **1982**, *49* (26), 1955–1958. https://doi.org/10.1103/PhysRevLett.49.1955.

(12) Barb, R. A.; Hrelescu, C.; Dong, L.; Heitz, J.; Siegel, J.; Slepicka, P.; Vosmanska, V.; Svorcik, V.; Magnus, B.; Marksteiner, R.; Schernthaner, M.; Groschner, K. Laser-Induced Periodic Surface Structures on Polymers for Formation of Gold Nanowires and Activation of Human Cells. *Appl. Phys. A Mater. Sci. Process.* **2014**, *117* (1), 295–300. https://doi.org/10.1007/s00339-013-8219-9.

(13) Torres, R.; Itina, T. E.; Vervisch, V.; Halbwax, M.; Derrien, T.; Sarnet, T.; Sentis, M.; Ferreira, J.; Torregrosa, F.; Roux, L. Study on Laser-Induced Periodic Structures and Photovoltaic Application. *AIP Conf. Proc.* **2010**, *1278*, 576–581. https://doi.org/10.1063/1.3507149.

(14) Gerke, T. D.; Baird, B. Pulsewidth Dependence of Laser-Induced Periodic Surface Structures Using a Picosecond Fiber Laser. *ICALEO 2012 - 31st Int. Congr. Appl. Lasers Electro-Optics* **2012**, *935*, 935–942. https://doi.org/10.2351/1.5062566.

(15) Gazizova, M. Y.; Smirnov, N. A.; Kudryashov, S. I.; Chen, J.; Ahmadeev, Y. H.; Goncharov, I. Y.; Shugurov, V. V.; Prokopenko, N. A. Correlation of the Tribological Properties of LIPSS on TiN Surface with 3D Parameters of Roughness. *IOP Conf. Ser. Mater. Sci. Eng.* **2021**, *1014* (1), 3–7. https://doi.org/10.1088/1757-899X/1014/1/012014.

(16) Kim, J. H.; Andeen, D.; Lange, F. F. Hydrothermal Growth of Periodic, Single-Crystal ZnO Microrods and Microtunnels. *Adv. Mater.* **2006**, *18* (18), 2453–2457. https://doi.org/10.1002/adma.200600257.

(17) Hung, Y.-J.; Lee, S.-L.; Wu, K.-C.; Tai, Y.; Pan, Y.-T. Antireflective Silicon Surface with Vertical-Aligned Silicon Nanowires Realized by Simple Wet Chemical Etching Processes. *Opt. Express* **2011**, *19* (17), 15792. https://doi.org/10.1364/OE.19.015792.

(18) Wang, G. G.; Lin, Z. Q.; Zhao, D. D.; Han, J. C. Enhanced Transmission and Self-Cleaning of Patterned Sapphire Substrates Prepared by Wet Chemical Etching Using Silica Masks. *Langmuir*. 2018, pp 8898–8903. https://doi.org/10.1021/acs.langmuir.8b01486.

(19) Ahn, S.; Park, H.; Cho, J.; Park, C.; Park, J.; Lee, H.; Hong, K.; Bong, S.; Yi, J. Reactive-Ion-Etched Glass Surface with 2D Periodic Surface Texture for Application in Solar Cells. *Optik (Stuttg).* **2021**, *229* (November 2020), 166304. https://doi.org/10.1016/j.ijleo.2021.166304.

(20) Silvestre, C. M.; Nguyen, V.; Jansen, H.; Hansen, O. Deep Reactive Ion Etching of 'Grass-Free' Widely-Spaced Periodic 2D Arrays, Using Sacrificial Structures. *Microelectron. Eng.* **2020**, *223* (January), 111228. https://doi.org/10.1016/j.mee.2020.111228.

(21) Chowdhury, D.; Ghose, D. Formation of Nearly Defect-Free Nanoripples by Sputtering of GaAs (001) Surface at High Temperature. *Surfaces and Interfaces* **2019**, *17* (July), 100364. https://doi.org/10.1016/j.surfin.2019.100364.

(22) Wang, M.; Zhang, N.; Chen, S.-C. Effects of Supra-Wavelength Periodic Structures on the Formation of 1D/2D Periodic Nanostructures by Femtosecond Lasers. *Opt. Laser Technol.* **2022**,

151 (February), 108058. https://doi.org/10.1016/j.optlastec.2022.108058.

(23) Albu, C.; Dinescu, A.; Filipescu, M.; Ulmeanu, M.; Zamfirescu, M. Periodical Structures Induced by Femtosecond Laser on Metals in Air and Liquid Environments. *Appl. Surf. Sci.* **2013**, *278*, 347–351. https://doi.org/10.1016/j.apsusc.2012.11.075.

(24) Fuerbacher, R.; Liedl, G.; Murzin, S. P. Experimental Study of Spatial Frequency Transition of Laser Induced Periodic Surface Structures. *J. Phys. Conf. Ser.* **2021**, *1745* (1). https://doi.org/10.1088/1742-6596/1745/1/012017.

(25) Bonse, J. Quo Vadis LIPSS?—Recent and Future Trends on Laser-Induced Periodic Surface Structures. *Nanomaterials* **2020**, *10* (10), 1–19. https://doi.org/10.3390/nano10101950.

(26) Dostovalov, A.; Bronnikov, K.; Korolkov, V.; Babin, S.; Mitsai, E.; Mironenko, A.; Tutov, M.; Zhang, D.; Sugioka, K.; Maksimovic, J.; Katkus, T.; Juodkazis, S.; Zhizhchenko, A.; Kuchmizhak, A. Hierarchical Anti-Reflective Laser-Induced Periodic Surface Structures (LIPSSs) on Amorphous Si Films for Sensing Applications. *Nanoscale* **2020**, *12* (25), 13431–13441. https://doi.org/10.1039/d0nr02182b.

(27) Mastellone, M.; Pace, M. L.; Curcio, M.; Caggiano, N.; De Bonis, A.; Teghil, R.; Dolce, P.; Mollica, D.; Orlando, S.; Santagata, A.; Serpente, V.; Bellucci, A.; Girolami, M.; Polini, R.; Trucchi, D. M. LIPSS Applied to Wide Bandgap Semiconductors and Dielectrics: Assessment and Future Perspectives. *Materials (Basel).* **2022**, *15* (4), 1378. https://doi.org/10.3390/ma15041378.

(28) Gao, Y. F.; Yu, C. Y.; Han, B.; Ehrhardt, M.; Lorenz, P.; Xu, L. F.; Zhu, R. H. Picosecond Laser-Induced Periodic Surface Structures (LIPSS) on Crystalline Silicon. *Surfaces and Interfaces* **2020**, *19* (April), 100538. https://doi.org/10.1016/j.surfin.2020.100538.

(29) Liu, R.; Zhang, D.; Li, Z. Femtosecond Laser Induced Simultaneous Functional Nanomaterial Synthesis, in Situ Deposition and Hierarchical LIPSS Nanostructuring for Tunable Antireflectance and Iridescence Applications. *J. Mater. Sci. Technol.* **2021**, *89*, 179–185. https://doi.org/10.1016/j.jmst.2021.02.024.

(30) Rivera, L. P.; Munoz-Martin, D.; Chávez-Chávez, A.; Morales, M.; Gómez-Rosas, G.; Molpeceres, C. Subwavelength LIPSS Formation on SS304 by Picosecond Laser Irradiation under Water Confinement. *Mater. Sci. Eng. B Solid-State Mater. Adv. Technol.* **2021**, *273*. https://doi.org/10.1016/j.mseb.2021.115393.

(31) Taher, M. A.; Chaudhary, N.; Thirunaukkarasu, K.; Rajput, V. K.; Naraharisetty, S. R. G. Controlled Periodicities of Ladder-like Structures via Femtosecond Laser of Wavelength from 400 Nm to 2200 Nm. *Surfaces and Interfaces* **2022**, *28* (November 2021), 101622. https://doi.org/10.1016/j.surfin.2021.101622.

(32) Banerjee, D.; Akkanaboina, M.; Ghosh, S.; Soma, V. R. Picosecond Bessel Beam Fabricated Pure, Gold-Coated Silver Nanostructures for Trace-Level Sensing of Multiple Explosives and Hazardous Molecules. *Materials (Basel).* **2022**, *15* (12), 4155. https://doi.org/10.3390/ma15124155.

(33) Song, S.; Lu, Q.; Zhang, P.; Yan, H.; Shi, H.; Yu, Z.; Sun, T.; Luo, Z.; Tian, Y. A Critical Review on the Simulation of Ultra-Short Pulse Laser-Metal Interactions Based on a Two-Temperature Model (TTM). *Opt. Laser Technol.* **2023**, *159* (November 2022), 109001. https://doi.org/10.1016/j.optlastec.2022.109001.

(34) Bonse, J.; Gräf, S. Maxwell Meets Marangoni—A Review of Theories on Laser-Induced Periodic Surface Structures. *Laser Photon. Rev.* **2020**, *14* (10), 2000215. https://doi.org/10.1002/lpor.202000215.

(35) Hermens, U.; Pothen, M.; Winands, K.; Arntz, K.; Klocke, F. Automated Polarization Control for the Precise Alignment of Laser-Induced Self-Organized Nanostructures. *Opt. Lasers Eng.* **2018**, *101* (September 2017), 44–50. https://doi.org/10.1016/j.optlaseng.2017.10.001.

(36) Lu, M.; Cheng, K.; Qin, Z.; Ju, J.; Liu, J.; Huo, Y. Electromagnetic Origin of Femtosecond Laser-Induced Periodic Surface Structures on GaP Crystals. *Opt. Express* **2022**, *30* (6), 10152. https://doi.org/10.1364/OE.452577.

(37) Rudenko, A.; Abou-Saleh, A.; Pigeon, F.; Mauclair, C.; Garrelie, F.; Stoian, R.; Colombier, J. P. High-Frequency Periodic Patterns Driven by Non-Radiative Fields Coupled with Marangoni Convection Instabilities on Laser-Excited Metal Surfaces. *Acta Mater.* **2020**, *194* (May), 93–105. https://doi.org/10.1016/j.actamat.2020.04.058.

(38) Nakhoul, A.; Maurice, C.; Agoyan, M.; Rudenko, A.; Garrelie, F.; Pigeon, F.; Colombier, J.-P. Self-Organization Regimes Induced by Ultrafast Laser on Surfaces in the Tens of Nanometer Scales. *Nanomaterials* **2021**, *11* (4), 1020. https://doi.org/10.3390/nano11041020.

(39) Gamaly, E. G.; Rode, A. V.; Luther-Davies, B.; Tikhonchuk, V. T. Ablation of Solids by Femtosecond Lasers: Ablation Mechanism and Ablation Thresholds for Metals and Dielectrics. *Phys. Plasmas* **2002**, *9* (3), 949–957. https://doi.org/10.1063/1.1447555.

(40) Behera, S.; Fry, P. W.; Francis, H.; Jin, C. Y.; Hopkinson, M. Broadband, Wide-Angle Antireflection in GaAs through Surface Nano-Structuring for Solar Cell Applications. *Sci. Rep.* **2020**, *10* (1), 1–10. https://doi.org/10.1038/s41598-020-63327-7.

(41) Margiolakis, A.; Tsibidis, G. D.; Dani, K. M.; Tsironis, G. P. Ultrafast Dynamics and Subwavelength Periodic Structure Formation Following Irradiation of GaAs with Femtosecond Laser Pulses. *Phys. Rev. B* **2018**, *98* (22), 224103. https://doi.org/10.1103/PhysRevB.98.224103.

(42) Ionin, A. A.; Klimachev, Y. M.; Kozlov, A. Y.; Kudryashov, S. I.; Ligachev, A. E.; Makarov, S. V.; Seleznev, L. V.; Sinitsyn, D. V.; Rudenko, A. A.; Khmelnitsky, R. A. Direct Femtosecond Laser Fabrication of Antireflective Layer on GaAs Surface. *Appl. Phys. B* **2013**, *111* (3), 419–423. https://doi.org/10.1007/s00340-013-5350-4.

(43) Kudryashov, S. I.; Emel'yanov, V. I. Structural Transitions in GaAs during Irradiation by a 100-Fs Laser Pulse. *Kvantovaya Elektron.* **2001**, *31* (7), 565–566. https://doi.org/10.1070/qe2001v031n07abeh002004.

(44) Apostolova, T.; Ionin, A. A.; Kudryashov, S. I.; Seleznev, L. V.; Sinitsyn, D. V. Self-Limited Ionization of GaAs at High Femtosecond Laser Intensities. In *AIP Conference Proceedings*; 2012; Vol. 1464, pp 146–157. https://doi.org/10.1063/1.4739869.

(45) Abere, M. J.; Torralva, B.; Yalisove, S. M. Periodic Surface Structure Bifurcation Induced by Ultrafast Laser Generated Point Defect Diffusion in GaAs. *Appl. Phys. Lett.* **2016**, *108* (15), 153110. https://doi.org/10.1063/1.4946861.

(46) Sarracino, A.; Ansari, A. R.; Torralva, B.; Yalisove, S. Sub-100 Nm High Spatial Frequency Periodic Structures Driven by Femtosecond Laser Induced Desorption in GaAs. *Appl. Phys. Lett.* **2021**, *118* (24), 242106. https://doi.org/10.1063/5.0053037.

(47) Lenzner, M.; Bonse, J.; Baudach, S.; Kruger, J.; Kautek, W. Threshold and Morphology of Femtosecond Laser Induced Damage in Silicon. In *Conference on Lasers and Electro-Optics (CLEO 2000). Technical Digest. Postconference Edition. TOPS Vol.39 (IEEE Cat. No.00CH37088)*; IEEE, 2000; pp 614–615. https://doi.org/10.1109/CLEO.2000.907463.

(48) Li, X.; Rong, W.; Jiang, L.; Zhang, K.; Li, C.; Cao, Q.; Zhang, G.; Lu, Y. Generation and Elimination of Polarization-Dependent Ablation of Cubic Crystals by Femtosecond Laser Radiation. *Opt. Express* **2014**, *22* (24), 30170. https://doi.org/10.1364/oe.22.030170.

(49) Mustafa, H.; Matthews, D. T. A.; Römer, G. R. B. E. Investigation of the Ultrashort Pulsed Laser Processing of Zinc at 515 nm: Morphology, Crystallography and Ablation Threshold. *Mater. Des.* **2019**, *169*, 107675. https://doi.org/10.1016/j.matdes.2019.107675.

(50) Abere, M. J.; Yalisove, S. M.; Torralva, B. Alignment of Morphology during High Spatial Frequency Periodic Structure Formation in GaAs. *J. Appl. Phys.* **2019**, *126* (14), 143102. https://doi.org/10.1063/1.5114930.

(51) Vakili-Farahani, F.; Lungershausen, J.; Wasmer, K. Process Parameter Optimization for Wobbling Laser Spot Welding of Ti6Al4V Alloy. *Phys. Procedia* **2016**, *83*, 483–493. https://doi.org/10.1016/j.phpro.2016.08.050.

(52) Zhang, S.; Yang, Q.; Lüpke, G. Spatial Beam Shaping of Ultrashort Laser Pulses: Theory and Experiment. *Appl. Opt.* **2005**, *44* (27), 5818. https://doi.org/10.1364/AO.44.005818.

(53) Borowiec, A.; Haugen, H. K. Femtosecond Laser Micromachining of Grooves in Indium Phosphide. *Appl. Phys. A* **2004**, *79* (3), 521–529. https://doi.org/10.1007/s00339-003-2377-0.

(54) Borowiec, A.; MacKenzie, M.; Weatherly, G. C.; Haugen, H. K. Femtosecond Laser Pulse Ablation of GaAs and InP: Studies Utilizing Scanning and Transmission Electron Microscopy. *Appl. Phys. A* **2003**, *77* (3–4), 411–417. https://doi.org/10.1007/s00339-002-1949-8.

(55) Nivas, J. J. J.; Valadan, M.; Salvatore, M.; Fittipaldi, R.; Himmerlich, M.; Rimoldi, M.; Passarelli, A.; Allahyari, E.; Oscurato, S. L.; Vecchione, A.; Altucci, C.; Amoruso, S.; Andreone, A.; Calatroni, S.; Masullo, M. R. Secondary Electron Yield Reduction by Femtosecond Pulse Laser-Induced Periodic Surface Structuring. *Surfaces and Interfaces* **2021**, *25* (May), 101179.

https://doi.org/10.1016/j.surfin.2021.101179.

(56) Camacho-López, S.; Evans, R.; Escobar-Alarcón, L.; Camacho-López, M. A.; Camacho-López, M. A. Polarization-Dependent Single-Beam Laser-Induced Grating-like Effects on Titanium Films. *Appl. Surf. Sci.* **2008**, *255* (5), 3028–3032. https://doi.org/10.1016/j.apsusc.2008.08.085.

(57) Loganathan, S.; Santhanakrishnan, S.; Bathe, R.; Arunachalam, M. Prediction of Femtosecond Laser Ablation Profile on Human Teeth. *Lasers Med. Sci.* **2019**, *34* (4), 693–701. https://doi.org/10.1007/s10103-018-2644-0.

(58) Bonse, J.; Rosenfeld, A.; Krüger, J. On the Role of Surface Plasmon Polaritons in the Formation of Laser-Induced Periodic Surface Structures upon Irradiation of Silicon by Femtosecond-Laser Pulses. *J. Appl. Phys.* **2009**, *106* (10). https://doi.org/10.1063/1.3261734.

(59) Glezer, E. N.; Siegal, Y.; Huang, L.; Mazur, E. Laser-Induced Band-Gap Collapse in GaAs. *Phys. Rev. B* **1995**, *51* (11), 6959–6970. https://doi.org/10.1103/PhysRevB.51.6959.

(60) Review, P. Dielectric Constant. *Phys. Rev.* **1963**, *129* (23), 1561.

(61) Huang, L.; Callan, J. P.; Glezer, E. N.; Mazur, E. GaAs under Intense Ultrafast Excitation: Response of the Dielectric Function. *Phys. Rev. Lett.* **1998**, *80* (1), 185–188. https://doi.org/10.1103/PhysRevLett.80.185.

(62) Siegal, Y.; Glezer, E. N.; Mazur, E. Laser-Induced Phase Transitions in GaAs. In *Femtosecond Chemistry*; Wiley-VCH Verlag GmbH: Weinheim, Germany, 2008; pp 581–602. https://doi.org/10.1002/9783527619436.ch19.

(63) Shin, S.; Park, J. K.; Kim, D.-H. Suppression of Spallation Induced Nanoparticles by High Repetition Rate Femtosecond Laser Pulses: Realization of Precise Laser Material Processing with High Throughput. *Opt. Express* **2021**, *29* (13), 20545. https://doi.org/10.1364/oe.427168.

(64) Attolini, G.; Chimenti, E.; Pelosi, C.; Lottici, P. P.; Carles, R. Surface Morphology and Raman Scattering in GaAs/InAs(111) Heterostructures Grown by MOVPE. *Mater. Sci. Eng. B* **1997**, *44* (1–3), 155–159. https://doi.org/10.1016/S0921-5107(96)01809-0.

(65) Campbell, I. H.; Fauchet, P. M. Cw Laser Irradiation of GaAs: Arsenic Formation and Photoluminescence Degradation. *Appl. Phys. Lett.* **1990**, *57* (1), 10–12. https://doi.org/10.1063/1.103564.

(66) Mangababu, A.; Sarang Dev, G.; Chandu, B.; Bharati, M. S. S.; Venugopal Rao, S.; Nageswara Rao, S. V. S. Structural Investigations of Picosecond Laser Ablated GaAs Nanoparticles in Different Liquids. *Nano-Structures & Nano-Objects* **2020**, *23*, 100509. https://doi.org/10.1016/j.nanoso.2020.100509.

(67) Mangababu, A.; Sarang Dev, G.; Chandu, B.; Bharati, M. S. S.; Debashish, P.; Venugopal Rao, S.; Nageswara Rao, S. V. S. Fabrication and Characterization of GaAs Nanoparticles Achieved Using Femtosecond Laser Ablation. *Mater. Today Proc.* **2020**, *33* (5), 2385–2389. https://doi.org/10.1016/j.matpr.2020.05.727.

(68) Je. Semjonow, A.; Lau, A.; Lenz, K.; Nechiporuk, B. D.; Strelchuk, V. V.; Ja. Walakh, M. The Changes of Raman Scattering in GaAs Crystals after UV-Excimer Laser Irradiation. *J. Mol. Struct.* **1992**, *267*, 155–161. https://doi.org/10.1016/0022-2860(92)87025-Q.

(69) Tsu, R.; Baglin, J. E.; Lasher, G. J.; Tsang, J. C. Laser-induced Recrystallization and Damage in GaAs. *Appl. Phys. Lett.* **1979**, *34* (2), 153–155. https://doi.org/10.1063/1.90710.

(70) Holtz, M.; Zallen, R.; Brafman, O.; Matteson, S. Raman-Scattering Depth Profile of the Structure of Ion-Implanted GaAs. *Phys. Rev. B* **1988**, *37* (9), 4609–4617. https://doi.org/10.1103/PhysRevB.37.4609.

(71) Ghita, R. V.; Negrila, C. C.; Cotirlan, C.; Logofatu, C. On the Passivation of Gaas Surface by Sulfide Compounds. *Dig. J. Nanomater. Biostructures* **2013**, *8* (3), 1335–1344.

(72) Jung, M.; Lee, S.; Park, M. C.; Byun, Y. T.; Jhon, Y. M.; Kim, S. H.; Mho, S. Il; Kim, K.; Woo, D. H. Enhancement of PL Intensity by Photonic Crystal Fabricated on GaAs Substrate Using Nanoporous Alumina Mask. *2006 IEEE Nanotechnol. Mater. Devices Conf. NMDC* **2006**, *1* (November), 436–437. https://doi.org/10.1109/NMDC.2006.4388804.

(73) Zou, X.; Li, C.; Su, X.; Liu, Y.; Finkelstein-Shapiro, D.; Zhang, W.; Yartsev, A. Carrier Recombination Processes in GaAs Wafers Passivated by Wet Nitridation. *ACS Applied Materials and Interfaces*. 2020, pp 28360–28367. https://doi.org/10.1021/acsami.0c04892.

(74) Ma, Y.; Du, Y.; Chen, Y.; Gu, C.; Jiang, T.; Wei, G.; Zhou, J. Intrinsic Raman Signal of Polymer Matrix Induced Quantitative Multiphase SERS Analysis Based on Stretched PDMS Film with Anchored Ag Nanoparticles/Au Nanowires. *Chem. Eng. J.* **2020**, *381* (September 2019), 122710. https://doi.org/10.1016/j.cej.2019.122710.

(75) Han, L.; Liu, H.; Zhang, J.; Zhou, J.; Jiang, T. Recyclable SERS Monitoring of Food Quality Based on the Shrubby Morphology of Titania Oxide-Triggered Electromagnetic "Hotspots." *Appl. Surf. Sci.* **2022**, *604* (July), 154456. https://doi.org/10.1016/j.apsusc.2022.154456.

(76) Stratakis, E.; Zorba, V.; Barberoglou, M.; Fotakis, C.; Shafeev, G. A. Femtosecond Laser Writing of Nanostructures on Bulk Al via Its Ablation in Air and Liquids. *Appl. Surf. Sci.* **2009**, *255* (10), 5346–5350. https://doi.org/10.1016/j.apsusc.2008.07.183.

(77) Akkanaboina, M.; Banerjee, D.; Kumar, K. R.; Goud, R. S. P.; Soma, V. R.; Rao, S. V. S. N. Gold Nanoparticles Coated LIPSS on GaAs for Trace Detection of RDX and Tetryl. *Surfaces and Interfaces* **2023**, *36*, 102563. https://doi.org/10.1016/j.surfin.2022.102563.

(78) Mangababu, A.; Sai Prasad Goud, R.; Byram, C.; Rathod, J.; Banerjee, D.; Rao Soma, V.; Nageswara Rao, S. V. S. Multi-Functional Gallium Arsenide Nanoparticles and Nanostructures Fabricated Using Picosecond Laser Ablation. *Appl. Surf. Sci.* **2022**, *589* (January), 152802. https://doi.org/10.1016/j.apsusc.2022.152802.

(79) De Bonis, A.; Galasso, A.; Santagata, A.; Teghil, R. Laser Ablation of GaAs in Liquid: The Role of Laser Pulse Duration. *J. Phys. D. Appl. Phys.* **2016**, *49* (3), 035301.

https://doi.org/10.1088/0022-3727/49/3/035301.

(80) Sharifi, T.; Dorranian, D.; Torkamany, M. J. Optimisation of GaAs Nanocrystals Synthesis by Laser Ablation in Water. *J. Exp. Nanosci.* **2013**, *8* (6), 808–817. https://doi.org/10.1080/17458080.2011.608729.

(81) Banerjee, D.; Moram, S. S. B.; Byram, C.; Rathod, J.; Jena, T.; Podagatlapalli, G. K.; Soma, V. R. Plasmon-Enhanced Ultrafast and Tunable Thermo-Optic Nonlinear Optical Properties of Femtosecond Laser Ablated TiO2 and Silver-Doped TiO2 Nanoparticles. *Appl. Surf. Sci.* **2021**, *569*, 151070. https://doi.org/10.1016/j.apsusc.2021.151070.

(82) Ganeev, R. A.; Baba, M.; Ozaki, T.; Kuroda, H. Long- and Short-Period Nanostructure Formation on Semiconductor Surfaces at Different Ambient Conditions. *J. Opt. Soc. Am. B* **2010**, *27* (5), 1077. https://doi.org/10.1364/JOSAB.27.001077.

(83) Wang, L.; Xu, B.-B.; Cao, X.-W.; Li, Q.-K.; Tian, W.-J.; Chen, Q.-D.; Juodkazis, S.; Sun, H.-B. Competition between Subwavelength and Deep-Subwavelength Structures Ablated by Ultrashort Laser Pulses. *Optica* **2017**, *4* (6), 637. https://doi.org/10.1364/OPTICA.4.000637.

(84) Ding, S.; Zhu, D.; Xue, W.; Liu, W.; Cao, Y. Picosecond Laser-Induced Hierarchical Periodic Near- and Deep-Subwavelength Ripples on Stainless-Steel Surfaces. *Nanomaterials* **2019**, *10* (1), 62. https://doi.org/10.3390/nano10010062.

(85) Zhang, D.; Ranjan, B.; Tanaka, T.; Sugioka, K. Multiscale Hierarchical Micro/Nanostructures Created by Femtosecond Laser Ablation in Liquids for Polarization-Dependent Broadband Antireflection. *Nanomaterials* **2020**, *10* (8), 1573. https://doi.org/10.3390/nano10081573.

(86) Schwarz, S.; Rung, S.; Esen, C.; Hellmann, R. Surface Plasmon Polariton Triggered Generation of 1D-Low Spatial Frequency LIPSS on Fused Silica. *Appl. Sci.* **2018**, *8* (9), 1624. https://doi.org/10.3390/app8091624.

(87) Gojani, A. B. Laser Ablation at the Hydrodynamic Regime. *EPJ Web Conf.* **2013**, *45*, 01124. https://doi.org/10.1051/epjconf/20134501124.

Chapter 6

Conclusions and Future scope

All the significant findings from this thesis study are compiled in this chapter. There is a brief discussion of the findings from the results chapters (i.e., chapters 3, 4, and 5). The future directions of the existing research and knowledge gaps in "Ultrafast Laser Ablation of GaAs" are thoroughly explained.

6.1 Conclusions of the thesis work

The work carried out in the present thesis and its significant outcomes are summarized in this chapter.

6.1 (a) Study of Ultrafast Laser Ablated HfO_2 NPs

This work[1] explains how the HfO_2 target's initial grain size affected the formation of the HfO_2 NPs and background structures by femtosecond LAL process. The smaller initial grain size resulted in the smaller spherical NPs after the ablation. More intriguingly, nano-fibre-like structures joining the spherical NPs can be seen regardless of the laser parameters and initial target conditions. Additionally, it is noted that the high-temperature HfO_2 phase coexists or emerges upon the high energy laser ablation process. After performing a preliminary study on the laser ablation of HfO_2, the focus has been shifted to the main topic of the thesis.

6.1(b) Structural Investigations of Ultrafast Laser Ablated GaAs NPs

This work[2,3] presents a detailed study on the GaAs colloidal solutions produced by ultrafast lasers. The femtosecond LAL method, carried out at various laser energies, demonstrated that the ablation yield and the particle size increase with increase in input energy. Along with the spherical GaAs NPs (which are in cubic zinc blend phase), it is also demonstrated that a background mesh-like material formed. The additional stoichiometry investigations revealed that the background is made up of amorphous oxide materials of Ga/As/GaAs and the spherical NPs are mostly of pure GaAs. Further, NPs are also generated using a picosecond laser to observe the impact of pulse duration on the formation of resulting structures. More background material, unstable/exotic phases (such as As_2O_3, Ga_2O_3, and $GaAsO_4$), and spherical GaAs NPs have been produced by picosecond pulses with 15 mJ of laser energy. This ps LAL technique produced a high temperature/high pressure stable phase (hexagonal) GaAs NPs, which is a significant outcome of the study.

Therefore, our study demonstrated that by adjusting the laser parameters and surrounding liquids during the ablation, it is possible to selectively generate exotic/high temperature phases of GaAs NPs or pure room temperature stable GaAs particles.

6.1 (c) Simultaneous Fabrication of Multifunctional GaAs NPs and NSs by Picosecond Laser Ablation

This work[4,5] describes the simultaneous production of GaAs NPs and NSs by employing a picosecond LAL technique. Room temperature stable (cubic zinc blende) GaAs NPs were generated by lowering the laser energy (5 mJ). Its NLO properties are studied using a

femtosecond MHz Z-scan method, and it is confirmed that these NPs have two photon absorption properties. Anti-reflective, hydrophilic, and SERS applications for GaAs NSs have been thoroughly researched. It also presents the effects of different experimental circumstances, including comparative research of GaAs NSs generated in Air and DW medium. Owing to the higher damage, picosecond laser ablation in air produced debris-like structures, whereas ablation in DW resulted in the formation of quasi-periodic surface structures. These surface structures are covered with a tiny layer of gold to record the SERS response. These hybrid SERS substrates (plasmonic Au-coated GaAs surface structures) demonstrated good SERS sensitivity with smaller relative standard deviations and higher signal repeatability.

6.1 (d) Effects of Laser Fluence on the Formation of GaAs Periodic Surface Structures by Femtosecond Laser Ablation in Air and Distilled Water

A thorough investigation was carried out using femtosecond laser pulses to generate GaAs LIPSS in air at various laser energies[6]. In ambient air, single-line laser scans are drawn with input laser energy ranging from 5 μJ to 100 μJ. The influence of laser energy on LIPSS periodicity and oxidation is investigated. The effect of laser beam profile on LIPSS quality at different radial positions of the beam point is demonstrated experimentally. Furthermore, when GaAs is ablated by femtosecond pulses in DW, numerous ablation mechanisms can act at different radial points along the ablated track. From the center to the extremities of the ablated track, fascinating features such as micron-sized cones, nano-pores, and nano-DNA-like structures (average size of 60-70 nm) were seen. The importance of models that include changes in the dynamics of the melt flow and surrounding media is examined. The most noteworthy outcome of this work is the creation of sub-70 nm surface nanostructures on GaAs.

6.1 (e) Brief outcomes of the thesis

(1)The GaAs NPs and the background mesh like material is thoroughly analyzed and presented in this work. It is important to note that there are only a few studies on the ultrafast laser ablation of GaAs. Particularly, to the best of our knowledge, this is a first attempt to analyze the background mesh like structures in great detail.

(2)PLAL revealed the possibility of synthesizing GaAs NPs in different phases including room temperature stable, non-equilibrium, and other exotic phases. This study suggests a systematic method to selectively produce exotic phases or the ambient phase of GaAs and associated compounds.

(3)Simultaneous fabrication of GaAs NPs and NSs with their possible applications was presented. This study demonstrated various applications for the produced nanoparticles and structures. Further, potential for many other important applications has also been highlighted.

(4)At various experimental conditions GaAs surface structures were created and studied. The femtosecond laser ablation in air has led to the formation of uniform large area LIPPS (or ripples), whereas the sub-70 nm structures are obtained in the case of ablation in DW. This is a closer and detailed look at the radial distribution of fine structures, their size, shape and orientation, within a single track. These results provide useful information to understand the laser matter interaction in great detail.

6.2 Future Scope of the current thesis

The experimental results presented in this thesis provided deep insights to understand the various mechanisms involved in the laser ablation of materials. However, most of these results have also left open ends and posed questions to the current understanding of these mechanisms. These studies suggested new systematic experiments to further elucidate these mechanisms at a more fundamental level. Further, these studies have also indicated the potential of resulting structures for various practical applications. Some of these points are listed below:

1. When studying the effect of different liquid media on laser-ablated GaAs NPs, it is recognized that many solvent parameters vary from one another, making it difficult to compare the effect due to solvent parameters. In the future, comprehensive research will be planned ablating GaAs in the same solvent and varying any one solvent parameter, such as viscosity or density.
2. GaAs NPs with smaller size, reproducibility, and stability should be achieved to use them in quantum LEDs and Photonic applications[7–9].
3. Further, it is known that the lower laser fluence leads to the high frequency LIPSS (lower feature size structures). Hence, utilizing the lower fluence laser beams, wide area, and uniform low frequency LIPSS will be achieved[10].
4. Detecting biomolecules using Au/GaAs LIPSS based hybrid SERS substrates will be another study[11,12].
5. GaAs LIPSS coated with plasmonic or non-plasmonic materials will be tested for making various sensors, detectors, and energy harvesting devices such as solar cells[13–15].
6. GaAs LIPSS should be tested for its applications as diffraction gratings and polarization tuning/modulators[16].

References

(1) Mangababu, A.; Sianglam, C.; Chandu, B.; Avasthi, D. K.; Rao, S. V.; Motapothula, M.; Rao, S. V. S. N. Effects of Initial Grain Size and Laser Parameters on HfO2 Nanoparticles Prepared Using Femtosecond Laser Ablation in Liquids. *J. Electron. Mater.* **2021**, *50* (4), 1742–1751. https://doi.org/10.1007/s11664-020-08610-z.

(2) Mangababu, A.; Sarang Dev, G.; Chandu, B.; Bharati, M. S. S.; Debashish, P.; Venugopal Rao, S.; Nageswara Rao, S. V. S. Fabrication and Characterization of GaAs Nanoparticles Achieved Using Femtosecond Laser Ablation. *Mater. Today Proc.* **2020**, *33* (5), 2385–2389. https://doi.org/10.1016/j.matpr.2020.05.727.

(3) Mangababu, A.; Sarang Dev, G.; Chandu, B.; Bharati, M. S. S.; Venugopal Rao, S.; Nageswara Rao, S. V. S. Structural Investigations of Picosecond Laser Ablated GaAs Nanoparticles in Different Liquids. *Nano-Structures & Nano-Objects* **2020**, *23*, 100509. https://doi.org/10.1016/j.nanoso.2020.100509.

(4) Mangababu, A.; Sai Prasad Goud, R.; Byram, C.; Rathod, J.; Banerjee, D.; Rao Soma, V.; Nageswara Rao, S. V. S. Multi-Functional Gallium Arsenide Nanoparticles and Nanostructures Fabricated Using Picosecond Laser Ablation. *Appl. Surf. Sci.* **2022**, *589* (January), 152802. https://doi.org/10.1016/j.apsusc.2022.152802.

(5) Mangababu, A.; Banerjee, D.; Ravi Kumar, K.; Sai Prasad Goud, R.; Rao Soma, V.; Nageswara Rao, S. V. S. Comparative Study of GaAs Nanostructures Synthesized in Air and Distilled Water by Picosecond Pulsed Laser Ablation and Application in Hazardous Molecules Detection. *Journal of Laser Applications*. 2022, p 032014. https://doi.org/10.2351/7.0000750.

(6) Akkanaboina, M.; Banerjee, D.; Kumar, K. R.; Goud, R. S. P.; Soma, V. R.; Rao, S. V. S. N. Gold Nanoparticles Coated LIPSS on GaAs for Trace Detection of RDX and Tetryl. *Surfaces and Interfaces* **2023**, *36*, 102563. https://doi.org/10.1016/j.surfin.2022.102563.

(7) Nayak, J.; Mythili, R.; Vijayalakshmi, M.; Sahu, S. N. Size Quantization Effect in GaAs Nanocrystals. *Phys. E Low-Dimensional Syst. Nanostructures* **2004**, *24* (3–4), 227–233. https://doi.org/10.1016/j.physe.2004.04.035.

(8) Jain, D.; Mangla, O.; Roy, S. Wide Band Gap Gallium Arsenide Nanoparticles Fabricated Using Plasma Method. In *AIP Conference Proceedings*; 2016; Vol. 1731, p 050143. https://doi.org/10.1063/1.4947797.

(9) Salminen, T.; Dahl, J.; Tuominen, M.; Laukkanen, P.; Arola, E.; Niemi, T. Single-Step Fabrication of Luminescent GaAs Nanocrystals by Pulsed Laser Ablation in Liquids. *Opt. Mater. Express* **2012**, *2* (6), 799. https://doi.org/10.1364/OME.2.000799.

(10) Sarracino, A.; Ansari, A. R.; Torralva, B.; Yalisove, S. Sub-100 Nm High Spatial Frequency Periodic Structures Driven by Femtosecond Laser Induced Desorption in GaAs. *Appl. Phys. Lett.* **2021**, *118* (24), 242106. https://doi.org/10.1063/5.0053037.

(11) Rastogi, R.; Arianfard, H.; Moss, D.; Juodkazis, S.; Adam, P. M.; Krishnamoorthy, S. Analyte Co-Localization at Electromagnetic Gap Hot-Spots for Highly Sensitive (Bio)Molecular Detection by Plasmon Enhanced Spectroscopies. *ACS Appl. Mater. Interfaces* **2021**, *13* (7), 9113–9121. https://doi.org/10.1021/acsami.0c17929.

(12) Tang, L.; Chun, I. S.; Wang, Z.; Li, J.; Li, X.; Lu, Y. DNA Detection Using Plasmonic Enhanced Near-Infrared Photoluminescence of Gallium Arsenide. *Anal. Chem.* **2013**, *85* (20), 9522–9527. https://doi.org/10.1021/ac401169c.

(13) Brawley, Z. T.; Bauman, S. J.; Abbey, G. P.; Darweesh, A. A.; Nusir, A. I.; Manasreh, O.; Herzog, J. B. Modeling and Optimization of Au-GaAs Plasmonic Nanoslit Array Structures for Enhanced near-Infrared Photodetector Applications. *J. Nanophotonics* **2017**, *11* (1), 016017. https://doi.org/10.1117/1.JNP.11.016017.

(14) Wu, J.; Yang, Z.; Qiu, C.; Zhang, Y.; Wu, Z.; Yang, J.; Lu, Y.; Li, J.; Yang, D.; Hao, R.; Li, E.; Yu, G.; Lin, S. Enhanced Performance of a Graphene/GaAs Self-Driven near-Infrared Photodetector with Upconversion Nanoparticles. *Nanoscale* **2018**, *10* (17), 8023–8030. https://doi.org/10.1039/c8nr00594j.

(15) Lin, F.; Cui, J.; Zhang, Z.; Wei, Z.; Hou, X.; Meng, B.; Liu, Y.; Tang, J.; Li, K.; Liao, L.; Hao, Q. GaAs Nanowire Photodetectors Based on Au Nanoparticles Modification. *Materials (Basel).* **2023**, *16* (4), 1735. https://doi.org/10.3390/ma16041735.

(16) Kesaev, V.; Nastulyavichus, A.; Kudryashov, S.; Kovalev, M.; Stsepuro, N.; Krasin, G. Nanopatterned Silicon Exhibiting Partial Polarization and Chirality. *Opt. Mater. Express* **2021**, *11* (7), 1971. https://doi.org/10.1364/ome.428047.

List of publications and conferences attended

Publications

[1] **Mangababu Akkanaboina**, Dipanjan Banerjee, Kanaka Ravi Kumar, R Sai Prasad Goud, Venugopal Rao Soma, SVS Nageswara Rao, Gold Nanoparticles Coated LIPSS on GaAs for Trace Detection of RDX and Tetryl, Surfaces and Interfaces 36, 102563 (2023); https://doi.org/10.1016/j.surfin.2022.102563.

[2] **A. Mangababu**, Dipanjan Banerjee, Kanaka Ravi Kumar, R. Sai Prasad Goud, Venugopal Rao Soma, and S. V. S. Nageswara Rao, Comparative study of GaAs nanostructures synthesized in air and distilled water by picosecond pulsed laser ablation and application in hazardous molecules detection. Journal of Laser Applications 34, 032014 (2022); https://doi.org/10.2351/7.0000750.

[3] **A Mangababu**, R Sai Prasad Goud, Chandu Byram, Jagannath Rathod, Dipanjan Banerjee, Venugopal Rao Soma, SVS Nageswara Rao. Multifunctional gallium arsenide nanoparticles and nanostructures fabricated using picosecond laser ablation. Applied Surface Science, Volume 589, July 2022, 152802; https://doi.org/10.1016/j.apsusc.2022.152802.

[4] **A. Mangababu**, Ch. Sianglam, B. Chandu, DK Avasthi, S. Venugopal Rao, M. Motapothula, and S. V. S. Nageswara Rao. Effects of Initial Grain Size and Laser Parameters on HfO_2 Nanoparticles Prepared Using Femtosecond Laser Ablation in Liquids.
Journal of Electronic Materials Volume 50, (2021), 1742–1751; https://doi.org/10.1007/s11664-020-08610-zÓ2021.

[5] **A. Mangababu**, G. Sarang Dev, B. Chandu, M.S.S. Bharati, S. Venugopal Rao, and S.V.S. Nageswara Rao. Structural Investigations of Picosecond Laser Ablated GaAs Nanoparticles in Different Liquids. Nanostructures & Nano-Objects, Volume 23, July 2020, 100509; https://doi.org/10.1016/j.nanoso.2020.100509.

[6] **A. Mangababu**, G. Sarang Dev, B. Chandu, M.S.S. Bharati, P. Debashish, S. Venugopal Rao, and S.V.S. Nageswara Rao. Fabrication and Characterization of GaAs Nanoparticles Achieved using Femtosecond Laser Ablation. Materials Today: Proceedings, 2020; https://doi.org/10.1016/j.matpr.2020.05.727.

[7] **A. Mangababu**, N. Arun, K Vinod Kumar, S.V.S. Nageswara Rao. Metal Nanoparticles in Dielectric Media: Physical Vapor Deposited HfO2 & Ag Multilayers for MOS Device and SPR Applications, AIP Conference Proceedings 2265, 030271 (2020); https://doi.org/10.1063/5.0016821.

[8] **Mangababu Akkanaboina**, S.A. Khan, S.V.S. Nageswara Rao, Venugopal Rao Soma, Amit Chawla, Deepti, Devesh Kumar Avasthi, Swift Heavy Ion irradiated Pd_Au Nanocomposite Thin Films for SERS Applications, 2022 International Conference on Electrical Engineering and Photonics (EExPolytech), 2022, pp. 293-296; https://doi.org/10.1109/EExPolytech56308.2022.9951002.

[9] **Mangababu Akkanaboina**, Dipanjan Banerjee, Kanaka Ravi Kumar, R Sai Prasad Goud, Venugopal Rao Soma, SVS Nageswara Rao, Sub-100 nm DNA-like Surface Structures on Femtosecond Laser Irradiated GaAs in Distilled Water and Sensing Application (Under review, Optics Letters).

Co-Authored Publications

[1] Kanaka Ravi Kumar, Dipanjan Banerjee, **A Mangababu**, R Sai Prasad Goud, AP Pathak, Venugopal Rao Soma, SVS Nageswara Rao, Resistivity dependence on nanostructure formation in picosecond ablation of silicon and SERS-based sensing applications, *J. Phys. D: Appl. Phys.* 55 405103; https://doi.org/10.1088/1361-6463/ac818b.

[2] Chandu Byram, Jagannath Rathod, Sree Satya Bharati Moram, **Akkanaboina Mangababu**, Venugopal Rao Soma. Picosecond Laser-Ablated Nanoparticles Loaded Filter Paper for SERS-Based Trace Detection of Thiram, 1, 3, 5-Trinitroperhydro-1, 3, 5-triazine (RDX), and Nile blue. Nanomaterials, 2022, Volume 12 Issue 13; https://doi.org/10.3390/nano12132150.

[3] Jagannath Rathod, Chandu Byram, Ravi Kumar Kanaka, Moram Sree Satya Bharati, Dipanjan Banerjee, **Mangababu Akkanaboina**, Venugopal Rao Soma. Hybrid Surface-Enhanced Raman Scattering Substrates for the Trace Detection of Ammonium Nitrate, Thiram, and Nile Blue. ACS Omega, Volume 7 (2022) 18, 15969–15981; https://doi.org/10.1021/acsomega.2c01095.

[4] Dipanjan Banerjee, **Mangababu Akkanaboina**, Subhasree Ghosh, Venugopal Rao Soma. Picosecond Bessel Beam Fabricated Pure, Gold-Coated Silver Nanostructures for Trace-

Level Sensing of Multiple Explosives and Hazardous Molecules. Materials 2022, 15(12), 4155; https://doi.org/10.3390/ma15124155.

[5] Dhanunjaya Munthala, **A. Mangababu**, SVS Nageswara Rao, S Pojprapai, AP Pathak, DK Avasthi. Swift heavy ion assisted growth of silver nanoparticles embedded in hafnium oxide matrix. Journal of Applied Physics 130, 044301 (2021); https://doi.org/10.1063/5.0054846.

[6] N Arun, LD Sangani, K Vinod Kumar, **A Mangababu**, M Ghanashyam Krishna, AP Pathak, SVS Nageswara Rao, Effects of swift heavy ion irradiation on the performance of HfO2-based resistive random access memory devices, Journal of Materials Science: Materials in Electronics volume 32, p2973–2986 (2021); https://doi.org/10.1007/s10854-020-05049-0.

[7] N. Arun, K. Vinod Kumar, **A. Mangababu**, S. V. S. Nageswara Rao & A. P. Pathak. Influence of the bottom metal electrode and gamma irradiation effects on the performance of HfO_2-based RRAM devices, Radiation Effects and Defects in Solids, (2019) 174:1-2, 66-75; https://doi.org/10.1080/10420150.2019.1579213.

[8] K. Vinod Kumar, N. Arun, **A. Mangababu**, Sunil Ojha, S. V. S. Nageswara Rao & A. P. Pathak. 120 MeV Ag ion irradiation induced intermixing, grain fragmentation in HfO_2/GaO_x thin films and consequent effects on the electrical properties of HfO_2/GaO_x/Si-based MOS capacitors, Radiation Effects and Defects in Solids, (2020) 175:1-2, 150-159; https://doi.org/10.1080/10420150.2020.1718140.

[9] Shristi Bist, Ratnesh K Pandey, Sejal Shah, **A Mangababu**, Parswajit Kalita, Amit Chawla, Devesh Kumar Avasthi, Behavior of Tungsten Carbide thin Films Grown at Different Substrate Temperatures, 2022 International Conference on Electrical Engineering and Photonics (EExPolytech), St. Petersburg, Russian Federation, 2022, pp. 297-300; https://doi.org/10.1109/EExPolytech56308.2022.9951001.

[10] D Banerjee, **A Mangababu**, R Beeram, RK Kanaka, VR Soma, Femtosecond Bessel Beam Produced Bimetallic Nanoparticles for Nonlinear Optical Switching and Sensing Applications, Technical Digest Series (Optica Publishing Group, 2022), paper FW6C.5; https://doi.org/10.1364/FIO.2022.FW6C.5.

[11] R Beeram, D Banerjee, **A Mangababu**, SV Rao, Femtosecond Laser Processed Web-like Silicon Nanostructures and Application in Surface Enhanced Raman Spectroscopy, Conference on Lasers and Electro-Optics/Pacific Rim, CThP5D_04.

Presentations in National/International Conferences/Workshops

[1] **Mangababu Akkanaboina**, S.A. Khan, S.V.S. Nageswara Rao, Venugopal Rao Soma, Amit Chawla, Deepti, Devesh Kumar Avasthi, Swift Heavy Ion irradiated Pd_Au Nanocomposite Thin Films for SERS Applications, International Conference on Electrical Engineering and Photonics, **EExPolytech-2022 [Oral Presentation]**.

[2] **Mangababu Akkanaboina**, Kanaka Ravi Kumar, Dipanjan Banerjee, R. Sai Prasad Goud, Venugopal Rao Soma, S.V.S. Nageswara Rao, The Role of Laser Fluence on the Quality and Periodicity of LIPSS on Gallium Arsenide Achieved by Femtosecond Laser Ablation Technique, Symposium on Electronics for Self-Reliance, **ESR-2023 [Poster Presentation].**

[3] **A. Mangababu**, Kanaka Ravi Kumar, Dipanjan Banerjee, R. Sai Prasad Goud, Venugopal Rao Soma, S.V.S. Nageswara Rao, Picosecond Laser Ablated GaAs Surface Structures for Antireflective and SERS Applications, International Conference of Frontier Areas of Science and Technology, **ICFAST-2022 [Poster Presentation].**

[4] **A. Mangababu**, Dipanjan Banerjee, Ravi Kumar Kanaka, R. Sai Prasad Goud, S. Venugopal Rao, and S.V.S. Nageswara Rao, Picosecond Laser Ablated GaAs Nanostructures in Air and Distilled Water for Detection of trace level molecules, International Congress on Applications of Lasers & Electro-Optics, **ICALEO-2022 [Oral Presentation].**

[5] **A. Mangababu,** N. Arun, K. Vinod Kumar, A. P. Pathak, and S. V. S. Nageswara RaoMetal Nanoparticles in Dielectric Media: Physical Vapor Deposited HfO_2 & Ag Multilayers for MOS Device and SPR Applications, 64^{th} DAE Solid State Physics Symposium, **DAE SSPS-2019 [Poster Presentation]**.

[6] M. Dhanunjaya, **A. Mangababu**, S.V.S. Nageswara Rao, Partha Ghosal, D.K. Avasthi and A.P. Pathak, 100 MeV Ag Ion Induced Silver Nanoparticles Embedded in Hafnium Oxide Matrix, Indo French seminar on Radiation Damage in Nuclear Materials, **RADIUM-2019 [Poster Presentation]**.

[7] **A. Mangababu**, CH. BinduMadhuri, A. P. Pathak, B. Sundaravel, S. Venugopal Rao, and S.V.S. Nageswara Rao, Comparative Study of Defect Passivation of H^+ and He^+ Ions in GaAs by using Raman Spectroscopy and Coherent Acoustic Phonon (CAP) Spectroscopy, 5^{th} International Conference on Nano structuring by Ion Beams, **ICNIB2019** [**Poster Presentation**].

[8] **A. Mangababu**, G. Sarang Dev, B. Chandu, M.S.S. Bharati, P. Debashish, S. Venugopal Rao, S.V.S. Nageswara Rao, Fabrication and characterization of GaAs nanoparticles achieved using femtosecond laser ablation, SCICON 19 International Conference on Material Science **[Poster presentation by co-author].**

Plagiarism-free statement

This is to certify that the thesis titled "**Studies on the Fabrication of GaAs Nanoparticles and Nanostructures by Ultrafast Laser Ablation: Applications in SERS and Photonics**" has been screened by the Turnitin software at the Indira Gandhi Memorial Library of the university of Hyderabad. The software shows a 25% similarity index, out of which 20% came from the student's own research articles related to this thesis, which are already published and available online. Thus, the effective similarity index excluding his research articles is 25% - 20= 5%, which is lower than the 10% stipulated by the university guidelines. Therefore, this thesis maybe considered free from plagiarism as per guidelines.

S.V.S. Nageswara Rao 22/06/2023.

Prof. S V S Nageswara Rao

Prof. S.V.S. NAGESWARA RAO
School of Physics
University of Hyderabad
Hyderabad-500 046, INDIA

Thesis Supervisor,
School of Physics,
University of Hyderabad.

Studies on the Fabrication of GaAs Nanoparticles and Nanostructures by Ultrafast Laser Ablation: Applications in SERS and Photonics

by Akkanaboina Mangababu

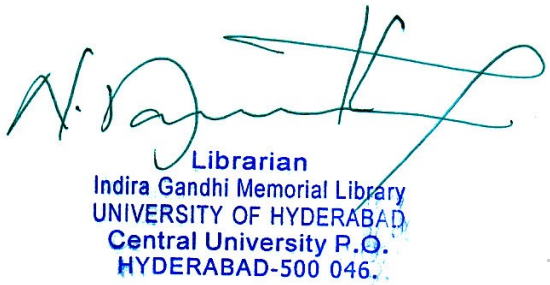

Studies on the Fabrication of GaAs Nanoparticles and Nanostructures by Ultrafast Laser Ablation: Applications in SERS and Photonics

ORIGINALITY REPORT

25%	4%	24%	1%
SIMILARITY INDEX	INTERNET SOURCES	PUBLICATIONS	STUDENT PAPERS

PRIMARY SOURCES

1	A. Mangababu, Ch. Sianglam, B. Chandu, D. K. Avasthi, S. Venugopal Rao, M. Motapothula, S. V. S. Nageswara Rao. "Effects of Initial Grain Size and Laser Parameters on HfO2 Nanoparticles Prepared Using Femtosecond Laser Ablation in Liquids", Journal of Electronic Materials, 2021 Publication	14%
2	A. Mangababu, G. Sarang Dev, B. Chandu, M.S.S. Bharati, S. Venugopal Rao, S.V.S. Nageswara Rao. "Structural investigations of picosecond laser ablated GaAs nanoparticles in different liquids", Nano-Structures & Nano-Objects, 2020 Publication	3%
3	A. Mangababu, R. Sai Prasad Goud, Chandu Byram, Jagannath Rathod, Dipanjan Banerjee, Venugopal Rao Soma, S.V.S. Nageswara Rao. "Multi-functional gallium arsenide nanoparticles and nanostructures fabricated	2%

(S. T. O).

using picosecond laser ablation", Applied Surface Science, 2022
Publication

4	www.researchgate.net Internet Source	1 %
5	Mangababu Akkanaboina, Dipanjan Banerjee, Kanaka Ravi Kumar, R. Sai Prasad Goud, Venugopal Rao Soma, S. V. S. Nageswara Rao. "Gold nanoparticles coated LIPSS on GaAs for trace detection of RDX and Tetryl", Surfaces and Interfaces, 2023 Publication	1 %
6	Dongshi Zhang, Bilal Gökce, Stephan Barcikowski. "Laser Synthesis and Processing of Colloids: Fundamentals and Applications", Chemical Reviews, 2017 Publication	1 %
7	A. Mangababu, G. Sarang Dev, B. Chandu, M.S.S. Bharati, P. Debashish, S. Venugopal Rao, S.V.S. Nageswara Rao. "Fabrication and characterization of GaAs nanoparticles achieved using femtosecond laser ablation", Materials Today: Proceedings, 2020 Publication	<1 %
8	Handbook of Nanoparticles, 2016. Publication	<1 %
9	Submitted to Panjab University Student Paper	

(P.T.O).

		<1 %
10	Submitted to University of Nottingham Student Paper	<1 %
11	dspace.uohyd.ac.in Internet Source	<1 %
12	eprints.soton.ac.uk Internet Source	<1 %
13	www.fedoa.unina.it Internet Source	<1 %
14	A. Mangababu, Dipanjan Banerjee, Kanaka Ravi Kumar, R. Sai Prasad Goud, Venugopal Rao Soma, S. V. S. Nageswara Rao. "Comparative study of GaAs nanostructures synthesized in air and distilled water by picosecond pulsed laser ablation and application in hazardous molecules detection", Journal of Laser Applications, 2022 Publication	<1 %
15	Submitted to Chester College of Higher Education Student Paper	<1 %
16	Maofeng Zhang, Zhiyuan Zheng, Honghui Liu, Dapeng Wang, Tun Chen, Jiaqin Liu, Yucheng Wu. "Rationally Designed Graphene/Bilayer Silver/Cu Hybrid Structure with Improved	<1 %

(P.T.O).

Sensitivity and Stability for Highly Efficient SERS Sensing", ACS Omega, 2018
Publication

17	Muidh Alheshibri, Sultan Akhtar, Abbad Al Baroot, Khaled Elsayed, Hassan S Al Qahtani, Q.A. Drmosh. "Template-free, single step preparation of hollow Coo nano spheres using pulsed laser ablation in liquid environment", Arabian Journal of Chemistry, 2021 Publication	<1 %
18	"Nanomaterials", Wiley, 2012 Publication	<1 %
19	Sree Satya Bharati Moram, Jagannath Rathod, Dipanjan Banerjee, Venugopal Rao Soma. "Ultrafast Laser-Ablated Nanoparticles and Nanostructures for Surface-Enhanced Raman Scattering-Based Sensing Applications", Journal of Visualized Experiments, 2023 Publication	<1 %
20	research-information.bris.ac.uk Internet Source	<1 %
21	www.jwent.net Internet Source	<1 %
22	Dongshi Zhang, Zhuguo Li, Koji Sugioka. "Laser ablation in liquids for nanomaterial synthesis: Diversities of targets and liquids", Journal of Physics: Photonics, 2021 Publication	<1 %

23	lup.lub.lu.se Internet Source	<1%

Exclude quotes	On	Exclude matches	< 14 words
Exclude bibliography	On		